

**UNIVERSITA' DEGLI STUDI DI NAPOLI**

**“FEDERICO II”**



**DOTTORATO DI RICERCA XVIII CICLO**

**INGEGNERIA CHIMICA DEI MATERIALI E DELLA  
PRODUZIONE**

**Surface and Inter-phase Analysis of Composite  
Materials using Electromagnetic Techniques  
based on SQUIDs Sensor**

Coordinatore del dottorato

Ch.mo Prof

NINO GRIZZUTI

Il candidato

**CARMELA BONAVOLONTÀ**

ANNO ACCADEMICO 2005 – 2006

# Contents

<b>Introduction</b> .....	i
---------------------------	---

## *Chapter 1: SQUIDs (Superconductive Quantum Interference Device)*

Introduction.....	1
1. Superconductivity .....	1
2. Flux quantization.....	5
3. Josephson junction .....	5
3.1 Josephson effect.....	8
4. DC SQUID .....	15
5. Noise in DC SQUID .....	20
6. Flux-Locked Loop (FLL) .....	23
7. DC SQUID magnetometer .....	28
8. Gradiometers .....	36

## *Chapter 2: Advanced Non-Destructive Testing*

Introduction .....	49
1. NDE .....	50
2. Eddy current technique.....	68
3. SQUID NDE applications .....	75
4. NDE prototype based on HTS dc-SQUID magnetometer .....	80
5. Zero field detector.....	84

## *Chapter 3: Composite Materials*

Introduction .....	93
1. Fiber-reinforced polymer composite .....	93
2. Fabrication in fiber-reinforced polymers.....	97

3. Mechanical properties .....	100
4. Applications.....	102
5. NDE of composite materials.....	104
6. Test specimens.....	107

**Chapter 4: Electromagnetic characterization of Carbon Fiber Reinforced Polymers (CFRPs)**

Introduction .....	110
1. Electrical Conductivity.....	112
2. Electromagnetic properties.....	116
3. Atomic force microscopy (AFM) analysis.....	121
4. Electromechanical effect.....	127
5. Impact loading.....	131
6. Magnetic Imaging.....	138
6.1 The Artificial Neural Network (ANN) system.....	139
6.2 Magnetic flux imaging.....	145
7. Conclusions.....	151

**Chapter 5: Fiber-glass aluminium (FGA) laminates electromagnetic characterization.**

Introduction.....	156
1. Impact loading detection.....	157
2. Modelization of corrosion activity in fiberglass laminates.....	165
3. Conclusions .....	172
<b>Conclusions .....</b>	<b>175</b>

# Ringraziamenti

Sono molte le persone che desidero ringraziare per avermi accompagnata durante lo svolgimento di questa tesi di dottorato. Ringrazio i professori A. Barone, G. Peluso e G.P. Pepe per le utili discussioni scientifiche e suggerimenti che hanno contribuito a migliorare questo lavoro.

Ringrazio il prof. G. Caprino e la Dr. V. Lopresto, del Dipartimento di Scienza dei Materiali, per i brillanti suggerimenti e le utili indicazioni necessarie per comprendere e interpretare al meglio la risposta magnetica dovuta alle caratteristiche meccaniche e strutturali dei materiali analizzati.

Ringrazio anche il professore V. Palmieri, dell'Istituto Nazionale di Fisica Nucleare (INFN) di Legnaro (Padova), per aver fornito il materiale necessario per l'analisi dei processi corrosivi nonché per gli indispensabili consigli e discussioni relativi allo studio della corrosione di superfici metalliche. Inoltre, lo ringrazio per aver sempre apprezzato il mio lavoro, e per l'incoraggiamento e le opportunità che hanno contribuito alla mia formazione scientifica.

Rivolgo un doveroso ringraziamento al sig. A. Maggio e sig. S. Marrazzo, dell'officina meccanica del CNR-INFM di Napoli, per l'efficienza del loro lavoro che ha reso possibile l'ottimizzazione del sistema sperimentale utilizzato nell'attività di ricerca.

Vorrei ringraziare anche il Dr. G. Lamura, Dr. M. Barra e Dr. A. Prigiobbo che con la loro simpatia e disponibilità mi sono stati vicini e mi hanno aiutata a superare anche i momenti difficili. Ringrazio tutti gli amici: Dr. G.M De Luca, Dr. F. Chiarella, Ing. M. Aurino, Dott. G. Cifariello, Dott. P. D'Angelo, e il Dr. A. Cassinese che con la loro allegria hanno contribuito a rendere piacevole l'intero periodo di dottorato.

Un ringraziamento particolare è rivolto all' Ing. M. Valentino, l'unica persona che in questi anni ha condiviso pienamente con me l'attività di ricerca. Gli sono grata per avermi trasmesso i contenuti scientifici indispensabili affinché il lavoro di tesi venisse svolto nel migliore dei modi. Lo ringrazio per le molteplici discussioni, per i brillanti suggerimenti, per aver saputo mantenere viva in me la passione e la curiosità necessarie in una attività sperimentale. Inoltre, gli devo un grazie particolare per la fiducia che ha sempre dimostrato nelle mie capacità, per la disponibilità e la dedizione con cui ha seguito il lavoro di tesi, e infine per le numerose opportunità che mi ha offerto perché io potessi raggiungere i migliori risultati possibili durante questo mio percorso di formazione scientifica.

*Ai miei genitori*

*“Se vuoi vincere il mondo, vinci te stesso”*

*Fëdor Dostoevskij*

## INTRODUCTION

In this research activity an electromagnetic characterization and a non-destructive evaluation of new advanced composite materials, Carbon Fiber Reinforced Polymers (CFRP) and Fiber-Glass Aluminium (FGA) laminates, using an eddy-current technique based on HTS dc-SQUID (Superconductive QUantum Interference Device) magnetometer is proposed.

The thesis has been performed in the CNR-INFM laboratory of Coherentia research center of Naples (Italy), where the NDE SQUID based prototype was realized. The work has been developed in the framework of the Italian MURST project “*Analisi non distruttive su materiali compositi strutturali per l’industria aeronautica*”, in collaboration with the Department of Materials and Production Engineering (DIMP), where the impacts loading was performed, and Alenia s.p.a that provides the test samples.

The main goal of this thesis is to propose a prototype based on a superconducting sensor, such as SQUID, to guarantee a more accuracy in the quality control at research level of the composite materials employed in the aeronautical applications. Today, the aerospace and aeronautical industry pays much attention to improve flight safety of the airlines. In aircraft design it is important to couple low structural weight with high damage tolerance. For this reason, a new class of advanced composite materials, characterized by a combination of metallic alloys and polymeric matrix layers, or carbon fiber and epoxy resin, are increasingly used.

Composite materials, specifically Carbon Fibre Reinforced Polymers (CFRPs), offer excellent mechanical behaviour, good damage tolerance, high strength and rigidity with low weight, good corrosion resistance and suitability for the production of complex-shape components with reduced manufacture time. However, due to low inter-laminar strength fibre composites are susceptible to delamination during manufacturing or in service. CFRPs are capable of absorbing the energy of impact thanks to the presence of a polymeric matrix that distributes the energy in the material. In this way the impact at first stage doesn’t produce a perforation of the composite structure, but may cause internal damage such as delamination, that is not visible to naked eyes. The presence and the growth of delamination may produce severe stiffness reduction in the structure, leading to a catastrophic failure. Delamination may be produced, for example, by runway debris, hail, maintenance damage (i.e., dropped tools) and bird strikes. Frequently, delaminations between the layers can develop in fibre fractures with no

visible surface manifestation. The degree of damage depends on various factors, for example, the energy of the impact, the thickness of structures and the fibre orientation of layers in the composite.

The other material tested in this work is one of the most widely used FGA, commercially called GLARE<sup>®</sup> (GLASS REinforced), which consists of alternating thin aluminium alloy layers and glass fibres pre-peg. The latter is a reinforced-plastics term for the reinforcing material that contains or is combined with the full complement of resin before the molding operation. The main advantages of FGAs are superior fatigue behavior with respect to conventional metallic alloys, better damage tolerance, inherent resistance to corrosion and good fire resistance to improve safety. In particular, FGA exhibit slower crack growth rate with respect to their monolithic constituents. This is mainly due to the fibres, which form a bridge at the crack tip, delaying crack growth. Consequently, longer inspection intervals can be adopted in service, and lowering maintenance costs.

Since FGA are employed principally in aircraft fuselage structures, which are prone to accidental impacts, it is important to investigate their damage features due to such impacts. Thanks to the plasticity of the aluminium layers, resulting in an evident indentation at the impact site, the deformation due to an impact event can be easily detected by visual inspection. However, this technique does not allow to detect internal defect of the aluminium layers.

Because of the increasing utilization of the composite materials in structural applications, the non destructive evaluation (NDE) of the CFRPs and FGAs receive considerable research and development attention.

Due to the heterogeneous nature of composites, the form of defects is often very different from metal, and fracture mechanism is more complex. For this reason suitable inspection techniques are required to assess the damage extent in the CFRPs and FGA composites. Usually, the conventional non destructive evaluation show limits to detect the possible cracking of hidden aluminium sheets in the FGA and the delamination inside the CFRPs.

However, to detect internal damage in FMLs, an ultrasonic (US) technique, eddy currents, and dye penetrants have been used. The latter method is only partially non-destructive, requiring the drilling of a small hole through the aluminium sheet into the pre-peg layers. In regard to FMLs, US exhibits some limitations because of the large acoustic impedance mismatch between metal and fibre reinforced layers. On the other

hand, the conventional eddy currents inspection fails due to the large indentation of the FGA surface. The surface deformation of the sample increases the lift off between probe and sample. This effect arises from the loss of coupling between coil and sample that reduces the sensitivity of the induction coil.

The low electrical conductivity and high anisotropy of CFRP composites generally doesn't allow conventional techniques, such as traditional ultrasound, thermography and eddy current with induction coils, to detect early stage damage in composite samples. In fact, the thermography was found unreliable when it tests bonded joints with a narrow gap between the unbounded surface, and when the damage in the material is few millimetres in depth. On the other hand, the ultrasound technique is not very sensitive when the material has a rough surface and a layered structure without using any coupling medium. Moreover, the eddy current technique shows a reduction of the sensitivity of induction coil to evaluate deep flaws in structures characterized by a low electrical conductivity.

The HTS SQUID probe can be considered as a suitable improvement to the conventional induction coil employed into electromagnetic technique. In fact, SQUIDS sensor can overcome the limitation related to the low frequency and the variation of lift off that obstruct the induction coil measurements. The success of the electromagnetic technique based on SQUID sensors to detect delaminations in CFRPs materials is principally due to the electromechanical effect presented in the carbon fibers. A range of experimental results over the last decade has shown that the mechanical deformation and the electrical resistance of CFRPs are coupled. Both the mechanical properties and the level of damage of CFRPs are correlated to the electrical conductivity of the reinforcing carbon fibres. It was demonstrated that the variation of fibres distance or fibres breakage changes the resistivity of the reinforced composite. In this way delaminations and fibre breakage alter the electrical conductivity of the material, producing a variation of the current distribution and consequently a change of the corresponding magnetic signal.

At present, HTS SQUID as magnetometer and gradiometer have been applied successfully to detect internal cracks and delamination in composite materials and traditional laminates, and to study the ongoing corrosion of the aluminium alloy plates for aeronautical applications. Moreover, the HTS SQUID magnetometer is characterized by high field sensitivity in an unshielded environment (about 0.2 pT/Hz<sup>1/2</sup>) and a wide dynamic range, about 130 dB. Thanks to these features, the HTS

SQUID analysis allows us to evaluate very small magnetic field variations produced by small cracks.

The thesis is divided in five chapters. In the first one a complete description of the SQUID properties and its basic working principles, flux quantization and the Josephson Effect, has been reported. Moreover, the DC SQUIDs electronics, its possible configurations, magnetometer and gradiometer, and the noise characterization are described.

The second chapter is dedicated to an overview of the most widely used non-destructive technique employed in several industrial and research fields. Particular attention is given to the eddy current testing, the technical improvement and the advantage obtained using SQUID in NDE. Moreover, the eddy current technique prototype system based on a HTS dc-SQUID magnetometer has been described, and the particular configurations between the excitation coil and the SQUID magnetometer are shown.

The third chapter is dedicated to the description of the composite materials properties, in particular the structural characteristics and the industrial applications of CFRPs and FGAs are shown.

The fourth and fifth chapters are dedicated to the experimental results of the electromagnetic characterization of the CFRPs and FGA composites. The electromagnetic characterization of the composite materials has been focused principally on the investigation of the damage due to impact loading, and the corrosion process of the metallic surface.

The investigation on the CFRPs composites starts from the study of the electrical properties, in particular the evaluation of the electrical conductivity and its variation respect to mechanical stress has been carried out. The effect of the impact loading on the surface and inter-phase of this composite has been analysed using the SQUID based prototype and other comparative technique, such as eddy currents using induction coil and ultrasounds. Moreover, the adhesion fiber-matrix has been analysed using an atomic force microscopy (AFM) too. This analysis aim to understand the relation between the damage process of the CFRPs and the dislocation of the fiber into the polymeric matrix.

In the last chapter the results obtained with the SQUID based prototype concerning the characterization of the FGA materials have been reported. The prototype capability to distinguish the different defects due to impact loading at several impact energies has been tested. Moreover, in a first approach to study the effects of the corrosion activity, that can take place on the FGA damaged aluminum surface, a copper made mock-up

was fabricated. In this way it was possible to amplify the corrosion activity and verify the magnetic field sensitivity to the ongoing corrosion process. The mock-up allows us to study two simple geometric configurations that can be modeled to calculate the current distribution during the corrosion process. The current distribution was obtained via electromagnetic inversion of the measured magnetic field. Finally, it is important to note that the copper made mock-up is useful to optimize the measurement set up and the magnetic field inversion algorithm for a future study of the FGAs corrosion activity.

# Chapter 1

## SQUIDs (Superconductive Quantum Interference Device)

### Introduction

*Superconducting Quantum Interference Devices*, are an extremely sensitive magnetic flux-to-voltage transducer and are used to measure extremely tiny magnetic fields. The extreme sensitivity of the SQUID has caused it to be incorporated into a great variety of systems for biomagnetic applications in magnetoencephalography, magnetocardiography and for geomagnetism, non destructive testing, radio frequency amplification and the measurement of fundamental constants. The focus of this chapter is on the description of working principle of the SQUIDs, concerning the applications on NDE system. Starting from a briefly introduction on the main superconductivity properties, the two main principles on which the SQUID is based: the flux quantization of a superconducting loop and the Josephson Effect, are described. In this chapter the attention is particularly focused on the description of DC SQUID which is reported in the third section follows by an overview of the noise sources that affect this device. The Flux Locked Loop (FLL), largely used to linearize the SQUID output, is introduced in the fifth section. The last two paragraph of this chapter are dedicated to overview the possible configuration of DC SQUID sensors: magnetometer and gradiometer. The basic characteristics, the advantages and drawbacks of these devices basically fabricated on HTS materials are reported.

### 1. Superconductivity

In 1908, the physicist Kammerlingh Onnes in Leiden successfully liquefied helium by cooling it to 4K, after that sufficiently low temperature was available. In 1911, Onnes

began to investigate the electrical properties of metals in extremely cold temperatures, measuring the electrical resistance of very pure mercury wire steadily lowered the temperature. The results of this investigation were unexpected: the resistance disappeared completely in a narrow temperature range across 4.2 K.

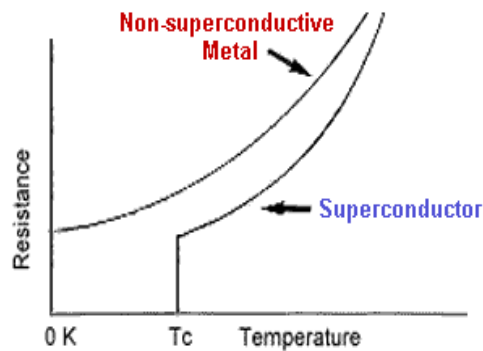


**Figure 1:** Electric resistance versus temperature in normal metallic and superconducting material.

Onnes asserted that the mercury had passed into a new discovered state, which on account of its extraordinary electrical properties, he called the superconductive state. Therefore, while in a normal metallic substance the resistivity reaches a residual value, in superconductors the resistivity is zero for temperature lower than its critical temperature,  $T_C$  that represents the temperature at which a superconductor loses its resistance (Figure 1) [1-3].

The loss of electrical resistance means for superconductors its ability to conduct electricity without the loss of energy. The microscopic interpretation of superconductivity was advanced in 1957 by three American physicists - John Bardeen, Leon Cooper, and John Schrieffer- through their Theories of Superconductivity, know as the *BCS Theory* [4-6]. This theory explains superconductivity at temperatures close to absolute zero. Cooper realized that atomic lattice vibrations were directly responsible for unifying the entire current. They forced the electrons to pair up into pairs that could pass all of the obstacles which caused resistance in the conductor. These pairs of electrons are known as *Cooper pairs*. Cooper and his co-workers knew that electrons normally repel one another but in superconductors there is an attractive force between the electrons of opposite spin and momentum that overcome the repulsion, due to the Coulomb's law, enabling them to form pairs. The Cooper pairs are able to move through the material effectively without being scattered, and thus carry a supercurrent with no energy loss. Therefore, while in metallic materials the current is due to single

electrons in a superconductor it is a flow of electron pairs, characterized by wave function,  $\Psi$ , with an spatial extension of about  $10^{-4}$  cm, called coherence length, and a phase  $\theta$ . The remarkable property of the superconductors is that all electron pairs have the same wave function, thus forming a macroscopic quantum state with a phase coherence extending throughout the material.

Another characteristic of the superconducting state is the *Meissner effect* [4,6]. When a superconductor is placed in a weak external magnetic field  $\mathbf{H}$ , the field penetrates the superconductor for only a short distance  $\lambda$  (typically of order of 10nm), called the penetration depth, after which it decays rapidly to zero. The Meissner effect is due to shielding currents arise in the superconductor surface. These currents create a field both inside and outside the superconductor such that on the inside the applied and the induced fields exactly cancel, while outside they are added. The observed result is the expulsion of H-field: zero fields inside and an increased field outside the sample. It is important to note that the Meissner effect is distinct from the kind of diamagnetism expected in a perfect electrical conductor, because a superconductor expels all magnetic fields, not just those that are changing. The Meissner effect breaks down when the applied magnetic field is too large. Superconductors can be divided into two classes according to how this breakdown occurs.

In Type I superconductors, superconductivity is abruptly destroyed when the strength of the applied field rises above a critical value  $H_c$ . Depending on the geometry of the sample, one may obtain an intermediate state consisting of regions of normal material carrying a magnetic field mixed with regions of superconducting material containing no field. Examples of such materials are Hg, Al, Sn, Pb, Ga. Figure 2 (left) shows a sketch of this behaviour.

Type II superconductors differ from Type I in that their transition from a normal to a superconducting state is gradual across a region of "mixed state". Raising the applied field past a critical value  $H_{c1}$  leads to a mixed state in which an increasing amount of magnetic flux penetrates the material, but there remains no resistance to the flow of electrical current as long as the current is not too large. At a second critical field strength  $H_{c2}$ , superconductivity is destroyed (Figure 2 (right)). The mixed state is actually caused by vortices, sometimes called fluxons because the flux carried by these vortices is quantized.

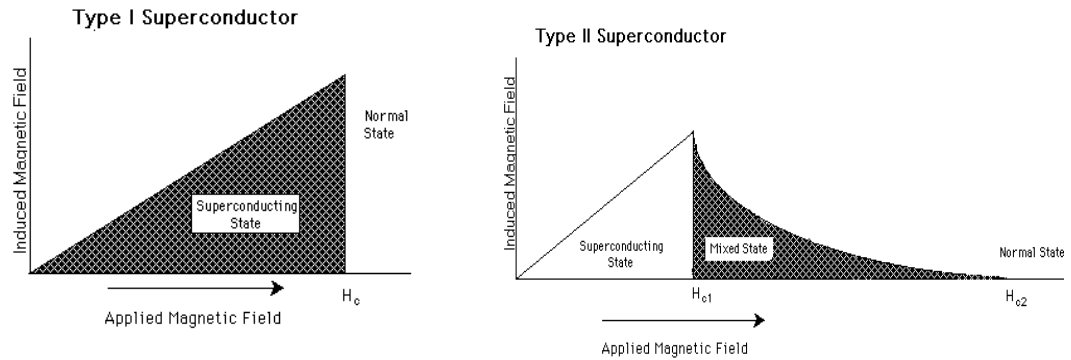


**Figure 2:** Variation of internal magnetic field with applied external magnetic field (H) for Type I and Type II superconductors.

Type II category of superconductors achieve higher critical temperature than the Type I examples are almost all impure and compound such as  $Nb_3Sn$ ,  $NbTi$  and all the cuprates. For the Type II the highest temperature attained at ambient pressure has been 138 K related to the compound  $(Hg_{0.8}Tl_{0.2})Ba_2Ca_2Cu_3O_{8.33}$ .

Depending on the transition temperature the superconductors can be differentiate as low- $T_c$  and high- $T_c$  superconductors. The discovery of the materials, such as ceramic oxide  $YBa_2Cu_3O_{7-x}$  with transition temperature above the boiling point of liquid nitrogen (77K) generated a worldwide furor to develop new superconducting technologies for both large and small scale applications. The interest for the new low temperature technology was driven by the perception that superconductors cooled in liquid nitrogen would quickly become much more widely applicable than superconductors cooled in liquid helium (4.2K), because liquid nitrogen is much cheaper and boils much more slowly than liquid helium. Today there are several example of large scale applications employed superconductivity, such as superconducting wires that are used in magnets for particle accelerators and magnetic resonance. Other prototype applications include cables for power transmission, large inductors for energy storage, power generators and electric motors, magnetically levitated trains [7]. On the other hand, one of the most important small scale application of the superconductivity regard the most sensitive magnetic field sensor so-called SQUID (Superconducting QUantum interference device). This device is successfully applied in biomagnetism, geophysics and non-destructive evaluation field, and it is the main object described in this chapter.

## 2. Flux quantization

If a superconducting ring, cooled below its  $T_c$ , is placed in a magnetic field, because of the Meissner effect, the field is forced out of the surface while remains in the hole. In other words, the superconducting ring entrapped the magnetic field. Field variations are forbidden by the law of electromagnetic induction; in fact, a change of magnetic field through the ring produces an induced current, obstructing any change. Since the ring is superconducting, the current does not attenuate, and therefore the magnetic flux remains unchanged. Moreover, the captured magnetic field appears to be able to take on only define values, in particular only an integer value of the unit flux  $\Phi_0=2.07 \times 10^{-15}$  Wb.  $\Phi_0$  is called flux quantum and it is a fundamental physical constant which is related to other fundamental constants by the relation:

$$\Phi_0 = \frac{\hbar c}{2e}$$

where  $\hbar$  the Plank constant,  $c$  is the velocity of light and  $e$  the electron charge. A magnetic flux is necessarily equal to a multiple number of quanta. This is the unique property of the superconducting ring only. Quantization of the flux through a ring can be considered an expression of quantum properties on large scales [8,9].

## 3. Josephson junction

When two superconductors are separated by a thin layer (on the scale of either the superconducting coherence length  $\xi$  or the penetration depth  $\lambda$ ), which can be an insulator, a normal conductor, or a constriction the superconductivity is weakened. Such a “weak link” is known as Josephson junction (JJ) [6].

A typical realization of a weak link is a SIS tunnel junction, consisting of two superconducting films, separated by a very thin oxide layer, typically 1-2 nm thick. The most commonly used superconductors are Nb and Pb, the critical current density of these junctions may be in the range  $10^3$ -  $10^4$  A/cm<sup>2</sup>, far below the typical critical current density of bulk superconductors, because the transport across the barrier is a tunnel process. Instead of a thin oxide layer other materials may be used, for instance a normal metal, corresponding to a SNS junction, in which case the metal layer can be much thicker. Another well established method is to create the whole system from a single superconductor, by splitting for example a continuous film into two regions, leaving just narrow constriction between, of typical dimension like the coherence length  $\xi$ . This

latter construction is called Dayem bridge. In this case the critical current density is the same in the bridge and in the bulk, but the overall critical current of the device is much lower than in two parts. This is sufficient to make it a weak link [9].

A recently developed method, specially suited for the high  $T_c$  superconductors, takes advantage of their very short, nanometer size coherence length  $\xi$ . In these superconductors a very narrow interruption of superconducting properties can be achieved by depositing a high  $T_c$  film across a naturally occurring grain boundary in a substrate like  $\text{SrTiO}_3$ .

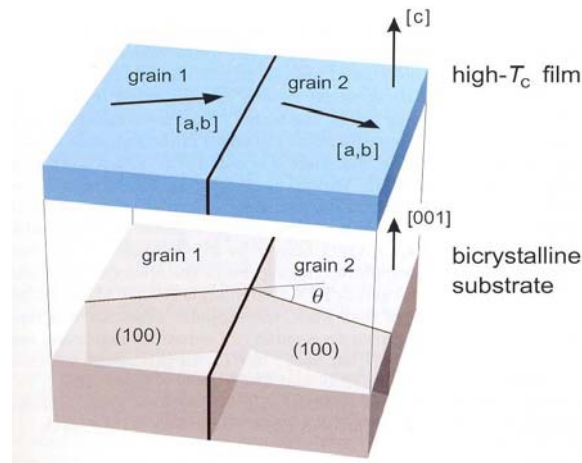


**Figure 3:** Sketch of thin-film bicrystal principle using the example of symmetric [001]-tilt grain boundary with grain boundary tilt angle  $\theta$ .

The grain boundary forced the superconductor to develop a chain of defects along the length of the grain boundary. Above the grain boundary, therefore, there is a weak link between the two parts of the superconductor film. Such contacts are commonly referred to as *grain boundary junctions* or *bicrystal junctions* (Figure 3) [10]. The grain boundaries are also nucleated by growing a high- $T_c$  film over a suitable step patterned into the substrate. Typically, two grain boundaries are nucleated at one substrate step, one at its bottom and one at its top. These grain boundaries are connected in series (see Figure 4). As the required substrate steps are easily defined by photolithography, for example by using an amorphous carbon mask and ion-beam etching or reactive ion-etching, such step-edge junctions can be positioned anywhere on the substrate. The stepheight is chosen to be larger than the film thickness, a characteristic value being 200-300 nm.

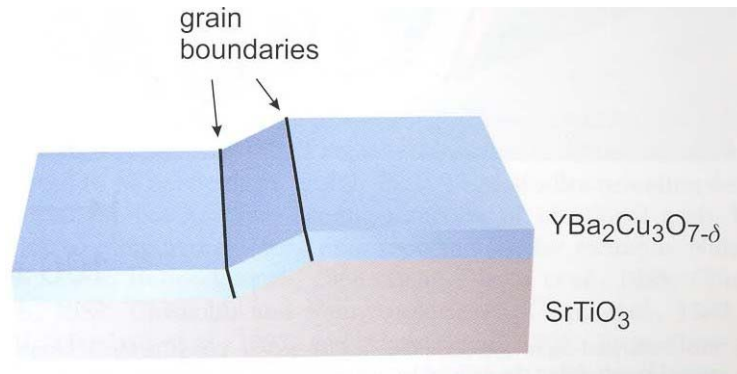


**Figure 4:** Sketch of step edge junction.

The step angle has been found to be a crucial parameter, as it controls the microstructure and the grain boundary configuration of the high- $T_c$  film [11,12]. Standard angles are in the range of 50-60°. The substrate materials is also of importance, because on some materials, e.g., MgO, the high- $T_c$  superconductors tends to grow with the [001]-axis parallel to the local substrate normal, giving rise to [100]-tilt boundaries with misorientation-angles determined by the slope of the substrate step edge, whereas on the other materials, e.g., SrTiO<sub>3</sub> and LaAlO<sub>3</sub>, the high- $T_c$  superconductors grow throughout with their [100] or [011]-axes parallel to the substrate [001]-direction, creating grain boundaries.

A technique was found to freely select the position of the grain boundary [13,14] so called biepitaxial process. This process utilizes changes of the orientation of high  $T_c$  films induced by epitaxial growth on structured template layers. Depending on the underlying layers, the high- $T_c$  films are rotated in-plane, resulting in rotational grain boundaries at the edge of the template structures, as shown schematically in Figure 5.

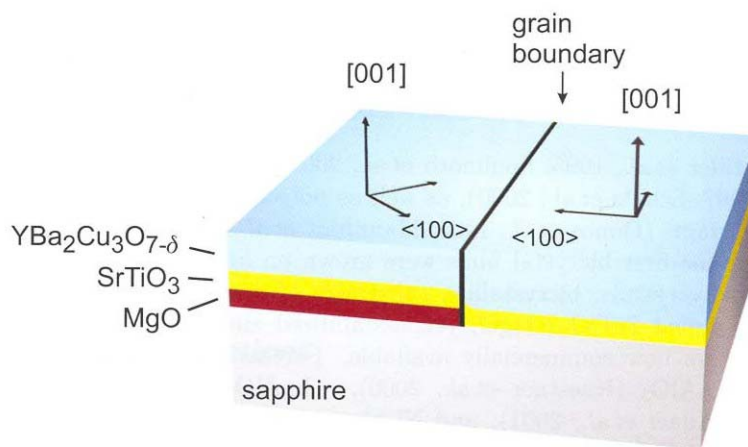


**Figure 5:** Sketch of biepitaxial principle as developed by Char et al.

Here it noted that Abacus grows with [001] parallel to [100] on SrTiO<sub>3</sub>, furthers various materials combinations can be employed to induce the variation of the in-plane orientation. In an alternative approach, a group at University of Naples uses (110)-oriented SrTiO<sub>3</sub> substrates and MgO seed layers (Figure 6)

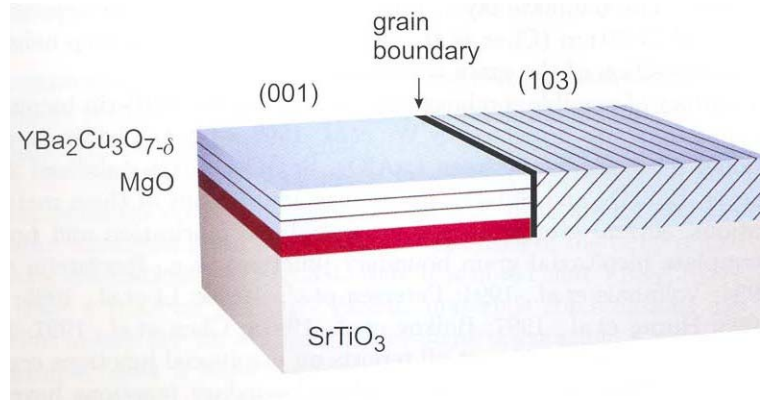


**Figure 6:** Sketch of biepitaxial principle as developed by Di Chiara et al.

With this, asymmetric 45° [100] tilt boundaries and symmetric [100] twist boundaries with promising properties can be fabricated [15-17].

### 3.1 Josephson effect

In a junction if the order parameter  $\Psi$  of the two superconductors is sufficiently overlapped Cooper pairs can be tunnelling through the barrier without energy loss. Moreover, the pairs tunnelling produce a Cooper pairs phase variation that depends on the critical current of the junction  $I_0$ . This effect is called *d.c. Josephson effect* that relates the applied current passing trough the junction with the phase and the critical current of the junction. This relation is expressed in the follow equation [6]:

$$I = I_0 \sin \varphi \quad (1)$$

where  $\varphi = \varphi_1 - \varphi_2$  is the difference between the phase of the two connected superconductors. In other words using equation (1), Josephson demonstrated that a junction is able to sustain a supercurrent without application of a voltage.

A very simple derivation of the DC Josephson equation has been proposed by Feynman, starting from the Schroedinger equation [11]:

$$i\hbar \frac{\partial \Psi}{\partial t} = E\Psi \quad (2)$$

in a superconductor  $\Psi = |\Psi|e^{i\varphi} = \rho_S^{\frac{1}{2}}e^{i\varphi}$ , with  $\varphi$  being the macroscopic superconducting phase and  $\rho_S$  the density of Cooper pairs. However, when a coupling with overlap exists between the wavefunction to the left,  $\psi_L$ , and to the right,  $\psi_R$ , a term must be added to account for the “leakage” of the wavefunction. Therefore,  $\psi_L$  changes with time at a rate which is proportional to the amount of leakage from  $\psi_R$  into the left side. Similarly, a symmetric equation must exist for the rate of change of  $\psi_R$ . The equation (2) written for the two superconductors wavefunction are:

$$\begin{aligned} i\hbar \frac{\partial \Psi_L}{\partial t} &= E_L \Psi_L + K \Psi_R \\ i\hbar \frac{\partial \Psi_R}{\partial t} &= E_R \Psi_R + K \Psi_L \end{aligned} \quad (3)$$

where  $E_L$  and  $E_R$  are the ground state energies of the unperturbed system when  $K=0$ , i.e. with no transfer of charge. It is not important to know the values of  $E_L$  and  $E_R$  but their difference  $E_L - E_R = -2eV$ , which is fixed by the potential difference  $V$ . For a thick barrier  $E_L = E_R$  when  $K=0$ , and sharing the potential energy difference between the two states symmetrically [11] by writing:

$$\begin{aligned} i\hbar \frac{\partial \Psi_L}{\partial t} &= eV \cdot \Psi_L + K \Psi_R \\ i\hbar \frac{\partial \Psi_R}{\partial t} &= eV \cdot \Psi_R + K \Psi_L \end{aligned} \quad (4)$$

The wave functions  $\Psi_L$  and  $\Psi_R$  may be written as

$$\begin{aligned} \Psi_L &= \rho_L^{\frac{1}{2}} e^{i\varphi_L} \\ \Psi_R &= \rho_R^{\frac{1}{2}} e^{i\varphi_R} \end{aligned}$$

assuming that each function has a well-defined macroscopic phase, constant in space and with a well defined Cooper-pair density. This first limitation will have to be lifted later, but for the moment the discussion is limited to a constant area that is very small, so that no spatial variation of phase is possible. Now substituting the wave function with time dependent  $\rho$  in the differential equations (4) and equate real and imaginary parts separately, with  $\varphi = \varphi_R - \varphi_L$ , the following four equations are obtained:

$$\begin{aligned}\frac{\partial \varphi_R}{\partial t} &= -\frac{K}{\hbar} \left( \frac{\rho_L}{\rho_R} \right)^{\frac{1}{2}} \cos \varphi + \frac{eV}{\hbar} \\ \frac{\partial \varphi_L}{\partial t} &= -\frac{K}{\hbar} \left( \frac{\rho_R}{\rho_L} \right)^{\frac{1}{2}} \cos \varphi - \frac{eV}{\hbar} \\ \frac{\partial \rho_R}{\partial t} &= -\frac{2K}{\hbar} (\rho_R \rho_L)^{\frac{1}{2}} \sin \varphi \\ \frac{\partial \rho_L}{\partial t} &= \frac{2K}{\hbar} (\rho_R \rho_L)^{\frac{1}{2}} \sin \varphi\end{aligned}$$

It should be noted that variations of phase ( $\varphi_R$  and  $\varphi_L$ ) are due to the combined effect of the phase difference  $\varphi$  across the contact, and the potential  $V$ , while variations in pair density are solely due to the phase difference  $\varphi$ .

The supercurrent across the contact is calculated by use of

$$I = 2e \frac{\partial \varphi_L}{\partial t} \text{ or } I = -2e \frac{\partial \varphi_R}{\partial t}$$

The time derivative is already given above, so that the followed relation is due:

$$I = \frac{4Ke}{\hbar} (\rho_R \rho_L)^{\frac{1}{2}} \sin \varphi$$

which it is possible to rewrite as

$$I = I_0 \sin \varphi$$

that represents the *dc Josephson effect*. It means that a supercurrent is driven across the thin barrier separating two superconductors simply by the superconducting phase difference across the barrier.

Moreover, another phenomenon would appear when the current is forced to exceed  $I_0$ . A voltage  $V$  developed across the junction, and the phase  $\varphi$  became time dependent, giving an a.c. current with so-called Josephson frequency  $\omega_J$  according to

$$\omega_J = \frac{\partial \varphi}{\partial t} = \frac{2e}{\hbar} V = \frac{2\pi V}{\Phi_0}. \text{ This effect is known as } a.c. \text{ Josephson effect, it is in an}$$

observable range, since  $V=1\mu\text{V}$  leads to  $f_J \equiv \frac{\omega_J}{2\pi} = 483.6\text{MHz}$ . This effect means that

there is an electromagnetic phenomenon related to the movement of charge at elevated frequency: the Josephson contact emits electromagnetic radiation at frequency  $\omega_J$ .

Therefore the current across the junction should now be written

$$I = I_0 \sin \left[ \varphi_0 - \left( \frac{2eV}{\hbar} \right) t \right] = I_0 \sin(\varphi_0 - \omega_J t)$$

where  $\varphi_0$  is the phase across the junction, without the presence of the voltage  $V$ . It is this oscillatory Cooper-pair current which generates the microwave electromagnetic radiation. In the opposite case, when microwave radiation is incident on the junction, steps appear at regular intervals  $V_n = n\left(\frac{\hbar}{2e}\right)\omega_J$  on the I-V curve. These steps, caused by absorption of  $n$  quanta of electromagnetic radiation at the Josephson frequency, are called Shapiro-steps after their discoverer.

The relation between the current and the voltage for a Josephson junction is represented by the I-V characteristic reported in Figure 7 (left).

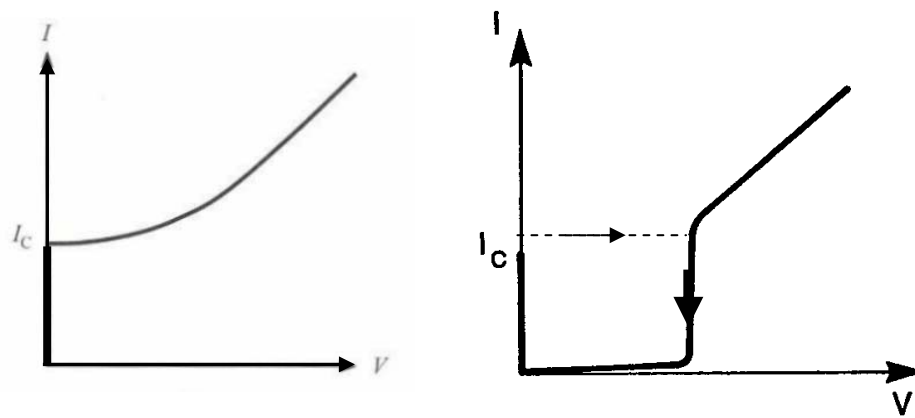


**Figure 7:** I-V characteristic: (left)non-hysteretic junction, (right) hysteretic junction

The I-V curve shows that if the junction is biased with a constant current source, lower than the critical current  $I_c$ , there will be no voltage drop across the junction, although the passage of the current through the device will introduce a phase difference across it. When the bias current exceeds the  $I_c$  a voltage will appear and the phase difference will become time-dependent.

Typically, the voltage returns to zero only for current values much lower than the  $I_c$ . Therefore, the junction shows an hysteretic behaviour (Figure 7 (right)).

Experience and theoretical analysis have solved the problem shunting the junction , i.e. by adding an external resistance in parallel. This modification is commonly referred to as the RSJ-model (Resistively Shunted Junction) as shown in Figure 8, which describes the Josephson junction with an equivalent circuit.

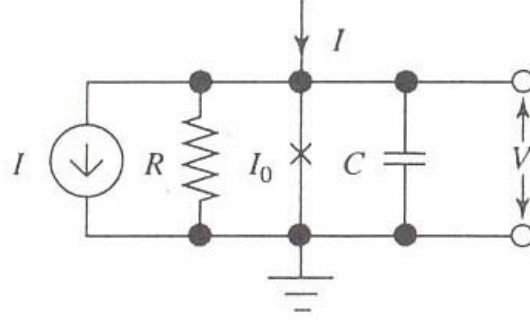


**Figure 8:** The RSJ model for a Josephson junction.

In the schematic diagram one identifies the current source, the resistive shunt  $R$ , the Josephson junction, a capacitance  $C$  and finally the voltage  $V$ . The resistance represents the dissipations associated with the passage of quasi-particle, which shunts the Josephson element and varying very strongly with voltage. On the other hand, the insulating barrier, with thickness of order 1-2 nm, between the two superconductors produces a significant capacitance between the two superconducting planes that is represented by the capacitance  $C$  in the equivalent circuit. To determine the DC current–voltage characteristic of a junction using the equivalent circuit, at first it can be noted that the bias current is the sum of three terms:

$$I = I_0 \cdot \sin \varphi + \frac{V}{R} + C \frac{dV}{dt} \quad (5)$$

Taking into account that the second Josephson relationship  $V = \frac{\hbar}{2e} \frac{d\varphi}{dt}$  correlates the voltage drop across the device to the time rate of change of  $\varphi$  so that this equation becomes a second-order non-linear differential equation for  $\varphi$ .

$$I - I_0 \cdot \sin \varphi = \left( \frac{\hbar}{2eR} \right) \frac{d\varphi}{dt} + \left( \frac{\hbar C}{2e} \right) \frac{d^2 \varphi}{dt^2} \quad (6)$$

upon defining the quantity

$$U = -\frac{\Phi_0}{2\pi} (I \cdot \varphi + I_0 \cos \varphi)$$

the equation (3) may be written as

$$-\frac{2e}{\hbar} \frac{\partial U}{\partial \varphi} = \left( \frac{\hbar}{2eR} \right) \frac{d\varphi}{dt} + \left( \frac{\hbar C}{2e} \right) \frac{d^2 \varphi}{dt^2} \quad (7)$$

this is recognized as the equation of motion for a mass point moving down a corrugated surface, often referred to as a “washboard potential”, where  $U$  is a function of  $\varphi$ . Two cases could be considered:  $I < I_0$  and  $I > I_0$ , as shown in Figure 9.

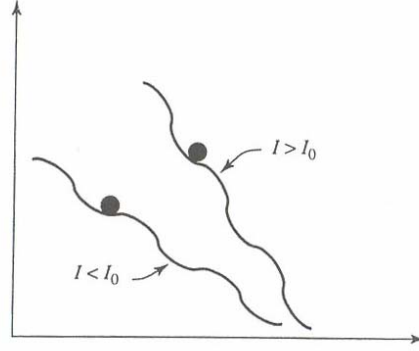


**Figure 9:**The washboard potential with a sliding point mass.  $I$  represents the tilt of the washboard.

In the first case the point mass gets trapped in one of the potential minima, and oscillates locally there. In the other case it goes on sliding. The first corresponds to zero time average phase difference, i.e.  $\frac{\partial \varphi}{\partial t} = 0$ . This corresponds to the average voltage across the junction being zero. The second type of the motion arises when the tilt is increased to make  $I > I_0$ . in this case the time average is  $\frac{\partial^2 \varphi}{\partial t^2} > 0$ , in other words, the point mass keeps sliding down the washboard. It is helpful also to note that in the mechanical analogue the capacitance  $C$  represent the particle mass, and the  $1/R$  is proportional to the friction coefficient, or damping of the motion.

If  $C=0$ , which is a reasonable approximation for a point-contact junction, or even for a small tunnel junction, the equation (6) can be solved directly by integration to give:

$$V = 0$$

$$V = I_0 R \left[ \left( \frac{I}{I_0} \right)^2 - 1 \right]^{\frac{1}{2}}$$

plotting the time-average voltage as a function of the bias current it clearly has a parabolic dependence (non hysteretic) as shown in Figure 7(left). This behaviour is well followed in practice for the types of junction with a rather small values of shunt resistance ( $R < 1\Omega$ ).

If the junction capacitance is not negligible,  $C \neq 0$ , the equation (6) can be solved numerically and it is then found that current-voltage characteristic may exhibit hysteretic: the path taken for increasing  $I$  is not the same as that for decreasing  $I$ . As a consequence the characteristic of the junction changes, as shown in Figure 7(right).

The numerical analysis shows that hysteresis is controlled by the parameter  $\beta_c$ , called the Stewart-McCumber parameter

$$\beta_c = \frac{2\pi \cdot I \cdot R^2 C}{\Phi_0}$$

It should be noted that the role of the capacitance, which analogous to inertia in the washboard model, when the junction is in the finite voltage regime (where the phase is evolving with time), is to maintain a time-evolving junction phase difference even when the current bias is reduced below the level which caused them to switch first into finite voltage state. This hysteretic behaviour has the unfortunate consequence of introducing high noise levels. The effect of the hysteresis is avoided if the condition  $\beta_c \leq 1$  is satisfied. Moreover, for a tunnel junction the hysteresis problem can be minimised by making the barrier as thin as possible, even though this also maximises the capacitance. It is just that the supercurrent density increases faster with decreasing thickness than does C, in fact the tunnelling supercurrent density depends exponentially on the barrier thickness  $t$  whereas C varies as  $t^I$ . Thus the best junctions have the highest possible current density, provided that the barrier can be made continuous and uniform.

Until now the fluctuating noise current  $I_n(t)$ , associated with the components of the circuit, has been neglected. For a better understanding of the Josephson junction the  $I_n(t)$  term should be introduced and its consequences analysed. The full equation of the motion become:

$$I + I_n(t) = I_0 \cdot \sin \varphi + \left( \frac{\hbar}{2eR} \right) \frac{d\varphi}{dt} + \left( \frac{\hbar C}{2e} \right) \frac{d^2 \varphi}{dt^2}$$

the effects of noise are usually discussed in terms of noise spectral density  $S_I(f)$ , which means the noise power per bandwidth due to current noise  $I_n(t)$ . Theoretical analysis shows that the noise spectral density of  $I_n(t)$  is given by Nyquist result:

$$S_I(f) = \frac{4k_B T}{R}$$

since the current I represents the tilt of the washboard potential, the physical effect of  $I_n(t)$  is to cause fluctuations in that tilt. If these fluctuations become large enough they will cause the particle to escape from its local trapping site. This creates a condition for  $\frac{\partial \varphi}{\partial t}$  to differ from zero, which again means that a voltage will appear, in this case corresponding to the appearance of voltage noise with increasing temperature. This will cause a rounding of the I-V curve before the steeper onset of current driven by the

external voltage  $V$ . The noise corresponds to an additional voltage  $dV_n$  and a total effective voltage  $V+dV_n$  causing the precursor “noise-rounding” effect in the hysteretic I-V characteristic. This current noise has an additional effect of lowering the effective critical current value, a potentially harmful consequence of noise since the critical current  $I_0$  must be above a certain value for proper operation of the junction. A criterion for  $I_0$  to be large enough to maintain coherent supercurrent or “coupling of the junction” is that the coupling energy exceeds the available thermal energy, expressed by the relation:

$$\frac{I_0 \Phi_0}{2\pi} \gg kT$$

the quantity  $\frac{I_0 \Phi_0}{2\pi}$  is the coupling energy of the junction and represents a measure of the energy associated with the current pattern for each flux quantum in the junction. A typical value of  $I_0$  is the 0.17  $\mu\text{A}$  at low temperature(4.2K) and 3.3 $\mu\text{A}$  at 77K. The condition to maintain a reasonable degree of Josephson coupling can be expressed also by means of the “noise parameter” defined as:

$$\Gamma = \frac{2\pi k_B T}{I_0 \Phi_0}$$

which must satisfied the relation  $\Gamma \leq 1$ .

#### 4. DC SQUID

The most wide-spread application of Josephson junctions is probably superconducting quantum interference devices (SQUIDS). The SQUID is considered as the most sensitive detector of magnetic flux, with an energy sensitivity that approaches the quantum limit. There are two major categories of SQUIDS: the so-called *DC SQUID*, based on the interference effects in the two junction SQUID loop; *RF SQUID* which is based on the variation of the RF impedance or loss in a one junction SQUID loop as the flux bias is changed. Both kind of SQUIDS have been used to make measurements that are more sensitive than can be made with non-superconducting devices. In addition to measuring magnetic field, they can be configured to measure gradients of the field as well as current and voltage. In particular the attention will be focused on the description of the DC SQUID which consists of a loop of superconductor, interrupted by two Josephson junctions, preferably with at least similar properties. As mentioned above a

superconducting loop will contain flux only in multiples of the flux quantum, i.e.  $n\Phi_0$ , and a change in the flux applied to the loop, will cause currents to flow to oppose that change and cause a phase difference across the junctions giving rise to a voltage across the loop, which can be detect.

High-Tc SQUID are still made with either bicrystal or step-edge grain boundary junctions, and typically they were fabricated in the geometry of a square washer, as shown in Figure 10.

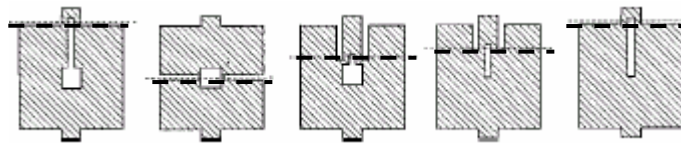


**Figure 10:** Five configurations of planar dc SQUID fabricated at Berkeley. Dashed lines indicate the bicrystal boundary along which the junctions are formed. Outer dimension is typically  $500 \times 500 \text{ mm}^2$ .

The basic mode of operation of the DC SQUID can be explained at least qualitatively by treating the device as possessing three distinct, but inseparably connected components: an oscillator, a parametric amplifier and a microwave detector. The oscillator consists of the two junctions biased at finite voltage so that an oscillating supercurrent at the Josephson frequency is driven round the loop. The second, parametric amplifier elements results from the fact that the amplitude, phase and frequency of the circulating current depend periodically on the flux applied to the ring. Finally, the amplitude of the circulating supercurrent is detected by the response of the junctions, so that the I-V characteristic of the paralleled junctions is affected in a measurable way as the applied flux is changed.

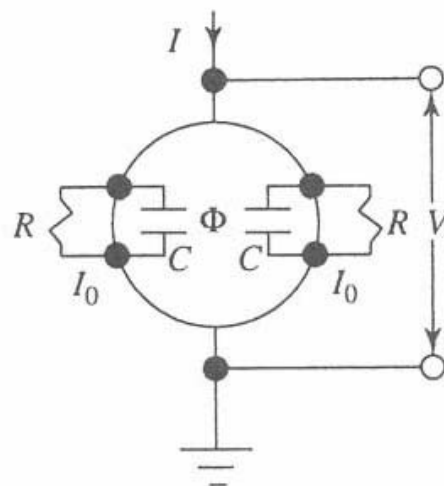


**Figure 11:** Schematic circuit diagram of DC SQUID.

A sketch of DC SQUID is reported in Figure 11 where for each junction the shunt resistance  $R$  and the capacitance  $C$  are shown. The current-voltage characteristic of the DC SQUID is reported in Figure 12.

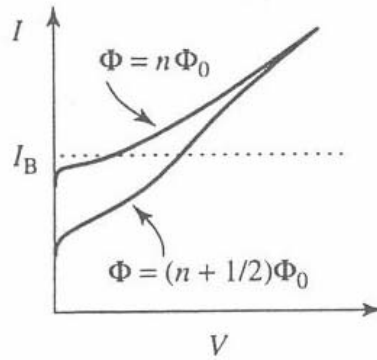


**Figure 12:** I-V characteristics

It looks at first sight just like that of a single junction with the total critical current a periodic function of the magnetic flux applied to the superconducting loop. The Figure shows two I-V curves corresponding to integer ( $n\Phi_0$ ) and odd half-integer  $(n+1/2)\Phi_0$  values of the applied flux in units of  $\Phi_0$ . The point to notice is that if the SQUID is biased by a constant current into the finite voltage regime, the time-averaged voltage appearing across the junctions is also a periodic function of flux, with a period  $\Phi_0$  (Figure 13).

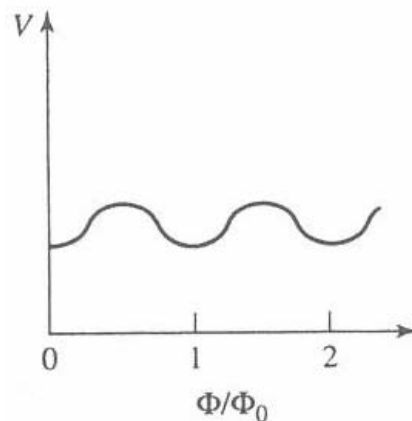


**Figure 13:** Voltage vs  $\Phi/\Phi_0$  at constant bias current  $I_B$ .

The DC SQUID operational properties have been explained qualitatively by Clarke [12]. Looking the Figure 14(a), the SQUID is sketched with two junctions arranged symmetrically, one on each side of the loop, so that the bias current  $I$  is divided equally

between the two paths, with  $I/2$  in each. As long as the current in a junction is below the critical current  $I_0$ , a supercurrent tunnels through the junction at zero potential difference.

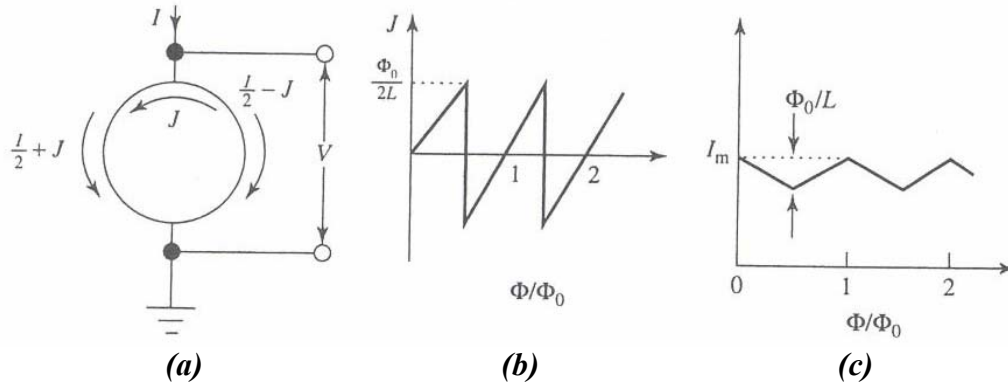


**Figure 14:** Simplistic view of the DC SQUID: (a) a magnetic flux  $\Phi$  generated a circulating current  $J$  that is periodic in  $\Phi$  as shown in (b); as a result (c), the maximum supercurrent  $I_m$  is also periodic in  $\Phi$ .

If an arbitrary amount of flux  $\Phi_a$  is applied to the ring, an additional supercurrent  $I_{circ}$  is set up, creating a self-generated flux  $LI_{circ}$  in the ring. Recalling that the total flux  $\Phi$  in a superconducting ring is quantized as  $n\Phi_0$  the following relation now applies:

$$\Phi = \Phi_a + LI_{circ} = n\Phi_0 \quad (8)$$

Taking the starting value of the applied flux as  $\Phi_a=0$  or  $\Phi_a=n\Phi_0$  the circulating current according to equation (8) is initially zero. On increasing the applied flux, a finite circulating current  $I_{circ} = \frac{(\Phi_a - n\Phi_0)}{L}$  develops in order to keep the total flux through

the loop at its starting, quantized value. This internally generated, circulating current adds to the externally applied bias current  $I/2$  in a junction (at left) and subtracts in the other (at right). The individual junction currents are related as  $I_1=I/2+2I_{circ}$  and  $I_2=I/2-2I_{circ}$ . Since the circulating current flows in opposite sense relative to the bias current in the two junctions, the junctions respond differently to the same amount of externally applied flux. Junction at left switches to the voltage state, i.e. a voltage develops across it, when it carries a total current equal to the critical current  $I_1=I/2+2I_{circ}=I_0$ . At this point the device current is  $I=2I_0-2I_{circ}$  which represents the device critical current at this applied flux. The maximum value clearly is  $2I_0$ . What is important for use of the device is how it further responds to applied flux.

At the same time as  $\Phi_a$  increases from zero to  $\Phi_0/2$ ,  $I_{circ}$  increases from zero to  $\Phi_0/2L$  according to the equation (8), and the device critical current decreasing to  $2I_0-\Phi_0/L$ , by the amount  $\Phi_0/L$  (Figure 14(c)). Then, increasing the applied flux beyond  $\Phi_0/2$  the

SQUID makes a transition from the flux state  $n=0$  to  $n=1$ , with reversal of the sign of  $I_{circ}$ . As  $\Phi_a$  is increased to  $\Phi_0$ , the critical current again increases to its maximum value  $2I_0$ . The sequence described is shown in Figure 14(b).

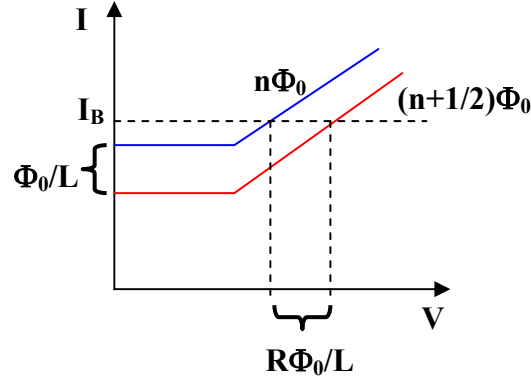


**Figure 15:** I-V curve with the relative variation of  $\delta I$  and  $\delta V$  due to the variation of the applied magnetic field.

This behaviour repeats periodically with increasing flux as thereby results for a the DC SQUID illustrated in Figures 12 and 13. These Figures also indicate that a practical device is biased at a constant current  $I_B(>I_0)$  that is above the critical current and therefore put the DC SQUID in the voltage state, which is necessary in order to make a flux to voltage transformer.

Thus, the DC SQUID sensor can be considered as a flux to voltage transducer because it converts the variation of magnetic flux through the superconducting ring into a voltage value.

To measure small changes in  $\Phi$  ( $\ll \Phi_0$ ) one generally chooses the bias current to maximize the amplitude of the voltage modulation and sets the external flux at  $(2n+1)$

$\Phi_0/4$  ( $n=0,1,2, \dots$ ), so that the flux-to-voltage transfer coefficient  $\left. \frac{\partial V}{\partial \Phi} \right|_I$  is a maximum,

which is denoted as  $V_\Phi$ . Thus the SQUID produces a maximum output voltage signal

$\delta V = V_\Phi \delta \Phi$  in response to a small flux signal  $\delta \Phi$ . The maximum value  $V_\Phi$  can be

obtained regarding that the maximum change in critical current which can be produced

by external flux is  $\frac{\Phi_0}{2L}$  that require a change of applied flux of  $\frac{\Phi_0}{2}$ . Thus  $\frac{\partial I}{\partial \Phi} \approx \frac{1}{L}$  and

the  $V_\Phi$  is

$$V_\Phi = \left. \frac{\partial V}{\partial \Phi} \right|_I = \left( \frac{\partial V}{\partial I} \right) \left( \frac{\partial I}{\partial \Phi} \right) = \frac{R}{2L}$$

where  $R$  is the shunt resistance of the junctions and  $L$  is the inductance of the superconducting loop. Taking into account the value of  $V_\Phi$  could be deduced the maximum output voltage  $\delta V = \frac{R}{2L} \delta \Phi$ .

Typically, in high- $T_c$  SQUID operating at 77 K,  $V_\Phi$  has values ranging from 10 to 100  $\mu\text{V}/\Phi_0$  [13].

## 5. Noise in DC SQUID

The dominant source of noise at frequency well below the Josephson frequency  $f_J = \frac{V}{\Phi_0}$  are represented by the two independent Nyquist noise currents in the shunt

resistors which produce voltage noise across the SQUID with a spectral density  $S_V(f) = \frac{4KTR}{2}$  [14] and a white current noise around the SQUID loop with a spectral

density  $S_J(f) = \frac{8KT}{R}$ ; in fact, these two noise terms are partially correlated [15].

The intrinsic white flux noise of the SQUID is given by  $S_\Phi(f) = \frac{S_V(f)}{V_\Phi^2} = \frac{4k_B TL^2}{R}$ ; it

is often convenient to introduce a noise energy per unit bandwidth  $\varepsilon(f) = \frac{S_\Phi(f)}{2L}$ . We

note that noise imposes a second constraint on the parameters, namely that the magnetic energy per flux quantum  $\frac{\Phi_0^2}{2L}$  must be substantially greater than  $k_B T$ :  $\frac{\Phi_0^2}{2L} \gg 2\pi k_B T$ . We

can express this requirement as  $\Gamma \beta_L = \frac{L}{L_{th}} \ll 1$ , where we define  $\beta_L = \frac{2LI_0}{\Phi_0}$ , and

$L_{th} \equiv \frac{\Phi_0^2}{4\pi k_B T}$ . This restriction corresponds to  $L \ll \frac{\Phi_0^2}{2k_B T}$  which requires value of

inductance  $L$  of the order of 5.6 nH at 4.2K and 0.33 nH at 77K. To optimize the reduction of the Nyquist noise, due to the shunt resistors, the conditions:  $\beta_L = 1$  and  $\beta_C \leq 1$ , must be satisfied. For typical parameter  $L=200$  pH,  $R=6\Omega$  and  $T=4.2\text{K}$ :

$S_\Phi^{\frac{1}{2}}(f) \approx 1.2 \cdot 10^{-6} \Phi_0 \text{Hz}^{-\frac{1}{2}}$  (as reported in Figure 16) and  $\varepsilon(f) = 10^{-32} \text{JHz}^{-1}$  ( $\approx 100 \hbar$ ).

Moreover, it is interesting to note that  $S_\Phi \propto T$  and for given L and R high- $T_c$  SQUID at 77K will have higher noise than low temperature SQUID at 4.2 K.

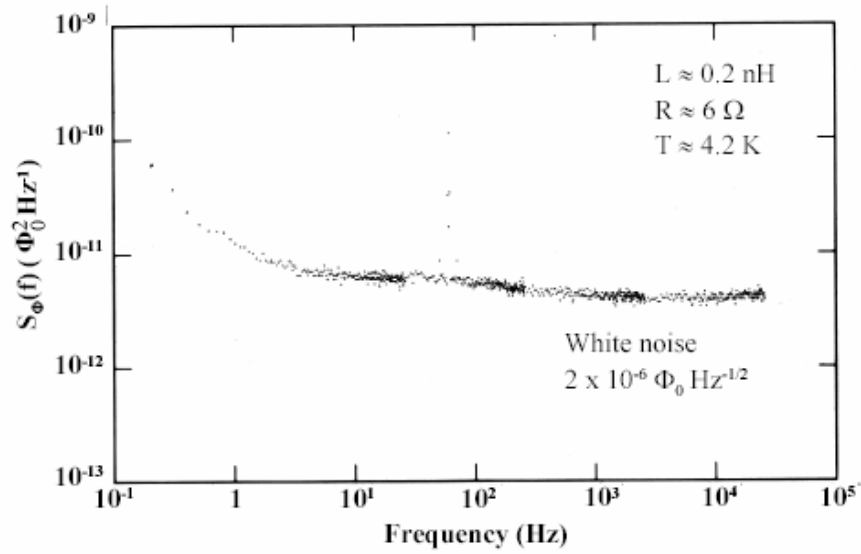


**Figure 16:** spectral density of flux noise in DC SQUID vs frequency.

In addition to the white noise, there is usually low-frequency  $1/f$  noise generated by both  $1/f$  noise in the critical current and by the motion of flux vortices trapped in the body of the SQUID.

For many applications, for example biomagnetism and magnetotellurics one requires the low level of noise to extend down to frequencies of 1 Hz or lower; if that were the case, high- $T_c$  SQUIDS would be adequate for most purposes. Unfortunately, low-frequency  $1/f$  noise, which is observed in low- $T_c$  SQUIDS but is generally not a serious issue, is a severe problem in high- $T_c$  SQUIDS and a great deal of effort has been expended in attempting to understand its origins and reduce its magnitude. Early high- $T_c$  dc SQUIDS made from polycrystalline YBCO films [16] exhibited large levels of  $1/f$  noise, which increased the noise energy at 1 Hz to above  $10^{-26}$  J Hz $^{-1}$ . Work on low- $T_c$  dc SQUIDS [17] showed that there are generally two separate sources of  $1/f$  noise. One arises from the motion of vortices in the body of the SQUID: even when the SQUID is cooled in zero field, some fraction of the vortices formed at  $T_c$  remain pinned at defects. The vortex hopping rate increases exponentially as the pinning energy is reduced, so that the microstructure of the film and the related pinning energies play an important role in determining the low-frequency noise [18]. The microstructural quality of films is particularly crucial. When the SQUID is cooled in a nonzero magnetic field, in general the additional vortices so formed create high noise levels. Unfortunately, one cannot

relate the magnitude of the  $1/f$  noise to any other measurable physical quantity, so that a direct noise measurement is the only means of characterizing the quality of a given film. It should be noted that even in high quality YBCO thin film with critical current up to  $10^6 \text{A/cm}^2$  there is a significant increase in  $1/f$  noise when the SQUID is cooled in presence of a magnetic field. Typically, the increase in flux noise was approximately one order of magnitude for a SQUID cooled in a magnetic field strength comparable to the earth field ( $50 \mu\text{T}$ ). In this way the applications of SQUIDs to low noise measurements in an unshielded environment is significantly limited. Significant progress reducing vortex motion and the associated  $1/f$  noise of SQUIDs can be obtained by restricting the linewidth of the SQUID to approximately  $4\text{-}6 \mu\text{m}$ , with this design criteria there was no significant increase of  $1/f$  noise up to a magnetic field of  $80 \mu\text{T}$  [19]. Moreover, the  $1/f$  noise can be reduced also making the superconducting film with hole or slots of different design [19]. Four designs are shown in Figure 17, together with the configuration of a “solid” SQUID in Figure 17(a); all five devices have outer dimensions of  $186 \times 204 \text{ mm}^2$ . Figure 17(b) shows a configuration in which eight slots, each 8 mm wide, separate nine YBCO strips, each 4 mm wide. The innermost slit is 4 mm wide and 100 mm long. Figure 17(c) shows the second design in which 248 holes, each  $838 \text{ mm}$ , divide the square washer into a grid of 4 mm wide lines. In Figures 17(d) and (e), we have reduced the number of slots to 5 and the number of holes to 125, respectively, leaving a superconducting band 40 mm wide around three sides of the devices.

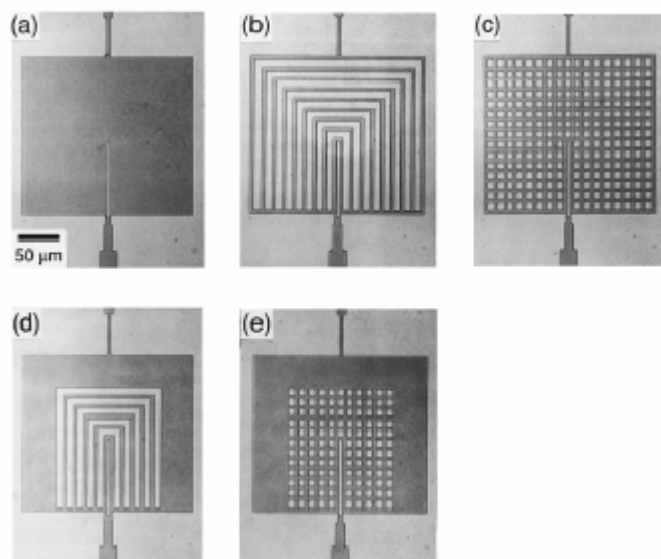


**Figure 17:** Photographs of the photomasks for (a) a solid, thin-film SQUID, and for a SQUID with (b) eight slots, (c) 248 holes, (d) five slots, and (e) 125 holes. The outer dimensions of each device are  $186 \times 204 \text{ mm}$ .

The second source of  $1/f$  noise is fluctuations in the critical current of the junctions which, can attain high levels. These fluctuations contribute in two independent ways: an “in-phase” mode, in which the critical currents of the two junctions fluctuate in phase to produce a voltage across the SQUID, and an “out-of-phase” mode in which the two fluctuating critical currents produce a current around the SQUID loop. Resistance fluctuations also contribute  $1/f$  noise. However, at the low voltages where SQUIDs are operated critical current fluctuations dominated and it will not address resistance fluctuation further. This kind of  $1/f$  noise can be reduced by means of an ac bias modulation scheme, which can be introduced in the next paragraph.

Typical order of magnitude for commercial HTS DC SQUID are: noise energy  $\varepsilon=10^{-31}$  J  $\text{Hz}^{-1}$ , magnetic flux noise  $S_{\Phi}^2 \sim 10^{-6} \Phi_0 \text{ Hz}^{-1/2}$  and magnetic field noise  $B_N=10$  fT  $\text{Hz}^{-1/2}$ .

## 6. Flux-Locked Loop (FLL)

To linearize the  $V-\Phi$  curve SQUIDs operate in a flux-locked loop configuration, in which the voltage change across the SQUID induced by an applied flux is amplified and fed back as an opposing flux. This feedback circuit linearizes the response of the SQUID, provides a straightforward means of measuring the intrinsic noise of the SQUID, and enables one to track inputs equivalent to many flux quanta. The input stage of the electronic circuitry is designed to add negligibly to the intrinsic noise of the SQUID. Drung [20] has given a detailed review of a variety of schemes, here only the two most commonly used are described.

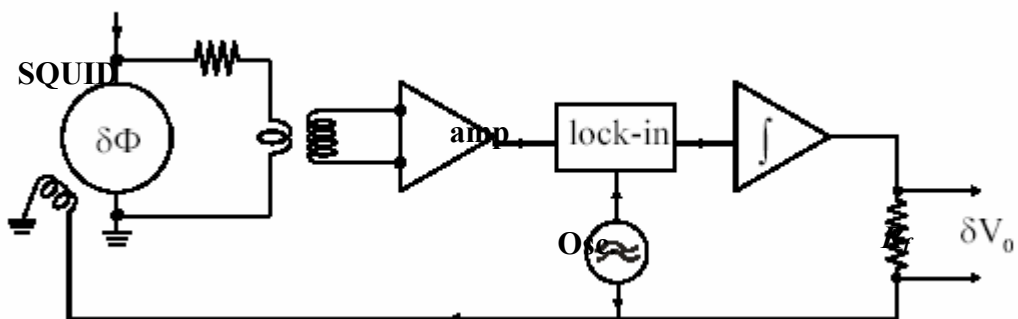


Figure 18: Flux Locked Loop for DC SQUID.

The widely used flux modulation scheme is shown in Figure 18 [21]. One applies a sinusoidal or square-wave flux modulation to the SQUID with a peak-to-peak amplitude of  $\Phi_0/2$  and a frequency  $f_m$  of typically 100 kHz. The resulting alternating voltage across the SQUID is coupled to a room-temperature preamplifier via either a cooled LC series-resonant circuit [22] or a cooled transformer [23]. The voltage gain of either coupling circuit is usually chosen to transform the dynamic resistance of the SQUID at its operating point to the value required to optimize the noise temperature of the preamplifier. Since this noise temperature is typically a few Kelvin, the preamplifier contributes negligible noise to a device operating at 77 K. After amplification, the signal is lock-in detected at the frequency  $f_m$ . If the quasistatic flux is  $n\Phi_0$  ( $n$  is an integer), the  $V$ - $\Phi$  curve is symmetric about this local minimum and the voltage contains components only at the frequency  $2f_m$ . Thus the output of the lock-in detector is zero. On the other hand, if the flux is shifted away slightly from the local minimum, the voltage across the SQUID contains a component at frequency  $f_m$  and there will be an output from the lock-in detector. After integration, this signal is fed back as a current through a feedback resistor  $R_f$  to a coil inductively coupled to the SQUID; usually the same coil is used for both flux modulation and feedback. The flux fed back opposes the applied flux to keep the flux in the SQUID constant; the voltage developed across  $R_f$  is proportional to the applied flux. One can measure the intrinsic flux noise of the SQUID by connecting the output voltage to a spectrum analyzer in the absence of any input signal. Ideally, the bandwidth for an optimized flux-locked loop extends to one half the modulation frequency.

For unshielded applications in which the SQUID is exposed to the magnetic noise of the environment, a more important Figure of merit is often the *slew rate*, that is, the maximum rate of change of flux that the system is able to track without losing lock. For an ideal single-pole integrator, the slew rate is  $2\pi f_1 \Phi_0/4$ , where  $f_1$  is the frequency at which the open-loop gain of the feedback loop falls to unity [24]. A considerable improvement in the slew rate at low frequencies can be achieved by means of a two-pole integrator [25,26].

It has already mentioned that fluctuations in the critical current and resistance of the junctions are a major source of  $1/f$  noise in dc SQUIDs. Fortunately, their contributions can be greatly reduced by a number of schemes [17, 27, 28], which have been successfully applied to high- $T_c$  SQUIDs [29-31]. At the operating point of SQUIDs, the critical-current noise dominates the resistance noise and contributes  $1/f$  noise in two

ways. Fluctuations at frequencies  $\ll f_m$  that are in phase at the two junctions give rise to a voltage noise across the SQUID that is eliminated by flux modulation at frequency  $f_m$ . Fluctuations that are out-of-phase at the two junctions are equivalent to a flux noise that is not reduced by this scheme. Instead, one makes use of the fact that the apparent shift of the  $V$ - $\Phi$  characteristic along the flux axis changes polarity if one reverses the polarity of the bias current whereas the flux due to an input signal (or “flux noise”) does not. As an example of one of the bias-reversal schemes, we briefly describe that developed by [17] Koch *et al.* (1983). The principle is illustrated in Figure 19 and its implementation in Figure 20.

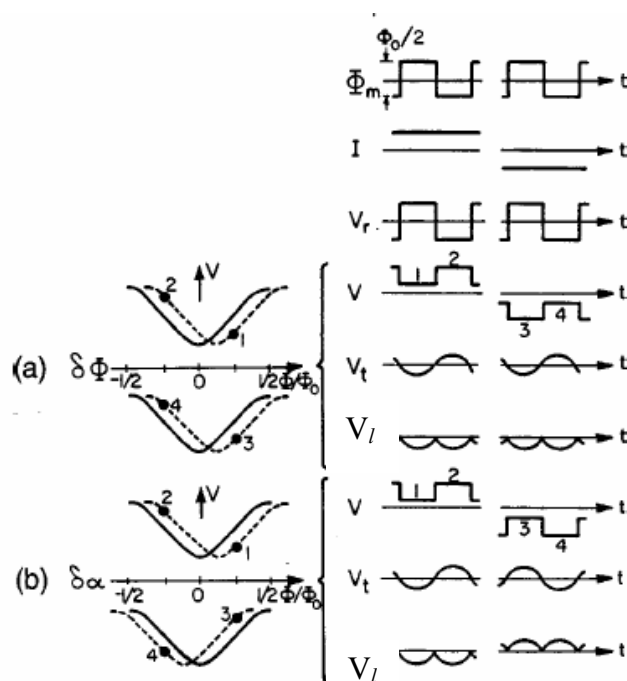


**Figure 19:** principle of bias-reversal scheme to reduce  $1/f$  noise to out-of-phase critical-current fluctuation.

The SQUID is flux-modulated with a 100-kHz square wave of peak-to-peak amplitude  $\Phi_m = \Phi_0/2$ . Synchronously with the modulation, the bias current  $I$  through the SQUID is reversed, for example, at a frequency  $f_r = 3.125$  kHz. The resistance bridge shown in Figure 20 minimizes the 3.125 kHz switching transients across the transformer. Simultaneously with the bias reversal, a flux  $\Phi_0/2$  is applied to the SQUID. In Figures 19(a) and (b) we see that the bias reversal changes the sign of the voltage across the SQUID while the flux shift ensures that the sign of the flux-to-voltage transfer function remains the same. The transformer coupling the SQUID to the preamplifier is often

tuned at the modulation frequency with a  $Q$  of about 3, so that any 100-kHz signals at the secondary are approximately sinusoidal.

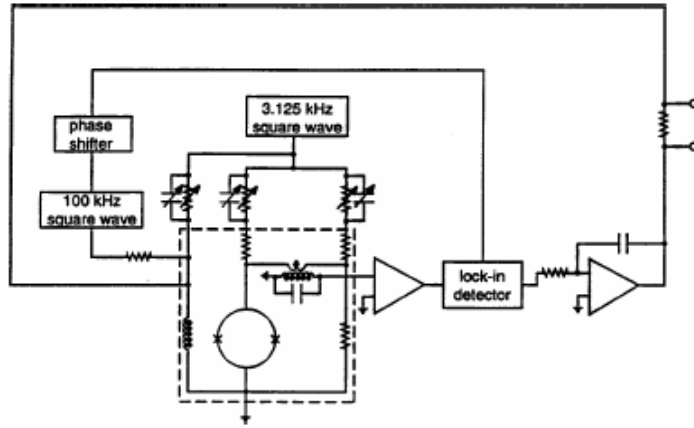


**Figure 20:** schematic for flux-locked loop with bias current reversal. Cryogenic components are enclosed in the dashed box.

One assumes that the SQUID is operated in the usual flux-locked loop, with the output from the lock-in detector integrated and fed back to the SQUID (Figure 20). Thus the 100-kHz signal across the SQUID consists of just the error signal. Suppose now that we apply a small external flux  $\delta\Phi$  to the SQUID at a frequency well below  $f_r$ . The  $V$ - $\Phi$  curves are shifted as in Figures. 19(a), and the 100-kHz flux modulation switches the SQUID between the points 1 and 2 for positive bias and 3 and 4 for negative bias. As a function of time, the voltage  $V$  across the SQUID is as shown in Figure 19, and the signal across the tuned transformer  $V_t$  is at the fundamental frequency. When this signal is mixed with the reference voltage  $V_r$ , the output from the lock-in detector  $V_l$  will consist of a series of negative-going peaks for both polarities of the bias current. The average of this output produces a negative signal proportional to  $\delta\Phi$  which is then used to cancel the flux applied to the SQUID. Thus, in the presence of bias reversal and flux shift, the SQUID responds to an applied flux in the usual way. We consider now the effects of  $1/f$  noise on the critical currents. The in-phase mode is eliminated by the 100-kHz flux modulation. Suppose, instead, we have an out-of-phase critical-current fluctuation at a frequency below  $f_r$ . Because the flux generated by this fluctuation *changes sign* when the bias current is reversed, the  $V$ - $\Phi$  curves are displaced in opposite directions. As a result, the voltage across the SQUID undergoes a phase change of  $\pi$  when the bias current is reversed, as shown in Figure 19. Consequently, the voltage at the output of the lock-in due to the out-of-phase critical-current fluctuation changes sign each time the bias current is reversed, and the time average of the signal over periods

much longer than  $1/f_r$  is zero. Thus the  $1/f$  noise due to both in-phase and out-of-phase critical-current fluctuations is eliminated by this scheme.

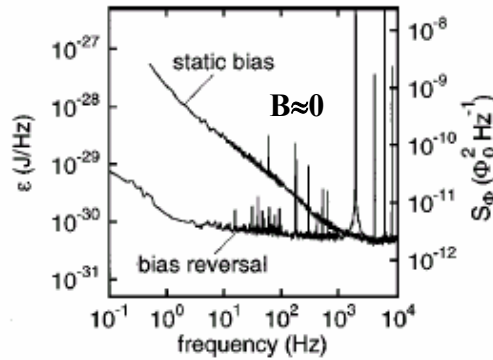


**Figure 21:** spectral density of flux noise of representative high- $T_c$  DC SQUID with flux modulation and bias current reversal.

Figure 21 shows the spectral density of the flux noise of a representative SQUID operated with flux modulation and with and without bias reversal. Without bias reversal,  $1/f$  noise is evident for frequencies below about 2 kHz. The application of bias reversal reduces the level of  $1/f$  noise dramatically, by two orders of magnitude at 1 Hz, demonstrating that the  $1/f$  noise indeed arose from critical-current fluctuations.

The second scheme is so-called “direct readout” which eliminates the need for a coupling network between the SQUID and the amplifier, and enable one to use particularly simple electronics for the flux-locked loop [32]. In addition, it allows one to achieve bandwidths around 10 MHz relatively easily [21]. The output of the current biased SQUID is connected directly to one terminal of a low-noise, bipolar amplifier; an offset bias voltage is applied to the other terminal. After amplification, the signal is integrated and fed back via a resistor to a coil coupled to the SQUID. Since the preamplifier noise, typically  $1 \text{ nV Hz}^{-1/2}$ , usually dominates the SQUID noise, typically  $0.1 \text{ nV Hz}^{-1/2}$  for low- $T_c$  SQUIDs, it must be reduced to a tolerable level by increasing the transfer function. In the additional positive feedback (APF) scheme [33] this increase is achieved by shunting the SQUID with an inductor  $L_a$ , with a mutual inductance  $M_a$  to the SQUID, in series with a resistor  $R_a$ .

To remove  $1/f$  noise due to critical-current fluctuations, as for the flux-modulation scheme, one has to reverse the bias current [34]; at the same time the bias voltage is reversed and a flux shift is applied to maintain the same polarity of the flux-to-voltage transfer function. Using this bias-reversal scheme, [35] Ludwig *et al.* (1997) recently reported a modified, directly coupled flux-locked loop for high- $T_c$  SQUIDs. Using a

preamplifier with a voltage noise of  $0.44 \text{ nV Hz}^{-1/2}$ , their high- $T_c$  SQUIDs could be operated with a total rms white noise typically 20% higher than the intrinsic rms noise of the SQUID. For an optimum bias-reversal frequency of around 100 kHz, it was demonstrated that  $1/f$  noise due to critical-current fluctuations can effectively be suppressed without increasing the white-noise level [24,35,36]. In addition, a maximum bandwidth of about 1 MHz and slew rates close to  $10^6 \Phi_0/s$  were achieved.

## 7. DC SQUID magnetometer

However, although SQUIDs are exquisitely sensitive to magnetic flux, their small area generally makes them relatively unsuitable to measure high magnetic field. To avoid this problem usually an additional superconducting structure is coupled to the SQUID to enhance its sensitivity to magnetic field. In particular the magnetic flux is coupled to the low inductance SQUID loop from a larger external pick up loop. The configuration of such a transformer is shown schematically in Figure 22.

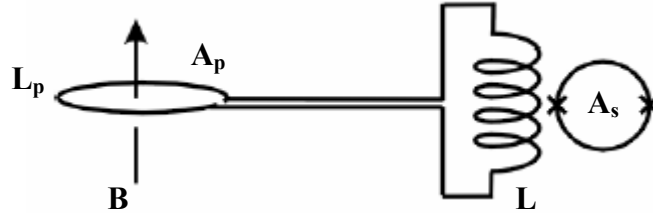


**Figure 22:** transformer used to enhance the SQUID sensitivity.

The magnetic-field noise is

$$S_B^2(f) = \frac{S_\Phi^2(f)}{A_{eff}^2}$$

where  $A_{eff}$  is the effective area of the magnetometer. Clearly, one wants to make  $A_{eff}$  as large as possible without increasing  $S_\Phi(f)$  so as to produce high sensitivity to magnetic fields.

The directly coupled magnetometer [37,38] shown in Figures 23 (left) and (right) consists of a large pickup loop of inductance  $L_p$  and area  $A_p$  directly connected to the SQUID body of inductance  $L \ll L_p$ . A magnetic field  $B$  applied the pickup loop induces a screening current  $I = BA_p/L_p$ , which in turn links a flux  $(L+L_j)I$  to the SQUID. Here  $L_j$

is the parasitic inductance of the striplines incorporating the junctions, to which the current does not couple. The effective area is

$$A_{eff} = \frac{(L + L_j)A_p}{L_p} \pm A_s \quad (9)$$

where  $A_s \ll A_{eff}$  is the effective area of the bare SQUID. The sign of  $A_s$  depends on the relative senses of the SQUID and the pickup loop.

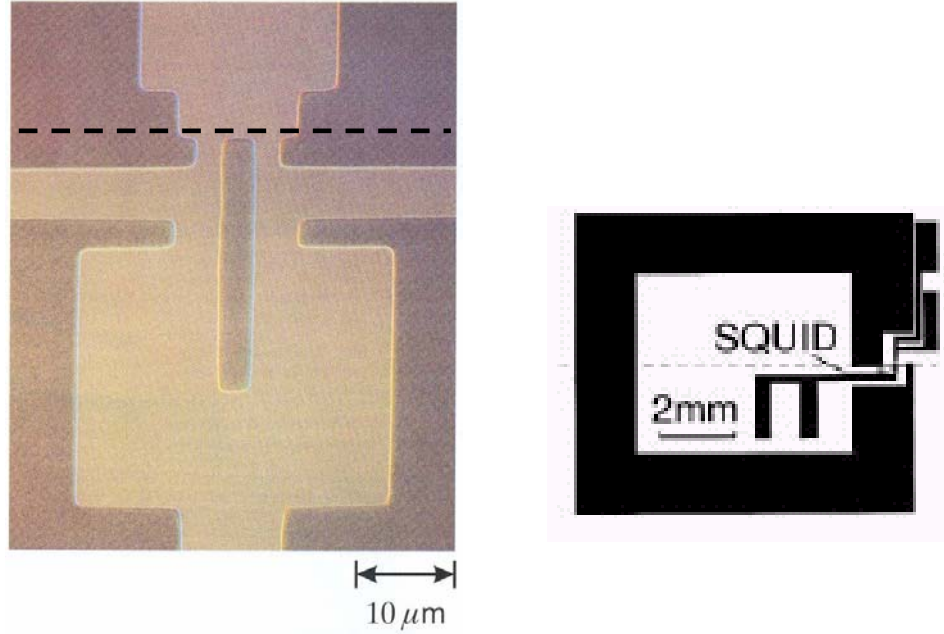


**Figure 23:** Directly coupled magnetometer: (left) Photograph of 20 pH DC SQUID connected to the pick up loop shown in (right). Dashed line indicates grain boundaries.

Koelle, Miklich, Ludwig al. [38] investigated devices grown on STO bicrystals. In their best device, a 20 pH SQUID with  $I_0=45 \mu\text{A}$  and  $R=3.4\Omega$  coupled to a  $47 \text{ mm}^2$  pickup loop, they achieved a flux noise of  $93 \text{ fT Hz}^{-1/2}$  at frequencies down to 1 Hz using bias reversal. Subsequently, improvements in performance were achieved by reducing the large mismatch between  $L_p$  and  $L$  [39,40]. One can increase the ratio  $A_p/L_p$  by using a pickup loop with a large linewidth,  $(d_1-d_2)/2$ , where  $d_1$  and  $d_2$  are the outer and inner dimensions. In the limit  $(d_1-d_2) > 2d_2$  in which  $A_p=d_1d_2$  and  $L_p=1.25 \mu_0d_2$ , from Eq. (9) we find  $A_{eff} = 4d_1(L+L_j)/5\mu_0$ ; we have neglected  $A_s$ . Given the dependence of  $S\phi(f)$  on  $L$ ,  $I_0$ , and  $R$ , one can then optimize  $S\phi(f)$ .

The performance of directly coupled magnetometers with near optimum parameters can be appreciably better than that of the earlier devices. For  $d_1=9.3 \text{ mm}$ ,  $d_2=3 \text{ mm}$ , and  $L=50 \text{ pH}$ , Lee *et al.* [40] and Cantor [41] achieved best results of about  $40 \text{ fT Hz}^{-1/2}$  at kHz and  $60 \text{ fT Hz}_{-1/2}$  at 1 Hz (with bias reversal). Using a  $19 \times 19 \text{ mm}^2$  pickup loop on a

20x20 mm<sup>2</sup> bicrystal, the same group achieved 14 fT Hz<sup>-1/2</sup> at 1 kHz and 26 fT Hz<sup>-1/2</sup> at 1 Hz [39]. In similar work, Glyantsev *et al.* [42] reported a noise level as low as 20 fT Hz<sup>-1/2</sup> at 1 kHz for a 150 pH SQUID coupled to a pickup loop with an outer diameter of mm. However, they did not use bias reversal, and the noise was well above 100 fT Hz<sup>-1/2</sup> at 1 Hz. Recently, using an STO bicrystal with a 30° misorientation angle and a pickup loop with  $d_1=9$  mm and  $d_2=3$  mm, Beyer *et al.* [43] obtained 23 fT Hz<sup>-1/2</sup> at 1 kHz and 67 fT Hz<sup>-1/2</sup> at 1 Hz. These values were achieved with bias reversal in the PTB magnetically shielded room; the noise at low frequencies was dominated by environmental noise.

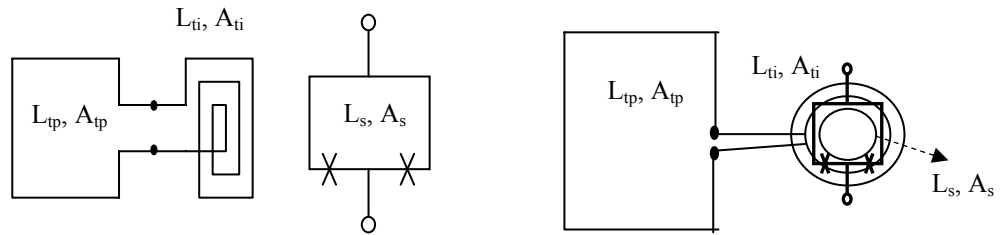


**Figure 24-P:** (left) typical configuration of inductive coupling magnetometer (ICM); (right) (ICM) in the “Ketchen scheme”.

It could be noted that the effective area of the directly coupled magnetometer can be further increased by coupling it in a *flip-chip arrangement* to a single-layer flux transformer on a separate substrate [38]. The small loop of the transformer (which is inductively coupled to the magnetometer pickup loop Figure 24) has inductance  $L_{ti}$  and area  $A_{ti}$  and is in series with the large loop of inductance  $L_{tp}$  and area  $A_{tp}$ . The effective area is

$$A_{eff} \approx \frac{L + L_j}{L_p} \left( A_p + \frac{A_{tp} \alpha_t (L_p L_{ti})^{1/2}}{L_{ti} + L_{tp}} \right)$$

where  $\alpha_t$  is the coupling coefficient between  $L_{ti}$  and  $L_p$ . For the devices shown in Figure 23, the transformer yielded a gain of 3.4 and the magnetic-field noise improved to 31 fT Hz<sup>-1/2</sup> at 1 kHz and 39 fT Hz<sup>-1/2</sup> at 1 Hz.

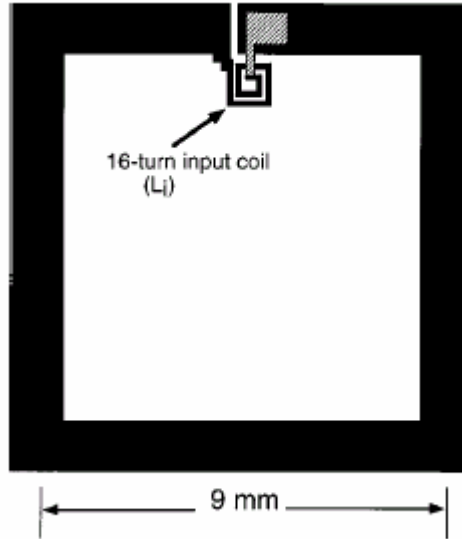


**Figure 25:** schematic layout of multilayer flux transformer (not to scale). Multiturn input coil (only two turns are shown) is either coupled to the SQUID in a flip-chip arrangement or deposited directly on top of it.

The effective area of a SQUID may be efficiently enhanced by coupling it to a superconducting flux transformer with a multiturn input coil (Figure 25). The transformer is a closed superconducting circuit consisting of a large-area pickup loop and a much smaller, multiturn input coil to couple flux into the SQUID. A magnetic field applied to the pickup loop induces a supercurrent that conserves the total magnetic flux and induces flux into the SQUID. The total effective area of the magnetometer is given by

$$A_{eff} = \frac{A_p M_i}{(L_i + L_p)} \pm A_s$$

where  $A_s$  is the effective area of the bare SQUID,  $A_p$  and  $L_p$  are the area and inductance of the pickup loop,  $M_i = \alpha(LL_i)^{1/2}$  is the mutual inductance between the SQUID inductance  $L$  and the input-coil inductance  $L_i$ , and  $\alpha$  is the coupling coefficient. The sign of  $A_s$  depends on the sense of the winding of the coil relative to the pickup loop. Assuming that  $\alpha$  does not depend on  $L_i$  and  $L$  and making certain approximations [44], one finds the effective area is maximum when  $L_i = L_p$ :

$$A_{eff} = \frac{\alpha A_p \left( \frac{L}{L_p} \right)^{1/2}}{2}$$

neglecting  $A_s$ . In contrast to the directly coupled magnetometer, the flux transfer into the SQUID can be optimized for a given value of  $L_p$  by varying the number of turns  $n$  on the input coil until  $L_i=L_p$ .

The advantage of the flip-chip configuration over the integrated magnetometer is that problems related to the junction process can be separated from those related to the interconnect technology. One forms a flip-chip magnetometer by clamping the SQUID and the flux transformer chips together with either photoresist or a thin mylar sheet between them. The input coil and pickup loop of the transformer are usually patterned in one YBCO layer, and the crossover between the innermost turn of the coil and the pickup loop in the other. The first YBCO flux transformer with a multiturn input coil operating at 77 K was made by Wellstood *et al.* [45] using shadow masks. The first multilayer flip-chip magnetometers were reported almost simultaneously by groups at Berkeley [46,47] and IBM [48]. Since this early work, many groups have described the fabrication of multiturn flux transformers [49,50] and the operation of flip-chip magnetometers at 77 K [31,30,51-59].

In an attempt to improve the inductive coupling between the SQUID and the input coil, several groups have integrated them on the same chip, thus reducing the spacing to the thickness of the insulating layer. Early monolithic SQUID magnetometers involving three YBCO layers and operating at 77 K [60,61] exhibited large levels of low-frequency flux noise. As a result, attention turned to a simplified design requiring only two superconducting layers [62-67]. In all cases, the insulator was SrTiO<sub>3</sub>. The SQUID washer is used as either a crossunder or crossover for the flux transformer, obviating the need for an extra superconducting layer. The input coil and SQUID of such a magnetometer are shown in Figure 26.

The lowest magnetic-field noise was reported by Drung, Ludwig *et al.* [36] using a magnetometer with 36° SrTiO<sub>3</sub> bicrystal junctions fabricated at NKT [67], namely 9.7 fT Hz<sup>-1/2</sup> at 1 kHz and 53 fT Hz<sup>-1/2</sup> at 1 Hz. Whereas the effective area  $A_{eff}=1.72\text{mm}^2$  for the 8.3x8.6mm<sup>2</sup> pickup loop is comparable to that measured by others for their integrated devices, the SQUID parameters  $R=9$  V and  $I_0=5.7$  mA for an inductance of about 130 pH are close to optimum.

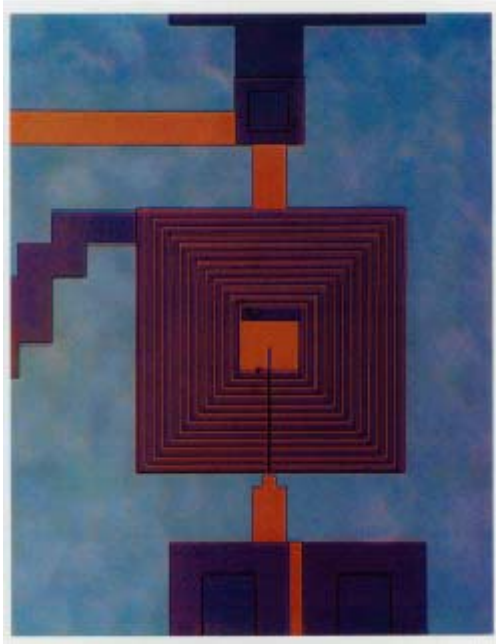


**Figure 26:** Photograph of 12-turn input coil and SQUID of an integrated magnetometer with 500- $\mu\text{m}$  SQUID washer located in lower YBCO layer. Bicrystal junctions are outside the washer.

Despite this impressive performance, integrated magnetometers have some disadvantages. One problem is that the  $V$ - $\Phi$  curves are often distorted by microwave resonances [36,63,66]. Such resonances have not been reported for flip-chip magnetometers.

These resonances in the input-coil-washer structure are well known from low- $T_c$  devices to degrade the SQUID performance [68]. Enpuku *et al.* [69] and Minotani, Enpuku *et al.* [70] reported the calculation of distorted  $V$ - $\Phi$  characteristics in good agreement with the data measured on high- $T_c$  devices under the assumption that there is a parasitic capacitance between the input coil and the SQUID washer. Hilgenkamp *et al.* [71] eliminated the resonances by means of a resistor between the SQUID and the input coil that shunted this parasitic capacitance.

Another drawback is that the yield of high-performance integrated devices is well below that of flip-chip, multilayer devices. Finally, there is no compelling evidence that the coupling coefficient of integrated magnetometers is significantly higher than that for flip-chip devices [66].

An alternative multilayer approach to achieving large effective areas is the multiloop magnetometer or fractional-turn SQUID, originally proposed and demonstrated by Zimmerman [72] with a machined niobium device. The essential idea is to connect  $N$  loops in parallel, thus reducing the total inductance to a level acceptable for a SQUID, while keeping the effective area large. Drung *et al.* [33,73] developed sensitive

multiloop SQUID magnetometers, based on their niobium thin-film technology; with eight parallel loops and a diameter of 7.2 mm these devices have a typical noise of 1.5 fT Hz<sup>-1/2</sup> down to a few Hz at 4.2 K. These devices have been used successfully for multichannel biomagnetic studies [74,75].

In the thin-film multiloop magnetometer, shown schematically in Figure 27 (a),  $N$  loops (for clarity, only four are drawn) are connected in parallel with the connection made at the center via coplanar lines.

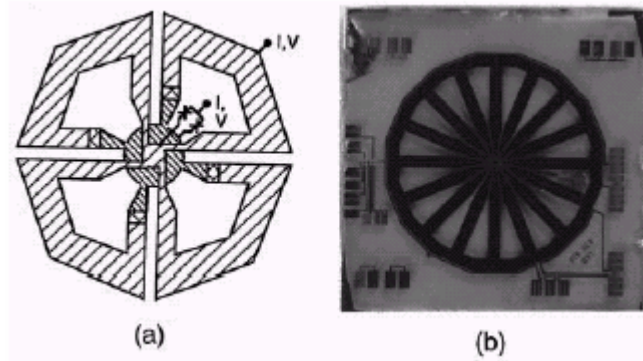


**Figure 27:** Multiloop magnetometer: (a) Schematic layout of  $\frac{1}{4}$  turn SQUID magnetometer. Cross-shaded regions indicate bias between upper and lower superconducting films. (b) Photograph of  $\frac{1}{16}$  turn YBCO SQUID with outer diameter of 7mm. Junctions are located close to the center (Ludwig, Dantsker, Kleiner *et al.*, 1995).

The two junctions connect the upper and lower superconducting films of the central trilayer. Compared with a flux-transformer coupled magnetometer, the multiloop magnetometer has the advantage that the current induced in each of the  $N$  loops when it is rotated in the earth's magnetic field is much smaller than that induced in a single loop of the same area. Furthermore, the device contains no closed superconducting loops, so that the maximum induced supercurrent is limited to the critical current of the junctions. A comprehensive theory for thin-film multiloop SQUIDs and their performance at 77 K has been given by [34]. The effective area  $A_{eff}$  and inductance  $L_{eff}$  are given by

$$A_{eff} = \frac{A_p}{N} - A_s$$

and

$$L_{eff} = \frac{L_p}{N^2} + \frac{L_s}{N} + L_j$$

Here,  $A_p$  and  $L_p$  are the area and inductance of the large, outer loop,  $A_s$  and  $L_s$  are the average area and inductance of one spoke of the cartwheel, and  $L_j$  is the

parasitic inductance of the connections from the pickup loops to the junctions. Calculation of the magnetic-field noise and transfer function as a function of  $N$ , based on the simulations of [76] for  $V_{\Phi}(L)$  and  $S_{\Phi}^{1/2}$ , shows that the optimum value of  $N$  for a minimum magnetic-field noise increases strongly with the overall size. For a diameter of 7 mm, the optimum number of loops is 15 to 20, considerably more than typically used in the low- $T_c$  case.

In the first practical realization of this magnetometer, Ludwig, Dantsker, Kleiner *et al.* [66] used their YBCO-SrTiO<sub>3</sub>-YBCO multilayer technology and bicrystal junctions to make the magnetometer shown in Figure 27(b). Most of the area of the pickup loops is patterned in the upper YBCO film, and each loop makes contact to the lower YBCO layer in the center (cross-shaded region). The two 24° bicrystal junctions are located in the lower YBCO film and also make contact to the upper and lower YBCO films in the central trilayer region.

A voltage modulation as high as 20 mV was observed despite the relatively high inductance, and resulted from the nearly ideal junction parameters,  $I_0=13$  mA and  $R=10\Omega$ . The effective area of 1.89 mm<sup>2</sup> was close to the predicted value. Using a flux-locked loop with 100 kHz flux modulation and bias reversal, the authors measured a magnetic-field noise of 18 fT Hz<sup>-1/2</sup> at 1 kHz and 37 fT Hz<sup>-1/2</sup> at 1 Hz. Similar multiloop magnetometers based on the same design were subsequently made, using step-edge junctions [24,77] or PBCO ramp junctions [78,79].

Two other high- $T_c$  magnetometers involving multiloops differ from the design discussed above. Fife *et al.* [55] coupled eight multiloop pickup coils with an outer diameter of 8.5 mm directly to a low-inductance washer SQUID with bicrystal junctions. The noise at 60K with bias reversal was 100 fT Hz<sup>-1/2</sup> above 3 Hz. Scharnweber and Schilling [80] recently reported an integrated magnetometer in which a flux transformer with a multiturn input coil and a multiloop pickup coil is inductively coupled to a low-inductance washer SQUID. For their best magnetometer, with four parallel loops 8.5 mm in diameter, at 77 K they measured a magnetic field noise of 44 fT Hz<sup>-1/2</sup> at 1 kHz with a static bias current and 100 fT Hz<sup>-1/2</sup> at 1 Hz with bias reversal.

## 8. Gradiometers

In many of these applications, good examples are magnetocardiology and non-destructive evaluation, one needs to detect weak signals against a background of magnetic noise that is many orders of magnitude higher. In urban environments, the dominant source of noise is the 50 or 60 Hz signals, and a large number of harmonics, from power lines: peak-to-peak amplitudes can range from 20 nT to 1 mT. Additionally, traffic (trains, subways, cars) can cause even stronger disturbances. For this reason, most sensitive measurements with low- $T_c$  magnetometers—particularly of biomagnetic signals—are currently made in a magnetically shielded room.

However, except for enclosures, such as that at the PTB, Berlin, with very high levels of attenuation, most shielded rooms do not reduce the 50 or 60 Hz fields sufficiently, and one requires a gradiometer to discriminate against distant noise sources with small gradients in favour of nearby signal sources. The traditional low- $T_c$  gradiometer is wound from niobium wire: two pickup loops wound in opposition and mounted on a common axis with a baseline (separation) of typically 0.1 m are connected in series with an input coil inductively coupled to a SQUID [72]. Such a device measures the first-derivative axial gradient  $\frac{\partial B_z}{\partial z}$ . The addition of a third coil midway between the two

loops results in a second-derivative gradiometer measuring  $\frac{\partial^2 B_z}{\partial z^2}$ . In the case of axial gradiometers, the separation of one pickup loop and the signal source is generally made rather less than the baseline, so that the instrument effectively detects the magnetic field from the source. Some typical designs for wire-wound gradiometers are shown in Figure 28.

Early wire-wound gradiometers were balanced (the “balance” is defined as the ratio of the output of the SQUID when a uniform magnetic field is applied to the gradiometer to the output when the same field is applied to one pickup loop) by adjusting the positions of small, superconducting pellets, sometimes to an accuracy of 1 part in 10<sup>6</sup>. However, a myriad of interacting, mechanically adjusted components becomes impractical for more than a few channels. Current practice is to use magnetometers and first-derivative gradiometers for the software generation of second or third derivatives [81].

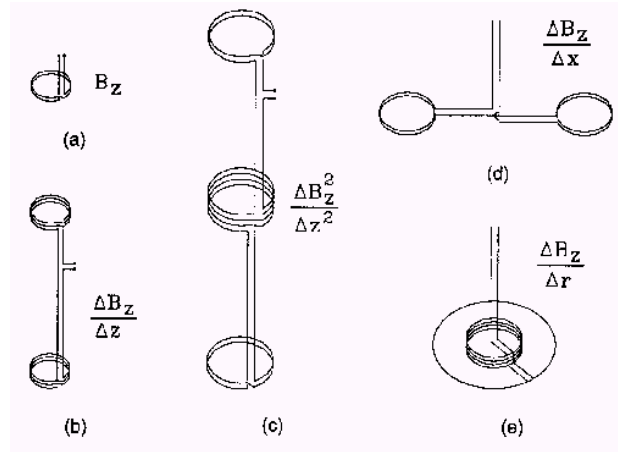


**Figure 28:** a variety of pick up coil designs and the physical quantity they measure: (a) magnetometer; (b) first order axial gradiometer; (c) second order axial gradiometer; (d) first order planar gradiometer; (e) first order radial gradiometer.

The lack of suitable wire eliminates the wire-wound, high- $T_c$  gradiometer as an option, and two alternative approaches have been adopted. The first is an *electronic gradiometer* made by subtracting the signals from separate magnetometers: the gradiometer can be axial or planar, and the baseline can be chosen at will. The second is a planar gradiometer with thin-film pickup loops.

A high- $T_c$ , axial gradiometer was demonstrated by Tavrín *et al.* [82], who mounted two rf SQUIDs one above the other, each with a bulk flux focuser [83]. One sensor was mounted rigidly while the plane inclination of the second, placed 60 mm above, could be adjusted from outside the cryostat to achieve a balance of about 1 part in 103. This system was used to measure magnetocardiograms (MCG) in an unshielded environment, against a 50 Hz background of 1 to 20 nT, although the quality of the cardiograms was limited by  $1/f$  noise in the magnetometers, about  $1 \text{ pT/Hz}^{1/2}$ . Subsequently, Tavrín *et al.* [84] added a third, vertically stacked sensor to form a second-derivative gradiometer. The lowest sensor was rigidly mounted, while the inclination of the other two, 60 and 120 mm above it, could be adjusted. The three channels,  $A$ ,  $B$ , and  $C$  could be added electronically to generate two first-derivatives,  $A-B$  and  $B-C$ , and the second derivative,  $A-2B+C$ . The system could be balanced to achieve a common mode rejection ratio of 1 part in 3000 and a gradient rejection of 1 part in 100. The magnetic-field noise referred to SQUID  $A$  or  $C$  was below  $300 \text{ fT Hz}^{-1/2}$ . A similar electronically formed axial gradiometer was recently reported by Borgmann *et al.* [85] who used a set of adjustable superconducting plates, similar to those in early low- $T_c$  gradiometers, to achieve the final balance. The authors achieved a balance better than 104 for uniform background

fields and better than 200 for gradient fields. Electronic gradiometers have also been constructed with the magnetometers in the same plane [86,87].

The balance of an electronic gradiometer is limited by the linearity of the flux-locked magnetometers and by the common mode rejection ratio of the subtraction system. In the presence of high background noise, the dynamic range and slew rate of the magnetometers may be challenged. None of these difficulties arises with superconducting gradiometers, which thus have an inherent advantage over electronic cancellation. However, the three-SQUID gradiometer (TSG) of Koch *et al.* [88], shown in Figure 29, also circumvents these problems by using electronic cancellation and subtraction. The center, reference magnetometer operates in a flux-locked loop and applies its output also to a coil coupled to each of the outer magnetometers. Thus the environmental noise at each of the two sensing magnetometers is greatly attenuated, reducing their linearity and slew-rate requirements. The signals from the outer two sensors are then subtracted to form a first-derivative gradiometer.

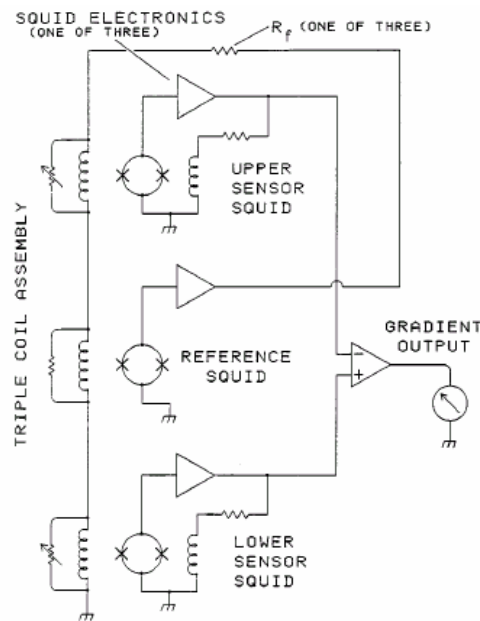


**Figure 29:** Configuration of three-SQUID gradiometer.

Koch and co-workers demonstrated several versions of the TSG, with baselines of 0.1 to 0.25 m and using both low- $T_c$  and high- $T_c$  SQUIDs. The balance can be adjusted to about 1 part in 4000 by adjusting the feedback currents with room-temperature resistors. A key advantage of this approach is that any noise generated by the central sensor is applied equally to the two outer magnetometers and eliminated in the subtraction. In their original publication, Koch *et al.* reported a white gradient noise of  $6 \text{ pTm}^{-2}/\text{Hz}^{-1/2}$

for SQUIDs with  $3 \times 3 \text{ mm}^2$  flux-focusing washers. For a baseline of 0.1 m, this result corresponds to a magnetic-field noise of  $600 \text{ fT Hz}^{-1/2}$  referred to one sensor.

Electronic subtraction enables one to choose an arbitrary baseline and to adjust the balance externally. Experience with low- $T_c$  devices, however, shows that it is notoriously difficult to operate such systems in the harsh environment of a laboratory or a hospital and to achieve an adequate signal-to-noise ratio for clinical applications. Low- $T_c$  systems intended for unshielded operation invariably have a gradiometric flux transformer to bear the brunt of the large level of background noise; even then, an adequate signal-to-noise ratio in unfavourable situations may not be possible [81]. Thus there are strong incentives to develop high- $T_c$  equivalents, albeit in planar geometries. An early gradiometer fabricated from a YBCO-STO-YBCO multilayer [89] employed a multiturn input coil coupled to two pickup loops of opposite senses in the same plane. The baseline was about 5 mm. The multiturn coil was coupled to a square-washer SQUID in a flip-chip arrangement. At the time, multilayer technology was still in its infancy and the device exhibited substantial levels of  $1/f$  noise. The best reported gradient noise at 10 Hz was  $400 \text{ pTm}^{-1} \text{ Hz}^{-1/2}$ . A similar flip-chip gradiometer with improved  $1/f$  noise was reported later by Keene, Chew *et al.* [90]. However, both gradiometers exhibited poor balance because of the unbalanced SQUID. The balance was improved by two orders of magnitude to about 1 part in 1000 by means of gradiometrically configured SQUIDs [53,90].

An alternative gradiometer configuration [23] consists of two pickup loops in parallel with a SQUID measuring the current induced along the common line (Figure 30(a)).

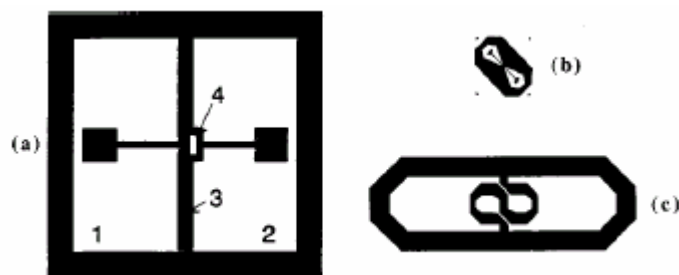


**Figure 30:** Gradiometers: (a) Principle of single-layer, planar gradiometer with parallel inductances 1 and 2. A gradient  $\partial B_z / \partial x$  induces a current in the central strip 3 that links flux to the SQUID 4 (Daalmans, 1995). (b) First-derivative planar gradiometer on a  $10 \times 10 \text{ mm}^2$  chip that is coupled to (c) the gradiometric structure on a two-inch substrate (Faley *et al.*, 1997).

This configuration has the disadvantage that large supercurrents are induced around the perimeter when the device is rotated in an ambient field. Knappe *et al.*, Zakosarenko *et al.*, Daalmans *et al.*, Schultze, Stolz *et al.*, Schmidl, Wunderlich, Dorrer, Specht *et al.*

[91-95] have all made single-layer, first-derivative gradiometers of this kind, using dc SQUIDs with either step-edge or bicrystal junctions. The baselines are limited by the size of the substrate to about 5 mm, and the best gradient sensitivities are about  $50 \text{ pTm}^{-1} \text{ Hz}^{-1/2}$ . All the dc SQUID-based gradiometers described above have the disadvantage that the SQUID itself has a nonzero response to magnetic field, producing an intrinsic imbalance. This problem is circumvented in the rf SQUID-based gradiometer by Zhang, Soltner, Krause *et al.* [96], resembling the configuration of Figure 30 (a), with a single, step-edge junction intersecting the central strip. This structure is a re-creation of the Nb “two hole” rf SQUID [97]. The device had a baseline of about 5 mm and was balanced to 1 part in 1000. The gradient field noise was about  $100 \text{ pTm}^{-1} \text{ Hz}^{-1/2}$  above 10 Hz. One of these gradiometers was used to perform eddy-current measurements of cracks in aluminium in an unshielded environment.

Several attempts have been made to extend the baseline using single-layer gradiometers in a flip-chip arrangement [93,98]. The concept is illustrated in Figs. 30 (b) and (c) [98], which shows a dc SQUID with quasi-planar PBCO junctions on a  $10 \times 10 \text{ mm}^2$  chip that is inductively coupled to a gradiometric flux transformer on a 50 mm substrate. The central strip in the transformer is intended to reduce the inductance and pickup area of the SQUID by screening. The baseline was 20 mm, the balance about 1 part in 1800 and the noise  $5 \text{ pTm}^{-1} \text{ Hz}^{-1/2}$  at 1 kHz. A comparable sensitivity was reported by Daalmans [93]. It should be noted that all the single-layer, thin-film gradiometers lose substantial sensitivity because the inductances of the pickup loops are mismatched to the input coil coupling them to the SQUID. This drawback, together with the relatively short baseline of even the largest devices (20 mm) implies that none of them is practicable for applications such as magnetocardiology.

However, they may be well suited to non-destructive evaluation (NDE). To achieve high enough sensitivity and a long enough baseline for magnetocardiology with this approach would require a multiturn input coil fabricated on a substrate at least 50 mm and preferably 100 mm in length. This somewhat daunting prospect has yet to be tackled.

A new approach to single-layer, thin-film gradiometers was recently demonstrated by [99] Dantsker, Froehlich *et al.* (1997) who fabricated the asymmetric, planar gradiometer shown schematically in Figure 31(a).

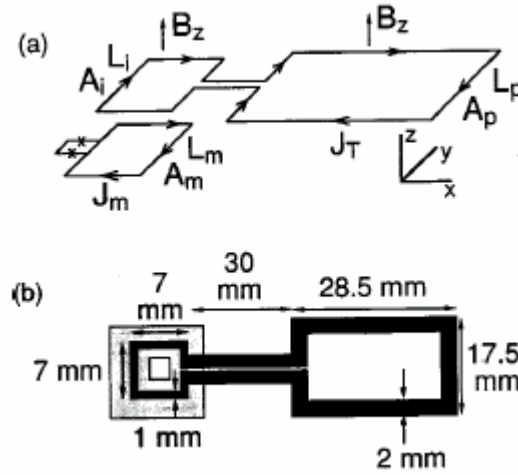


**Figure 31:** Configuration of asymmetric, planar gradiometer coupled to a directly coupled magnetometer: (a) schematic, (b) experimental (shaded square represents magnetometer) (Dantsker, Froehlich *et al.*, 1997).

The gradiometer consists of a directly coupled SQUID magnetometer with a pickup loop of inductance  $L_m$  and area  $A_m$ , and a superconducting flux transformer with an input loop of inductance  $L_i$  and area  $A_i$  connected to a pickup loop of inductance  $L_p$  and area  $A_p$ . The mutual inductance between the magnetometer and input loop is  $M_i = \alpha(L_m L_i)^{1/2}$ . With a suitable choice of these parameters, one attains the balance condition

$$\alpha = \left[ \frac{A_m}{(A_p + A_i)} \right] \frac{(L_p + L_i)}{(L_i L_m)^{1/2}}$$

for which the directly coupled magnetometer produces zero response to a uniform magnetic field  $B_z$ . The physical configuration of the gradiometer is shown in Figure 31(b). The single-layer directly coupled magnetometer was patterned in a 150-nm-thick YBCO film laser-deposited on a  $10 \times 10 \text{ mm}^2$  SrTiO<sub>3</sub> bicrystal. The outer and inner dimensions of the magnetometer loop are 10 and 2 mm, respectively, yielding an estimated inductance  $L_m = 4$  nH and area  $A_m = 20 \text{ mm}^2$ . The flux transformer was fabricated from a 260-nm-thick YBCO film co-evaporated on a 100 mm  $r$ -plane sapphire wafer. For these dimensions, balance is predicted to occur for  $\alpha = 0.43 \pm 0.04$ . The baseline, the separation between the midpoints of the two loops, is 48 mm.

The gradiometer was balanced by sliding the flux transformer over the magnetometer, immersed in liquid nitrogen, thereby varying the coupling coefficient  $\alpha$ . A balance of about 1 part in 3000 was achieved with respect to magnetic fields perpendicular to the plane of the gradiometer, while the intrinsic balance with respect to in-plane fields was

about 1 part in 1400. Operated in an unshielded environment, the gradiometer reduced the 60 Hz peak by a factor of 1600 compared with the bare magnetometer.

This approach to gradiometers has several advantages. The fact that the intrinsic magnetic-field sensitivity of the magnetometer is reduced by only a few percent by the presence of the transformer is particularly appealing for high- $T_c$  devices, for which resolution is at a premium. It should not be necessary to use particularly

high quality films, since vortex motion in a flux transformer with a relatively large area and inductance does not contribute significantly to the overall  $1/f$  magnetic-field noise [38]. The general principle can be extended to other derivatives of the magnetic field: for example, the addition of a second, identical pickup loop on the opposite side of the

input loop would produce a gradiometer sensitive to  $\frac{\partial^2 B_z}{\partial z^2}$ . The high degree of balance

and long baseline make this gradiometer eminently suitable for multichannel arrays for biomagnetic measurements. However, would be impracticable to balance these gradiometers mechanically, a more realistic approach might be to mount the transformer permanently on the magnetometer and to achieve the final balance by laser trimming.

For NDE, one generally does not require particularly high sensitivity, and a relatively compact, single-layer gradiometer with a baseline of 5–10 mm is likely to be adequate.

For biomagnetism, the situation is more complex. Good results have been achieved with electronic subtraction of magnetometers, but limitations of slew rate and linearity present difficulties for unshielded operation. Still, this approach is the only one that can measure an axial gradient. For the immediate future, at least, gradiometric flux

transformers are limited to planar configurations. Ideally, one would like to fabricate a long-baseline gradiometer with a multiturn, multilayer input coil, with an inductance to match that of the pick-up loops, inductively coupled to the SQUID. In practice, the cost of manufacturing such structures on large substrates, say, four inch, is likely to be prohibitive. The best alternative would seem to be the asymmetric, planar gradiometer, provided it can be balanced adequately without recourse to mechanical adjustment.

## References

[1] Heike Kamerlingh Onnes, “Sur les resistances electriques,” *Communications from the Physical Laboratory of the University of Leiden*, Supplement **29** (1911), 1–11.

[2] Kostas Gavroglu and Yorgos Goudaroulis, “The Remarkable Work of ‘Le Gentleman du Zero Absolu’”, in *Through Measurement to Knowledge :The Selected*

*Papers of Heike Kamerlingh Onnes, 1853– 1926*, ed. Gavroglu and Goudaroulis (Boston: Kluwer Academic Publishers, 1991), xiii–xcvi.

[3] Per F. Dahl, “Kamerlingh Onnes and the Discovery of Superconductivity: The Leyden Years, 1911–1914,” *Historical Studies in the Physical Sciences*, **15** (1984), 1–37. See also Dahl, *Superconductivity : Its Historical Roots and Development from Mercury to the Ceramic Oxides* (New York: American Institute of Physics, 1992).

[4] A. Barone and G. Paternò, *Physics and Applications of the Josephson Effect*, edited by Wiley, publisher, New York, 1982.

[5] D. Koelle, R. Kleiner, F. Ludwig, E. Dantsker, John Clarke, *Reviews of modern physics*, vol 71, No.3 April 1999.

[6] Michael Tinkham, “Introduction to superconductivity”, Courier Dover publication.

[7] Lubkin, Gloria B., Power Applications of High- Temperature Superconductors, *Physics Today* 49, March 1996, p48.

[8] J. C. Gallop “SQUIDS, the Josephson effects and Superconducting electronics” The Adam Hilger series on Measurement Science and Technologies, IOP Publishing Ltd 1991.

[9] Kristian Fosheim, Asle Sudbo “Superconductivity Physics and Applications” John Wiley & Sons, Ltd.

[10] Hans Hilgenkamp, Jochen Mannhart “Grain boundaries in High-Tc Superconductors” *Review Modern Physics*, April 2002.

[11] R.Feynman, R. B. Leighton, and M. Sands. “The Feynman Lectures on Physics”, volume III. Addison-Wesley, Reading, Massachusetts, 1965.

[12] J. Clarke. in H. Weinstock and R. W. Ralston eds. “The new superconducting electronics, 123-180. Kluwer publisher, The Netherlands, 1993.

[13] G. Koren, E. Polturak, E. Ahroni and D. Cohen „Characteristics of all YBCO edge junctions operating above 80 K“ *Appl. Phys. Lett.* **59**, 2747-2754 (1991).

[14] Tesche, C. D., and J. Clarke, 1977, *J. Low Temp. Phys.* **29**, 301.

[15] Tesche, C. D., and J. Clarke, 1979, *J. Low Temp. Phys.* **37**, 397.

[16] Koch, R. H., W. J. Gallagher, B. Bumble, and W. Y. Lee, 1989, *Appl. Phys. Lett.* **54**, 951.

[17] Koch, R. H., J. Clarke, W. M. Goubau, J. M. Martinis, C. M. Pegrum, and D. J. Van Harlingen, 1983, *J. Low Temp. Phys.* **51**, 207.

[18] Ferrari, M. J., M. Johnson, F. C. Wellstood, J. J. Kingston, T. J. Shaw, and J. Clarke, 1994, *J. Low Temp. Phys.* **94**, 15.

- [19] E. Dantsker, S. Tanaka, and John Clarke, "High- Tc super conducting quantum interference devices with slots or holes: Low 1/ f noise in ambient magnetic fields" *Appl. Phys. Lett.* **70** (15), 14 April 1997.
- [20] Drung, D., 1996, in *SQUID Sensors: Fundamentals, Fabrication and Applications*, NATO ASI Series, edited by H. Weinstock (Kluwer Academic, Dordrecht), p. 63.
- [21] Forgacs, R. L., and A. F. Warnick, 1967, *Rev. Sci. Instrum.* **38**, 214.
- [22] Clarke, J., W. M. Goubau, and M. B. Ketchen, 1976, *J. Low Temp. Phys.* **25**, 99.
- [23] Ketchen, M. B., W. M. Goubau, J. Clarke, and G. B. Donaldson, 1978, *Appl. Phys.* **49**, 4111.
- [24] Drung, D., E. Dantsker, F. Ludwig, H. Koch, R. Kleiner, J. Clarke, S. Krey, D. Reimer, B. David, and O. Doessel, 1996, *Appl. Phys. Lett.* **68**, 1856.
- [25] Giffard, R. P., 1980, in *Superconducting Quantum Interference Devices and Their Applications*, edited by H. D. Hahlbohm and H. Lübbig (de Gruyter, Berlin), p. 445.
- [26] Wellstood, F., C. Heiden, and J. Clarke, 1984, *Rev. Sci. Instrum.* **55**, 952.
- [27] Foglietti, V., W. J. Gallagher, M. B. Ketchen, A. W. Kleinsasser, R. H. Koch, S. I. Raider, and R. L. Sandstrom, 1986, *Appl. Phys. Lett.* **49**, 1393.
- [28] Dossel, O., B. David, M. Fuchs, W. H. Kullmann, and K.-M. Ludeke, 1991, *IEEE Trans. Magn.* **MAG-27**, 2797.
- [29] Koch, R. H., W. Eidelloth, B. Oh, R. P. Robertazzi, S. A. Andrek, and W. J. Gallagher, 1992, *Appl. Phys. Lett.* **60**, 507.
- [30] Miklich, A. H., D. Koelle, E. Dantsker, D. T. Nemeth, J. Kingston, R. F. Kroman, and J. Clarke, 1993, *IEEE Trans. Appl. Supercond.* **3**, 2434.
- [31] Grundler, D., R. Eckart, B. David, and O. Doessel, 1993, *Appl. Phys. Lett.* **62**, 2134.
- [32] Drung, D., 1994, *IEEE Trans. Appl. Supercond.* **4**, 121.
- [33] Drung, D., R. Cantor, M. Peters, H.-J. Scheer, and H. Koch, 1990, *Appl. Phys. Lett.* **57**, 406.
- [34] Drung, D., 1995, *Appl. Phys. Lett.* **67**, 1474.
- [35] Ludwig, F., J. Beyer, D. Drung, S. Bechstein, and Th. Schurig, 1997, *Appl. Supercond.* **5**, 345.
- [36] Drung, D., F. Ludwig, W. Müller, U. Steinhoff, L. Trahms, Y. Q. Shen, M. B. Jensen, P. Vase, T. Holst, T. Freltoft, and G. Curio, 1996, *Appl. Phys. Lett.* **68**, 1421.

- [37] Matsuda, M., Y. Murayama, S. Kiryu, N. Kasai, S. Kashiwaya, M. Koyanagi, and T. Endo, 1991, IEEE Trans. Magn. **MAG-27**, 3043.
- [38] Koelle, D., A. H. Miklich, F. Ludwig, E. Dantsker, D. T. Nemeth, and J. Clarke, 1993, Appl. Phys. Lett. **63**, 2271.
- [39] Cantor, R., L. P. Lee, M. Teepe, V. Vinetskiy, and J. Longo, 1995, IEEE Trans. Appl. Supercond. **5**, 2927.
- [40] Lee, L. P., J. Longo, V. Vinetskiy, and R. Cantor, 1995, Appl. Phys. Lett. **66**, 1539.
- [41] Cantor, R., 1996, in *SQUID Sensors: Fundamentals, Fabrication and Applications*, NATO ASI Series, edited by H. Weinstock (Kluwer Academic, Dordrecht), p. 179.
- [42] Glyantsev, V. N., Y. Tavrín, W. Zander, J. Schubert, and M. Siegel, 1996, Supercond. Sci. Technol. **9**, A105.
- [43] Beyer, J., D. Drung, F. Ludwig, T. Minotani, and K. Enpuku, 1998, Appl. Phys. Lett. **72**, 203.
- [44] Martinis, J. M., and J. Clarke, 1985, J. Low Temp. Phys. **61**, 227.
- [45] Wellstood, F. C., J. J. Kingston, M. J. Ferrari, and J. Clarke, 1990, Appl. Phys. Lett. **57**, 1930.
- [46] Miklich, A. H., J. J. Kingston, F. C. Wellstood, J. Clarke, M. S. Colclough, K. Char, and G. Zaharchuk, 1991, Appl. Phys. Lett. **59**, 988.
- [47] Wellstood, F. C., A. H. Miklich, J. J. Kingston, M. J. Ferrari, J. Clarke, M. S. Colclough, K. Char, and G. Zaharchuk, 1992, in *Superconducting Devices and their Applications*, edited by H. Koch and H. Lübbig, Springer Proceedings in Physics (Springer, Berlin/Heidelberg), Vol. 64, p. 162.
- [48] Oh, B. D., R. H. Koch, W. J. Gallagher, R. P. Robertazzi, and W. Eidelloth, 1991, Appl. Phys. Lett. **59**, 123.
- [49] Freltoft, T., Y. Q. Shen, and P. Vase, 1993, IEEE Trans. Appl. Supercond. **3**, 2937.
- [50] Hilgenkamp, J. W. M., R. P. J. Ijsselsteijn, A. J. H. M. Rijnders, P. A. C. Tavares, J. Flokstra, and H. Rogalla, 1993, J. Alloys Compd. **195**, 707.
- [51] Roas, B., L. Bärr, M. Kühnl, G. Daalmans, and F. Bommel, 1993, in *Proceedings of European Conference on Applied Superconductivity (EUCAS'93)*, edited by H. C. Freyhardt (DGM Informationsgesellschaft, Oberursel), p. 1335.
- [52] Keene, M. N., S. W. Goodyear, N. G. Chew, R. G. Humphreys, J. S. Satchell, J. A. Edwards, and K. Lander, 1994, Appl. Phys. Lett. **64**, 366.
- [53] Keene, N. M., J. S. Satchell, S. W. Goodyear, R. G. Humphreys, J. A. Edwards, N. G. Chew, and K. Lander, 1995, IEEE Trans. Appl. Supercond. **5**, 2923.

- [54] Dantsker, E., F. Ludwig, R. Kleiner, J. Clarke, M. Teepe, L. P. Lee, N. McN. Alford, and T. Button, 1995, *Appl. Phys. Lett.* **67**, 725.
- [55] Fife, A. A., G. Anderson, V. Angus, C. Backhouse, K. Betts, M. B. Burbank, R. A. Cragg, K. Ferguson, F. Habib, P. R. Kubik, J. Nomura, M. Smith, P. Spear, W. Westera, Hu Zhou, S. Govorkov, B. Heinrich, J. C. Irwin, and W. B. Xing, 1995, *IEEE Trans. Appl. Supercond.* **5**, 3113.
- [56] Ludwig, F., D. Koelle, E. Dantsker, D. T. Nemeth, A. H. Miklich, J. Clarke, and R. E. Thomson, 1995, *Appl. Phys. Lett.* **66**, 373.
- [57] Scharnweber, R., K.-O. Subke, and M. Schilling, 1995, in *Proceedings of the Second European Conference on Applied Superconductivity (EUCAS'95)*, Edinburgh, edited by D. Dew-Hughes (Institute of Physics, Bristol/Philadelphia) Institute of Physics Conference Series No. 148, p. 1609.
- [58] Schilling, M., R. Scharnweber, and S. Voßl, 1995, *IEEE Trans. Appl. Supercond.* **5**, 2346.
- [59] Kugai, H., T. Nagaishi, and H. Itozaki, 1996, in *Advances in Superconductivity VIII*, edited by H. Hayakawa and Y. Enomoto (Springer, Tokyo), p. 1145.
- [60] Lee, L. P., K. Char, M. S. Colclough, and G. Zaharchuk, 1991, *Appl. Phys. Lett.* **59**, 3051.
- [61] DiIorio, M. S., S. Yoshizumi, K.-Y. Yang, M. Maung, and B. Power, 1993, in *Advances in Superconductivity V*, edited by Y. Bando and H. Yamauchi (Springer, Tokyo), p. 1161.
- [62] Kromann, R., J. J. Kingston, A. H. Miklich, L. T. Sagdahl, and J. Clarke, 1993, *Appl. Phys. Lett.* **63**, 559.
- [63] Hilgenkamp, J. W. M., G. C. S. Brons, J. G. Soldevilla, R. P. J. Ijsselsteijn, J. Flokstra, and H. Rogalla, 1994, *Appl. Phys. Lett.* **64**, 3497.
- [64] David, B., D. Grundler, J.-P. Krumme, and O. Dössel, 1995, *IEEE Trans. Appl. Supercond.* **5**, 2935.
- [65] DiIorio, M. S., K.-Y. Yang, and S. Yoshizumi, 1995, *Appl. Phys. Lett.* **67**, 1926.
- [66] Ludwig, F., E. Dantsker, D. Koelle, R. Kleiner, A. H. Miklich, D. T. Nemeth, J. Clarke, D. Drung, J. Knappe, and H. Koch, 1995, *IEEE Trans. Appl. Supercond.* **5**, 2919.
- [67] Shen, Y. Q., Z. J. Sun, R. Kromann, T. Holst, P. Vase, and T. Freltoft, 1995, *Appl. Phys. Lett.* **67**, 2081.
- [68] Ryhänen, T., H. Seppä, R. Ilmoniemi, and J. Knuutila, 1989, *Low Temp. Phys.* **76**, 287.

- [69] Enpuku, K., T. Maruo, and T. Minotani, 1997, IEEE Trans. Appl. Supercond. **7**, 3355.
- [70] Minotani, T., K. Enpuku, and Y. Kuroki, 1997, J. Appl. Phys. **82**, 457.
- [71] Hilgenkamp, J. W. M., F. J. G. Roesthuis, S. Hoogeveen, L. D. Vargas Llona, J. Flokstra, and H. Rogalla, 1995, in *Proceedings of the 2nd Workshop on HTS Applications and New Materials*, edited by D. H. A. Blank (Enschede, The Netherlands), p. 117.
- [72] Zimmerman, J. E., 1971, J. Appl. Phys. **42**, 4483.
- [73] Drung, D., R. Cantor, M. Peters, T. Ryh nen, and H. Koch, 1991, IEEE Trans. Magn. **MAG-27**, 3001.
- [74] Koch, R. H., M. B. Ketchen, W. J. Gallagher, R. L. Sandstrom, A. W. Kleinsasser, D. R. Gambrel, T. H. Field, and H. Matz, 1991, Appl. Phys. Lett. **58**, 1786.
- [75] Drung, D. and H. Koch, 1993, IEEE Trans. Appl. Supercond. **3**, 2594.
- [76] Enpuku, K., Y. Shimomura, and T. Kisu, 1993, J. Appl. Phys. **73**, 7929.
- [77] David, B., D. Grundler, S. Krey, V. Doormann, R. Eckart, J. Krumme, G. Rabe, and O. D ssel, 1996, Supercond. Sci. Technol. **9**, A96.
- [78] Reimer, D., M. Schilling, S. Knappe, and D. Drung, 1995, IEEE Trans. Appl. Supercond. **5**, 2342.
- [79] Reimer, D., F. Ludwig, M. Schilling, S. Knappe, and D. Drung, 1995, in *Proceedings of the Second European Conference on Applied Superconductivity (EUCAS'95)*, Edinburgh, edited by D. Dew-Hughes (Institute of Physics, Bristol, Philadelphia) Institute of Physics Conference Series No. 148, p. 1605.
- [80] Scharnweber, R., and M. Schilling, 1997, IEEE Trans. Appl. Supercond. **7**, 3485.
- [81] Vrba, J., 1996, in *SQUID Sensors: Fundamentals, Fabrication and Applications*, NATO ASI Series, edited by H. Weinstock (Kluwer Academic, Dordrecht), p. 117.
- [82] Tavr n, Y., Y. Zhang, M. Mu ck, A. I. Braginski, and C. Heiden, 1993a, IEEE Trans. Appl. Supercond. **3**, 2477.
- [83] Zhang, Y., M. Mu ck, K. Herrmann, W. Zander, J. Schubert, A. I. Braginski, and Ch. Heiden, 1992, Appl. Phys. Lett. **60**, 645.
- [84] Tavr n, Y., Y. Zhang, W. Wolf, and A. I. Braginski, 1994, Supercond. Sci. Technol. **7**, 265.
- [85] Borgmann, J., P. David, G. Ockenfu , R. Otto, J. Schubert, W. Zander, and A. I. Braginski, 1997, Rev. Sci. Instrum. **68**, 2730.

- [86] David, B., O. Doessel, V. Doormann, R. Eckart, W. Hoppe, J. Kruiger, H. Laudan, and G. Rabe, 1997, *IEEE Trans. Appl. Supercond.* **7**, 3267.
- [87] ter Brake, H. J. M., N. Janssen, J. Flokstra, D. Veldhuis, and H. Rogalla, 1997, *IEEE Trans. Appl. Supercond.* **7**, 2545.
- [88] Koch, R. H., J. R. Rozen, J. Z. Sun, and W. J. Gallagher, 1993, *Appl. Phys. Lett.* **63**, 403.
- [89] Eidelloth, W., B. Oh, R. P. Robertazzi, W. J. Gallagher, and R. H. Koch, 1991, *Appl. Phys. Lett.* **59**, 3473.
- [90] Keene, M. N., S. W. Goodyear, N. G. Chew, R. G. Humphreys, J. S. Satchell, J. A. Edwards, and K. Lander, 1994, *Appl. Phys. Lett.* **64**, 366.
- [91] Knappe, S., D. Drung, T. Schurig, H. Koch, M. Klinger, and J. Hinken, 1992, *Cryogenics* **32**, 881.
- [92] Zakosarenko, V., F. Schmidl, H. Schneidewind, L. Dorrer, and P. Seidel, 1994, *Appl. Phys. Lett.* **65**, 779.
- [93] Daalmans, G. M., L. Baer, M. Kuhn, D. Uhl, M. Selent, and J. Ramos, 1995, *IEEE Trans. Appl. Supercond.* **5**, 3109.
- [94] Schultze, V., R. Stolz, R. Ijsselsteijn, V. Zakosarenko, L. Fritzsche, F. Thrum, E. Il'ichev, and H.-G. Meyer, 1997, *IEEE Trans. Appl. Supercond.* **7**, 3473.
- [95] Schmidl, R., S. Wunderlich, L. Dorrer, H. Specht, S. Linzen, Schneidewind, and P. Seidel, 1997, *IEEE Trans. Appl. Supercond.* **7**, 2756.
- [96] Zhang, Y., H. Soltner, N. Wolters, W. Zander, J. Schubert, M. Banzet, and A. I. Braginski, 1997, *IEEE Trans. Appl. Supercond.* **7**, 2870.
- [97] Zimmerman, J. E., P. Thiene, and J. T. Harding, 1970, *J. Appl. Phys.* **41**, 1572.
- [98] Faley, M. I., U. Poppe, K. Urban, H.-J. Krause, H. Soltner, R. Hohmann, D. Lomparski, R. Kutzner, R. Wördenweber, H. Bousack, A. I. Braginski, V. Y. Slobodchikov, A. V. Gapelyuk, V. V. Khanin, and Y. V. Maslennikov, 1997, *IEEE Trans. Appl. Supercond.* **7**, 3702.
- [99] Dantsker, E., O. Froehlich, S. Tanaka, K. Kouznetsov, J. Clarke, Z. Lu, V. Matijasevic, and K. Char, 1997, *Appl. Phys. Lett.* **71**, 1712.

# Chapter 2

## Advanced Non-Destructive Testing

### Introduction

This chapter is focused on the introduction of the non destructive evaluation prototype used in this research activity. To better understand the capability and the advantages of the NDE prototype system based on the HTS dc-SQUID magnetometer is necessary to discuss the non destructive NDE evaluation based on the conventional technique and their applications. At first an overview of the mainly and widely used non destructive techniques is reported. A briefly description of the working basic principles and the most important application for each methods are mentioned.

The second section is entirely dedicated to the eddy current technique based on the induction coil. The basic topics, the data representation and the most commonly used probe are described. Moreover, in this paragraph is described the conventional eddy current instrument, used in this work to validate the results of the NDE SQUID based prototype. In section 3, the attention has been focused on the application of SQUID concerned with the analysis of damage in complex and non-homogeneity structure such as composite materials, and to investigate the corrosion damage of metallic plate. These two applications of the SQUID sensor has been widely discussed because represent the two main topics of this activity research. Moreover, in the fourth section the eddy current system based on the HTS dc-SQUID magnetometer is introduced. It includes the description of the cryogenic system, the characteristics of the SQUID magnetometer, the eddy current source, the electronic used for the data acquisition and the x-y positioning system. Finally, the configuration of the SQUID respect to the excitation coil to realize a zero field detector is shown. The last section includes also the typical signal response due to a defect in metallic structure using two representations: the impedance plane and the spatial domain.

## 1. NDE

Non Destructive Evaluation (NDE) is a technical method to examine materials or components, in ways that do not impair their future usefulness and serviceability, in order to detect, locate and measure discontinuities, defects and other imperfections (porosity, wall thinning from corrosion and many sorts of disbands) which arise during manufacturing process and in service life, and to evaluate integrity, properties, composition and geometrical characteristics [1]. NDE is used in process control, in post-production quality control, and in the testing of system that are already in use. It is concerned in a practical way with the performance of the test piece: how long may the piece be used and when does it need to be checked again? As an interdisciplinary field, NDE benefited from capabilities that develop in many other fields of material science and engineering to improve the NDE technique, leading to smarter instruments, which are computer controlled, smaller, lighter and more capable. The requirements for NDE are continuing to be driven by the need for lower cost methods and instruments with greater reliability, sensitivity, user friendliness and high operation speed as well as applicability to complex materials, such as composites, and structures with complex geometries such as aircraft, bridges, pipelines, and pressure vessel. Non-destructive testing in the industry has become an increasingly vital factor in the effective conduct of research, development, design and manufacturing programs. Only with appropriate use of non-destructive testing techniques can the benefits of advanced materials science be fully realized. Tables 1 and 2 summarize information about non-destructive testing methods arranged to show their purposes and similarities. The National Materials Advisory Board (NMAB) Ad Hoc Committee on Non-destructive Evaluation adopted a system that classified methods into six major categories: visual, penetrating radiation, magnetic-electrical, mechanical vibration, thermal and chemical-electrochemical [2,3]. A version of the classification system is presented in Table 1, with additional categories included to cover new methods. The first six categories involve basic physical processes that require transfer of matter or energy to the object being tested.

Two auxiliary categories describe processes that provide for transfer and storage of information, and evaluation of the raw signals and images common to non-destructive testing methods.

<b>TABLE 1. Non-destructive testing method categories</b>	
<b>Basic Categories</b>	<b>Objectives</b>
<i>Mechanical and optical</i>	colour, cracks, dimensions, film thickness, gaging, reflectivity, strain distribution and magnitude, surface finish, surface flaws, through-cracks
<i>Penetrating radiation</i>	cracks, density and chemistry variations, elemental distribution, foreign objects, inclusions, microporosity, misalignment, missing parts, segregation, service degradation, shrinkage, thickness, voids
<i>Electromagnetic and electronic</i>	alloy content, anisotropy, cavities, cold work, local strain, hardness, composition, contamination, corrosion, cracks, crack depth, crystal structure, electrical and thermal conductivities, flakes, heat treatment, hot tears, inclusions, ion concentrations, laps, lattice strain, layer thickness, moisture content, polarization, seams, segregation, shrinkage, state of cure, tensile strength, thickness, disbonds
<i>Sonic and ultrasonic</i>	crack initiation and propagation, cracks, voids, damping factor, degree of cure, degree of impregnation, degree of sintering, delaminations, density, dimensions, elastic module, grain size, inclusions, mechanical degradation, misalignment, porosity, radiation degradation, structure of composites, surface stress, tensile, shear and compressive strength, disbonds, wear
<i>Thermal and infrared</i>	bonding, composition, emissivity, heat contours, plating thickness, porosity, reflectivity, stress, thermal conductivity, thickness, voids
<i>Chemical and analytical</i>	alloy identification, composition, cracks, elemental analysis and distribution, grain size, inclusions, macrostructure, porosity, segregation, surface anomalies
<b>Auxiliary Categories</b>	<b>Objectives</b>
<i>Image generation</i>	dimensional variations, dynamic performance, anomaly characterization and definition, anomaly distribution, anomaly propagation, magnetic field configurations
<i>Signal image analysis</i>	data selection, processing and display, anomaly mapping, correlation and identification, image enhancement, separation of multiple variables, signature analysis

Each method can be completely characterized in terms of five principal factors:

- energy source or medium used to probe the test object (such as X-rays, ultrasonic waves or thermal radiation);

- nature of the signals, image or signature resulting from interaction with the test object (attenuation of X-rays or reflection of ultrasound, for example);
- means of detecting or sensing resulting signals (photo emulsion, piezoelectric crystal or inductance coil);
- method of indicating or recording signals (meter deflection, oscilloscope trace or radiograph);
- basis for interpreting the results (direct or indirect indication, qualitative or quantitative, and pertinent dependencies).

The objective of each test method is to provide information about the following material parameters:

- discontinuities (such as cracks, voids, inclusions, delaminations);
- structure (including crystalline structure, grain size, segregation, misalignment);
- dimensions and metrology (thickness, diameter, gap size, discontinuity size);
- physical and mechanical properties (reflectivity, conductivity, elastic modulus, sonic velocity);
- composition and chemical analysis (alloy identification, impurities, elemental distributions);
- stress and dynamic response (residual stress, crack growth, wear, vibration); and
- signature analysis (image content, frequency spectrum, field configuration).

The terms used above are defined in Table 2. The limitations of a method include conditions required by that method: conditions to be met for technique application (access, physical contact, preparation) and requirements to adapt the probe or probe medium to the test object. Other factors limit the detection or characterization of discontinuities, properties and other attributes and limit interpretation of signals or generated images.

<b>TABLE 2. Objectives of non-destructive testing methods</b>	
<b>Objectives</b>	<b>Attributes Measured or Detected</b>
<b>Discontinuities</b>	
Surface anomalies	roughness, scratches, gouges, crazing, pitting, inclusions and imbedded foreign material
Surface connected anomalies	cracks, porosity, pinholes, laps, seams, folds, inclusions
Internal anomalies	cracks, separations, hot tears, cold shuts, shrinkage, voids, lack of fusion, pores, cavities, delaminations, disbonds, poor bonds, inclusions, segregations
<b>Structure</b>	
Microstructure	molecular structure, crystalline structure and/or strain, lattice structure, strain, dislocation, vacancy, deformation
Matrix structure	grain structure, size, orientation and phase, sinter and porosity, impregnation, filler and/or reinforcement distribution, anisotropy, heterogeneity, segregation
Small structural anomalies	leaks (lack of seal or through-holes), poor fit, poor contact, loose parts, loose particles, foreign objects
Gross structural anomalies	assembly errors, misalignment, poor spacing or ordering, deformation, malformation, missing parts
<b>Dimensions and metrology</b>	
Displacement, position	linear measurement, separation, gap size, discontinuity size, depth, location and orientation
Dimensional variations	unevenness, non-uniformity, eccentricity, shape and contour, size and mass variations
Thickness, density	film, coating, layer, plating, wall and sheet thickness, density or thickness variations
<b>Physical and mechanical properties</b>	
Electrical properties	resistivity, conductivity, dielectric constant and dissipation factor
Magnetic properties	polarization, permeability, ferromagnetism, cohesive force
Thermal properties	conductivity, thermal time constant and thermoelectric potential
Mechanical properties	compressive, shear and tensile strength (and module), Poisson's ratio, sonic velocity, hardness, temper and embrittlement
Surface properties	colour, reflectivity, refraction index, emissivity
<b>Chemical composition and analysis</b>	
Elemental analysis	detection, identification, distribution and/or profile
Impurity concentrations	contamination, depletion and doping
Metallurgical content	variation, alloy identification, verification and sorting
Physiochemical state	moisture content, degree of cure, ion concentrations and corrosion, reaction products
<b>Stress and dynamic response</b>	
Stress, strain, fatigue	heat-treatment, annealing and cold-work effects, residual stress and strain, fatigue damage and life (residual)
Mechanical damage	wear, spalling, erosion, friction effects
Chemical damage	corrosion, stress corrosion, phase transformation
Other damage	radiation damage and high frequency voltage breakdown
Dynamic performance	crack initiation and propagation, plastic deformation, creep, excessive motion, vibration, damping, timing of events, any anomalous behavior

<b>Signature analysis</b>	
Electromagnetic field	potential, strength, field distribution and pattern
Thermal field	isotherms, heat contours, temperatures, heat flow, temperature distribution, heat leaks, hot spots
Acoustic signature	noise, vibration characteristics, frequency amplitude, harmonic spectrum and/or analysis, sonic and/or ultrasonic emissions
Radioactive signature	distribution and diffusion of isotopes and tracers
Signal or image analysis	image enhancement and quantization, pattern recognition, densitometry, signal classification, separation and correlation, discontinuity identification, definition (size and shape) and distribution analysis, discontinuity mapping and display

The number of inspection methods seems to grow daily, but a quick summary of the most commonly used methods is provided below.

**Visual and Optical Testing (VT):** The most basic NDT method is visual examination. Visual examiners follow procedures that range from simply looking at a part to see if surface imperfections are visible, to using computer controlled camera systems to automatically recognize and measure features of a component. Visual inspection represents the highest percentage of the inspection procedures that are applied to aircraft in service. To enhance the inspection capability, new tools were developed including improved illumination techniques, miniature video and dexterous small-diameter boroscopes. In recent years, two visual inspection techniques have emerged that worth noting and they are the *D-Sight* and the *Edge of Light (EOL)*. While D-Sight already found its way to practical use, the EOL technique is relatively new and it is still in development stages.

**Dual-Pass Light Reflection (*D-Sight*<sup>TM</sup>):** Surface and near-surface flaws, such as corrosion in metals and impact damage in composites, are causing a local surface deformation. The visual inspection technique called D-Sight (Diffrauto Limited) [4] enhances the appearance of this deformation and increases its visibility [5]. A D-Sight inspection system consists of a CCD camera, a white light source mounted slightly above the camera lens, and a retro-reflective screen. In figure 1, a schematic view is showing the principle of D-sight operation and on the right an example of cold worked holes is shown. The system's screen is made of a reflective micro-bead layer and is the most important element of the D-Sight system. While the screen returns most of the light in the same direction of the incidence, a slight amount of light is dispersed.

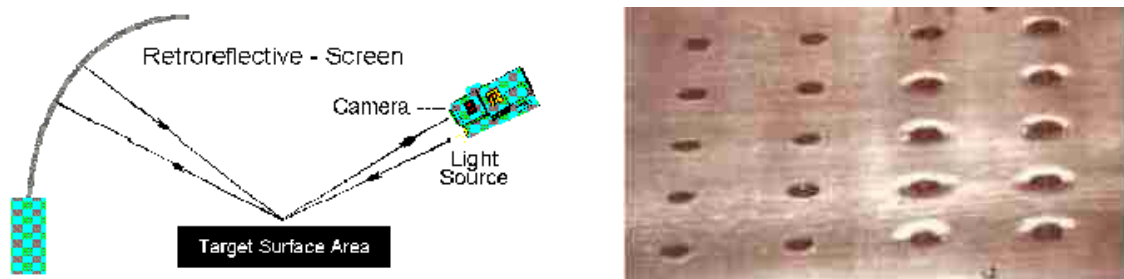


**Figure 1:** D-Sight principle of operation (left) and an example of the test result for cold worked holes (Diffrauto).

When a surface is illuminated by a light source, local surface curvatures are focusing or dispersing the light onto the retro-reflective screen. A light pattern is formed on the screen and is reflected back to the source with a slight dispersion. This path of the light is backlighting the part surface and enhances the scattering effect of surface deformations. By viewing the surface slightly off-axis from the light source a unique pattern appears near local surface deformations. This pattern consists of bright and dark gray scale variations, where higher curvatures appear more intense due to the effect of focusing and diffusing the light. To obtain a sufficient level of diffused light the surface must be reflective, otherwise a thin layer of liquid needs to cover the surface to increase its reflectivity.

***Edge Of Light™ (EOL):*** Another method of enhancing the surface deformation that is caused by flaws is the Edge of Light™ (EOL), which was developed by the National Research Council Canada [5]. It employs elements commonly used in optical scanners and it uses the scattered light from surface deformation and variations in the surface slope to produce an image that consists of light intensity variations. The technique is relatively quick, with scanning speeds on the order of 2 to 20-linear cm/sec with line scan widths of 10-cm or more. EOL inspection results are easy to interpret since they closely resemble the actual subject. The technique has been demonstrated to be effective in detecting corrosion on surfaces and joints, as well as flaws in gas turbine components and turbine disks. For some applications, EOL was shown to have greater detection capability than liquid penetrants, magnetic particle, ultrasonic inspections, or optical microscopy. In figure 2, a comparison is shown between an unaided view and EOL image of corrosion pillowing in a lap-splice joint of a Boeing 727 aircraft.

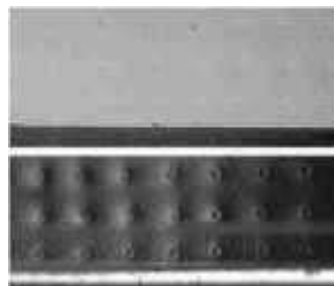


**Figure 2:** Top Lap splice joint from a Boeing 727, as seen by the unaided eye. Bottom - EOL image of the same joint clearly showing corrosion pillowing [5]

**Radiography (RT):** RT involves the use of penetrating gamma- or X-radiation to examine materials and product's defects and internal features. An X-ray machine or radioactive isotope is used as a source of radiation. Radiation is directed through a part and onto film or other media. The resulting shadowgraph shows the internal features and soundness of the part. Material thickness and density changes are indicated as lighter or darker areas on the film. The capability of radiography to provide an image that is relatively easy to interpret made it an attractive NDE method for both industrial and medical applications. The health hazard associated with the exposure to this ionizing radiation and the use of films to record the images constrained the application of radiography. The development of real time imaging techniques for radiographic visualization helped overcoming the time consuming process that was involved with film recording. Moreover, computer processing of digitized images enabled the enhancement of the images as well as the quantification of the inspection criteria. Several radiographic techniques that deserve attention include the *CT scan*, *Reverse Geometry X-ray* and *Microfocus X-ray microscopy*.

**Compute Tomography Scan:** Computer processing of the distribution of the X-ray transmission coefficient in a structure using a series of viewing angles is used to produce computed tomography (CT) scans [6]. For over three decades, this radiographic technique has been widely in use as an important medical tool. At the early 80's the technique was transferred to industrial use as a result of a research effort at the Air Force Materials Laboratory. The method is highly effective in testing composite structures and it provides a quantitative information about the distribution of the material density. Images can be produced and manipulated in a real-time format and allow recognition, localization and classification of material defects (e.g. pores, blowholes, foreign bodies). The inspection can be done automatically in arbitrary test samples (e.g. in metal, ceramic, glass or synthetic material castings). Three-dimensional position and extension of flaws can be determined by evaluating pairs of stereoscopic transmission images [7]. Depending on the object geometry, the acquisition of stereoscopic images can be done alternatively by translation or rotation of the sample.

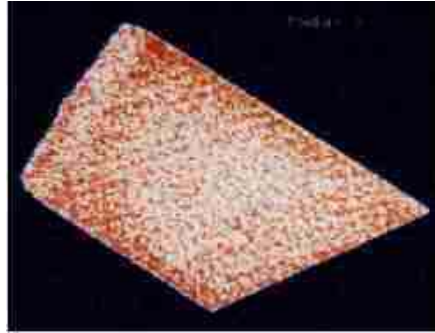


**Figure 3:** CT image of the density distribution in a reference graphite/epoxy sample

The defect extension in the direction of transmission is calculated by using the absorption law adapted for polychromatic radiation. An example of a graphite/epoxy sample tested by CT scanning is shown in figure 3.

**Reverse Geometry X-Ray (RGX) Imaging:** In contrast to conventional radiography, RGX reverses the relative sizes of source and detector as well as the location of the object [8]. The object is placed adjacent to the large, computer controlled raster-scanning source at a distance from the point detector. This arrangement allows scattered radiation to bypass the detector, thereby increasing the contrast sensitivity (signal-to-noise ratio). The method has been demonstrated to detect such flaws as corrosion, impact damage, and water entrapment in aluminium and composites. In the case of corrosion on aircraft, it was possible to detect the loss of material down to as little as 1.0%, even when the material loss is disguised by the presence of corrosion products. Generally, the distance between object and detector can be easily increased to reduce parallax effects and increase throughput for large area honeycomb and/or thick honeycomb inspection. An example of a Reverse Geometry image of graphite/epoxy blades of the NASA tilt-rotor type aircraft, XV-15, is shown in figure 4.

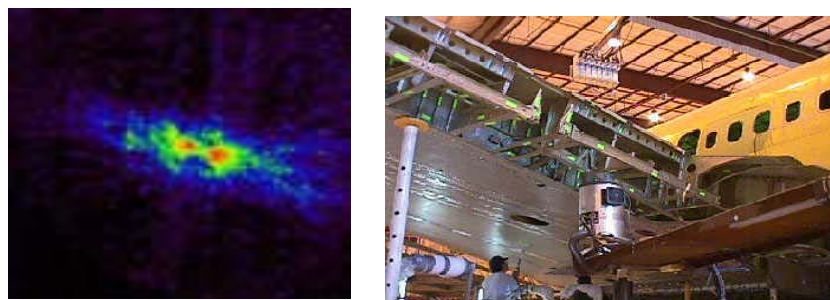


**Figure 4:** (left) Reverse Geometry test of an aluminium casting showing various slices (Digiray), (right) A view of a Reverse Geometry X-ray system inspecting a Boeing 707 wing area.

**Microfocus X-ray Microscopy:** Using a small source to provide a great magnification of the inspected object, Microfocus X-ray Microscopy operates similarly to conventional radiographic techniques [9]. Conventional radiographic techniques generate X-rays from a thick target, typically tungsten, oriented at 30° or 45° angles to the electron beam source. X-ray images are produced with limited magnification. Through the use of a thin film target oriented normal to the electron beam source, samples are positioned opposite to the beryllium window thereby minimizing working distance and maximizing magnification. The microfocused beam (~3μm) further enhances the resolution by increasing sharpness of the image as compared to the one obtained using larger focal spot sizes. Geometric magnification for typical fine-focus applications are ranging from 3X to 1000X with capabilities of extending beyond 2000X. For conventional transmission microfocus X-ray, the tube voltage ranges from 10-225kV with focal dimensions from 3 to 200μ m. By manipulating the sample and viewing a real-time image, defects normally obscured by background noise in conventional 2-D can be readily imaged. The technique is widely used for NDE of microelectronics and aerospace applications for parts with miniature internal components. An example of images obtained using Microfocus X-ray from two different viewing angles is shown in Figure 5, where a hydrophone with a microns size tunnelling tip was examined.

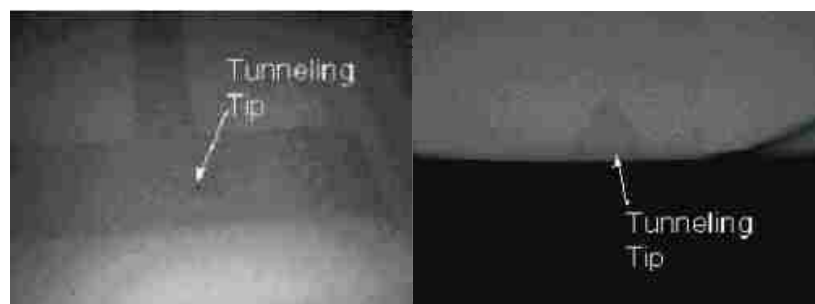


**Figure 5:** Microfocus X-ray image of a hydrophone tunnelling tip as viewed from isometric (left) and profile (right) views.

**Magnetic Particle Testing (MT):** This NDT method is accomplished by inducing a magnetic field in a ferromagnetic material and then dusting the surface with iron particles (either dry or suspended in liquid). Surface and near-surface flaws produce magnetic poles or distort the magnetic field in such a way that the iron particles are attracted and concentrated. This produces a visible indication of defect on the surface of the material.

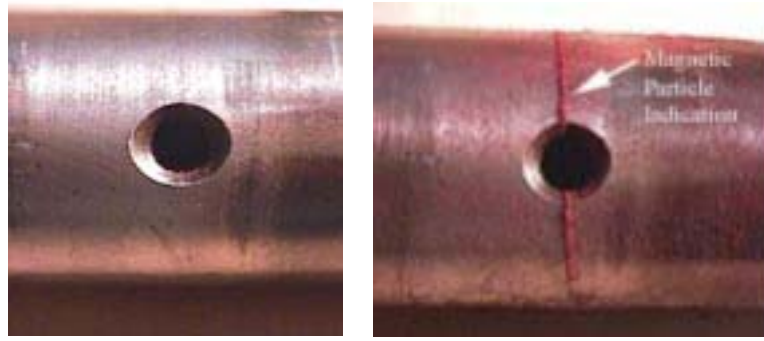


**Figure 6:** The images above demonstrate a component before and after inspection using dry magnetic particles

**Ultrasonic Testing (UT):** Ultrasonics is one of the most versatile and informative NDE methods and [10]. In ultrasonic testing, high-frequency sound waves are transmitted into a material to detect imperfections or to locate changes in material properties. The most commonly used ultrasonic testing technique is pulse echo, whereby sound is introduced into a test object and reflections (echoes) from internal imperfections or the part's geometrical surfaces are returned to a receiver. In figure 7 there is an example of shear wave weld inspection. Notice the indication extending to the upper limits of the screen. This indication is produced by sound reflected from a defect within the weld.

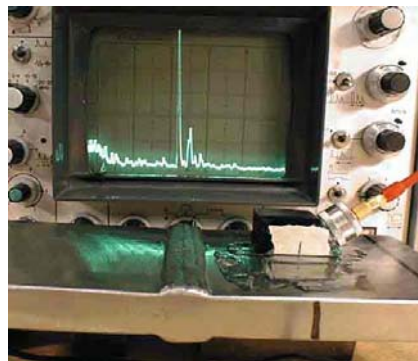


**Figure 7:** Example of shear wave weld inspection

The various modes that these waves can support allow the extractions of detailed information about flaws as well as determining various material properties. Techniques were developed employing the various wave modes as well as scattering and mode-conversion that are associate with the wave interaction. Examples of such techniques include the Acousto-Ultrasonics, which is practically used for flaw screening, and the ultrasonic angular insonification to induce the polar backscattering and leaky Lamb

waves. Also, to perform rapid inspection portable scanners were developed with some that can crawl on the surface of the test structures and conduct scanning. To simplify the imaging process without the use of mechanical scanning array transducers and CCD (charge coupled device) technology can now be used to form the ultrasonic equivalence of the video cameras. The difficulties associated with the need for liquid couplant, which mostly affects field application, led to the development of various fixtures including water filled boots and wheels, bubblers and squirters. Alternative dry coupling methods were also developed including the use of air-coupled piezoelectric transducers, Electro-Magnetic Transducers (EMAT) and Laser Ultrasonics [11].

***Dry Coupling Techniques:*** The inability to transmit and receive ultrasonic waves through air or gas was a limiting factor in developing rapid field inspection, testing porous or water sensitive materials, and others. Most ultrasonic NDE applications operate at frequencies in the range of 1- 10 MHz, where travelling through air is highly attenuative. The acoustic impedance of air differs significantly from the one for the piezoelectric transmitter and the test part causing reflection of most of the energy. Therefore, only a very small fraction of the energy is transmitted through the part and back to the transducer.

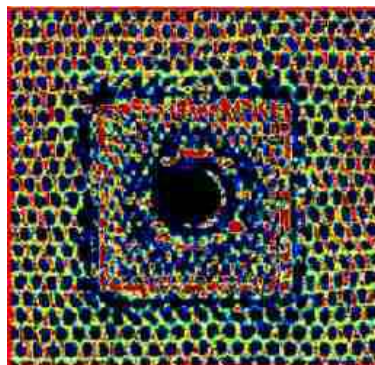


**Figure 8:** A 400 KHz air-coupled through-transmission C-scan of solar honeycomb panel with a 5x5-cm stiffener insert [12].

***Air-Coupled transducers:*** One solution to overcoming this air-coupling problem without using additional transition media has been the induction of sufficiently high sound level and using high-gain, low-noise amplification [12]. To enhance the transmitted energy, the transducer is used with no backing layers and thus taking advantage of the high mechanical-quality factor  $Q$  of piezoelectric disks. To improve the generation and reception efficiencies of the transducer, its front protection layer is made of a thin porous material having low specific impedance. The transducer is driven

by tone-bursts with a center frequency that exactly matches its thickness- mode resonance and using focused transducers further increases the sound pressure. Such transducer and hardware modifications allowed the operation of air-coupled ultrasonic C-scans at frequencies in the low Megahertz range. While it is still limited to materials with relatively low acoustic impedance, such as composites, it is already being used extensively for applications where water can not be used as a couplant. In Figure 8, an example of a C-scan is shown where a solar honeycomb panel with a 5x5-cm stiffener insert was tested using a 400 KHz air-coupled through-transmission. The bonded honeycomb core, the area of the insert and the missing core can be easily seen.

***Electromagnetic acoustic transducer (EMAT):*** EMAT is a transducer that uses eddy current to generate and receive acoustic signals that operates without a coupling medium [13]. The transducer can induce specific ultrasonic modes including normal beam and angle-beam shear wave, Shear Horizontal (SH) plate wave, Rayleigh wave and Lamb wave. The ability to induce horizontally polarized shear waves has a great significance for the inspection of austenitic welds. Another advantage of EMAT is the ability to operate at high temperatures. The main disadvantage of EMAT arises from its relatively low transmitted ultrasonic energy causing electronic noise to constrain its dynamic range. Also, the induced energy is critically dependent of the probe proximity to the test object, which for practical applications it is commonly maintained below 1-mm. Generally, EMAT transducers are used at frequencies below 2-4MHz.

***Laser induced ultrasound:*** Laser ultrasonics is one of the effective methods of inducing and receiving ultrasonic waves without the need for couplant. The received signals are evaluated very similar to the pulse-echo technique and parts can easily be scanned from a distance of about 3-4 meters. The method induces short pulses in the range of 10- $\mu$ sec causing a rapid heating and expansion of the surface forming elastic pulses. The reflected signals are examined by interferometry and such systems were developed by several research organization including the Center for NDE at John Hopkins University, Hughes Research Lab and the Canadian National Research Council [14]. Also, a commercial system was developed by UltraOptec (Québec, Canada), who delivered one of its products to the Air Force maintenance facility at McClellan Air Force Base for inspection of composite and bonded structures [15]. The method is effective for inspection of structures with complex geometry allowing examination of surfaces with a slope of up to about  $\pm 45^\circ$ . This allows mapping defects in parts that are contoured and

presenting the results in 3-D (see figure 9) with is no critical orientations requirement for the incident beam.

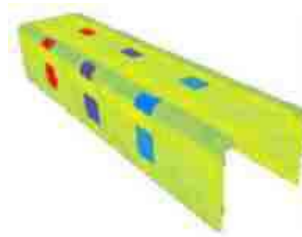


**Figure 9:** A 3-D C-scan image of a curved part with flaws at various depth (identified in colours) using laser ultrasonic time-of-flight. [13]

The limiting factor in the scanning speed is the inability to induce pulses at high rate, where an average of 100 pulses/sec is commonly used. Overall, the cost and the sensitivity of the laser ultrasonic technique are limiting the wide usage of laser-ultrasonics. New techniques are continuously being introduced in an effort to reduce the cost of the hardware. However, the sensitivity is fundamentally limited to about 45dB because there is a lower bound on the sensitivity of detecting a single phonon, whereas the upper limit is set by thermal damage prevention. Commercially available systems are offering user friendly imaging software, which displays A-scans, B-scans and C-scans, as well as 3-D ultrasonic images that can be easily manipulated for various angles of view.

**Penetrant Testing (PT):** The test object is coated with a solution that contains a visible or fluorescent dye. Excess solution is then removed from the surface of the object but leaving it in surface breaking defects. A developer is then applied to draw the penetrant out of the defects. With fluorescent dyes, ultraviolet light is used to make the bleedout fluoresce brightly, thus allowing imperfections to be readily seen. With visible dyes, vivid colour contrasts between the penetrant and developer make "bleedout" easy to see.

**Shearography:** The ability of holography to produce flaw indications superpositioned onto a 3-D image of parts has been a desirable feature, which was well documented since the 60's. The process involves double exposure of the structure at two different stressing levels. Unfortunately, the method has been very sensitive to vibrations or displacement of the setup and therefore was not practical for field use. The introduction of the shearography as a technique of forming double exposure without concern to the system mechanical stability made it highly attractive. A digital interferometry system is used to detect areas of stress concentration caused by anomalies in the material [16].

The technique senses out-of-plane surface displacements in response to an applied load. Data is presented in the form of a fringe pattern produced by comparing two states of the test sample, one before and the other after a load is applied. Electronic shearography incorporates a CCD camera and frame grabber for image 20 acquisition at video frame rates. Fringe patterns are produced by real time digital subtraction of the deformed object image from the reference object image. Shearography also uses a 'common-path' optical arrangement, which provides reasonable immunity to environmental disturbances such as room vibrations and thermal air currents. As a result, shearography can be implemented without the need for sophisticated vibration isolation that is required for conventional holography. The capability of Shearography to inspect a large area in real time has significant advantages for many industrial applications and is being practically used for inspection of composite structures and pressure vessels. Northrop Grumman Corp. has been using shearography on the B-2 program since 1988. The method is being applied for inspection of bonded composites and metallic assemblies for which experience has shown inspection time reduction of about 75% compared to other NDE methods. Further, there are many cases where this method was found to be the only one capable of detecting the specific flaws. To address the requirement to stress the test structure, various techniques are used, where the most effective are thermal and surface vacuum techniques. The thermal shearography is used to inspect near skin-to-core bondline, ramp areas and solid graphite laminates, whereas, vacuum stress shearography is used to examine both near and far side bond lines in the honeycomb areas. Thermal stress shearography has been shown to be capable of inspecting large areas of composite and honeycomb materials at a rate of 60-ft /hour [17]. Example of testing an aircraft is shown in Figure 10 (left) and a typical view of flaws are shown in Figure 10 (right). Generally, due to the method of forming the shearographic image the flaws tend to appear as bull's eyes.

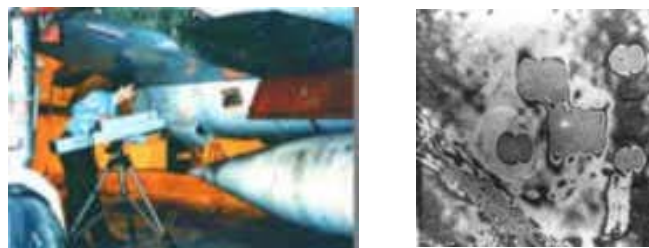


**Figure 10:** (left) Tripod mounted shearography camera/laser is shown inspecting an aircraft (Laser Technology, Inc.), (right) The bull's eyes shape of flaws' shearographic image.

**Thermography:** The effect of flaws on the thermal conductivity and emissivity of test materials is analyzed by the thermographic NDE method [18]. Its attractive features are the capability to cover large areas in a single frame and it does not require coupling. Unfortunately, this method was found unreliable when testing bonded joints with a narrow gap between the unbounded surfaces. In the early stages, liquid crystals were used to map the surface distribution of the 21 different temperature. The improvement of infrared systems made such tools highly sensitive and effective for mapping the cooling or heating profiles to rapidly indicate flaws. Examining the temporal gradient of the thermal maps, i.e., thermal flux, significantly improved the detectability of flaws.

**Thermal Wave Imaging:** Thermal waves transmitted through test parts can be received and used to produce an image of the internal uniformity. In addition to imaging the pattern of subsurface flaws and corrosion, the technique can rapidly (a few seconds) make quantitative measurements of less than 1% material loss for various regions in the image [19]. It can use as a heat source pulses from photographic flash-lamps. The heat source box traps and funnels the light uniformly onto the test structure, and an infrared (IR) focal plane array camera, aimed and focused at the surface through an opening in the rear of the hand-held shroud, monitors the rapid cooling of the surface. The system operates by sending a heat pulse from the surface into the material, where it undergoes thermal wave reflection at either the rear surface or at any interior surface at which the thermal impedance changes, e.g., at disbonds, delaminations, etc. The effect of these thermal wave reflections is to modify the local cooling rate of the surface. The cooling rate, in turn, is monitored through its effect on the IR radiation from the surface, which is detected by the camera, and processed as a sequence of images by the control computer. The contrast in the processed images reveals the presence of defects in the interior or variations in the thickness of the material. In Figure 11, Thermal Wave Image an example is shown for corrosion and unbound near a tear strap/stringer of a Boeing 737.

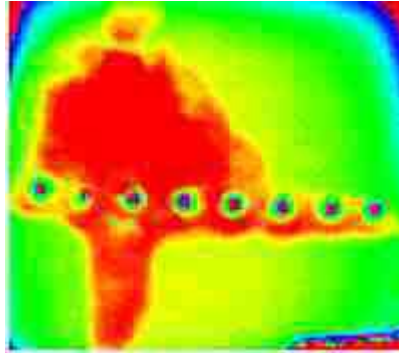


**Figure 11:** Thermal Wave Image of Corrosion and Disbonding near tear strap/stringer of a Boeing 737.

**Electromagnetic Testing (ET):** For over three decades, eddy current has been one of the leading in-service inspection methods for crack detection around and inside fastener holes. Significant improvement has been made to enhance the method capability, reliability and user friendliness. In this technique electrical currents (eddy currents) are generated in a conductive material by a changing magnetic field. The strength of these eddy currents can be measured. Material defects cause interruptions in the flow of the eddy currents which alert the inspector to the presence of a defect. Eddy currents are also affected by the electrical conductivity and magnetic permeability of a material, which makes it possible to sort some materials based on these properties. The modelling of the effect of flaws contributed significantly to the understanding of the key parameters as well as the reduction in the effect of noise and lift-off. Improved probes and instrumentation were developed and the effective use of low frequencies enabled inspection of metallic layered structures for detection of flaws in the second and third layer. The Magneto-Optics Imager (MOI) has been one of the eddy current technique spin-offs and it is being practically implemented by the aircraft industry. Another eddy current technique that has emerged in recent years is the pulse eddy current.



**Figure 11:** A technician is inspecting an aircraft wing for defects.

**Magneto-Optics Imager (MOI):** In order to simplify the detection of flaws, the Magneto-Optics Imager (MOI) was developed as a means of visualizing the eddy current response [20]. The Magneto-Optic Imager (MOI) combines planar eddy current and magneto optic imaging and it is applicable to inspection of metallic structures for surface and subsurface flaws. MOI is able to image through paint and other surface coverings in real time and to project the results on a heads up display and/or a monitor. MOI is employed in a hand-held (see figure 12) portable instrument that requires minimal training and its capability greatly increases the speed and reliability of inspection. This method is currently being used extensively for aircraft inspection by airlines, maintenance facilities and the military.

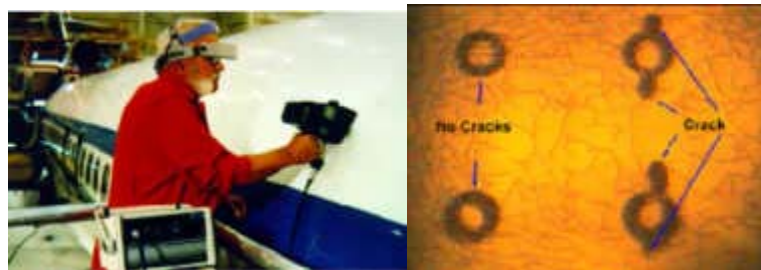


**Figure 12:** A photographic view of an MOI inspection (left) and an image of indication of cracks around fasteners (right) (PRI, Torrance, CA).

**Pulsed Eddy Current (PEC):** Conventional eddy current techniques use single frequency sinusoidal excitation and measure flaw responses as impedance or voltage changes on an impedance plane display. To detect flaws, inspectors interpret the magnitude and phase changes, but the method is sensitive to variety of parameters that are hampering the characterisation of flaws. Multiple frequency measurements can be combined to more accurately assess the integrity of a structure by reducing signal anomalies that may otherwise mask the flaws. Initial development led to the use of dual frequency eddy-current where frequency-mixing functions allowed the quick application of the technique. This approach has been shown to be useful in reducing the effects of plate separation variations when inspecting for second layer corrosion in lap spllices [21]. The dual frequency method offers advantageous when performing large area inspections by means of eddy current C-scans of specimens with corrosion under fasteners [22]. Unfortunately, conventional multiple frequency methods can provide limited quantitative data and are difficult to use for flaw visualisation in an intuitive manner. Swept frequency measurements using impedance analysers perform well in quantitative corrosion characterisation studies, especially when they are interpreted in

conjunction with theoretical models [23]. However, the application of these techniques is too laborious. In contrast to the conventional eddy current method, pulsed eddy current (PEC) excites the probe's driving coil with a repetitive broadband pulse, such as a square wave. The resulting transient current through the coil induces transient eddy currents in the test piece, associated with highly attenuated magnetic pulses propagating through the material. At each probe location, a series of voltage-time data pairs are produced as the induced field decays, analogous to ultrasonic inspection data. Since a broad frequency spectrum is produced in one pulse, the reflected signal contains flaw depth information. Physically, the pulse is broadened and delayed as it travels deeper into the highly dispersive material. Therefore, flaws or other anomalies close to the surface will affect the eddy current response earlier in time than deep flaws. Similar to ultrasonic methods, the modes of presentation of PEC data can include A-, B- and C-scans [24]. Interpretation, therefore, may be considered more intuitive than conventional eddy current data. The excitation pulse, signal gain and sensor configurations can be modified to suit particular applications.

**Leak Testing (LT):** Several techniques are used to detect and locate leaks in pressure containment parts, pressure vessels, and structures. Leaks can be detected by using electronic listening devices, pressure gauge measurements, liquid and gas penetrant techniques, and/or a simple soap-bubble test.

**Acoustic Emission Testing (AE):** When a solid material is stressed, imperfections within the material emit short bursts of acoustic energy called "emissions." As in ultrasonic testing, acoustic emissions can be detected by special receivers. Emission sources can be evaluated through the study of their intensity and arrival time to collect information about the sources of the energy, such as their location.

## **2. Eddy current technique**

Eddy current inspection is one of several NDT methods that use the principal of "electromagnetism" as the basis for conducting examinations. Eddy currents are created through a process called electromagnetic induction. When an alternating current is used to excite a coil, an alternating magnetic field is produced and the magnetic flux lines are concentrated at the center of the coil. Then, when this coil is brought near an electrically

conductive material, the alternating magnetic field penetrates the material and generates continuous, circular eddy currents. Larger eddy currents are produced near the test surface; as the penetration of the induced field increases, the eddy current becomes weaker. The induced eddy current produces an opposing (secondary) magnetic field in the opposite direction to the generated (primary) magnetic field. This opposing magnetic field, coming from the material, has a weakening effect on the primary magnetic field and this change can be sensed by the test coil. In effect, the impedance of the coil is reduced proportionally as eddy currents are increased in the test piece. A crack in the test material obstructs the eddy current flow, lengthens the eddy current path, reduces the secondary magnetic field, and increases the coil impedance. The inductive reactance of the coil continues to increase as the severity of the defect increases. Eddy currents get their name from “eddies” that are formed when a liquid or gas flows in a circular path around obstacles when conditions are right. Eddy current inspection is used in a variety of industries to find defects and make measurements. One of the primary uses of eddy current testing is for defect detection when the nature of the defect is well understood. In general the technique is used to inspect a relatively small area and the probe design and test parameters must be established with a good understanding of the flaw that is trying to be detected. Since eddy currents tend to concentrate at the surface of a material, they can only be used to detect surface and near surface defects. In thin materials such as tubing and sheet stock, eddy currents can be used to measure the thickness of the material. This makes eddy current a useful tool for detecting corrosion damage and other damage that causes a thinning of the material. The technique is used to make corrosion thinning measurements on aircraft skins and in the walls of tubing used in assemblies such as heat exchangers. Eddy current testing is also used to measure the thickness of paints and other coatings. Eddy currents are also affected by the electrical conductivity and magnetic permeability of materials. Therefore, eddy current measurements can be used to sort materials and to tell if a material has seen high temperatures or been heat treated, which changes the conductivity of some materials. Eddy currents are closed loops of induced current circulating in planes perpendicular to the magnetic flux. They normally travel parallel to the coil's winding and flow is limited to the area of the inducing magnetic field. Eddy currents concentrate near the surface adjacent to an excitation coil and their strength decreases with distance from the coil as shown in figure 13.

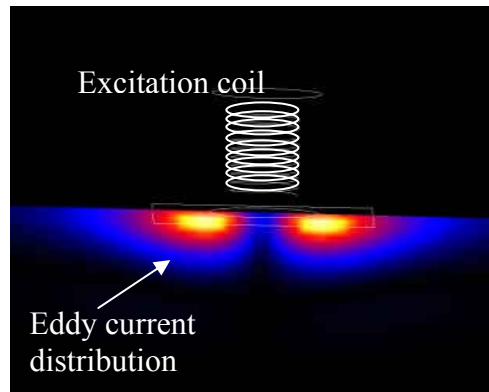


**Figure 13:** Image of the eddy current distribution produced by an solenoid coil.

Eddy current density decreases exponentially with depth. This phenomenon is known as the skin effect. Skin effect arises when the eddy currents flowing in the test object at any depth produce magnetic fields which oppose the primary field, thus reducing net magnetic flux and causing a decrease in current flow as depth increases. Alternatively, eddy currents near the surface can be viewed as shielding the coil's magnetic field, thereby weakening the magnetic field at greater depths and reducing induced currents.

The depth that eddy currents penetrate into a material is affected by the frequency of the excitation current and the electrical conductivity and magnetic permeability of the specimen. The depth of penetration decreases with increasing frequency and increasing conductivity and magnetic permeability. The depth at which eddy current density has decreased to  $1/e$ , or about 37% of the surface density, is called the standard depth of penetration ( $\delta$ ) defined as [25]:

$$\delta = \frac{1}{\sqrt{\pi\sigma\mu f}}$$

$\delta$  = Standard Depth of Penetration (mm)

$f$  = Test Frequency (Hz)

$\mu$  = Magnetic Permeability (H/mm)

$\sigma$  = Electrical Conductivity (% IACS or S/m)

The word '*standard*' denotes plane wave electromagnetic field excitation within the test sample (conditions which are rarely achieved in practice). Although eddy currents penetrate deeper than one standard depth of penetration they decrease rapidly with depth. At two standard depths of penetration ( $2\delta$ ), eddy current density has decreased to

1/e squared or 13.5% of the surface density. At three depths (3δ) the eddy current density is down to only 5% of the surface density.

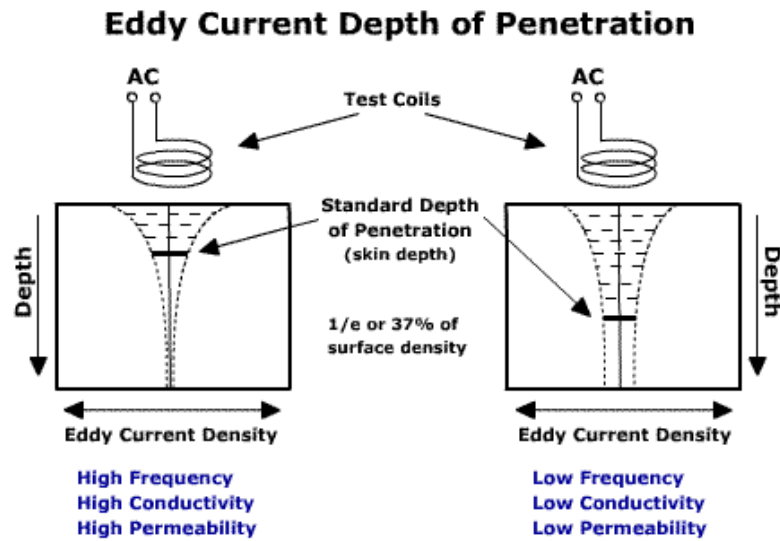


**Figure 14:** (left) and (right) schematisation of the eddy current penetration depth for low and high conductivity materials, respectively.

Electrical Impedance ( $Z$ ), is the total opposition that a circuit presents to an alternating current. Impedance, measured in ohms, may include resistance ( $R$ ), inductive reactance ( $X_L$ ), and capacitive reactance ( $X_C$ ). Eddy current circuits usually have only  $R$  and  $X_L$  components. The resistance component and the reactance components are not in phase so vector addition must be used to relate them with impedance. For an eddy current circuit with resistance and inductive reactance components, the total impedance is calculated using the following equation.  $Z = \sqrt{R^2 + X_L^2}$ . This can be graphically displayed using the impedance plane diagram as seen in Figure 15.

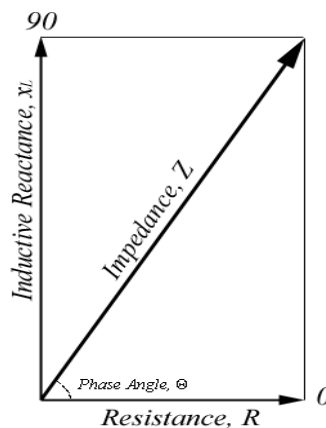


**Figure 15:** Impedance plane.

Impedance also has an associated angle, called the phase angle of the circuit, which can be calculated by the following equation  $\Theta = \tan^{-1} \frac{X_L}{R}$ . The impedance plane diagram is a very useful way of displaying eddy current data. As shown in the figure 16, the strength of the eddy currents and the magnetic permeability of the test material cause the eddy current signal on the impedance plane to react in a variety of different ways.

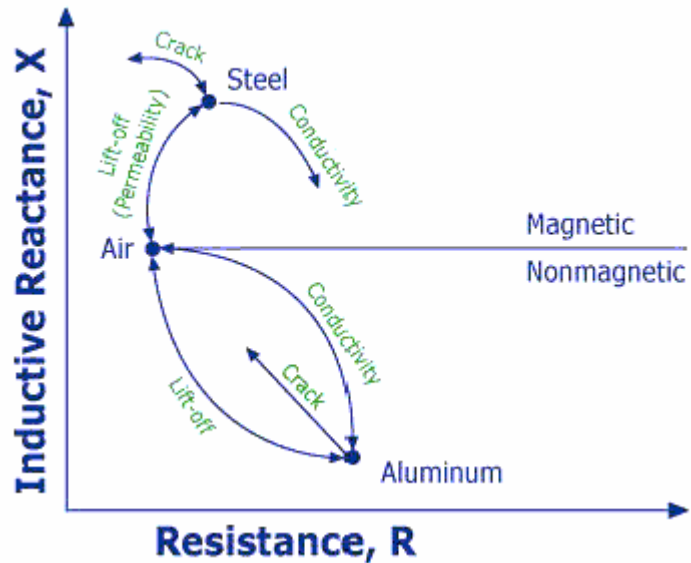


**Figure 16:** Eddy current impedance plane responses.

If the eddy current circuit is balanced in air and then placed on a piece of aluminium, the resistance component will increase (eddy currents are being generated in the aluminium and this takes energy away from the coil and this energy loss shows up as resistance) and the inductive reactance of the coil decreases (the magnetic field created by the eddy currents opposes the coil's magnetic field and the net effect is a weaker magnetic field to produce inductance). If a crack is present in the material, fewer eddy currents will be able to form and the resistance will go back down and the inductive reactance will go back up. Changes in conductivity will cause the eddy current signal to change in a different way. When a probe is placed on a magnetic material such as steel, something different happens. Just like with aluminium (conductive but not magnetic) eddy currents form which takes energy away from the coil and this shows up as an increase in the coils resistance. And, just like with the aluminium, the eddy currents generate their own magnetic field that opposes the coils magnetic field. However, you will note for the diagram that the reactance increase. This is because the magnetic

permeability of the steel concentrates the coil's magnetic field this increase in the magnetic field strength completely overshadows the magnetic field of the eddy currents. The presence of a crack or a change in the conductive will produce a change in the eddy current signal similar to that seen with aluminium.

Eddy current equipment and probes can be purchased in a wide variety of configurations. Eddyscopes and a conductivity tester come packaged in very small and battery operated units for easy portability. Computer based systems are also available that provide easy data manipulation features for the laboratory. Signal processing software has also been developed for trend removal, background subtraction, and noise reduction. Impedance analyzer is also sometimes used to allow improved quantitative eddy-current measurements. A few portable scanning systems also exist for special applications such as scanning regions of aircraft fuselage.

Eddy current probes are available in a large variety shapes and sizes. In fact, one of the major advantages of eddy current inspection is that probes can be custom designed for a wide variety of applications. Eddy current probes are classified by the configuration and mode of operation of the test coils. The configuration of the probe generally refers to the way the coil or coils are packaged to best "couple" to the test area of interest. An example of different configurations of probes would be bobbin probes, which are inserted into a piece of pipe to inspect from the inside out, versus encircling probes, in which the coil or coils encircle the pipe to inspect from the outside in. The mode of operation refers to the way the coil or coils are wired and interface with the test equipment. The most widely used mode of operation of a probe is Absolute and differential.

Absolute probes generally have a single test coil that is used to generate the eddy currents and sense changes in the eddy current field. When the probe is positioned next to a conductive material, the changing magnetic field generate eddy currents within the material. The generation of the eddy currents take energy from the coil and this appears as an increase in the electrical resistance of the coil. The eddy currents generate their own magnetic field that opposes the magnetic field of the coil and this changes the inductive reactance of the coil. By measuring the absolute change in impedance of the test coil, much information can be gained about the test material. Absolute coils can be used for flaw detection, conductivity measurements, lift-off measurements and thickness measurements. They are widely used due to their versatility. Since absolute probes are sensitivity to things such as conductivity, permeability lift-off and

temperature, steps must be taken to minimize these variables when they are not important to the inspection being performed. It is very common for commercially available absolute probes to have a fixed "air loaded" reference coil that compensates for ambient temperature variations.

Differential probes have two active coils usually wound in opposition, although they could be wound in addition with similar results. When the two coils are over a flaw-free area of test sample, there is no differential signal developed between the coils since they are both inspecting identical material. However, when one coil is over a defect and the other is over good material, a differential signal is produced. They have the advantage of being very sensitive to defect yet relatively insensitive to slowly varying properties such as gradual dimensional or temperature variations. Probe wobble signals are also reduced with this probe type. There are also disadvantages to using differential probes. Most notably, the signals may be difficult to interpret. For example, if a flaw is longer than the spacing between the two coils, only the leading and trailing edges will be detected due to signal cancellation when both coils sense the flaw equally.

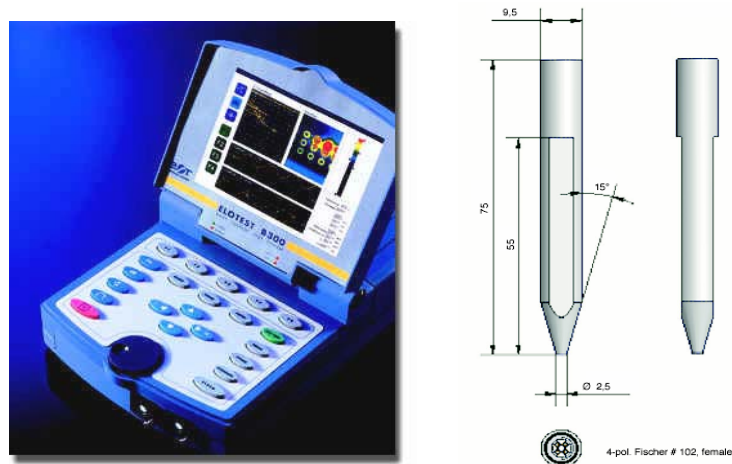


**Figure 17:** Elotest B-300 by Rohmann GmbH and the absolute probe KAS 2-2.

In this work an eddy current instrument Elotest B300 by Rohmann GmbH, with absolute probe has been used. The probe is characterized by a ferrite core, shielded, an effective area of 1.5 mm and an operation frequency range from 100kHz to 3 MHz. A picture of the instrument and the probe is reported in figure 17.

### 3. SQUID NDE applications

SQUID magnetometry can be an alternative solution to conventional electromagnetic technique for NDE applications [26].

**Table 3. Comparison of several magnetic sensors properties**

Sensor	Sensitivity (T/ $\sqrt{\text{Hz}}$ )	Bandwidth	Spatial resolution
Coils	$10^{-13}$	kHz-MHz	mm-cm
Flux gate	$>10^{-13}$	20 kHz	mm-m
Magnetoresistive	$10^{-9}$	dc-MHz	0.3-3 mm
SQUID	$10^{-14}$	dc-MHz	2 $\mu\text{m}$ -cm

In comparison with the other magnetic sensors (see table 3), SQUID has unparalleled sensitivity to small changes in magnetic flux that makes them highly desirable when it is not possible to place a sensing coil or solenoid directly around the object. Therefore, the inspection methods accommodated by the SQUID sensor are advantageous because there is not a need for contact between the sensor and the sample being testing. The very high magnetic field sensitivity, which is nearly independent of frequency from dc to few MHz, offers an advantage for application where a low excitation frequency is necessary for detections at large depth penetration in multilayer structures, rivet plates and aircraft wheels [27,28]. Another very important feature of SQUID sensor is its good spatial resolution, with superior sensitivity respect to the induction coil where a compromise between the spatial resolution and the signal strength is requested. Additionally, the high bandwidth available with certain SQUID systems makes measurements over a wide frequency range possible without having to change the sensor. The high dynamic range (the ratio between the highest field change which can be measured before the system goes into saturation and the lowest detectable field) allows one to detect small field changes in the presence of large background fields, produced by edge effects or inhomogeneities of the conductivity. The large dynamic range of SQUID allows shorter integration time and therefore faster scanning is possible.

Apart from the physical properties of SQUIDS like sensitivity and slew rate, the general interest in, and acceptance of superconducting devices is tightly related to aspects of cooling. High- $T_c$  SQUIDS are distinctly preferable to low- $T_c$  SQUIDS because their associated dewars can be lighter and more compact. As an alternative to liquid coolants, cryocoolers have been proposed and demonstrated [29-31] for SQUID cooling. Especially for field operation in remote areas, a cryocooler is a promising competitor to

liquid coolants. A cryocooler additionally offers the potential for a three dimensional moving or tilting of the SQUID, which is not possible when using conventional dewars. However, a significant obstacle in using cryocooler is not only magnetic noise from the cooler, but also periodic temperature fluctuations of its cold stage, which can give rise to an increased low frequency excess noise of the SQUID. An example of SQUID system cooling by a closed cycle Joule-Thomson cryocooler perform wheels testing is realized by Holmann et al [32] (see figure 18).



**Figure 18:** Example of cryocooler applied in aircraft wheels inspection.

High-Tc SQUIDs are useful devices for a number of applications in geophysics, as radiomagnetic sounding for exploring soil properties from few hundred meters down to few kilometres ground depth; magnetocardiography (MCG and MEG) research, to map the sources of arrhythmias, ischemia, ventricular tachycardia, and Wolff-Parkinson-White syndrome, and to study of the cardiac tissue slices [33]; biomagnetic research, and diagnostics as well as non-destructive evaluation (NDE) for inspection of clad pipes, airplane wings, corrosion pits and stress fracture [34]. Eddy current based on SQUID sensor is a useful technique to test several materials such as conductive materials, ferromagnetic and non-ferromagnetic materials.

In this work the attention is focused on two particular application of the SQUID magnetometer: detection of impact damage and study of the ongoing corrosion process in aircraft components. During the in service life the degradation of the aerospace and aircraft components can be produced by two major types of flaws: crack due to low velocity impact and corrosion damage with a resulting deterioration of the mechanical properties of the components. Corrosion in aluminium alloys and plated steel surfaces can often be recognized by dulling or pitting of the area, and sometimes by white or red powdery deposits. It may also be the origin of, or revealed by, delamination, cracking,

metal thinning, fretting, etc. Corrosion can appear in many forms, depending on the type of metal, how it is processed, its surrounding structure and service conditions. Corrosion results from exposure to humid or corrosive environments and involves primarily electrochemical action at chemical/ metallurgical/physical heterogeneity, with dissimilar potentials. In Table 4, a list of corrosion types that may appear in aircraft metallic components, their sources of formation and by-products, is given.

Aircraft are designed and manufactured with built-in corrosion-prevention features. However, most metals used in aircraft structures are subjected to degradation due to exposure to adverse environments including humidity-induced stresses and wide temperature excursions. Corrosion-protection systems are widely in use and they consist of a combination of materials, sealants, paints, design details, drainage, assembly practice, and preventive maintenance. The corrosion-prevention system cannot be guaranteed to work so that corrosion does occur and effective NDE techniques are needed to detect them as early as possible. The SQUID based system has been used successfully to monitor the ongoing corrosion process in electrochemical application and in the aluminium aircraft components, because of its ability to image the temporal and spatial variation of the magnetic field ( $\sim 10^{-12}$  T) associated with ongoing, hidden corrosion in aluminium lap joints or other complex structures. In terms of basic studies on corrosion, the SQUID sensor should be ideal because it can be used to map steady or time-varying currents deep within a sample without having to make contact with the sample or expose the metal that is undergoing corrosion for visualization or measurement. An example of an imaging performed by SQUID sensor in the detection of hidden corrosion has been referred to Wikswo research group [27] and it is shown below.

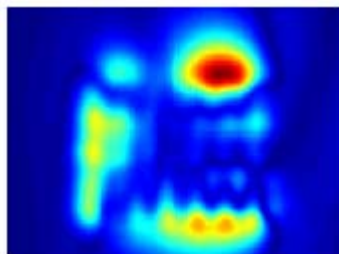


**Figure 19:** Image of magnetic activity on a KC 135 lap joint.

Moreover, concerning to the SQUID application in non destructive testing fatigue stress on steel, deep flaw in metallic alloy and impact damage detection, in literature there are several examples. Weinstock and Nisenoff [35,36] were the first to demonstrate the applicability of SQUID magnetometry for the study of stress-strain behaviour in a ferromagnetic material. In their experiment, a second-order gradiometer was placed 20 cm away from a steel bar undergoing stress. They showed that the magnetic flux measured outside the bar changes as the strain is increased. Gordon Donaldson and his group at the University of Strathclyde, Scotland, utilized SQUIDS for the detection of flaws in steel plates [37-40]. Experiments on steel plates showed that machined slots with cross sections as small as  $2 \times 1 \text{ mm}^2$  could be detected at a lift-off distance of 4.2 cm.

Bruno *et al* [41], of the Catholic University in Rio de Janeiro, in collaboration with Wikswo's group at Vanderbilt University demonstrated the detection of  $0,1 \text{ mm}^3$  surface breaking flaws in a steel plate by using a SQUID desensitized to work near the surface of ferromagnetic materials. They showed that, at close range, the depth of a shallow flaw could be estimated by the SQUID response. It was also reported that with extreme low pass filtering the SQUID could detect flaws 1 cm below the surface. The detection of cracks in the steel reinforcing rod (rebar) of concrete structures has been demonstrated by Braginski's group at KFA in Jülich, Germany [42, 43].

A promising SQUID NDT application is testing of very thick aircraft lap-joint structures, where currently no standard testing method achieves satisfactory results. For example, ultrasonic technique fails due to reflection at the sealing mass and air gaps between the different layers. Therefore, the standard testing method for lap joints in part of fuselage and wings is eddy current testing. However, since very low frequencies are necessary to detect deep flaws, induction coils are limited so that other sensors such as SQUIDS can be used.

Kreutzbruck *et al* [44] applied SQUID magnetometer in the testing of aluminium multilayer plate with rivet to detect cracks inside the structure. In figure 20 the test sample with rivet and a crack is shown. In this case the eddy current excitation is a wire. Moreover, the comparison of the results obtained with SQUID sensor and conventional technique are reported. It is clear that eddy current technique using conventional induction coil is limited, because of their high noise level at low frequency.

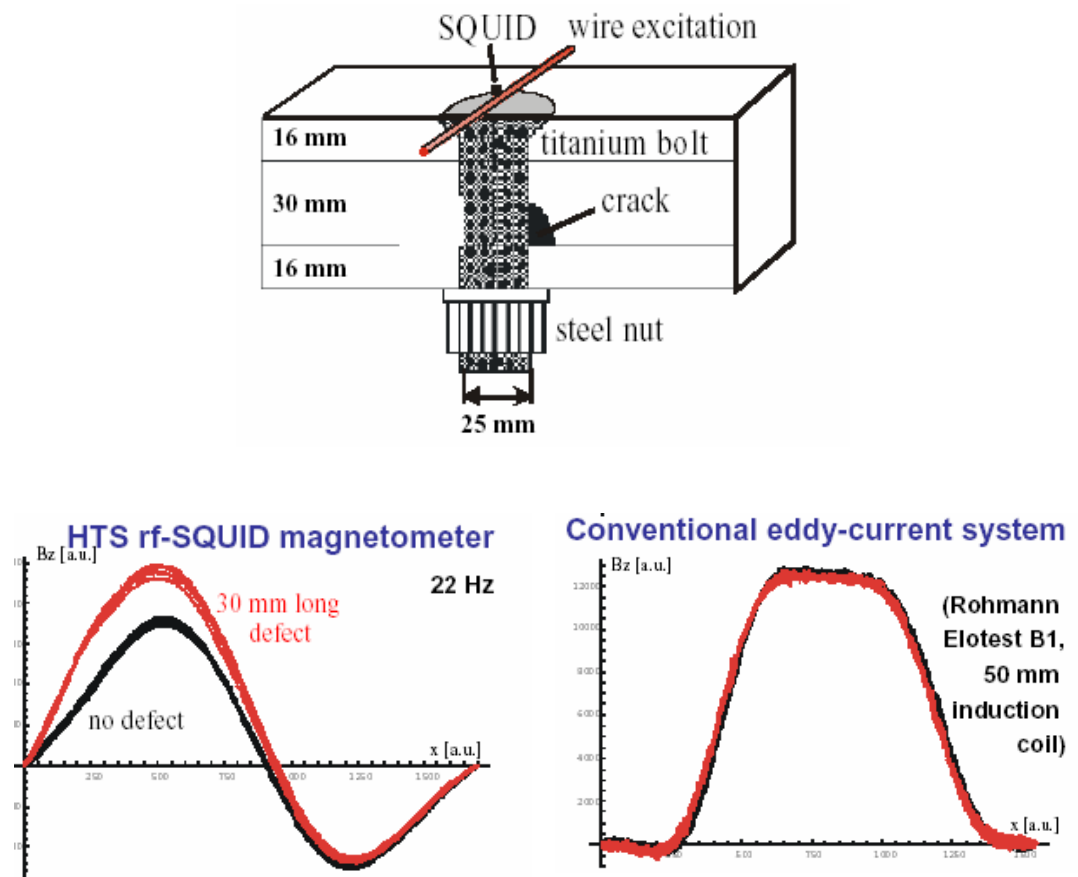


**Figure 20** : (up) Test sample with rivet and a crack Kreutzbruck et al [43]; (down) comparison of the results obtained in the NDE testing of the sample using SQUID sensor and eddy current conventional induction coil (left and right, respectively).

In the last years the interest for SQUID system in the NDE of aircraft component is grown, because of the development of new advanced materials that require a more suitable non destructive technique. The increasing requirement for more efficient aircraft has led to the development of stronger and lighter materials such as new aluminium alloys, and composites. The use of composite materials for aerospace structures is rapidly increasing in part because of the fact that they offer a weight reduction and high stress resistance compared to conventional materials such as aluminium alloys. Composite materials now form a significant part of the total weight of an aircraft. Where they only accounted for about 1% of the total weight of B707, they now account for as much 10% of the structural weight of a B777 and as 15% of a A320. New composites materials such as honeycomb sandwich and hybrid structures have been introduced and these have lead to a requirement for more specialistic and diverse NDE technique during manufacture and in-service. Because of their anisotropic and heterogeneous nature the non-destructive inspection of such materials remains a challenging task. Ultrasonic C-scan is probably one of the most widely used non-

destructive testing technique for inspection of composites. Still, there are no widely accepted standards or procedures for ultrasonic C-scan testing of composites. In addition, ultrasonic testing of composites requires the use of a water couplant, the inspection is often complex and defect sizing difficult. In order to overcome some of the limitations of ultrasonic testing of composites (e.g. need of a couplant), non-contact methods such as infrared thermography and shearography have been developed by industry. Still such methods remain costly and there is also a need for an efficient and low cost technique for composites testing. Interest is growing in the aerospace industry in using electromagnetic techniques such as eddy current to non-destructively assess the structural integrity of carbon fibre reinforced plastics (CFRPs). Eddy current based on SQUID sensors is a potential alternative to detect and quantify low energy impact in CFRPs [45-49]. For example, in the case of impact damage, infrared thermography may reveal impact location but provides very little details regarding the extent of the damage. In contrast, eddy current based on SQUID can also reveal sub-surface delaminations and broken fibres [50].

#### **4. NDE prototype based on HTS dc-SQUID magnetometer.**

The experimental set up is a prototype based on eddy current technique using a HTS dc-SQUID magnetometer. It was realized in the CNR-INFN laboratory of Naples from the NDE research group. The main components of the set up system are:

- Cryogenic dewar
- HTS dc-SQUID magnetometer
- Excitation coil
- x-y positioning system
- electronics for data acquisition

A scheme of the experimental system based on the HTS dc-SQUID magnetometer is shown in figure 21.

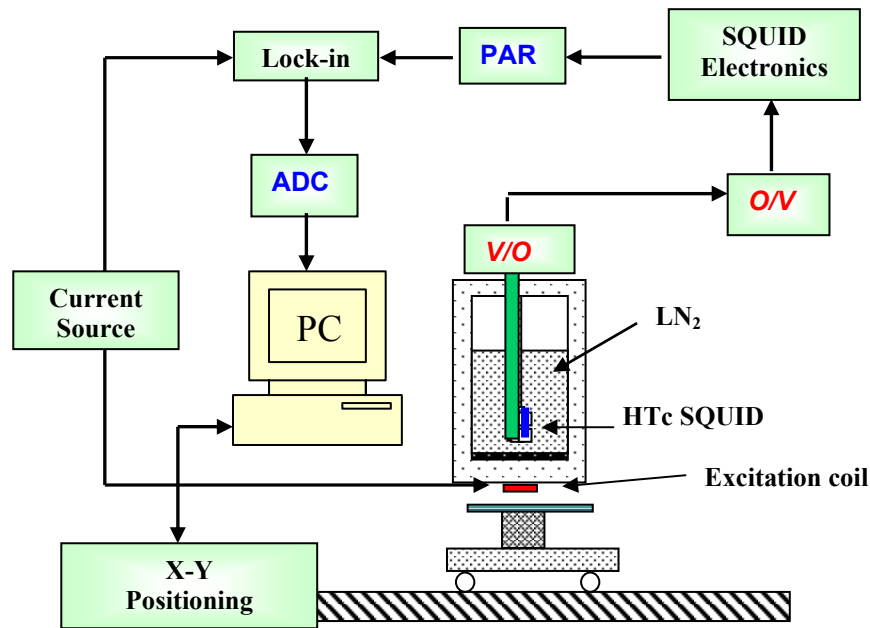


**Figure 21:** HTS dc-SQUID NDE system realized at CNR-INFM laboratory of Naples

### *Cryogenic dewar*

To guarantee the superconducting transition temperature of the HTS dc-SQUID sensor it is located into a head insulator fiber glass dewar at the temperature of the liquid nitrogen (77K). The thermal insulation is ensured by a vacuum inner shell that avoids ice condensation on the dewar surface and reduces the liquid nitrogen evaporation. The dewar is made of non-magnetic material (fiber glass) to avoid magnetic noise, it is characterized by a volume of 1.19 l, an evaporation rate of 0.26 l/hour. In the inner area of the dewar there are over-pressure valves, which reduce the turbulence of the liquid nitrogen bath creating working instability for the SQUID, a inlet valve that allows to introduce liquid nitrogen into the dewar also during the operation time. The HTS SQUID sensor is fixed at the bottom of a cryogenic insert, which is immersed into the dewar and allows to locate the sensor at the bottom of the dewar. It is necessary to minimize the distance between the sensor and the test sample (4 mm). The cryogenic insert is made of non-magnetic material, G10, to avoid thermal stress and assure the best thermal stability during the operation time of the SQUID magnetometer. The sensor is connected to an electro-optical converter by cables that pass through the flange on the top of the dewar. The electro-optical converter is used to transmit the detected signals from the sensor to the external SQUID electronics by means of fiber optical

cables, to reduce the  $rf$  noise of the sensor. A picture of the cryogenic dewar and insert is shown in figure 22.



**Figure 22:** (left) cryogenic dewar, (right) cryogenic insert with the SQUID magnetometer at the bottom.

### ***HTS dc-SQUID magnetometer***

The eddy current probe used by the NDE prototype is a high- $T_c$  dc-SQUID magnetometer, inductively coupled. The effective area of the SQUID is  $0.3 \text{ mm}^2$ , it is oriented to measure the in plane component of the magnetic field,  $B_x$  or  $B_y$ . The SQUID magnetometer operates in a flux-locked loop (FLL) configuration with a modulation frequency of 100 kHz. The field-flux transfer is  $1.14 \text{ nT}/\Phi_0$ , the magnetic field sensitivity in unshielded environment is less than  $0.3 \text{ pT}/\sqrt{\text{Hz-rms}}$  for frequencies above 100 Hz. Moreover, the SQUID has a slew-rate of  $10^3 \Phi_0/\text{s}$  and a dynamic range of about 130 dB.



**Figure 23:** picture of the HTS dc- SQUID magnetometer used in this work.

### ***Excitation coil***

Eddy currents were induced by a wire-wound circular coil with a diameter of 5 mm and 10 turns, realized winding a copper wire of diameter  $10\mu\text{m}$ . The coil is fed by a current generator HP 3245A, with typical operating current less than 20 mA in a frequency range of 1kHz-26kHz. The coil is mounted on a Plexiglas slide that allows to move the coil under the dewar. In figure 24 is shown a picture of the circular coil located into the slide.

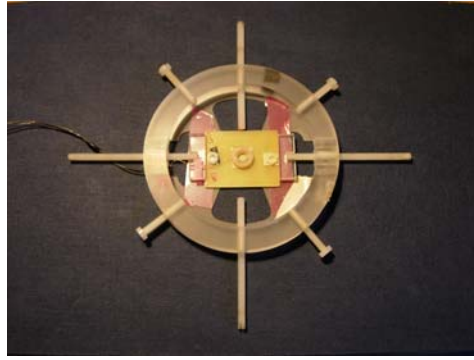


**Figure 24:** Excitation coil used to generate eddy currents into test sample.

### ***x-y position system***

The test samples are moved under the dewar using an non-metallic and non-magnetic computer controlled x-y positioning system. The table, where the sample is located, is made of Teflon and Plexiglas and it is constituted by two slides of Teflon that can shift on a couple of guide block obtained one on the Plexiglas plane and the other on the Teflon plane. The upper slide is moved by means of a toothed belt, while the lower slide is moved using a resin endless crew. The table is connected by means of two bars of length 1.5m with carding hinges, with a stepper motor (CC of 30W), characterized by a minimum step of 0.1 mm and positioning accuracy better than 0.1 mm. The maximum excursion along the x and y axis is 200 mm and the maximum speed is 10 mm/s. The system is capable to move samples with a maximum dimension of 1m and a weight of 5 Kg. The x-y- positioning system is completely automated and controlled by a personal computer using a serial connection.

### ***Data acquisition***

The NDE prototype is formed by the several read out electronics components. At first there is the electronic SQUID controller (iMAG) which provides for the tuning of the SQUID, SQUID reset, trapped flux removal (by heating the SQUIDs), dc offset, low and high pass filtering, and amplification. The output channels of the SQUID read-out electronics send the signal in a parametric amplifier to reduce the electrical noise in the range 1kHz-30kHz. Afterwards, the signal is synchronously demodulated using a dual channel lock-in amplifiers, locked at the frequency of the excitation current and set so that the module and phase of the magnetic field are acquired. The demodulated signals are converted in a digital signal using an analogic digital converter (DAC) at 16 bit that

assures a dynamic range of 96 dB with an amplitude of  $\pm 5V$ , and it is acquired by software from the PC. The x-y positioning system is controlled through software by a PC connected to an interface RS232. The acquisition program is realized in Labview® language and it is capable of control the x-y positioning system and acquires in continuous mode the data with an opportune sampling rate.

## 5. Zero field detector

In the eddy current based SQUID prototype the SQUID magnetometer is used as a zero field detector. A zero field detector measures the variation of magnetic field respect to a “reference” field that in a theoretical approximation, in absence of test samples and neglecting the environmental noise, is about zero. In practice the magnetic field signal detected by the sensor is never zero, but at least coincides with the sensor internal noise. When an excitation coil is used to generate eddy currents into the test sample the configuration between the SQUID sensor and the coil have to guarantee the maximum sensitivity in the detection of reflected magnetic field variations. Therefore, the SQUID sensor does not detect the magnetic field generated by the excitation coil but only the field produced by the test sample. To realize this best operational condition it is necessary to consider the magnetic field distribution of the circular excitation coil, reported below (Figure 25).

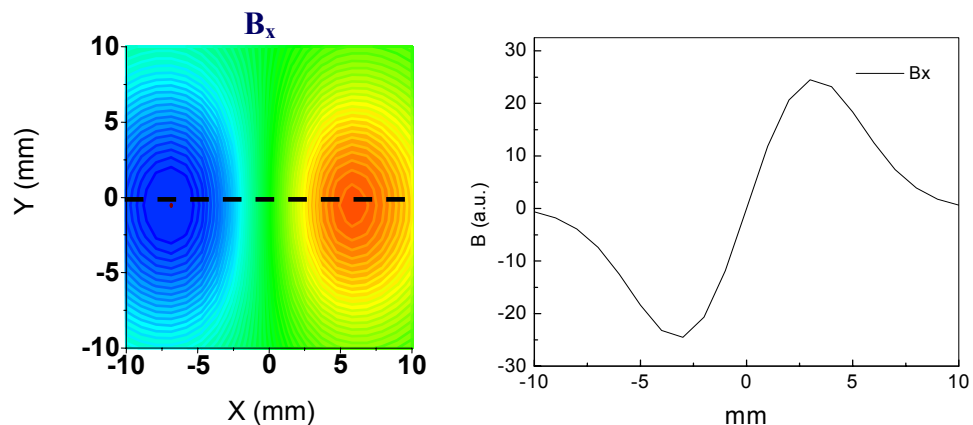


**Figure 25:** (left) The 2-D imaging of the in plane component of magnetic field produced by the circular coil with 5mm in diameter, (right) the graph of the single line scan (dashed line at left) passing across the center of the coil.

At left of Figure 22 the two dimensional distribution of the in plane magnetic field component of the excitation coil is shown. At right the single line scan across the center of the coil, represented by the dashed line of the map at left, is reported. Therefore, to

realize a zero field detector the SQUID pick-up coil of the magnetometer have to be located at the center of the circular coil, where the magnetic field induced by the excitation coil is theoretically zero (see Figure 26).

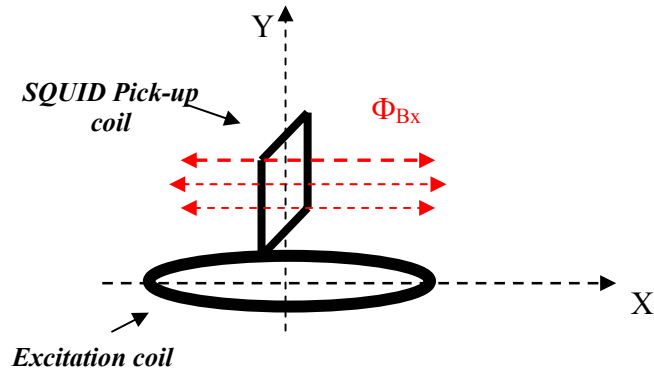


**Figure 26:** Configuration to realize a zero field detector using a circular coil and to measure the in-plane component of the magnetic field.

To realize this configuration a particular procedure is followed.

- At first, the alignment between the SQUID magnetometer and the excitation coil is carried out without any test sample. The coil is moved under the dewar using the slide until the amplitude of the signal displayed on the lock-in amplifier is minimum.
- Then, the test sample is positioned under the system. If the area of the specimen is undamaged and the signal amplitude on the lock-in display is higher than previous stage (in the absence of sample), the coil have to be shifted to reach, in the presence of test sample, the minimum of the detected signal. It is important to note that the minimization of the magnetic field signal have to be performed every time a different material is tested. It depends on the different reflection capability of the materials respect to the induced magnetic field.
- The last step of the optimisation procedure is represented by the acquisition of a line scan across a damaged and undamaged area. Usually, a standard test sample, made of the same material of the test specimens, is used to check the alignment condition. A comparison between two lines scan (related to damaged and undamaged area) will be executed in the impedance plane or in the spatial domain (signal vs. displacement). The first is the conventional Eddy Current-signal representation where the real and imaginary components of the detected signal are combined in the complex plane-like diagram. In this representation the best alignment condition is

reached when the signal of the undamaged area appears as a dot point respect to the line scan of the damaged area (see Figure 27(left)).

On the other hand, in the spatial domain the best condition for the zero field detector is represented by dipole-like shape signal for the damaged area and a straight line for the undamaged area (see Figure 27(right)). The magnetic field signals reported in Figure 27 are related to an aluminium sample where the defect is represented by a circular hole with a diameter of 6 mm and a depth of 1 mm.

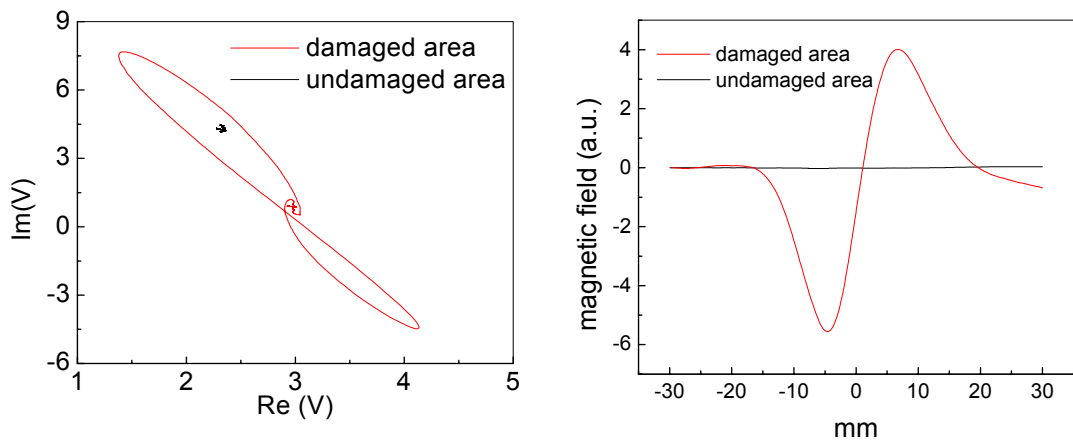


**Figure 27:** Comparison of magnetic signals related to virgin and damaged area, using the impedance plane representation (left) and the spatial (signal vs. displacement) representation (right).

The SQUID prototype response of a defect is represented, in the spatial domain, as a dipole-like shape, while in the impedance plane the damage produces a close trajectory

In the spatial domain the magnetic field signal looks like the in-plane component of magnetic signal generated by the excitation coil. It is due to the fact that the detected signal is the convolution between the eddy current distribution and the defect geometry. In other words, the presence of the damage diverted the eddy currents producing a signal like the field of the excitation source, so that a magnetic imaging of the defect appear such as the magnetic field distribution generated by the eddy current excitation source.

It is interesting to note how the signal can change in both representations when there is a variation of the defects dimension. This is reported in figure 28 where the detected defects are circular holes with the same diameter 6mm and several depth: 1, 2 and 3 mm.

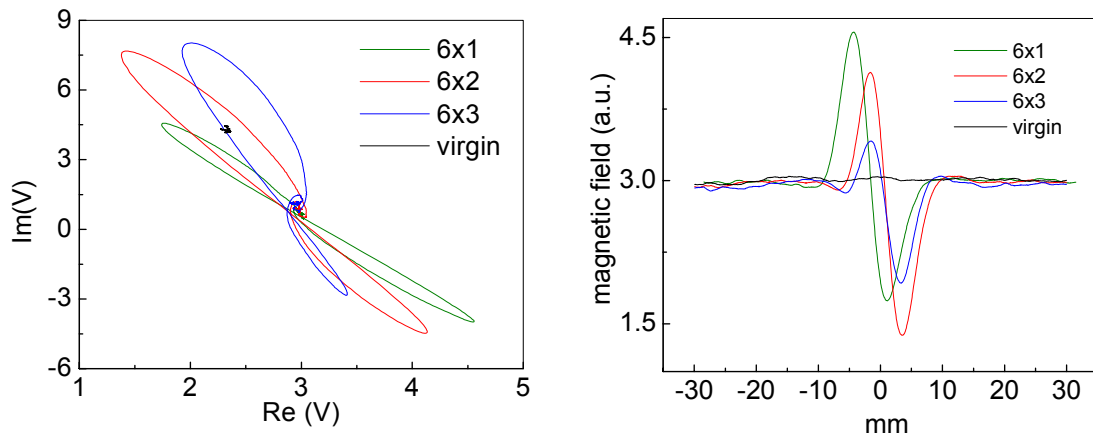


**Figure 28:** Variation of the signal respect to the different defects dimensions, in the impedance plane and in the spatial domain.

It could be noted that the signals related to the different defect dimensions are distinguishable in both representations. Moreover, the impedance plane allows to compare the signal response of the prototype with the conventional eddy current instruments, but information about the position of the defect are lost, while the spatial domain allows not only to distinguish the different defect but allows to localize the position of the defect spatially.

The circular coil is one of the possible excitation source that could be used in the eddy current technique. Another typical excitation source widely used in the eddy current technique based on SQUID sensors is the gradiometric coil, characterized by a 2-D shape. It can be used to detect the in-plane and z-component of the magnetic field. To realize a zero field detector the SQUID pick-up coil must be located in the center of the coil, because only in this position the magnetic field distribution produced by the 2-D coil is minimum.



**Figure 29:** picture of a 2-D coil, made of copper wire.

The configurations of the zero field detector used to detect the in-plane and z-component of magnetic field using the gradiometric coil are shown in Figure 30.

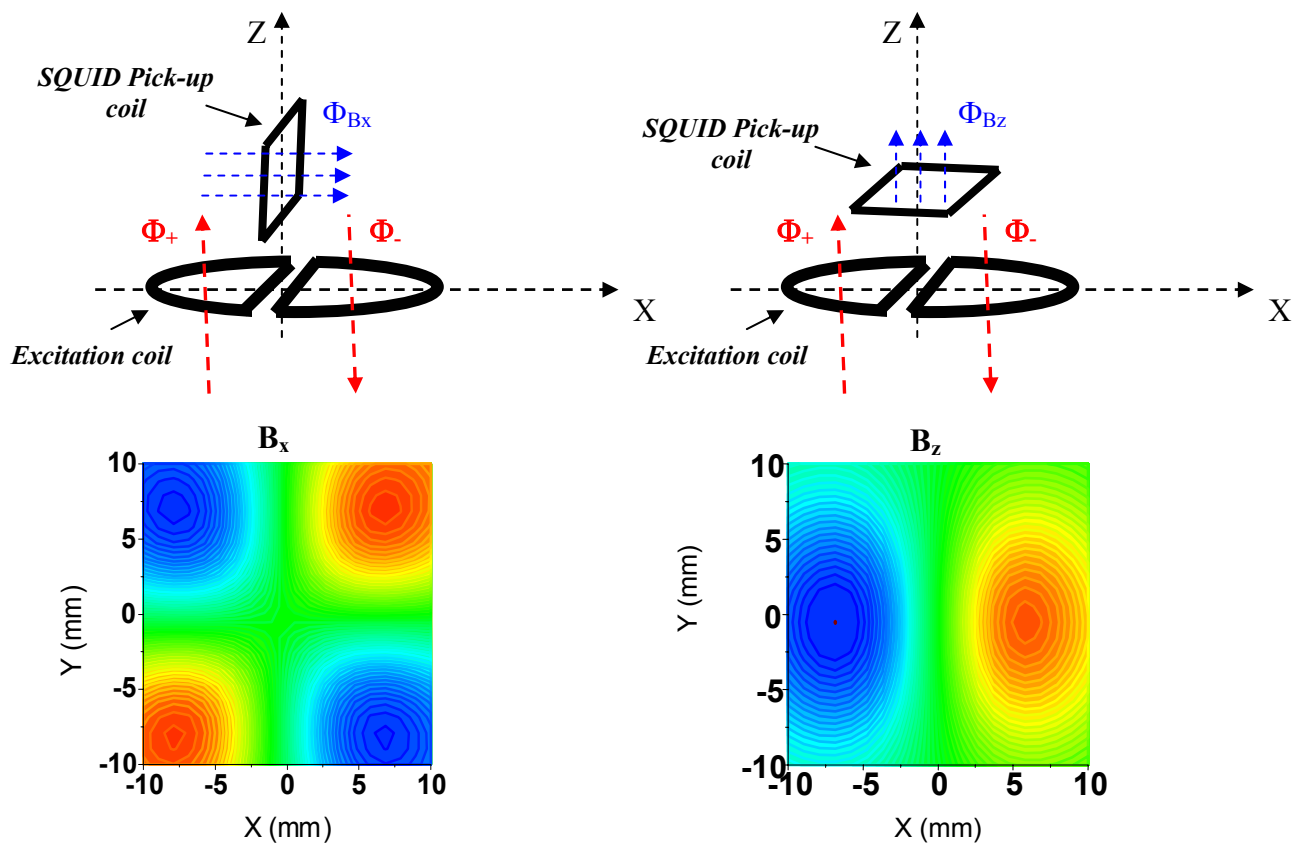


**Figure 30:** (up) Configuration of zero field detector to measure the in-plane component (left) and the vertical component (right). (Down) the in plane and vertical component (left and right, respectively) of the magnetic field distribution produced by the gradiometric coil. Both components have a minimum field in the center.

Moreover, the configuration between the excitation coil and the SQUID sensor is chosen concerning the magnetic field component that one wants to measure. Generally, the circular coil is preferred to detect the in-plane component of magnetic field, while the gradiometric coil is used for the z-component, because in these two cases it is simpler the alignment between the excitation coil and the SQUID pick-up coil.

## References

- [1] *Non-destructive Testing Handbook*, 2nd ed., edited by R. C. McMaster, P. McIntire, and M. L. Mester ~The American Society for Non-destructive Testing, Columbus, OH, 1986; See, in particular, *Electromagnetic testing: Eddy current, Flux Leakage, and Microwave Non-destructive Testing*, *ibid.* Vol. 4.
- [2] Wenk, S.A. and R.C. McMaster. *Choosing NDT: Applications, Costs and Benefits of Non-destructive Testing in Your Quality Assurance Program*. Columbus, OH: American Society for Non-destructive Testing (1987).

[3] McMaster, R.C. and S.A. Wenk. *A Basic Guide for Management's Choice of Non-destructive Tests*. Special Technical Publication No. 112. Philadelphia, PA: American Society for Testing and Materials (1951).

[4] <http://www.diffracto.com/products/dsight/dsight.htm>.

[5] Forsyth D. S., J.P. Komorowski, R.W. Gould, A. Marincak, "Automation of Enhanced Visual NDT Techniques," Proceedings 1st Pan-American Conference for NDT, Toronto, Canada, Sept 14-18 1998, pp. 107-117

[6] Kak A.C., and M. Slaney, *Principles of Computerized Tomographic Imaging*, IEEE, Inc., New York: IEEE Press, (1988)

[7] Chen C.M., S.Y. Lee, and Z.H. Cho, "A parallel implementation of 3D CT image reconstruction on hypercube multiprocessor," *IEEE Transactions on Nuclear Science*, Vol. 37, No. 3 (1990), pp. 1333 – 1346

[8] Dolan K.W., D.J. Schnebeck, R.D. Albert, and T.M. Albert, "Reverse Geometry X-Ray Imaging for NDT Applications," Proceedings of the JANNAF NDE Subcommittee Meeting, CPIA, (1993).

[9] Olivas J. D., S. Bolin, Y. Bar-Cohen, E. J. Chern and J. J. Shaw, "NDE of Space Flight Hardware: Case Study - Microelectromechanical Systems," Proceedings of the 97'ASNT Spring Conference, Houston Texas, March 17-20, (1997), p. 71-73.

[10] Bar-Cohen Y., "Non-destructive Inspection and Quality Control," *ASM International Handbook*, Vol. 3, Adhesive and Sealant, Section 9, (1990), pp. 727-798

[11] Green, 1997

[12] Grandia W.A., and C.M. Fortunko, "NDE Applications of Air-coupled Ultrasonic Transducers," Proceedings of the 1995 IEEE Ultrasonic Symposium, ISSN 1051-0117, Vol. 1 (1995), pp. 697-709.

[13] Oursler & Wagner, 1995

[14] Monchalin, J.-P., C. Néron, M. Choquet, D. Drolet, M. Viens, "Laser-Ultrasonics Inspection And Characterization of Aeronautic Materials," Proceedings 1st Pan-American Conference for NDT, PACNDT '98, Canadian Society for NDT, Toronto, Canada, 14-18 September 1998

[15] Fiedler C. J., T. Ducharme and J. Kwan, "The laser ultrasonic inspection system (LUIS) at the Sacramento Air Logistic Center," *Review of Progress in Quantitative NDE*, Plenum Press, NY, Vol. 16, (1997), pp. 515-522.

[16] Maji A. K., "Assessment of Electronic Shearography for Structural Inspection", *Experimental Mechanics J.*, Vol. 34, No. 2, (1997), pp. 197-204.

[17] Davis C.K., "Shearographic and Thermographic NDE of the Space Shuttle Structure and Thermal Protection Systems," Proceedings of the Technology 2006,

Anaheim, California, <http://www.abpi.net/T2007/papers/mr/docs/shear.htm> October 29-31, 1996.

[18] Jones T., and H. Berger, "Thermographic Detection of Impact Damage in Graphite Epoxy Composites", *Materials Evaluation*, Vol. 50, No. 12, (1992), pp. 1446-1453.

[19] Favro L.D., and R.L. Thomas, "Thermal Wave Hardware Evolution Using the NDI Validation Center", *Materials Evaluation*, 53, 840-843 (1995).

[20] Fitzpatrick G. L., D. K. Thome, R. L. Skaugset, W. C. L. Shih, "Magneto-Optic/Eddy Current Imaging of Subsurface Corrosion and Fatigue Cracks in Aging Aircraft", *Review of Progress in Quantitative NDE*, Vol. 15A, D. O. Thompson and D. E. Chimenti (Eds.), Plenum Press, NY, (1996), pp. 1159-1166

[21] Thompson J.G., "Subsurface Corrosion Detection in Aircraft Lap Splices Using a Dual Frequency Eddy Current Inspection Technique," *Materials Evaluation*, Vol. 51 (Dec. 1993), pp 1398-1401.

[22] Lepine B.A., and R.T. Holt, "An Eddy Current Scanning Method for the Detection of Corrosion Under Fasteners in Thick Skin Aircraft Structures", *Canadian Aeronautics and Space Journal*, (March 1997), pp. 28-33.

[23] Mitra S., E. Uzal, J.H. Rose, J.C. Moulder, "Eddy Current Measurements of Corrosion-Related Thinning in Aluminium Lap Splices", *Review of Progress in Quantitative NDE*, Vol.12, Plenum Press, NY, (1993) pp. 2003-2010.

[24] Bieber J.A., C. Tai, J.C. Moulder, "Quantitative Assessment of Corrosion in Aircraft Structures Using Scanning Pulsed Eddy Current", *Review of Progress in QNDE*, Vol. 17A, D. O. Thompson and D. E. Chimenti (Eds.), Plenum Press, NY (1998), p 315.

[25] Jack Blitz, "Electrical and magnetic methods of Non-destructive Testing" Chapman & Hall, London.

[26] Harold Weinstock lecture at European/american summer school funded by SCENET, ESF, AFOSR and ONRG at Il Ciocco, Tuscany, Italy, 2005.

[27] J.P. Wilksw, "SQUID magnetometers for biomagnetism and nondestructive testing: important questions and initial answers, *IEEE Trans. Appl. Supercond.* 5 2 1995 74-120.

[28] Kreutzbruck, M.V., M. Mück, U. Baby and C. Heiden, "Studies in Applied Electromagnetics and Mechanics" <http://www.ndt.net/article/ecndt98/aero/005/005.htm> (NDT.net - September 1998, Vol.3 No.9), Vol. 13, IOS Press, Amsterdam (1998)

[29] Fujita, M. Suzuki, S. Ikegawa, T. Ohtsuka, and T. Anayama in *Proceedings of the ICEC 9*, edited by K. Yasukochi and H. Nagano, (Butterworth, Guildford, 1982) p. 369.

[30] N.Khare and P. Chaudari, *Appl. Phys. Lett.* **65**, 2353 (1994).

- [31] G. Thummes, M. Mück, R. Landraf, F. Giebeler, and C. Heiden, Cryogenic Engineering Conference, Columbus, Ohio, in *Advances in Cryogenic Engineering*, (1995).
- [32] Hohmann, R., H.-J. Krause, H. Soltner, Y. Zhang, C. A. Copetti, H. Bousack, and A. I. Braginski, 1997, *IEEE Trans. Appl. Supercond.* **7**, 2860.
- [33] d. J. Staton, R. N. Friedman, J. P. Jr. Wikswo, 1993, *IEEE trans. Appl. Supercond.* **3**, 1934-1936.
- [34] R.L. Fagaly, Superconducting sensors: instruments and applications, *Sensors* **13** 10 1996 18–27.
- [35] Weinstock H and Nisenoff M 1985 Nondestructive evaluation of metallic structures using a SQUID gradiometer *SQUID '85, Proc. 3rd Int. Conf. On Superconducting Quantum Devices* ed H D Hahlbohm and H Lübbig (Berlin: deGruyter) pp 843–7
- [36] Weinstock H and Nisenoff M 1986 Defect detection with a SQUID magnetometer *Review of Progress in QNDE* vol 5 ed D O Thompson and D Chimenti (New York: Plenum) pp 669–704 Weinstock .
- [37] Bain R J P, Donaldson G B, Evanson S and Hayward G 1985 SQUID gradiometric detection of defects in ferromagnetic structures *SQUID '85, Proc. 3rd Int. Conf. on Superconducting Quantum Devices* ed H D Hahlbohm and H Lübbig (Berlin: deGruyter) pp 841–6
- [38] Bain R J P, Donaldson G B, Evanson S and Hayward G 1987 Design and operation of SQUID-based planar gradiometers for non-destructive testing of ferromagnetic plates *IEEE Trans. Magn.* **23** 473–76.
- [39] Evanson S 1988 The evaluation of a SQUID based noncontact magnetic NDE technique for application to the inspection of offshore steel structure *PhD Thesis* University of Strathclyde, Glasgow, Scotland
- [40] Evanson S, Bain R J P, Donaldson G B, Stirling G and Hayward G 1989 A comparison of the performance of planar and conventional second-order gradiometers coupled to a SQUID for the NDT of steel plates *IEEE Trans. Magn.* **25** 1200–3
- [41] Bruno A C, Ewing A P and Wikswo J P Jr 1995 Measurements of surface-breaking flaws in ferromagnetic plates by means of an imaging SQUID susceptometer *IEEE Trans. Appl. Supercond.* **5** 2484–5
- [42] Sawande G, Straub J, Krause H-J, Bousack H, Neudert G and Ehrlich R 1995 Signal analysis methods for the remote magnetic examination of prestressed elements *Proc. Int. Symp. on Non-Destructive Testing in Civil Engineering (Berlin, September 1995)* (Berlin:DGZP EV)
- [43] M.Valentino, A. Ruosi, G. Pepe, G. Peluso “superconductive and traditional electromagnetic probes in eddy-current NDE for detection of deep defects”

Electromagnetic Non-Destructive Evaluation (ENDE), D. Lesselier and A. Radzek (Eds.), IOS Press (1999)

[44] M.v. Kreutzbruck et al defect detection in thick aircraft samples using HTS SQUID magnetometer, *Physica C* 368,2002,85-90.

[45] A. Ruosi, M. Valentino, G. Peluso, G. Pepe, "Analysis of low-velocity impact damage in reinforced carbon fibre composites by HTS-SQUID magnetometers," *IEEE Trans. App. Supercond*, vol.11, 2001, pp. 1172-1175.

[46] A. Ruosi, M. Valentino, V. Lopresto, and G. Caprino, "Magnetic response of damaged carbon fibre-reinforced plastics measured by HTS-SQUID magnetometer," *Composite Structures*, 2002, vol. 56, 2002, pp. 141-149.

[47] Y. Hatsukade, N. Kasai, H. Takashima, M. Kurosawa and A. Ishiyama, "Detection of internal cracks and delamination in carbon-fibre-reinforced plastics using SQUID-NDI system," *Physica C*, vol. 372-376, 2002, pp. 267-270.

[48] Bonavolontà, G. Peluso, G. P. Pepe, A. Ruosi and M. Valentino, "Detection of artificial defects in Carbon Fibre Reinforced Polymers for aeronautical applications using a HTS SQUID magnetometer," in *Proc. EUCAS Conf. Sorrento Italy*, 2003.

[49] C. Carr, D. Graham, J. C. Macfarlane and G. B. Donaldson, "SQUID based non destructive evaluation of carbon fibre reinforced polymer," *IEEE Trans.App. Supercond.*, vol. 13, 2003, pp.196-199.

[50] C. Bonavolontà, G. Peluso, G.P. Pepe, M. Valentino "Detection of early stage damage in Carbon Fiber Reinforced Polymers for aeronautical applications using an HTS SQUID magnetometer" *Eur. Phys. J. B.* 42, 491-496, 2004.

# Chapter 3

## Composite Materials

### Introduction

In this chapter the main characteristics of new advanced composite materials, such as carbon fiber reinforced polymers (CFRPs) and Fiber-glass aluminium (FGA) laminates are described. Their typical fabrication processes are reported and a particular attention is dedicated to the mechanical properties of these composites. A briefly description of the applications in which the composite materials are employed is reported in the fourth paragraph. Moreover, the NDE topics related to the quality control during the manufacturing and in service of CFRPs and FGAs are shown. Finally, the description of the tested sample analysed in this thesis is reported.

### 1. Fiber-reinforced polymer composite

A fiber-reinforced polymer (FRP) composite is a combination of fibers within a matrix of a plastic or resin material. The fibers are the principal constituent in a FRP, they occupy the largest volume fraction in a composite laminate and share the major portion of the load acting on a composite structure. Proper selection of the type, amount, and orientation of fibers is very important, since it influences the following characteristics of a composite laminate, such as tensile and compressive strength and modulus, fatigue strength as well as fatigue mechanism, electrical and thermal conductivity, and cost. The fibers usually used are:

- Glass
- Carbon
- Aramid (often known through the trade names Kevlar or Twaron)

Glass fibers are used for the majority of composite applications because they are cheaper than the main alternatives. There are different forms known by names like E-glass (the most frequently used), and S2- or R-glass. The main characteristics of glass fibres are their high strengths, moderate Elastic (or Young's) modules and density, and their low thermal conductivity. Special corrosion resistant glass fibres are also available. Carbon fibers, manufactured by the controlled carbonisation of organic precursors (such as the textile fibre PAN and pitch), are produced in many grades. The main characteristics of carbon fibres are their high strengths and Young's module, and their very low densities and thermal expansivity. The characteristics of these fibres are often indicated in their commercial names by codes such as HS (High Strength), HM (High Modulus), UHM (Ultra High Modulus) etc. the wide range of fibre and properties that are available, offer the maximum possibility for optimisation of the material to provide properties specifically matched to a particular application.

The aramid fibers are polymeric fibres, the main characteristics of which are their high strengths, impact resistance due to their energy absorbing properties, moderate Young's module and low densities. Laminates formed from aramid fibres are known for their low compressive and shear strengths. The fibres themselves are susceptible to degradation from UV light and moisture but exhibit resistance to acids and alkalis. They are more resistant than other fibres to chemical attack from hydrochloric acid. Kevlar is the trade name of the original aramid patented by Dupont, and Twaron is the name of a similar fibre produced by Hexcel.

The fibers can be used in three significantly different ways, with the performance changing for each.

1. the highest performance in terms of strength in one direction comes from *unidirectional* fibers. The fibers are parallel and give their maximum possible performance in this single direction.
2. by arranging the fibers in a weave or mat, strength can be gained in more directions, although the limit strength is reduced.
3. by chopping the fibers into short lengths and arranging them randomly, equal strength is achieved in all directions. This is generally the cheapest technique, used for the least structurally demanding cases.

The role of the matrix in the fiber-reinforced composite is to transfer stress between the fibers, to provide a barrier against an adverse environment, and to protect the surface of the fibers from mechanical abrasion. The selection of the matrix has a major influence

on the interlaminar shear as well as in-plane shear properties of the composite material. The interlaminar shear strength is an important design consideration for structures under bending loads, whereas the in plane shear strength is important under torsional loads. The matrix provides lateral support against the possibility of fiber buckling under compression loading, thus influencing to some extent the compressive strength of the composite material. The interaction between the fibers and matrix is also important in designing damage-tolerant structures. Finally, the processability and defects in a composite material depend strongly on the physical and thermal characteristics, such as viscosity, melting point, and curing temperature of the matrix.

The polymeric matrices are divided into two major groups: thermoplastics and thermosets.

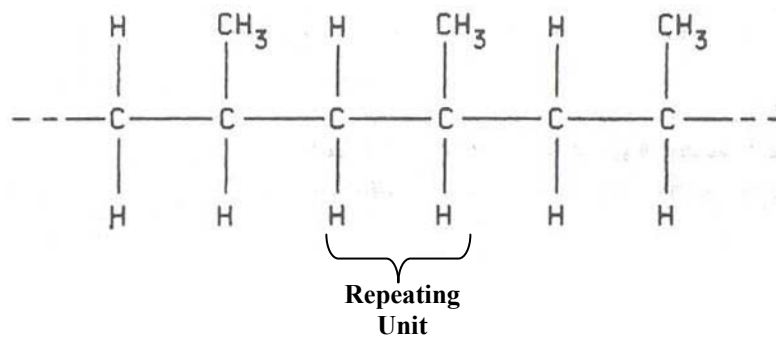


**Figure 1:** Example of repeating units in polymer molecules in polypropylene.

In a thermoplastic polymer, individual molecules are linear in structure with no chemical linking between them (fig.1). they are held in place by weak secondary bounds (intermolecular forces), such as van der Waals bonds and hydrogen bonds. With the application of heat and pressure, these intermolecular bonds in a solid thermoplastic polymer can be temporarily broken, and the molecules can be moved relative to each other to flow into new positions. Upon cooling, the molecules freeze in their new positions, restoring the secondary bonds between them and resulting in a new solid shape. Thus, a thermoplastic polymer can be heat softened, melted, and reshaped (postformed) as many times as desired.

Examples of thermoplastics matrices are:

- polyamides (nylon)
- thermoplastic polyesters (e.g. PET)
- polypropylene

All this material can be used on their own, but can benefit from the reinforcing provided by fibers.

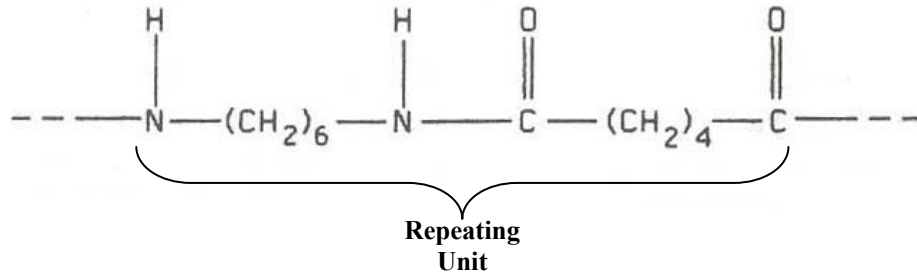


**Figure 2:** Example of repeating units in polymer molecules in nylon 6-6 molecules.

In a thermoset polymer, on the other hand, the molecules are chemically joined together by cross-link, forming a rigid, three-dimensional network structure (fig.2). Once these cross-link are formed, during the polymerisation reaction (also the curing reaction), the thermoset polymer can not be melted and reshaped by the application of the heat and pressure. However, if the number (frequency) of cross-link is low, it may still be possible to soften them at elevated temperatures.

The most commonly encountered thermoset polymers that are used as matrices for fiber-reinforced polymer (FRP) composites are:

- polyesters
- vinyl-esters
- epoxies
- phenolics

The advantages and the benefits offered by the FRP composites vary depending on the choice of resin, fibre and process of manufacture. There needs to be a process of optimisation of the design of the composite since not all of the best properties can be achieved at the same time. The main advantages of the FRP are summarized below.

- weigh saving
- time saving: its high strength-to-ratio means that components can be light and so construction time can be reduced in time-critical project, i.e. Bridge repairs.
- Able to add to a structure: its high strength to weight ratio means that they can be add to a structures without further strengthening of existing structure

- Low maintenance requirements: ideal where access is difficult or expensive, for example for high roofs, underwater.
- Resistance to an harsh or corrosive environment
- Impact resistance, can be designed to absorb blast or ballistic loads and other impacts.
- Fire resistance, the FRP composites can be designed to meet the most stringent fire requirements.
- Freedom of shape: moulding technique allow unique shape/complex geometry .

## **2. Fabrication in fiber-reinforced polymers**

A wide range of processing methods is available for FRP composites, although generally the underlying principle is the same. There are differences between the technique available for thermoset and thermoplastic resins, due to their different properties. A thermosetting resin, which may be in either a liquid-solid state, is combined with an array of reinforcing fibres and, by the application of heat and/or pressure, combination is converted to a rigid mass as the resin polymerises. One of the most important features of the manufacture of polymer composites is that the structural material (i.e. the composite) and the product are formed simultaneously in a single process. Composite structures may be building in situ from the raw materials, as in hand lay-up methods, or they may be made by shaping semi-finished products, in which the components are already combined in the correct properties. In the case of reinforced thermoplastics the fibers are combined with a polymer, which is already polymerised so that the final fabrication is a forming process only. The manner of combining fibers and matrix into a composite material depend on the fiber/resin combination and on the scale and geometry of the structure to be manufactured. The microstructure and the properties of the end product will depend on the fabrication process that is chosen in order to meet specific design requirements.

### ***Poltrusion***

In the poltrusion process (fig.3), tightly packed tows of fibers, impregnated with catalysed resin, are pulled through a shaped die to form highly aligned, continuous sections of simple or complex geometry.

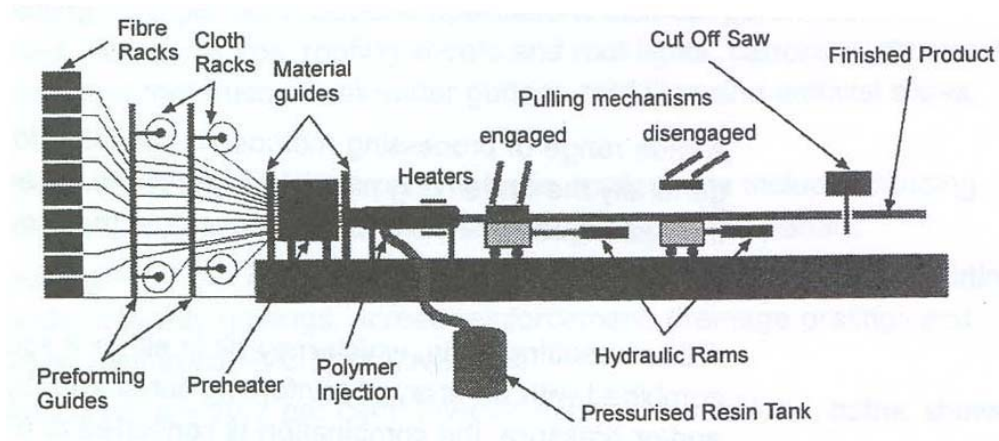


**Figure 3:** The pultrusion process (SO system Ltd)

Curing of the resin may be achieved either by heating the die itself or by the use of dielectric heating. Solid and hollow sections may be produced by this process, and because of the high content (70% by volume is achieved) and the high degree of fibre alignment resulting from the tensile force used to pull the fibre bundle through the die, extremely good mechanical properties can be obtained (the highest achievable in any variety of composite). Off-axis fibres may also be introduced into the structure if required. Typical applications of pultruded shaped are concrete reinforcing bars and space frames, I beam etc. Some of the most common manufacture techniques are described as following.

### ***Filament winding***

Cylindrically symmetric structures such as pressure vessel, tanks and a variety of pipes, can be made by winding fibres. This technique involves the building up of layers of fibres impregnated with the resin by winding them on a rotating frame. Generally, continuous length of carbon fibers is used in this technique. Carbon fibres are passed through a bath containing the thermosetting resin and wound around a mandrel in the conventional manner according to a programmed lay-up pattern, and then cured to yield a plastic structure which is strengthened and stiffened in the desired direction. There are two types of patterns used in this technique: helical winding in which a fixed angle is chosen; and biaxial winding where two winding angles ( $0^\circ$  and  $90^\circ$ ) are selected. Helical winding is more common because of its simplicity, but biaxial winding enables the structure with special design and property. Filament winding has been used to aerospace hardware, sporting goods, and components for the automotive industry.

### ***Hand lay-up technique***

This is a manual process, using simple inexpensive items of equipment, and suitable for crosslinkable plastic resins. The normal basis of the method is a unidirectional fabric where most of the yarns or bundles of fibers are in the warp direction, with just a few weft yarns to provide location (fig.4a).

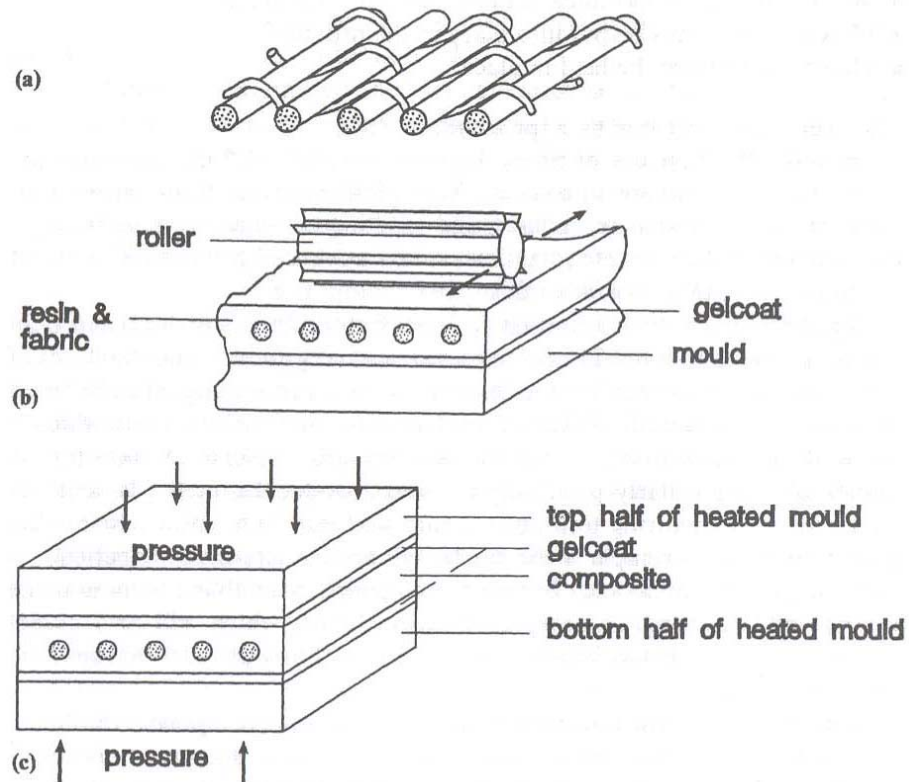


**Figure 4:** (a) unidirectional fabric; (b) the principle of hand lay up, (c) basic press (compression) moulding.

It is a flimsy fabric which is easy to distort. The simplest mould surface is a flat polished sheet of glass, metal or wood. The waxed sheet is covered with a thin coat of unreinforced crosslinkable resin (called a gelcoat), then covered with the fabric, taking care to ensure that the fibres are as aligned as possible. Resin (with added catalyst and accelerator) is then poured on, and ribbed rollers are used to wet out the cloth, coating each fibre, removing air pockets (voids), and consolidating the lay up (fig. 4b). In such a basic process it is difficult to ensure uniformity of thickness and volume fraction of fibres, and to ensure that the fibres are parallel. An alternative is to transfer the mold to a press, and squeeze out excess air resin, to obtain a more uniform product with a defined thickness. (fig 4c).

### ***Pre-preg technique***

A prepreg is a convenient thin sheet of fibres traditionally pre-impregnated with a slightly crosslinked resin to hold the fibres in place. If the fibres are lined in one direction the prepreg is rather flimsy in the transverse direction. But overall a prepreg is much easier and cleaner to handle than any wet lay-up process, and the proportion of fibres is already precisely fixed, and usually high, typically in the range 0.5 to 0.7. prepregs are usually destined for the manufacture of high-performance precision laminates. It is also possible to make prepreg based on one of a small number of speciality thermoplastics. One basic process is to pull fibres from many large capacity spools through a resin bath, remove excess resin, and then wind the fibres helically on to a large diameter drum at a very small angle to the circumference. In this way a very thin-walled tube is made with the fibres arranged in the circumferential direction. The tube is then cut along its length, removed with great care from the drum, and flattened between the platens of a heated press. The heat causes the resin to just begin to crosslink, so it loses much or all of its stickiness and can then be conveniently handled.

### **3. Mechanical properties**

In common with all structural materials, the behaviour of composites under cyclic or repetitive loading must be considered. The fatigue behaviour of composites differs from that of, say, steel. With steel, failure tends to result from the intermittent propagation of single crack, and the material even quite close to the crack is virtually unchanged. The inhomogeneous, and isotropic nature of composites results in fatigue damage in a general, rather than localised manner, and failure does not always occur through the propagation of a single crack.

Damage modes for composites include fibre breakage, matrix cracking, debonding, delamination and transverse ply cracking, and the predominance of one mode, or the interaction of several is dependent on the properties of the fibre and resin. It is not certain whether composites exhibit the familiar “fatigue limit” known to users of steel. Few experimental results have shown any clear indication of such a limit, although in modern aircraft design the any clear indication of such a limit, although in modern aircraft design the concept of a zero-growth threshold for pre-existing damage is now being used. it is not safe to assume that fatigue can be ignored if working stresses are kept low (perhaps to avoid creep deformations). Stresses in the direction normal to the

fibres could possibly be high as a result of load/fibre misalignment, which could lead to fatigue damage. In order to minimize the risk from fatigue problems it is appropriate to make use of design data where available and sensible use of generous safety factors.

Composites differ from conventional materials in the way in which they respond to stress. Under load, many local microstructural damage events occur, including resin crack, fibre breakage, local fiber/resin debonding, and delaminations. Depending on the particular laminates lay-up, the damage processing may begin to occur even at low very strain level and the accumulation of the damage strain continues as long as loading as sustained. This damage is usually widely distributed throughout the stressed composite, and in the early stages of life it does not seriously impair the load-bearing ability of the material. Moreover, this gradual accumulation of damage gives rise to changes in the material physical properties that can be detected by means of suitable optical, dielectric or ultrasound technique. This complex mode of damage accumulation has important implications for the toughness of composites and for their fatigue response. Because of the interaction of the effects of these microstructural damage mechanisms and their energy-absorbing ability, many fibre composites exhibit excellent toughness and resistance to impact by comparison with conventional engineering materials. The structural use of reinforced plastics depends on primarily on their mechanical response to load and also to their ability to absorb energy, either as a means of inhibiting crack growth or as a means of controlling the effects of impact. On the other hand, low velocity impacts may cause local sub-surface delaminations, which can result in a reduction in the compression strength. Indeed, the compression strength after impact (CAI) is used as an indicator of severity of impact damage sustained by a composite.

In order to improve procedure to designing with this class of composite materials that accumulate damage under load, and permit their use beyond the point where damage is first initiated, the concept of damage-tolerance design has gained considerable attention in recent years. The concepts is not new: in effect it adopts the principle that the microstructural damage events, which can occur in the neighbourhood of a stress concentrator ( i.e. a crack) can have a beneficial effect in reducing the rate of crack growth in a manner somewhat analogous to that in which the plastic zone ahead of a crack tip in a metal can also inhibit crack growth.

## 4. Applications

The basic characteristics important to all applications of carbon fiber composites are high specific strength and stiffness together with lightweight. There is a greater degree of flexibility in carbon fiber-reinforced materials, in that the strength and stiffness can be varied significantly in different areas of a composite part by selecting the type, form, and suitable orientation of the fiber in the composite and by controlling the local concentration of the fiber. In addition several physical properties of carbon fiber composite, such as their thermal stability, electrical conductivity, and corrosion resistance, can be varied by suitable choice of the matrix material and by varying the processing conditions for preparation of the composite.

Aerospace has been a primary influence in the progress of CFRP and still constitutes the largest market sector[1-3]. This expansion is likely to take place in using CFRP in helicopter and civilian aircraft. In addition, consumption in military aircraft and other space and defence applications is also likely to increase. carbon fibers are preferred in those stiffness-critical components where design specifications on deflection limits, buckling, and dynamic response cannot be met without them. Important advances include major use of CFRP for control surface (e.g. spoilers and ailerons) and tail plane assemblies for the Airbus 320 and Boeing 777 aircraft. These high successful passenger planes not only use CFRP extensively for secondary structures such as fairings, brakes, spoilers, ailerons, landing gear, and doors but also employ CFRP in the vertical and horizontal fins in the A310 and 320 Aseries, making them the first passenger planes to use a composite in their primary structure. The new generation of military combat aircraft fabricated by French company, Dassault Aviation, has also utilized composite in a large portion of structure design [4]. In this structure the composite materials represent approximately 24% of the airframe mass and 70% of the wet surface. The most significant area of the application of CFRP has been in the main and tail rotor blades of helicopter, where the prospects for improved fatigue resistance over all metal blades and the greater freedom in design and fabrication have been recognized and exploited rapidly. The use of composite unidirectional prepeg permits better optimisation of rotor blade mechanical and dynamic characteristics, and they have demonstrated better static and fatigue strength than those of metal blades. The largest pieces of CFRP structure in service to date are to be found on a space vehicle, the NASA Space Shuttle. The payload bay doors of the Shuttle (fig.5), which are 18.3 meter long and 139.4 a square meter in area, are fabricated of CFRP [5].

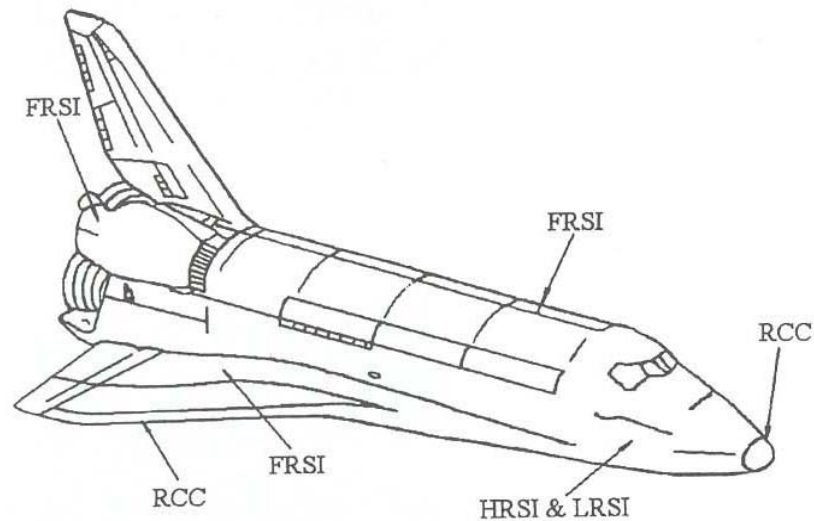


**Figure 5:** A schematic drawing of the space shuttle

This has resulted in an estimated weight saving of 23% over used as components in aluminium alloy. Laminates CFRP now flying successfully on several aircraft include land gear doors on the F-14 fighter and wing spoilers on more than 100 Boeing 737s in the NASA fleet. The floor decking of the Boeing 747 is also made from laminated carbon fiber prepeg and Dupont's Nomex® aramid. The CFRP has applied also in some marine applications where the demand of light-weight and corrosion-reduced structure is increased. There is an increased interest in the development of the application of composites in the structure components of ships and submarine. A significant technical limitation of the composites used on the ships or submarine is the combustible nature (fire, smoke, and toxicity) of the organic matrixes based composites. Because the safety requirement is more stringent, the composite materials used on the US Navy vessels is requested to be sufficiently fire resistant not to be a source of spontaneous combustion. Among the many possible thermoset resins, phenolic resins have the inherent characteristics of low flammability, produce little smoke on burning, and have good thermal stability. The Asean Lady motor cruiser, the world's largest CFRP boat, has 48 m long hull and deck made up to Torayaca CFRP to reduce weight and thus higher speeds.

Also the racing car industrial world pays much attention to the CFRP composites. In particular, the Formula 1 race cars in the last ten years increased the use of the new advanced materials, especially CFRP[6]. More and more components, such as wings, have been replaced by the carbon fiber reinforced composite materials.

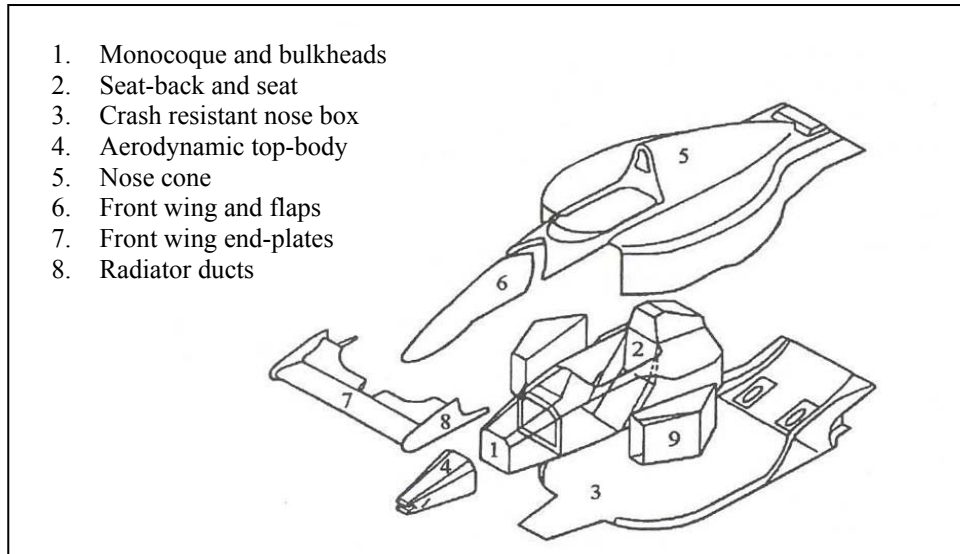


**Figure 6:** Simplified modification of the structural components of 1991 McLaren MP4/6 racing car made from carbon fiber composites.

Figure 6 shows a schematic drawing of the composite parts of the 1991 McLaren MP4/6 racing car [7]. This formula 1 racing car consists of approximately 75% by weight of carbon fiber composites in the structure, resulting in a higher performance and safety for its occupant. Crash safety is a very important aspect of racing car design. The enormous energy absorbing capability of fibre reinforced composite has largely reduced the instance of serious injury in the race. The structural component of racing cars are mainly composed of continuous fiber reinforcement, thus, the stiffness and strength of the composite is dominated by the fiber properties. The applications of composites in today's rail vehicles are mainly adopted on the three-dimensional molded nose cap at the front part of trains and internals of passenger train [8]. The carbon fiber reinforced composite incorporated train structure saves about 30-40 % weight than a conventional steel cab, and exhibits a strong impact resistance to prevent penetration by a 0.9 Kg steel cube when travelling at 350 km/hour. A recent French TGV high speed train was fabricated with different types of composites for the nose section, to provide extra rigidity and resistance to impact when runs as high as 300 km/hour.

## 5. NDE of composite materials

The high stiffness to weight ratio, low electromagnetic reflectance and the ability to embed sensors and actuators has made fiber-reinforced composites an attractive construction material for primary aircraft structures.

Currently, there are several critical issues that are still challenging the NDE community with regards to inspection of composites.

**Table 1:** Effect of defects in composite materials

Defect	Effect on the material performance
Delamination	Catastrophic failure due to loss of interlaminar shear carrying capability. Typical acceptance criteria require the detection of delaminations that are $>$ or $=$ 0.64-cm.
Impact damage	The effect on the compression static strength <ul style="list-style-type: none"> <li>• Easily visible damage can cause 80% loss</li> <li>• Barely visible damage can cause 65% loss</li> </ul>
Ply gap	Degradation depends on stacking order and location. For $[0,45,90,-45]_{2S}$ laminate: <ul style="list-style-type: none"> <li>• 9% strength reduction due to gap(s) in <math>0^\circ</math> ply</li> <li>• 17% reduction due to gap(s) in <math>90^\circ</math> ply</li> </ul>
Ply waviness	<ul style="list-style-type: none"> <li>• Strength loss can be predicted by assuming loss of load-carrying capability.</li> <li>• For <math>0^\circ</math> ply waviness in <math>[0,45,90,-45]_{2S}</math> laminate, static strength reduction is: <ul style="list-style-type: none"> <li>• 10% for slight waviness</li> <li>• 25% for extreme waviness</li> <li>• Fatigue life is reduced at least by a factor of 10</li> </ul> </li> </ul>
Porosity	<ul style="list-style-type: none"> <li>• Degrades matrix dominated properties</li> <li>• 1% porosity reduces strength by 5% and fatigue life by 50%</li> <li>• Increases equilibrium moisture level</li> <li>• Aggravates thermal-spike phenomena</li> </ul>
Surface notches	<ul style="list-style-type: none"> <li>• Static strength reduction of up to 50%</li> <li>• Local delamination at notch</li> <li>• Strength reduction is small for notch sizes that are expected in service</li> </ul>
Thermal Over-exposure	Matrix cracking, delamination, fiber debonding and permanent reduction in glass transition temperature

These issues include:

- *Material Properties Characterization:* Production and service conditions can lead to property degradation and sub-standard performance of primary structures. Causes for such degradation can be the use of wrong constituent (fiber or matrix), excessive content of one of the constituent (resin rich or starved), wrong stacking order, high porosity content, micro-cracking, poor fiber/resin interface aging, fire damage, and excessive environmental/ chemical/radiation exposure. Current destructive test

methods of determining the elastic properties are using representative coupons. These methods are costly and they are not providing direct information about the properties of represented structure.

- *Need for Rapid Large Area Inspection:* Impact damage can have critical effect on the structure capability to operate in service (see Table 1). This critical type of flaw can be induced during service life anywhere on the structure and it requires detection as soon as possible rather than waiting for the next scheduled maintenance phase. Repeated application of conventional NDE for verification of the structural integrity can be very expensive and takes aircraft out of their main mission. Since impact damage can appear anywhere, there is a need for a low-cost system that can be used to rapidly inspect large areas in field condition.
- *Real-Time Health Monitoring:* A system of health-monitoring is needed to reduce the periodic inspection, which requires the temporary removal of the aircraft from service. Fundamentally, such health monitoring systems emulate biological systems, where onboard sensors track the structural integrity throughout the life cycle. The life cycle starts from production and continues through service and it is essential to have an alarm to indicate that a critical parameter was exceeded.
- *Smart Structures:* The availability of compact actuators, sensors and artificial intelligence has made it possible to develop structures that self-monitor their own integrity and use actuators to avoid or timely respond to threats. The changing environment or conditions can be counteracted by adequate combination of actuators and sensors that change the conditions and/or dampen the threat. Artificial intelligence can be used to assure the application of the most effective response at the shortest time. An example of the application of smart structures is the reduction of vibrations that lead to fatigue.
- *Residual Stresses:* Current state of the art does not provide effective means of non-destructive determination of residual stresses. Technology is needed to detect and relieve residual stresses in structures made of composite materials.
- *Weathering and Corrosion Damage:* Composites that are bonded to metals are sensitive to exposure to service fluids, hygrothermal condition at elevated temperatures and to corrosion. Particular concern rises when aluminium or steel alloys are in a direct contact with graphite/epoxy or with graphite/polyimide laminates. The graphite is cathodic to aluminium and steel and therefore the metal, which is either fastened or bonded to it, is eroded. In the case of graphite/epoxy, the

metal deteriorates, whereas in the case of graphite/polyimide defects are induced in the composite in the form of microcracking, resin removal, fiber/matrix interface decoupling and blister (e.g. delaminations). When an aluminium panel is coupled to a Gr/Ep protective coating the aluminium is subjected to a significant loss of strength. To prevent such degradation, a barrier layer is needed between the metal and the graphite/epoxy, where many times glass/epoxy or Kevlar/epoxy layers are used.

## 6. Test specimens

In this thesis two kind of composite materials have been analysed: CFRPs and FGA (or GLARE<sup>®</sup>). The CFRP tested samples were multidirectional composites 70-mm x 70-mm based on an epoxy-matrix (HMF 934) reinforced with prepreg layers made of T400 carbon fibres fabricated by hand lay-up and autoclave curing. The fibre content in the composite was 55% by volume. Each sample is made of six blocks of layers stacked together, and each block has a number of overlapping layers with the same fibre orientation, as shown in Figure 7. The number of layers in each block depends on the total thickness of the sample, which ranges from 2-mm to 4-mm.

The multidirectional specimens were loaded at the centre by a hemispherical steel indenter, having a diameter of 12.7-mm, and falling from different heights using a drop weight tower machine. Specimens with a thickness of 2-mm, 3-mm and 4-mm thick samples were damaged with impact energies ranging from 1.8J up to 36J.

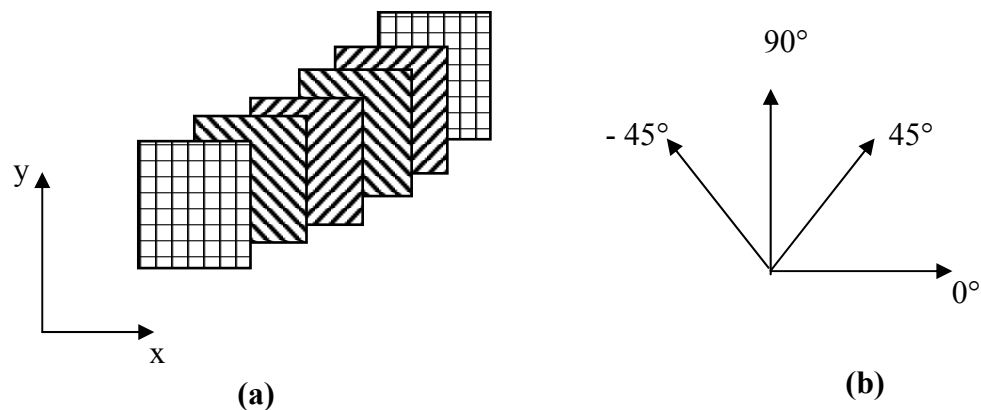


**Figure 7.** (a) Stacking sequence of a multi-layer sample  $[(0/90),\pm 45]_s$ ; (b) fibre orientations.

Moreover, the FGAs tested in this work were made of 2024 T3 aluminium 0.3-mm thick sheets and FM94 S2-glass/epoxy pre-peg 0.125-mm thick layers. The resin content in the pre-peg was 27% by weight. The stacking sequence of the specimens is shown in Figure 8.

Square specimens, 150 mm x 150 mm x 1.32 mm, were adopted for the impact tests. The latter were performed in a CEAST modular falling weight machine type MK3, equipped with a DAS 4000 data acquisition system, using a hemispherical steel impactor 15 mm in diameter and 2.1 kg in mass, which struck the sample at the centre. Different damage depths were produced in the material by varying the impact energy  $U$ , setting suitably the impact height. In particular, three energy levels  $U = 12$  J, 20 J and 36 J were adopted.

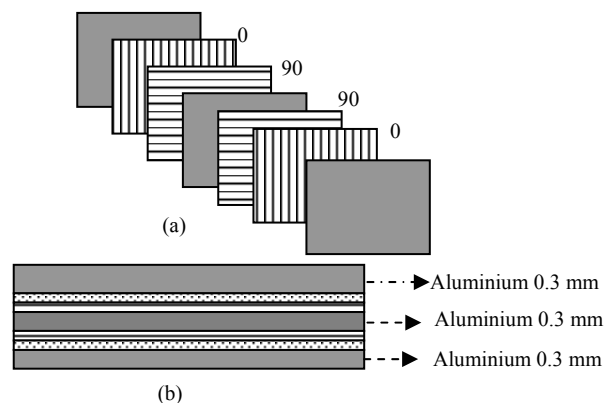


**Figure 8:** (a) Stacking sequence, and (b) cross section of the FML specimens examined.

## References

- [1] Dauphin, J. High Temp. Chem. Process 3, 139 (1994)
- [2] Baker, A. A., et al. Composite 2, 154 (1971)
- [3] Reinforced Plastics, September 1996, p.44.
- [4] Patè, F., Nouvelle Revue D'aeronautique et DiAstronautique, No.3, p.31 (1995).
- [5] Thomas, D. K., Plastics Rubber Intern. 8,53,(1983)
- [6] European Plastic News, p.34 February 1996.

[7] Savage, G., Polymers & Composites, p.617, October 1991

[8] Robinson, M., Carruthers, J., "Composites make tracks in railway engineering", Reinforced Plastics, November 1995, p.20.

# Chapter 4

## Electromagnetic characterization of Carbon Fiber Reinforced Polymers (CFRPs)

### Introduction

Carbon fiber reinforced polymers (CFRPs) are new advanced composite recently used in the aerospace structures. The well know properties that contribute to the success of composite within the industry application are weight reduction, corrosion resistance, high thermal stability, freedom of design, cost reduction and increased performance. Because these structures are exposed to impact loading (dropping of tool, stone, bird strike, etc.) non-destructive testing (NDT) to detect defects occurring in the structures is very important for safety reasons. Impacts are the main cause of delamination in composite reducing their residual strength by up 50%. Moreover, the low energy impacts often leave the top surface of the component unchanged but produce internal deformation and matrix breaking of the back surface of the component. The heterogeneous and anisotropic composition makes such materials complex structures to inspect using conventional non-destructive testing method. A reasonable alternative to the conventional NDT technique is represented by the superconducting quantum interference device (SQUID), that thanks its high magnetic field sensitivity even in a low frequency range, can be considered as suitable sensor for detection of defects in CFRPs materials.

In this chapter a characterization of electromagnetic and electromechanical properties of CFRPs material by using eddy current based HTS dc-SQUID magnetometer is performed. Unidirectional and cross-ply  $[(0/90), \pm 45]_{3s}$  CFRPs with thickness ranging from 2mm to 4mm have been analysed. The electromagnetic non destructive and contact less technique based on SQUID sensor has been mainly applied. The results obtained using the SQUID prototype have been compared and joined with results of traditional diagnostic methods such as Eddy Current with induction coil and Ultrasounds.

In the first section a preliminary evaluation of the electrical conductivity has been carried out using the traditional four probe method. The electrical resistance variation respect to thickness and the conductivity values for the unidirectional and cross ply material has been compared.

In the second section electromagnetic properties such as the shielding capability of the CFRPs respect to electromagnetic wave has been investigated. The SQUID magnetometer has been located behind the test sample, and the transmitted electromagnetic dipole signal through the samples has been revealed.

In the third section the electromechanical properties has been studied using the four probe technique and the SQUID based prototype. A bending stress has been applied to the test sample and the variation of magnetic field has been measured during a loading cycle. The results of the SQUID system have been compared with the electrical resistance variation measured using the traditional four probe technique.

In the fourth section the characterization of damage produced by impact loading using the eddy current technique based on SQUID magnetometer is presented. The damage process in the CFRPs plays an important role especially for the aeronautical and aerospace applications. Therefore, it is very useful to understand the mechanical response of these materials after impact loading produced during service and manufacture time. For this reason defects similar to the real damage, caused by the hail or bird strikes, have been made artificially. To characterize damage from the early stage (not visible to naked eyes) to the sample perforation a range of impact energy from 1.8 J to 16 J have been considered.

The fifth section has been dedicated to the magnetic field imaging representation used to localize defects in the composite structures. It has been demonstrated that the maps of the magnetic field data don't give directly information about the extension and the local position of the structural deformations. Therefore, some techniques, such as the Artificial Neural Network, have been presented to overcome this limitation. The advantages and the drawbacks of this method will discuss. Moreover, the damage localization using the magnetic field flux representation is reported. The results obtained applying the magnetic flux imaging has been compared with the results achieved using traditional non destructive techniques such as Eddy Current with induction coil and Ultrasound.

The last section deals with the analysis of the interphase fiber-matrix using an Atomic Force Microscopy (AFM). This analysis aim to understand the relation between the damage process of the CFRPs and the deformation of the fibers into the epoxy matrix.

## 1. Electrical Conductivity

An estimation of CFRPs electrical conductivity using the conventional four-probe technique has been carried out. This is a very simple and assessed method to measure the electrical conductivity. The four probes consisted of two outer current probes that fed d.c current inside the sample and two inner voltage probes for the voltage measurement. The connection between the current probes and the test samples is realized by two copper electrodes located at the ends of the sample as shown in figure 1.

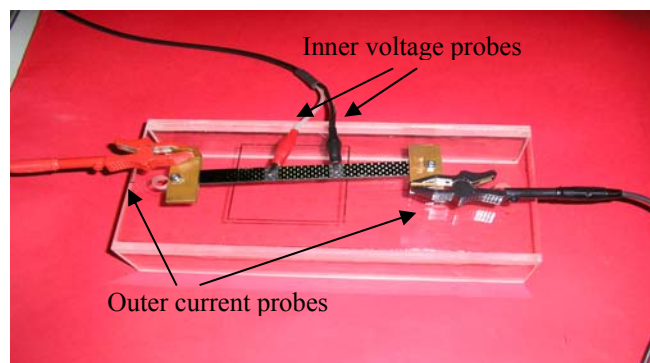


**Figure 1:** Configuration of the four probes.

It is necessary to remove the insulating coating layer from the sample surface to obtain good connections between the electrodes and the fibers. Increasing the d.c. current using a current supply HP 3245, the I-V characteristic has been obtained measuring the voltage by means of HP 34401. Then, thanks the linear trend between the I and V, applying the Ohm law, the electrical resistance  $R$  has been calculated. Let  $L$  and  $S$  the length between the two inner voltage probes and the cross-section of the test sample respectively, the resistivity can be written as:

$$\rho = \frac{RS}{L}$$

where the electrical conductivity is:

$$\sigma = \frac{1}{\rho} = \frac{L}{RS}$$

in the above equation the unit are  $\rho = [\Omega \cdot m]$  and  $\sigma = [1/(\Omega \cdot m)] = [S/m]$ .

The unidirectional test samples with dimensions of 29mm x 12.5mm x 2.1mm has been used to measure the longitudinal ( $0^\circ$  direction) and transverse ( $90^\circ$  direction) fiber electrical resistance. In the first case the current is injected in the fiber direction, while to measure the resistance at  $90^\circ$  the current flow perpendicularly to fibers orientation. In figure 2(a) the I-V characteristic related to the longitudinal resistance of the unidirectional sample is reported.

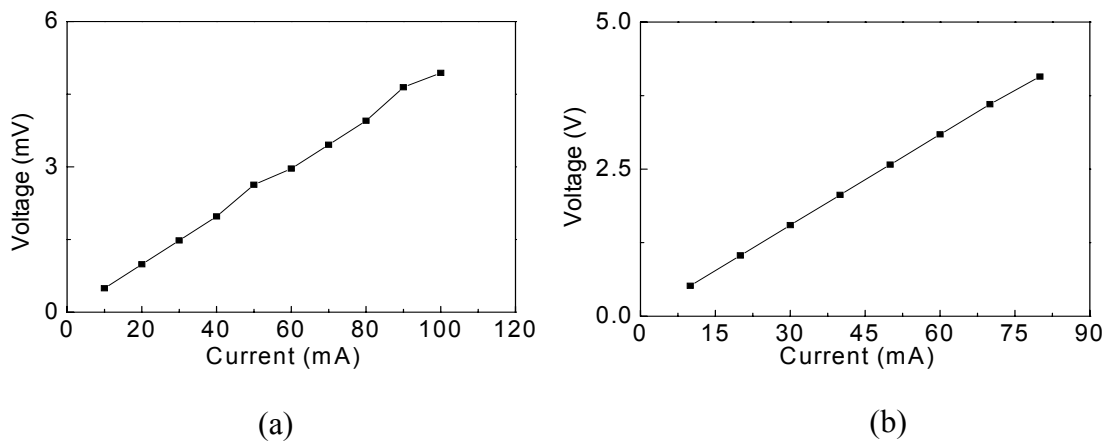


**Figure 2:** V-I characteristic of unidirectional sample along the fiber direction (a) and transverse to the fiber direction.

The linear fit of the voltage versus current curve gives the resistance value. The electrical resistance value in the  $0^\circ$  direction is  $0.050\Omega$  with a conductivity of  $22095 \pm 5\% S/m$ .

In the same way, the transverse resistance and conductivity of the unidirectional CFRPs have been estimated. In this case the V-I characteristic, obtained injecting the current perpendicularly to the fibers, is shown in figure 2(b). The resistance is  $R=51\Omega$ , and the conductivity is  $\sigma=21.4 \pm 5\% S/m$ .

The difficulty of the current to flow through the insulating matrix is reflected by the lower transverse conductivity value respect to the longitudinal value, due to the current path along the fiber direction. The results demonstrate the low electrical conductivity of the CFRPs respect to the metallic material and especially their electrical anisotropy due to the carbon fiber orientations.

The measurement of the cross-ply resistance has been performed with the same technique applied above.

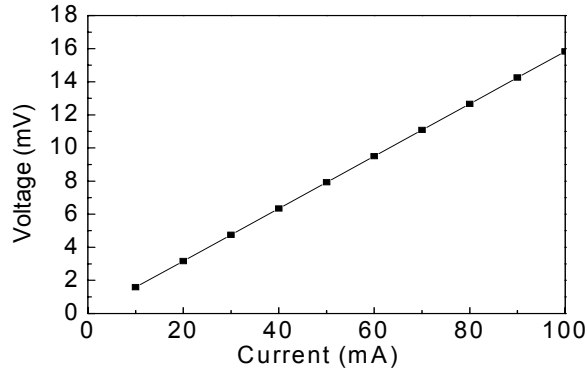


**Figure 3:** V-I characteristic for cross-ply sample.

In figure 3 the I-V of the cross-ply is shown and the corresponding linear fit gives a resistance of  $R=0,16\Omega$  and a conductivity  $\sigma = 7633 \pm 5\% S/m$ . It is important to note that in this case is not possible to distinguish transverse and longitudinal resistance because of different fiber layers orientations. In each layer the injected current goes through different resistance value, so that the measured conductivity could be considered as an average value, produced by the current that can flow between the electrodes. The experimental results related to the resistance and the conductivity of the unidirectional and cross-ply samples are summarized in Table1.

**Table1:** Summary of the electrical properties of unidirectional and cross-ply composites.

Specimen	Resistance ( $\Omega$ )	Conductivity (S/m)
Unidirectional	$R_{longitudinal}= 0.050$	$\sigma=22095$
Unidirectional	$R_{transverse}= 51$	$\sigma = 21.4$
Cross-ply	$R_{mean}= 0.158$	$\sigma =7633$

The results shown in the Table 1 reveal the CFRPs anisotropic electrical conductivity that depends on the different fibres orientations respect to the current direction. The resistance and conductivity values of the cross ply samples are included in the transverse and longitudinal unidirectional because of their anisotropy fiber configuration. It is interesting to note that the electrical resistance of cross ply depends on samples thickness. The measured test specimens have a length of 60mm and a width

of 5mm and 12mm. For each width the thickness is 2mm, 3mm and 4mm. In figure 4 the V-I characteristics for these samples are reported.

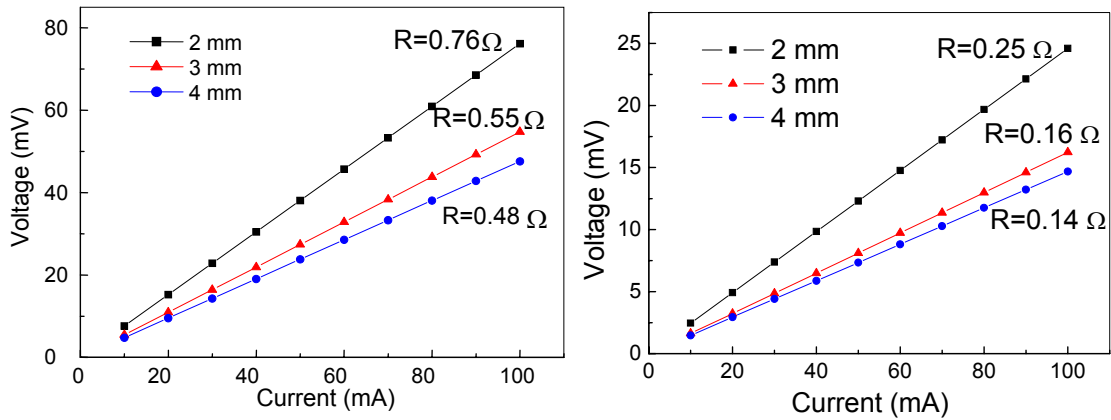


**Figure 4:** I-V curve for cross-ply samples with width of 5mm (left) and 12mm (right). The resistance values for each thickness are reported.

In Tables 2 and 3 the electrical properties for the tested specimens are summarized. It could be noted that increasing the thickness the electrical resistance decreases for both the samples with width of 5mm and 12mm.

**Table 2:** The electrical resistance and conductivity of cross-ply composites 5mm width

Thickness (mm)	Resistance ( $\Omega$ )	Conductivity (S/m)
2	0.76	7882
3	0.55	7310
4	0.48	6306

**Table 3:** The electrical resistance and conductivity of cross-ply composites 12mm width

Thickness (mm)	Resistance ( $\Omega$ )	Conductivity (S/m)
2	0.25	10163
3	0.16	10097
4	0.14	8509

Moreover, the broader sample the higher the conductivity for each thickness. These results demonstrate that the electrical properties of the CFRPs could depend on the specimens' thickness.

It is important to note that the results obtained applying the four-probe method are an approximation of the CFRPs electrical resistivity produced by only the composites conducting components. Taking into account that the matrix is characterized by a very low conductivity value  $\sigma = 10^{-8}$  S/m [1], the estimated resistance value depends mainly on the presence of the carbon fibers. It means that the fibers length and both the volume

content of fibers and their orientation respect to the direction in which the current is injected are very important to characterize electrically these materials [2,3,4]. Even if the results obtained using the four probe method depends on the sample fiber orientation respect to the injected current direction, they are confirmed by results reported in literature obtained using different measurement techniques [5].

## 2. Electromagnetic properties

The value of the electrical conductivity is useful to estimate the CFRPs penetration depth  $\delta$  that is very important when an electromagnetic field invests the material. According to the Maxwell equations the penetration depth of e.m. plane wave inside a material is described as [6]:

$$\delta = \frac{1}{\sqrt{\mu \cdot \pi \cdot \sigma \cdot f}}$$

where  $f$  is the frequency of the e.m. source,  $\sigma$  is the electrical conductivity of the material and  $\mu$  the magnetic permeability . In Table 4 the penetration depth in a frequency range from 25 kHz to 3MHz for the unidirectional (considering the longitudinal conductivity) and cross-ply samples are reported.

**Table 4:** Penetration depth of unidirectional and cross-ply composites.

Frequency	$\delta$ (mm) Unidirectional	$\delta$ (mm) Cross-Ply
25 kHz	21.3	36
600 kHz	4.4	7.4
1 MHz	3.4	5.7
3 MHz	1.9	3.3

For each frequency the unidirectional CFRPs have a penetration depth value lower than the cross-ply samples, because of their higher electrical conductivity. The decreasing of the penetration depth increasing the frequency means that the CFRPs could be considered an electromagnetic interference (EMI) shielding material, in appropriated frequency range.

When an e.m. wave goes through a material three events are possible: transmission, reflection and absorption. Reflection is due to the impedance mismatch between the air and the sample at the frequency of interest; absorption happens because of the energy dissipation during the interaction of the e.m wave with the material. Because of the

inhomogeneities within the material multiple reflections are possible too. Typically, to evaluate the shielding capability of a material the EMI shielding effectiveness (SE) is defined as:  $SE(dB)=10 \log_{10}(I_i/I_t)$  where  $I_i$  and  $I_t$  are the intensity of the incident and transmitted beam, respectively. Concerning the SE definition, it follows that the higher the SE value in decibel, the less energy passes through the sample. In particular, it has already demonstrated [7] that the higher the resistivity, the lower the shielding effectiveness and the higher the attenuation upon reflection. Taking into account the values of the resistivity reported in Table 4, it is possible to note that the unidirectional CFRPs can be considered more conducting, more reflecting and more shielding than the cross-ply samples.

Using the Eddy Current technique based on SQUID magnetometer some experiments about the propagation of the electromagnetic wave through CFRPs materials have been carried out. The magnetic signal is produced by a dipole source represented by a wire-wound circular coil with a diameter of 5mm, positioned behind the test sample (see figure 5) and fed with a.c. current of 5mA at 15 kHz. At this frequency the e.m. wave skin depth is higher than the samples thickness. Using the SQUID magnetometer located few millimetres far from the sample surface, the in plane component,  $B_x$ , of the magnetic field, generated by the dipole source, has been detected along a 40 mm length scanning.

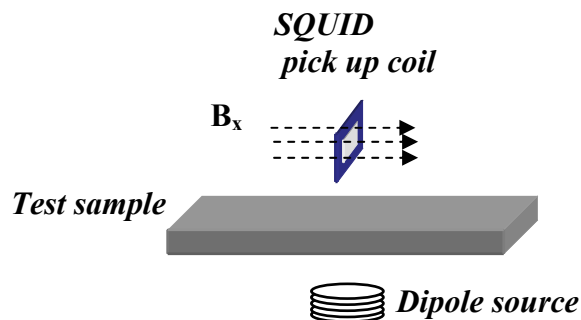


**Figure 5:** Schematization of the experimental set up used to measure the electromagnetic shielding properties of CFRPs.

The dipole source signal in air and its propagation through unidirectional and cross-ply samples, with different thickness, have been measured and the reflected percentage of the magnetic source signal is deduced.

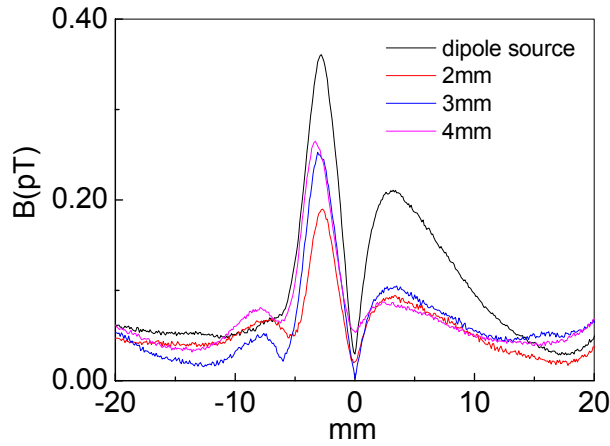


**Figure 6:** Magnetic signals of the dipole source and its propagation through cross-ply samples with thickness of 2,3 and 4mm.

In figure 6 the comparison of the dipole source signal in air and through cross-ply CFRPs with thickness of 2mm, 3mm and 4mm, have shown.

The black line represents the in-plane component of the magnetic field due to the dipole source measured in air. This signal is consistent with the magnetic field signal obtained using the analytical equation:

$$\vec{B}(\vec{m}, \vec{r}) = \frac{\mu_0}{4\pi} \left[ \frac{3(\vec{m} \cdot \vec{r}) \cdot \vec{r}}{r^5} - \frac{\vec{m}}{r^3} \right]$$

(with  $\vec{m}$  the dipole momentum of the coil) that gives the in plane component of magnetic field expressed as:

$$B_x = \frac{\mu_0}{4\pi} \frac{3mxz}{(x+r)^{5/2}}$$

It could be noted that increasing the thickness of the specimens the attenuation increases. In other words the signal transmitted through the sample prevails on the reflected signal so the lower the amplitude the higher the reflection. In particular, the peak-to-peak difference between the maximum amplitude of the dipole source signal in air respect to the maximum amplitude of the propagated signal, gives the amplitude of the reflected signal of each thickness.

In figure 7 the reflected and propagated magnetic field percentage versus the cross-ply sample thickness is reported. Increasing the thickness the reflected signal decreases as a consequence the transmitted wave increases, so the higher the thickness the less reflection.

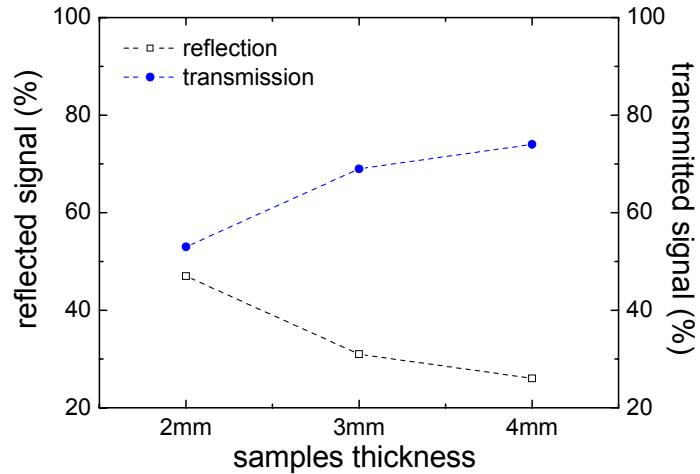


**Figure 7:** Reflected and transmitted magnetic field percentage for cross-ply samples with thickness of 2,3 and 4mm.

In the previous paragraph, it has been demonstrated (Table 2 and 3) that the 4mm cross-ply sample has a conductivity lower than the 2mm and 3mm thick samples, therefore its reflection capability is lower. Moreover, it can be interested to evaluate the shielding capability of the unidirectional composites which have an anisotropic conductivity. Changing the orientation of the SQUID magnetometer respect to the fiber orientation, two configurations have been realized. In the first one, the SQUID sensitive area is parallel to the fibers, and the propagation due to the longitudinal conductivity is measured, In the second one, the SQUID sensitive area is normal to the fibers. These two configurations are called longitudinal and transverse, respectively, and they are shown in figure 8.

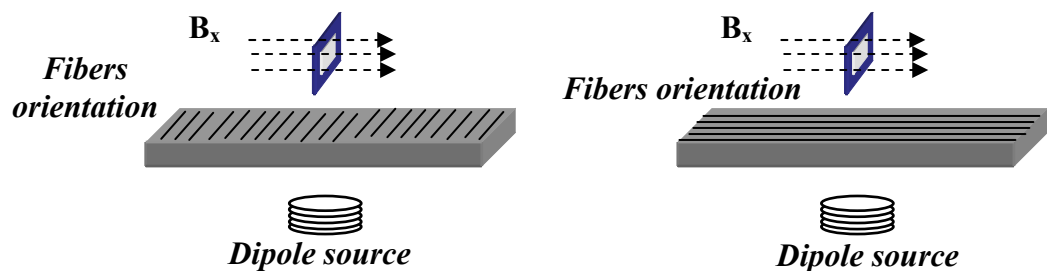


**Figure 8:** Unidirectional CFRPs in the longitudinal (left) and transverse(right) configuration.

In figure 9 the comparison of the magnetic source signal in air and attenuated by the unidirectional CFRPs in longitudinal and transverse configurations are shown.

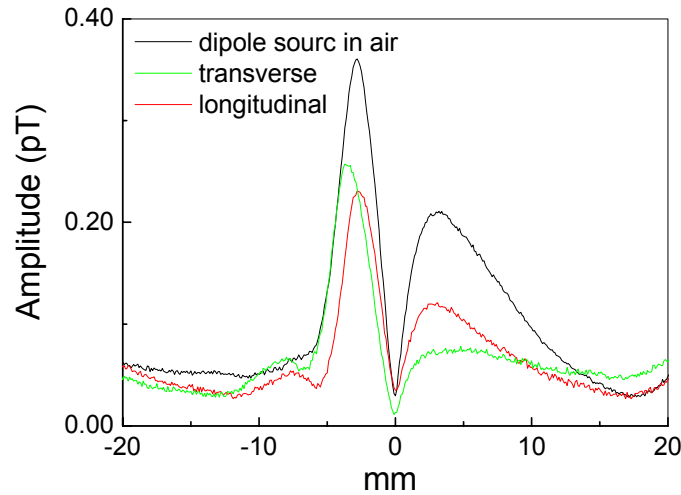


**Figure 9:** magnetic signals of the dipole source and its transmitted intensity through unidirectional CFRPs for the longitudinal and transverse configurations.

The amplitude of the transmitted wave due to the transverse conductivity is higher than the amplitude due to the longitudinal fibers orientation. In other words, the transverse configuration reflects less than the longitudinal configuration, because of its lower conductivity due to the high resistance between the fibres. As a result the in plane components of the electromagnetic field are reflected with different intensity, because of the electrical anisotropy of the unidirectional samples. It is also interesting to compare the magnetic signal propagation for the two unidirectional configurations and the cross-ply samples.

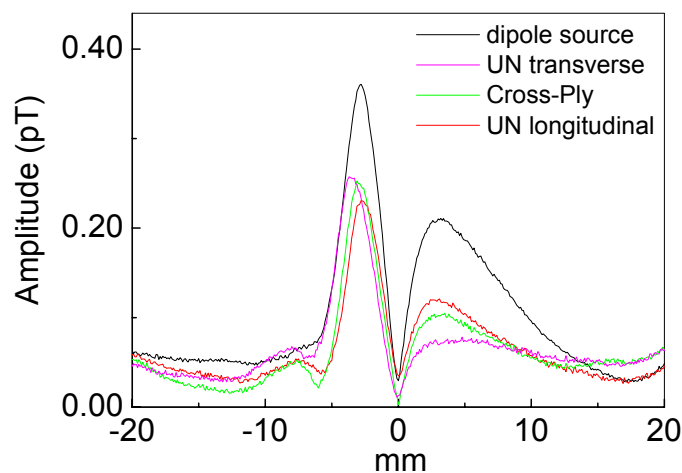


**Figure 10:** Comparison of magnetic dipole source in air, its transmitted intensity through unidirectional longitudinal and transverse CFRPs configurations, and in presence of a cross-ply sample.

As expected the cross-ply signal is included between the two unidirectional configurations, so it can be concluded that the unidirectional composite reflect much more than the cross-ply when the in plane component of the magnetic field orthogonal to the fiber orientation is considered. These results are shown in figure 10.

In Table 5 are summarized the value of the reflection and transmission for the three different fiber orientation: longitudinal, transverse and cross-ply.

**Table 5** : percentage of the reflected and transmitted magnetic field

<b>Fiber orientation</b>	<b>Transmission</b>	<b>Reflection</b>
Unidirectional longitudinal	87%	13%
Cross-ply	86%	14%
Unidirectional transverse	84%	16%

Moreover, the results related to the shielding capability of the CFRPs demonstrate the high sensitivity of the SQUID sensor to distinguish the anisotropic very low conductivity of the unidirectional composites.

It could be noted that thanks the shielding capability of the CFRPs, these materials can be considered useful for lightning protection, electrostatic dissipation and as a microwave waveguides.

### **3. Atomic force microscopy (AFM) analysis**

The Atomic Force Microscope (AFM ) is being used to solve processing and materials problems in a wide range of technologies affecting the electronics, telecommunications, biological, chemical, automotive, aerospace, and energy industries. The materials being investigating include thin and thick film coatings, ceramics, composites, glasses, synthetic and biological membranes, metals, polymers, and semiconductors. The AFM is being applied to studies of phenomena such as abrasion, adhesion, cleaning, corrosion, etching, friction, lubrication, plating, and polishing. By using AFM one can not only image the surface in atomic resolution but also measure the force at nano-Newton scale. The principles on how the AFM works are very simple. An atomically sharp tip is scanned over a surface with feedback mechanisms that enable the piezo-electric scanners to maintain the tip at a constant force (to obtain height information), or

height (to obtain force information) above the sample surface. Tips are typically made from  $\text{Si}_3\text{N}_4$  or Si, and extended down from the end of a cantilever. The nanoscope AFM head employs an optical detection system in which the tip is attached to the underside of a reflective cantilever. A diode laser is focused onto the back of a reflective cantilever. As the tip scans the surface of the sample, moving up and down with the contour of the surface, the laser beam is deflected off the attached cantilever into a dual element photodiode. The photodetector measures the difference in light intensities between the upper and lower photodetectors, and then converts to voltage. Feedback from the photodiode difference signal, through software control from the computer, enables the tip to maintain either a constant force or constant height above the sample. In the constant force mode the piezo-electric transducer monitors real time height deviation. In the constant height mode the deflection force on the sample is recorded. The latter mode of operation requires calibration parameters of the scanning tip to be inserted in the sensitivity of the AFM head during force calibration of the microscope. The primary purpose of these instruments is to quantitatively measure surface roughness with a nominal 5 nm lateral and 0.01nm vertical resolution on all types of samples. Depending on the AFM design, scanners are used to translate either the sample under the cantilever or the cantilever over the sample. By scanning in either way, the local height of the sample is measured. Three dimensional topographical maps of the surface are then constructed by plotting the local sample height versus horizontal probe tip position [8].

In this thesis a Multi Mode AFM (Atomic Force Microscopy) Digital Instruments Nanoscope IIIa® has been used to investigate the tomography of carbon fiber surfaces and to analyse interphase between the fibre and the matrix of the CFRPs test samples. The application of this technique aim to understand what happen in composites between the matrix and the fiber from a microscopic point of view. The AFM microscopy has been used in the configuration of *Contact Mode* (CM) and *Tapping Mode* (TP) [8-10]. In the first case the cantilever is in contact with the surface sample so the display of the surface roughness of fibers as a function of the position is obtained. In the TP Mode the amplitude of the deflection of an oscillating cantilever tip is used to obtain the sample surface image. In both configurations the vertical resolution is few Angstrom and the spatial resolution in x-y plane is about few nanometres. The test samples analysed using the AFM technique was cut from the specimens investigated by using the electromagnetic technique. In particular unidirectional and cross-ply samples of dimensions 10 mm x 10 mm and 2 mm thickness were positioned under the cantilever.

In figure 11(left) the scanning surface 10 x 10  $\mu\text{m}$  of a virgin cross-ply (0/90) is shown. The fibers texture due to the fiber orientation which characterized the composite layer is evident.

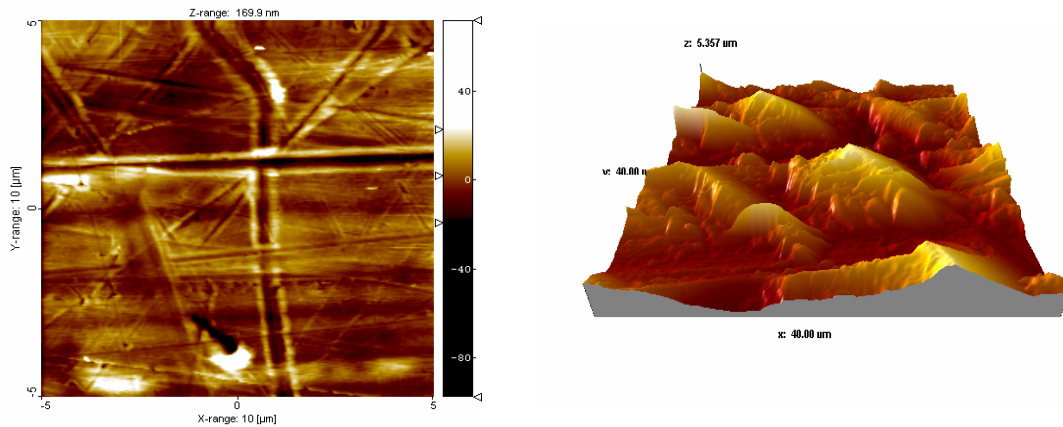


**Figure 11:** (left) 10 x 10  $\mu\text{m}$  surface map of virgin sample, (right) 3-D 40 x 40  $\mu\text{m}$  map of an internal layer measure in contact mode.

To investigate the internal characteristic of the matrix-fiber interphase the sample analysed in figure 11 (right) was severed using a milling machine and the surface of an internal layer with the fiber orientation of  $45^\circ$  was obtained . In figure 11 (right) the AFM-CM 3-D image of cross-ply internal layer is reported. In this case it is very difficult to distinguish the fiber orientation respect to the surface roughness. The latter play an important role in the AFM analysis, in fact, they cause high bending of the cantilever in z direction so that a lost of its sensitivity. For this reason it is not possible to obtain an image that reflects the surface characteristics such as the fiber orientation and fiber-matrix adhesion. To overcome this problem a metallographic polishing of the samples surface has been performed. The samples have been fixed on the honing machine support (Buehler, Minimet 1000<sup>TM</sup>) using a thermoplastic resin, that could be removed from the sample after the polishing process without any structure alterations. The first stage of the polishing process was performed by means of grinding discs with grain of 200, 400 and 800 mesh applied with a weight of about 6 lbs and a speed of 10 mm/s. To rough the sample surface 5 cycles of 3 minutes with the grinding discs of 200 meshes was applied, after 3 cycles of 3 minutes using the other grinding mesh were carried out. The last step of the polishing was represented by the surface clining, using oily solutions made of alumina micrograins with dimensions of 3  $\mu\text{m}$ , 0.1  $\mu\text{m}$  e 50 nm, dissolved on velvet discs, and applied for each solution with a weight of 3 lbs and during 2 cycles of 3 minutes.

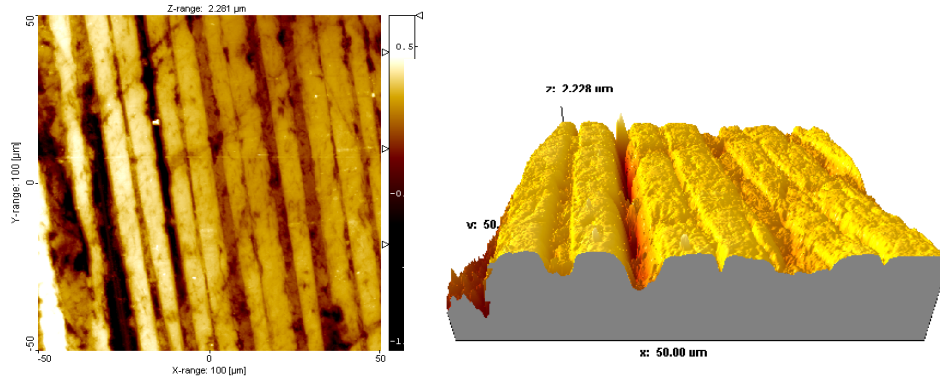


**Figure 12:** (left) unidirectional 100 x 100 μm, (right) 3-D imaging 50 x 50 μm, in contact mode, of a sample surface after a metallographic polishing.

In figure 12 the 2-D and 3-D AFM CM analysis of a polishing unidirectional composite are shown. The orientation of the fiber is distinguishable and the estimated fiber diameter is from 4.5 to 6 μm. The holes between the fibers probably are due to the polishing process that could notch the epoxy matrix, more brittle than the carbon fibers. The latter appear levelled in the plane x-y because of the milling process, therefore it is not possible to evaluate accurately their diameter. These results demonstrate that even if the AFM analysis is capable to reveal the fiber orientations and matrix-fiber interface integrity, the necessary polishing process, to delete the high roughness of the surface, can change the fiber surface properties. To overcome this limitation some tests have been performed with high accuracy to establish the best polishing process. It was necessary to minimize the drawbacks of the polishing process on the fiber–matrix interphase, when the damage due to loading stress on the CFRPs will be studied. The AFM imaging of samples perforated by a quasi static loading has been carried out.

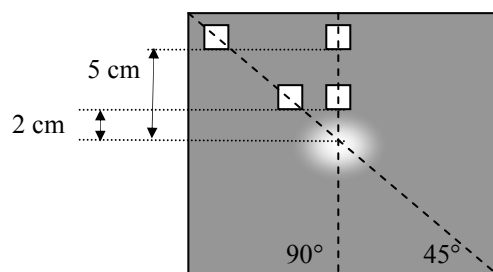


**Figure 13:** Picture of the damage sample analysed using AFM technique. The white squares are the inner layers cut from the punched sample with fibers oriented at 45°. They are at 2mm and 5mm far from the center of the defect in the 45° and 90° direction.

In figure 13 the picture of the damaged specimen is shown. The test specimens used in the AFM analysis are represented by the white squares, cut in the 90° and 45° direction at 2 cm and 5 cm from the edge of central defect. The analysed layers were internal layers with the fiber orientation of 45°.

The aim of this analysis is to understand the damage propagation in an internal layer with fiber orientation of 45°, respect to the direction of 90° and 45°. In figure 14 the comparison between the 50x50 μm AFM imaging of the internal layer positioned at 5mm far from the defect in the two directions, are reported. It could be noted that in both cases the fibers don't present fractures and the interphase matrix-fiber integrity is preserved. It means that at 5 cm far from the defect, even when there is a perforation of the sample, there are not alteration and degradation of the fiber and the matrix-fiber adhesion.

In fact, the fiber structure is distinguishable and any breaking or distortion are present especially in the 45° direction (figure 14(right)).

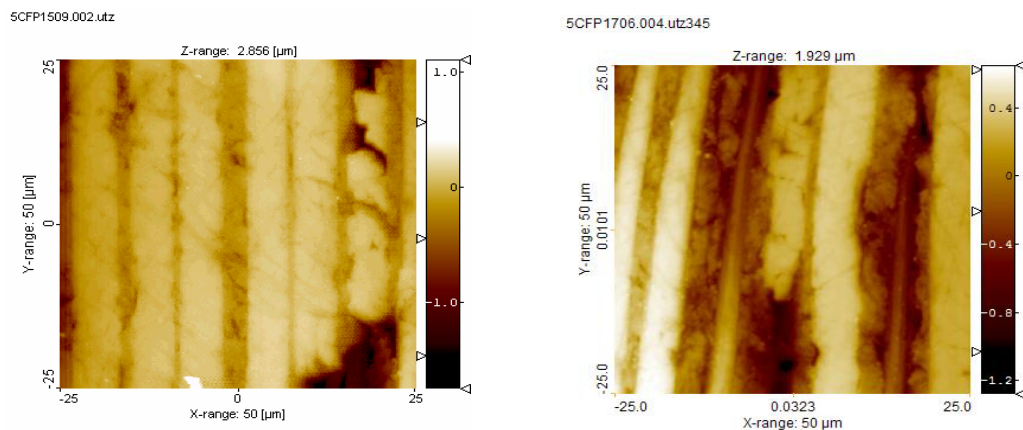


**Figure 14:** AFM imaging of samples cut at 5mm from the defect in the direction 90° (left) and 45° (right).

Figure 43 shows the comparison between the two directions (45° and 90°) of the specimens cut at 2 cm far from the defect. In this case the sample at 90° doesn't show fiber rupture or fiber dislocation respect to the matrix.

On the other hand, at 45° there is a changing of the fibers position of about few degrees. It means that in the direction parallel to the fiber orientation (45°) the defect propagation degrades the fiber-matrix adhesion. In particular, the matrix that is more brittle than the carbon fiber is removed and as a result the fiber can change its position.

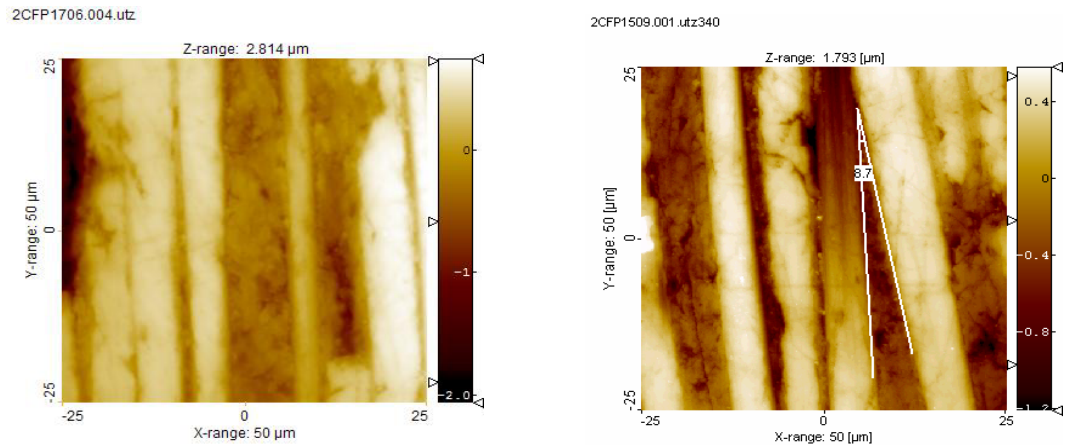


**Figure 15:** AFM imaging of samples cut at 2mm far from the defect in the direction  $90^\circ$  (left) and  $45^\circ$  (right).

In figure 15 (right) the evident displacement of the fiber is about  $8.7^\circ$ . This result demonstrates that the perforation of the sample produces a modification of the interphase fiber/matrix even far from the impacted point. The AFM imaging in Figure 15 (b) shows that the damage produces a fiber displacement that generates, in the same time, an overlapping and separation of fibres. This alteration of the interphase fiber/matrix is the basic principle of the electromechanical effect presents in the CFRPs composite [11]. The electromechanical effect asserts that the fibers can reduce or increase their distances, consequently a change of resistivity arises. It is very interesting to note that the results obtained with the AFM technique demonstrate that an applied loading on a CFRP sample does not produce necessarily fiber rupture, but in the early stage it can degrade the matrix and change the fiber positions without their breaking. Further important information arises from the AFM analysis concerning the damage propagation respect to the fiber orientation. The results highlight that in the cross ply composite the damage moves forward the fiber orientation, for example, in a layer characterized by a fiber orientation at  $45^\circ$  the major damage of this layer is detected along the fiber direction ( $45^\circ$ ).

The AFM analysis demonstrates an evident propagation of the damage inside the composite structure. Moreover the severity of the damage depends on the position and the fiber orientations. In particular the alteration of the composite mechanical and electrical properties is due not only by fiber breaking, but also by fiber displacements, that produce a variation of the electrical resistivity and a decreasing of the stiffness.

#### 4. Electromechanical effect

The CFRPs material are widely used in aerospace and aeronautical industry thanks the advantages that their offer such as excellent mechanical behaviour, good damage tolerance, high strength and rigidity with low weight, good corrosion resistance and suitability for the production of complex-shape components with reduced manufacture time. The composite structures are often subjected to cyclic loading that causes damage and material property degradation in a cumulative manner. Many researchers [12,13] have investigated the relation between the mechanical damage and the change of electrical conductivity under the tensile and fatigue stress. The four-probe technique and the SQUID based prototype have been applied to monitor the electrical resistivity changing respect to the fatigue loading of CFRPs cross-ply [0/90]. The bending stress has been applied to the sample by turning two screws located at the opposite side of the specimen (figure 16). The mechanical test system is made of a wood basement and brass gauge. Those materials have been preferred to the traditional steel to reduce as possible as the residual magnetic field due to the tensile stress in the system metallic components.

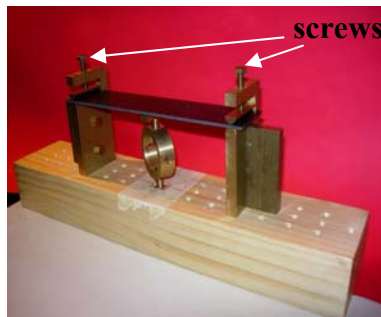


**Figure 16:** Mechanical test system.

The quasi-static loading was applied to the perpendicular direction of the sample surface, increasing the sample's bending, as shown in figure 17 (left). The bending stress produces in the specimen a tensile and compressive stress,  $\sigma_t$  and  $\sigma_c$ , respectively. Therefore, in each layer the distance between adjacent carbon fibres changes. In particular, tensile stress causes this distance to increase, as a result the electrical resistivity increases, while compressive stress causes this distance to decrease, thereby decreasing the electrical resistivity. The effect described is called electro-mechanical effect in which the strain and the electrical resistance of CFRPs are coupled [2].

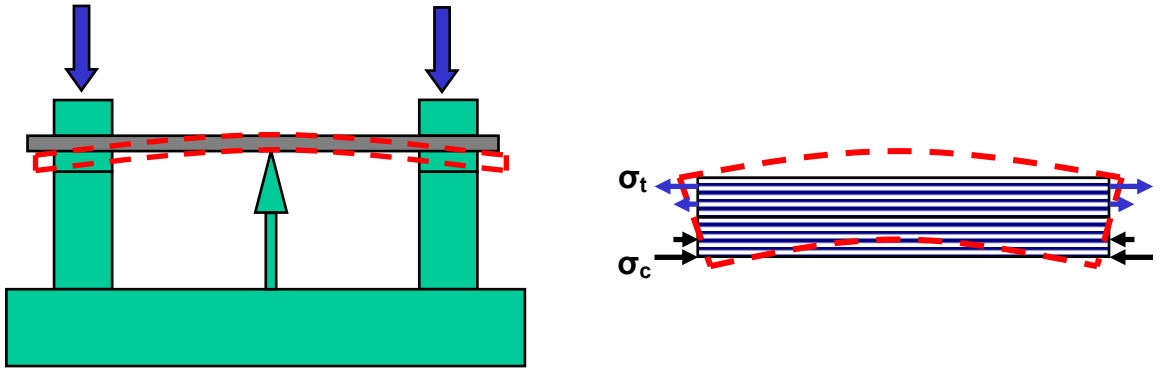


**Figure 17:** Bending stress applied to the sample

The sample's bending depends on the mechanical properties of the composite material, in this work its variation ranging from 1mm to 12mm.

In figure 18 the current-voltage (I-V) characteristics of a loaded and a virgin composite sample measured using the four-probe method are shown. The linear fit of these curves represent the electrical resistance before and after the loading. The electrical resistance of the virgin sample is 0.158 Ohm with an electrical conductivity of 7633 S/m +/- 5%, while after the loading the electrical resistance is 0.174 Ohm and the conductivity decrease to 7108 S/m +/-5%.

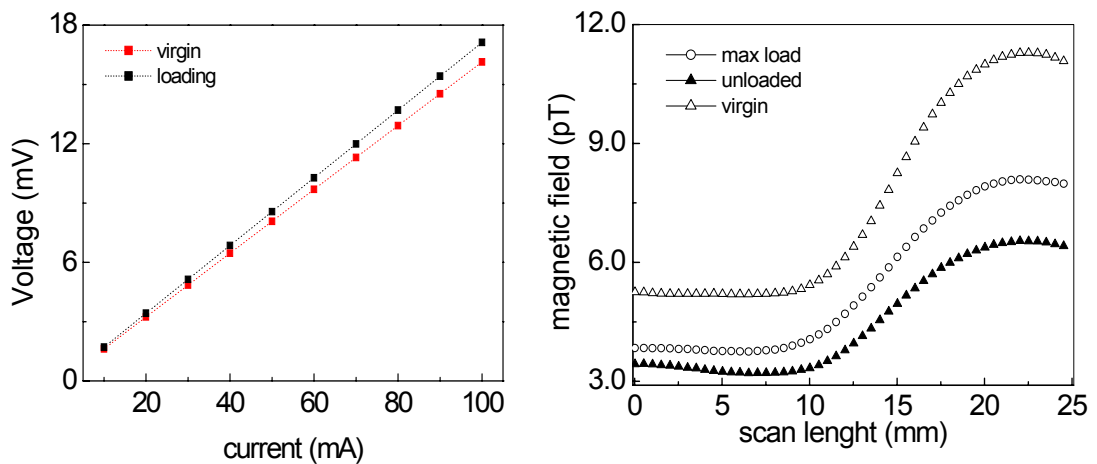


**Figure 18:** (left) Voltage vs Current characteristic of virgin (red points) and loaded (black points) multidirectional composites. (right) Line scans of the magnetic field signal measured during a loading cycle.

The magnetic field signals detected, using the SQUID magnetometer are shown in the Figure 18 (right). The signal represents a line scan with a length of 25 mm of virgin, loaded and unloaded sample, after one fatigue cycle. During the SQUID measurement the lift-off, between sample and sensor, at the borders of the specimen increased

symmetrically, while it remained constant in the middle of the sample. For this reason no tilting effect has been detected during SQUID measurements. The experimental results indicate that, changing the applied mechanical loading, the magnetic dipole signals show a variation both in the amplitude and in the slope of the inflection.

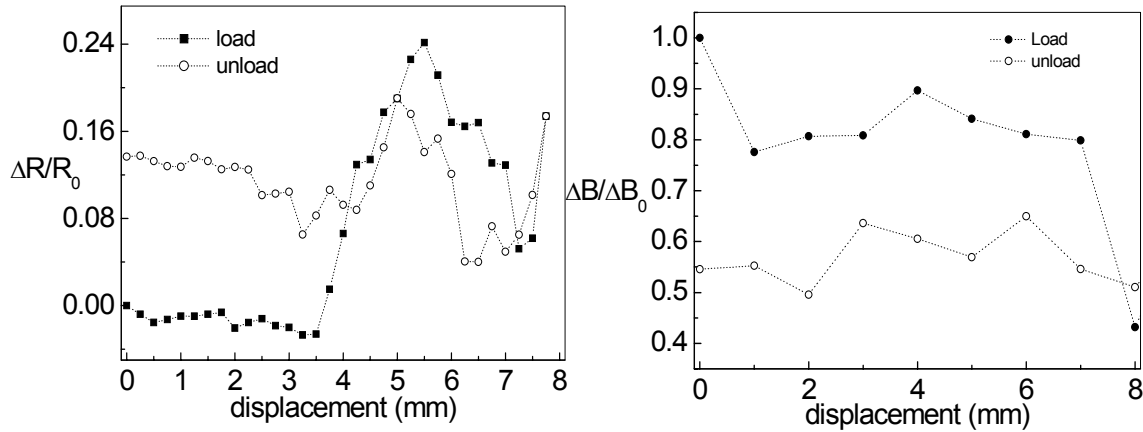


**Figure 19:** (left) Electrical normalized resistance of a multidirectional CFRP composite during a fatigue cycle measured with a four-probe technique. (right) Normalized magnetic field slope measured during a fatigue cycle on a CFRP composite.

The inflection that characterizes the virgin line scan is magnified to the presence of the brass punch behind the sample. The magnetic field produced by the induction coil passes through the whole sample thickness, so that the magnetic signal measured by the SQUID is the superposition of the field reflected by the sample and the brass punch. It is not possible to increase the frequency of the induction coil to penetrate only the sample because of the SQUID electronics limited frequency range. On the other hand, work in progress focuses on the realization of a punch made of non-magnetic material. In this work to delete the effect of the punch included in the magnetic field measurements a normalization has been used. In figure 19 (left) the normalized electrical resistance ratio  $\Delta R/R_0$ , where  $R_0$  is the electrical resistance of the virgin sample, has been measured during a loading cycle using the four-probe method. The reported electrical resistance ratio increases with the load and after a fatigue cycle it shows a hysteretic behaviour. The magnetic dipole slope  $\Delta B/\Delta x$  measured during a loading has been normalized to the slope value of the virgin sample  $\Delta B_0/\Delta x$ . The normalized SQUID measurements  $\Delta B/\Delta B_0$  are shown in figure 19 (right) and confirm the hysteretic behaviour, after a loading cycle. It is interesting to note that both the parameter  $\Delta R/R_0$  and  $\Delta B/\Delta B_0$  after a loading cycle are higher than their values at the

beginning of the fatigue cycle. Therefore the applied bending stress produces an irreversible changing of the fiber electrical resistance.

In particular, the electrical resistivity of a carbon fibre epoxy-matrix composite increases reversibly upon tension due to increase of the distance between adjacent fibres and decreases reversibly upon compression due to decrease of the distance between adjacent fibres [14].

In figure 20 ( left and right) the variation of electrical resistance, measured with the four-probe technique, and the  $\Delta B/\Delta B_0$ , evaluated using the SQUID prototype, versus the displacement up to 13mm, are reported, respectively. It is interesting to note that at 11mm an abrupt increasing of resistance and a corresponding decreasing of magnetic field variation, indicated with red arrows, happened .

It means that magnetic field measurements give the same results of the four probe technique, and the same trend of the  $\Delta B/\Delta B_0$  respect to the  $\Delta R/R_0$  reflect the proportionality between the magnetic field responses and the changing of the electrical properties due to the displacement of the fibres. This effect is due to a macroscopic fiber fracture that produces an irreversible damage of the material.

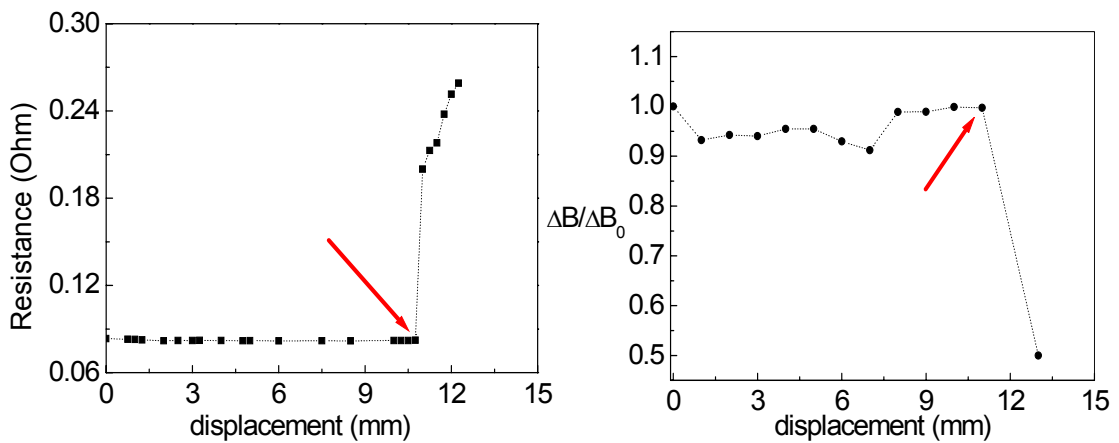


**Figure 20:** (left) Electrical resistance measurements increasing the loading. (right) Normalized magnetic field slope measured increasing the loading.

The comparison of the results obtained with the two techniques demonstrate that there is an inverse proportionality between the electrical resistance and the magnetic field signals produced by the eddy current inside the specimen. Since the conductivity is proportional to  $R^{-1}$  (with R the electrical resistance of the specimen), the fiber fracture produce a decreasing of the conductivity. As a result, the detected magnetic field reported in figure 20 (right), because of its direct proportionality with the current that

flow into the sample, decreases. The lower the magnetic field the higher the resistance. The SQUID based prototype measurements demonstrate that non invasive and contact less technique using SQUID sensors is capable to monitor the electro-mechanical effect also in very low conducting materials such as CFRPs.

The variation of the electrical resistance is very useful when loading produces in CFRPs damage not visible to naked eyes, such as delamination. The latter occur when the distance between the layers change, producing a variation of the fiber distance with no visible surface manifestation. As already mentioned, when an overlapping or a contact between the fibers occurs, the electrical resistance increases and the conductivity changes. The variation of the fiber positions and their residual stress causes a variation of the current inside the structure, both for injected or induced current, producing a variation of magnetic field detectable using non invasive contact less magnetic sensors like SQUID.

Until today the strain sensing in a CFRPs structure is commonly achieved by attaching to or embedding between the fibre layers one or more strain sensors, which can be piezoresistive, piezoelectric or other types of sensors. The embedded sensors are intrusive and degrade the mechanical properties of the composite, while attached sensors are less intrusive but they are not durable. For this reason the possibility to applied a contact less diagnostic method is very advantaged above all in the case of very complex composites structures. Moreover, the SQUID based prototype allows to monitor the components in real time, during the loading and the fatigue stress without any perturbation of the composites structure. The experimental results demonstrated that the electro-mechanical effect of CFRPs plays an important role because it allows to detect very little variation of the fiber resistance due to dynamic or static loading using electromagnetic technique based on high sensitive magnetic sensors.

## **5. Impact loading**

During the in service time the composite materials employed to made the aerospace component can be damage, for example, by runway debris, hail, maintenance damage (i.e., dropped tools) and bird strikes. The CFRPs are capable of absorbing the energy of impact thanks to the presence of a polymeric matrix that distributes the energy in the material. In this way the impact doesn't produce a direct perforation of the composite structure but may cause internal damage such as delamination (Fig.21). The presence

and the growth of delamination may produce severe stiffness reduction in the structure, leading to a catastrophic failure. The degree of damage depends on various factors, for example, the energy of the impact, the thickness of structures and the fibre orientation of layers.



**Figure 21:** Schematization of the impacted cross-ply CFRP at energy less than 1J (up). the delamination arises inside the sample and is confirmed by a microscopic inspection (down) [15].

It has already demonstrated in the previous section that thanks to the electro-mechanical effect the variation of fibre distance or fibre breakage changes the resistivity of the reinforced composite. Therefore, delaminations and fibre breakage alter the electrical conductivity of the material because of the variation of the current distribution in the composite. As a result a change of the corresponding magnetic signal happens. The low electrical conductivity and high anisotropy of CFRP composites generally doesn't allow conventional techniques, such as traditional ultrasound, thermography and Eddy Current with induction coils, to detect early stage damage in composite samples [16].

In this thesis some experiments have been carried out to detect early stage damage using a non-invasive and contactless technique using the Eddy Current SQUID-based prototype. The multidirectional CFRP test specimens were loaded at the centre by a hemispherical steel indenter, having a diameter of 12.7mm, and falling from different heights using a drop weight tower machine. Specimens with a thickness of 2mm were impacted with an energy level up to 12J, while 3mm and 4mm thick samples were damaged with impact energies up to 25J. In particular, we focus our attention on a 2mm thick sample impacted at 2.4 J, 7.8 J, 12J, and on a 4mm thick sample at 1.8 J. The variable depth of the damage, i.e. indentation, located at the centre of the sample was measured using a micrometer.

In figure 22 the phase of the magnetic field for the virgin ( $\alpha$  lines) and the damaged ( $\beta$  and  $\gamma$  lines) 2mm-thick samples are presented. The  $\beta$  and  $\gamma$  line scans were obtained by moving the sensor across the center of the defects due to an impact energy level of 2.4J and 12J, respectively. Each line represents a 60mm scan over the sample. The phase of

the magnetic field related to the damaged samples presents a variation along the line scan. The difference between the signal of virgin and damaged specimen could be predicted by the slope of the phase signal among the  $x=0$  coordinate. An inflexion that corresponds to a presence of damage characterizes the lines of impacted samples.

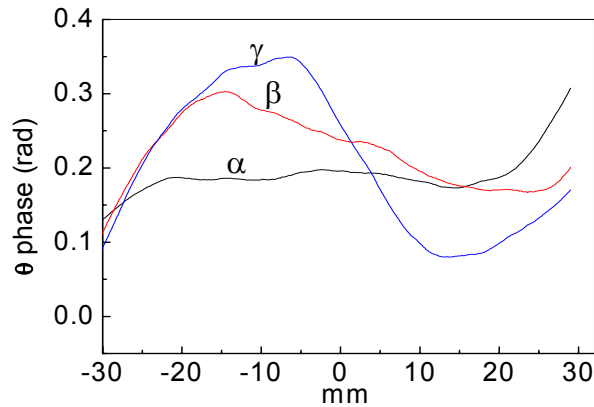


**Figure 22:** The phase of the magnetic field for 2mm thick specimens. ( $\alpha$ ) is the line-scan related to the virgin sample, ( $\beta$ ) and ( $\gamma$ ) are the line-scans of the damaged samples impacted at 2.4 J and 12 J respectively.

Moreover, for specimens with a visible damage the variation of the magnetic phase is correlated with the damage location. In particular, it has checked that the defect center coincides with the center of the inflexion ( $x=0$ ). It should be noted that the decreasing and increasing phase value, at the beginning and the end of the scan is purely edge effects. This is due to the comparable dimension of the specimen and the line-scan length. Experimental results demonstrate that the slope of the magnetic phase ( $d\theta/dx$ ) is correlated with the damage severity. In other words, it is possible to discriminate the different damage using the slope value, in fact the greater the slope value of the magnetic phase the more visible the damage and the greater the defect depth [17]. This result confirms the electromechanical effect presented by the carbon fibers. The slope  $d\theta/dx$  represents the variation of magnetic field due to the alteration of the electrical properties of the sample, due to the displacement of the fibers after an impact.

In Figure 23 (a) the trend of the slope value against the impact energy levels is shown. For each thickness (2,3 and 4mm) increasing the impact energy the slope value increases. In the case of 2mm thick samples there aren't slope values for energy higher than 12J because the specimens are already perforated, as is evident from an inspection of the sample.

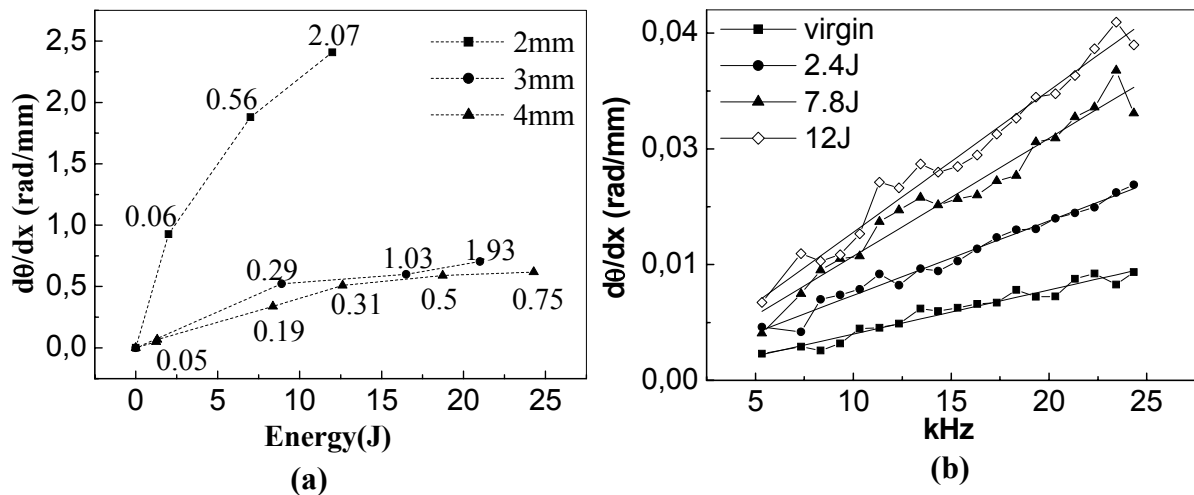


**Figure 23:** (a) slope of the phase of the magnetic field versus the impact energy level for 2mm, 3mm and 4mm thick specimens. In correspondence of each slope value the defect depth or indentation (in mm) is reported; (b) slope of the phase of the magnetic field versus frequency of the excitation coil for the 2mm thick samples impacted at different energy levels. The error bars related to the slope value are about 2%.

Comparing the slopes for each energy level, the values for the 2mm thick samples are always higher than those for the 3mm and 4mm thick samples. It is reasonable that specimens with small thickness are more brittle than samples with a bigger thickness, for this reason also comparable impact energies produce higher indentations in the 2mm thick specimen. The slope is similar at different value of indentations in the case of the 3mm and 4mm thick samples. In other words, composites with smaller thickness have a lower mechanical tolerance than specimens with bigger thickness. Probably a threshold value of the thickness exists between 2mm and 3mm that discriminates the mechanical response of the loaded CFRPs, and for this reason in specimens with a thickness above this threshold the magnetic response became similar. It should be noted that the experimental results shown in figure 23(a) don't depend on the particular frequency chosen for the excitation coil. As shown in figure 23(b) the slope of the magnetic phase measured by the NDE SQUID based system follows a linear trend versus the frequency of the excitation coil in the range 5kHz-25kHz.

It has already demonstrated using the SQUID based prototype that different steps characterize the damage in CFRP samples with a thickness of 4mm [18].

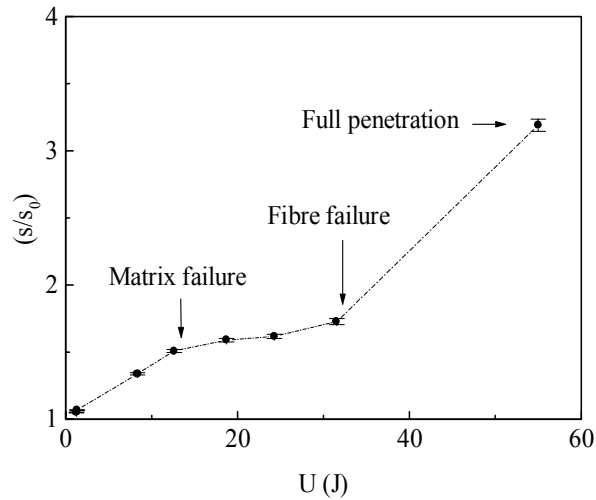


**Figure 24:** Non-dimensional slope,  $s/s_0$ , against imparted energy,  $U$  [18].

In figure 24 the variation of the normalized slope of the magnetic field signal versus the impact energy is reported. At the beginning, the CFRP materials offer an elastic behaviour up to an impact energy level of about 1.6 J; above that matrix failure and delaminations take place. For impact energy higher than 12 J fibres failure occurs in the layer opposite to the impact point. Increasing the energy, perforations and penetrations are clearly visible on the sample surface.

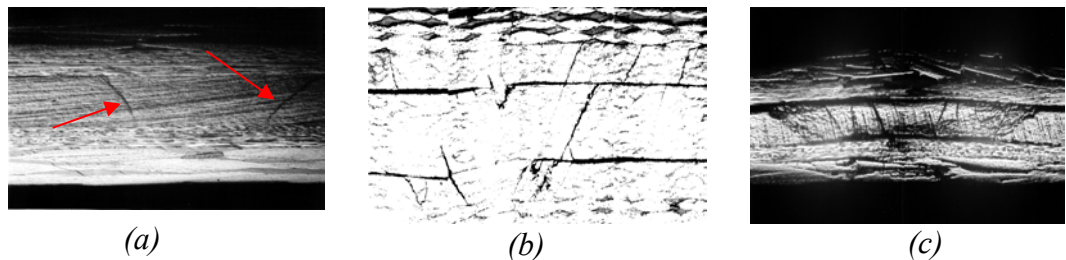


**Figure 25:** Micrographs of specimens' cross section impacted at different energies: (a) 1.8 J, (b) 11.5 J and (c) 13.5 J [18]. The arrows represent the delamination that occurs at 1.8 J.

A micrograph analysis of the cross section of the impacted sample area can demonstrate the degradation of the composites increasing the loading. In figure 25 the three images represented the cross-section of the 4mm thick samples impacted with the energy of 1.8J, 11.5 J and 13.5J, are reported. It is clearly visible that for the 1.8J damage sample only internal delaminations are present ( red arrows), while increasing the energy, fiber failure and visible damage appear (figure 25(b) and 25(c)). Generally, the focus of attention is on the detection of the initial delaminations, because when they occur a reduction in the stiffness and the strength of the composite components happens.

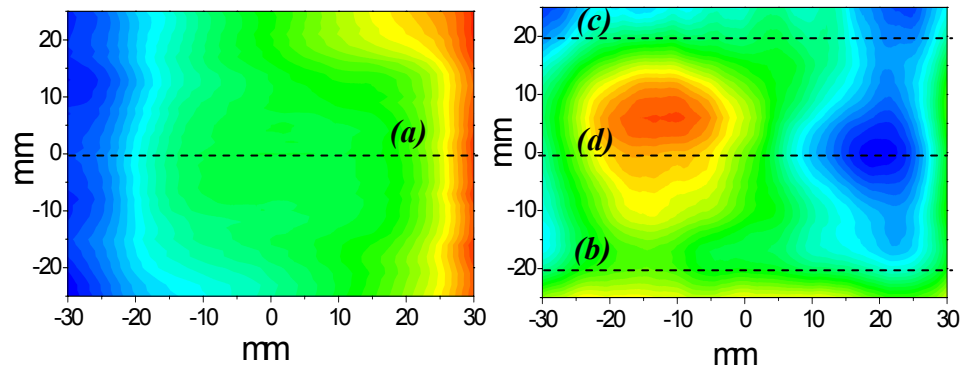


**Figure 26:** Image of the magnetic field phase (rad.) for cross-ply composite: (a) 4mm thick virgin sample; (b) 4mm thick sample impacted with an energy level of 1.8J.

In figure 26(left) and (right) the image of magnetic phase for a 4mm thick virgin and impacted sample with an energy level of 1.8J, are shown, respectively. The image of the damaged sample (figure 26 (right)) is obtained without any data processing technique. The dipole-like image is related to the non-homogeneous eddy current distribution around the center of the impact located at the position (0,0). It must be noted that in the picture of the damaged sample figure 26 (right) the edge effect, which characterizes the virgin map in figure 26 (left), is negligible compared with variations of the phase of magnetic field due to the damage inside the specimen. Though the impact energy is very weak, the magnetic signal reveals the presence of the defect even when it isn't visible to naked eye.

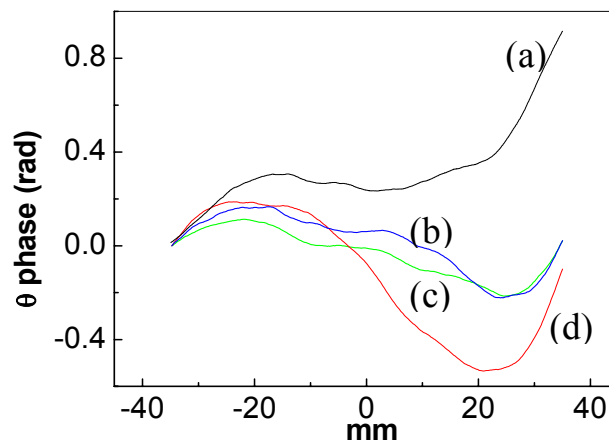


**Figure 27:** Line-scan taken from the map in the fig.4 (b). (a) is the line of virgin sample 4mm thick, (b) and (c) are the line-scans located at  $\pm 20$ mm from the center of impact point, (d) is the line-scan at impacted point.

It appears more evident in figure 27, where the line-scan (taken from the maps of figure 26) at the center of impact point (line (d)), at  $\pm 20$  mm from it (lines (b) and (c)), and the

line scan of the virgin sample with the same thickness (line (a)), are compared. The slope variation between the lines (a) and (d) means that, although the sample surface appears to be intact, the sample has internal damage such as delaminations.

Moreover, focusing the attention on the comparison among the virgin line scan and the line scans collected at  $\pm 20$ mm from the centre of the impacted area. Even through the 4mm thick sample is damaged with a very low energy level,  $U=1.8$  J, the damage propagates 20mm away the centre, as shown from the non negligible slope variation of the magnetic phase with respect to the virgin one. It means that the variation of the magnetic phase along the line-scan expressed by the slope  $d\theta/dx$  is a suitable parameter to investigate at an early stage not only the severity of the damage but also its extension inside the laminates. This effect is also confirmed by Table 5, where the slope of the magnetic field phase  $(d\theta/dx)_0$  along a line scan 20mm far away the center is shown. Laminates with a thickness of 4, 3 and 2mm, damaged with the same level of energy  $U=12$  J exhibit an increasing slope of the magnetic field far away the center. This confirms that laminates with smaller thickness have a lower mechanical tolerance, in fact they are characterized by deeper indentation, and smaller extension of the damage in the nearby impacted area. Indeed, thinner the material is, more localized and severe the damage is, since the sample is less able to distribute the transverse load on the whole structure. The relation between the magnetic field slope and the damage allow to distinguish the different defects in specimens impacted with the same energy and with different thickness.

**Table 6:** Slope of the magnetic field for the line-scan measured at 20 mm from the center of impact in 2 mm, 3 mm and 4 mm thick samples damaged with  $U=12$  J.

<b>Sample thickness [mm]</b>	<b><math>(d\theta/dx)_0</math> [rad/m]</b>
2	<i>0.004</i>
3	<i>0.015</i>
4	<i>0.022</i>

The correlation of the phase and the structural integrity of the sample (i.e., delaminations and fibre ruptures) demonstrated by the experimental results can be confirmed by an electrical model generally used to describe the sensor and the test sample, in electromagnetic non-destructive inspections based on an Eddy Current technique [19]. Since this model establish that the real part is linked to sample conductivity and the imaginary part represents the leakage inductance of the specimen

(i.e. structural variation of the sample) it is possible to correlate the phase and the amplitude of the magnetic field to the structural integrity of the sample and the variation of the electrical conductivity, respectively.

## 6. Magnetic Imaging

In the last section the damage due to the quasi-static loading has been analysed using the information offered by single line scans collected across the impacted area. As it has already demonstrated the slope inflection can be considered as a useful parameter to evaluate damage inside the composites. Moreover, a more accurate diagnosis of damage specimens can be performed using the 2-D magnetic field imaging.

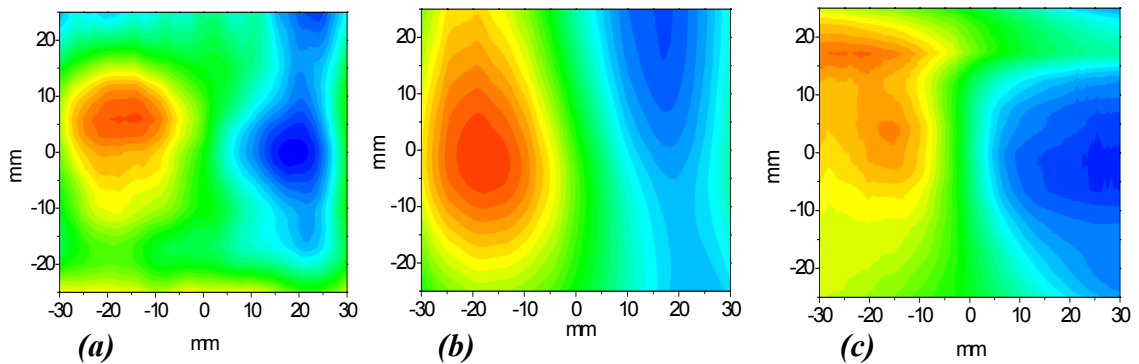


**Figure 28:** Magnetic field imaging of 4mm thick specimens impacted at different energies: (a) 1.8 J, (b) 11.5J and (c) 13.5 J.

The figure 28 (a, b, c) shown the magnetic field phase imaging of 4mm thick plates damaged by impacts having a level of energy  $U= 1.8, 12\text{J}$  and  $55\text{J}$ , respectively. The magnetic imaging offers the possibility to evaluate the relation between the extensions of the magnetic field distortion to the severity of the damage.

In these pictures a notable distortion of the magnetic field above the sample is already present in the magnetic map of the laminate damaged at energy level of  $U=1.8\text{ J}$  (figure 28 (a)), which does not show any visible damage on its surface. The extension of the two regions around the points of the magnetic field maximum variation slightly increases in figure 28 (b) where the laminate is damaged with an energy  $U=12\text{J}$ , and increase in a more dramatic way, in the picture of figure 28 (c) where the energy level of damage is  $U= 55\text{ J}$ . The images in figure 28 (b) and (c) show that it is not possible any discrimination, due to their size or shape, between the two failure mechanism by the size of the two areas. It means that the fibre failure, particularly at the energy level of 12

J, is prevalently localized around the impact point of the sample and only slightly affects its neighbourhood. Instead, for  $U=55$  J (figure 28 (c)) the much larger size of the perturbed magnetic field shows the more severe damage even far away the impact point due to the fully perforated sample. As can be observed from the images of figure 28 they are not able to give the dimensions and the shape of the defect inside the test sample.

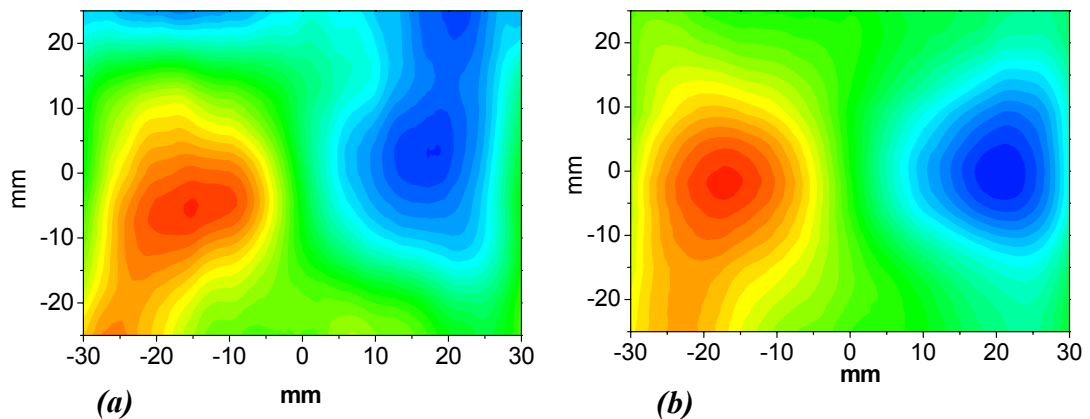


**Figure 29:** Two dimensional magnetic maps related to the 2mm (a) and 3mm (b) thick samples impacted at 12J.

This limitation is present even when test samples with different thickness and the same impact energy are compared, as shown in figure 29 where the maps of the imaginary component of magnetic field for 2mm and 3mm thick samples impacted at 12 J are reported. A part from the different distribution of the magnetic field dipole that represents the different damage severity, it is not easy to deduce the shape and the extension of the damage. In this thesis it has been tried to overcome this limitation at first utilizing an Artificial Neural Network that should recognize the different defect dimensions with a post processing algorithm.

### 6.1 The Artificial Neural Network (ANN) system

Today, the ANN computing represents one of the most powerful tools to solve complex non-linear problems like pattern classification and forecasting predictions, with a short time computation respect to the conventional numerical simulation programs such as the Finite Element Method (FEM). Thanks the capability of the ANN systems to resolve different prediction and computational problems it constitutes a good candidate to process the analysis of composite-material (and more generally multi-layer) structures.

The ANN systems have been successfully used to process signals related to the analysis of composite materials using different NDE techniques such as ultrasound, infrared thermography and acoustic emission [20-22].

An Artificial Neural Network (ANN) is a system composed by some elements called neurons which simulate the functionality of the human brain. As in biological system the neurons are connected through synaptic paths, in the neural computing the different neurons (nodes) are linked by means of weighted interconnections. The latter are initialised to random values and iteratively adapted to achieve the desired response.

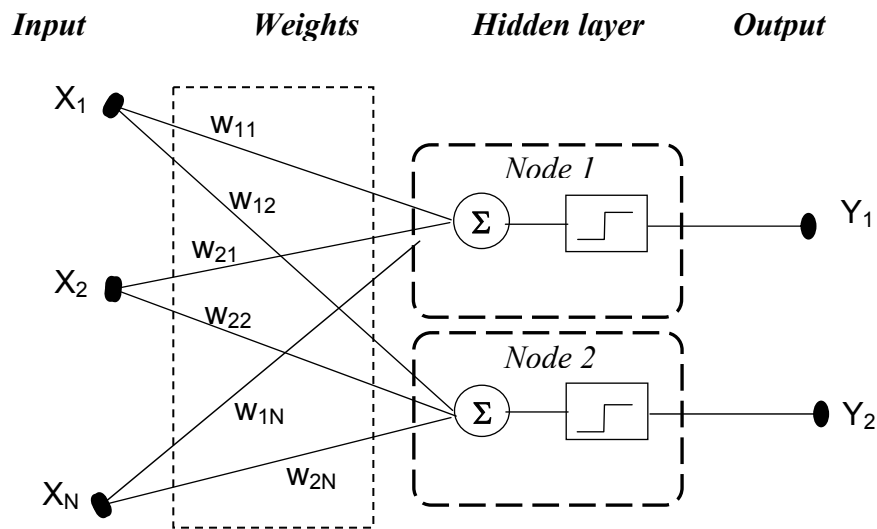


**Figure 30:** Architecture of a feed forward neural network system with  $X_N$  input nodes, two hidden nodes and two output nodes ( $Y_1$  and  $Y_2$ ).

In this thesis a multi layer supervised artificial neural network trained with the back propagation algorithm is presented (figure 30). This system was realized during collaboration with the research group of prof. G. Donaldson at the University of Straightclyde (Scotland) in the framework of SCENET exchange project. It is characterized by different layers of neurons: input layer, hidden layer and output layer. The nodes of each layer aren't connected each other but only with the nodes of the following layer. By a theoretical point of view was demonstrated by the Kolmogorov's theorem [23] that two intermediate layers are sufficient to model any problem, but most of the practical problems are successfully solved used one hidden layer. The most important stage in the realization of an ANN is the training or learning of the system because it defines the number of nodes for each layer, the connection and their weights. During the training each hidden neuron performs a weighted sum of its inputs that after

are processed by an activation function, typically a sigmoid or a hyperbolic tangent (*tanh*) function, determining the final output neurons [24]. The realized ANN makes use of a supervised learning, it means that the training set formed by an input pattern and an output target is processed by the network that adapts the weights minimizing the error between the desired outputs and the produced outputs. The condition to stopping the learning is that the root mean square error of the network for all the input signals is less than a predefined threshold. Once the training is performed the network is tested using a test set composed with data not contained in the training set. In this way is possible to check that the network can generalize which has learnt during the training set. The flow chart of the stages that constitute the network system is shown in figure 31.

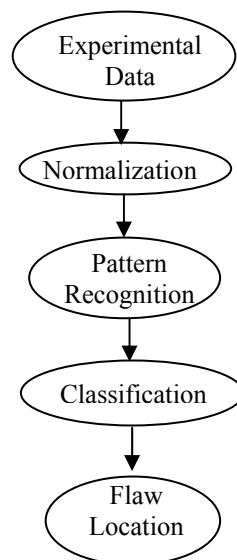


**Figure 31:** Flow chart used to the data analysis process.

The ANN examined here is characterized by 400 input nodes, a single hidden layer with 70 nodes and 5 output nodes. The training was performed by a *tanh* activation function with an error threshold of 0.2%. The 400 input nodes are represented by the points of the line scan acquired by the SQUID magnetometer. Since the magnetic field parameter that can distinguish the different damage is represented by the magnetic phase slope, the system was been trained to associate each impact energy level to the corresponding value of the magnetic phase slope. The network was realized to distinguish the magnetic signals associated to the damaged samples, the virgin (undamaged) sample and the edge effect. For this reason the experimental line scans of magnetic phase signals, related to the virgin sample, edge effect and different impact energies, have been used as output nodes of the network. In particular, for the 2mm thick samples the impact energies are

2J, 7.7J and 12J, while for the specimens with a thickness of 3mm impact energies of 9J, 12J and 16J are considered. The training set for each thickness containing 40 patterns represented by the experimental data that was normalized into 0 to 1 range, before the pattern recognition process. The latter is performed using a classification subsystem that selects the output nodes and gives the flaw position.

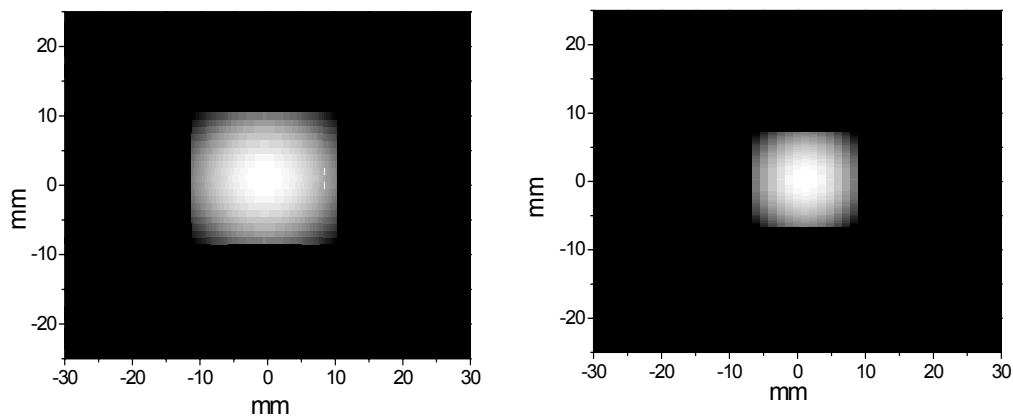


**Figure 32:** Imaging obtained using the ANN realized for the specimens of thickness 2mm (left) and 3mm(right) impacted at 12J.

At first, the system has been tested with the magnetic maps related to the samples of 2mm and 3mm thickness impacted at the same energy of 12J. Figure 32 shows the maps produced by the ANN for the 2mm and 3mm thick specimens. The damaged and undamaged areas correspond to the white and the black colour, respectively. It should be noted that the imaging obtained using the ANN system can localize the defect into a delimited area that corresponds to the damage, thanks a previously introduction in the system of the right dimensions of the damaged area. The ANN realized recognize the right impact energy level for each thickness and the centre of the damaged area.

The second test has been performed using the 2mm and 3mm thick samples impacted at energy of 2J, 7.7J and 9J, 16J, respectively.

The results obtained processing the magnetic field imaging with the ANN system, for the 2mm and 3mm thick samples are shown in figure 33 and 34, respectively. In this test the recognition of the impact energies is not correct. In fact, the system does not distinguish the 2J from 7.7J for the 2mm thick samples, and the 9J respect to the 16J for the 3mm thick samples. In other words, the NN system classifies, in the case of 3mm thickness the sample impacted at 16J as the 9J, and for the 2 mm thick samples the 7.7J impacted samples as the 2J. Since the incorrect classification, the maps in white and black colours do not reflect the dimensions (held previously in the NN system) of the damaged area present on the samples

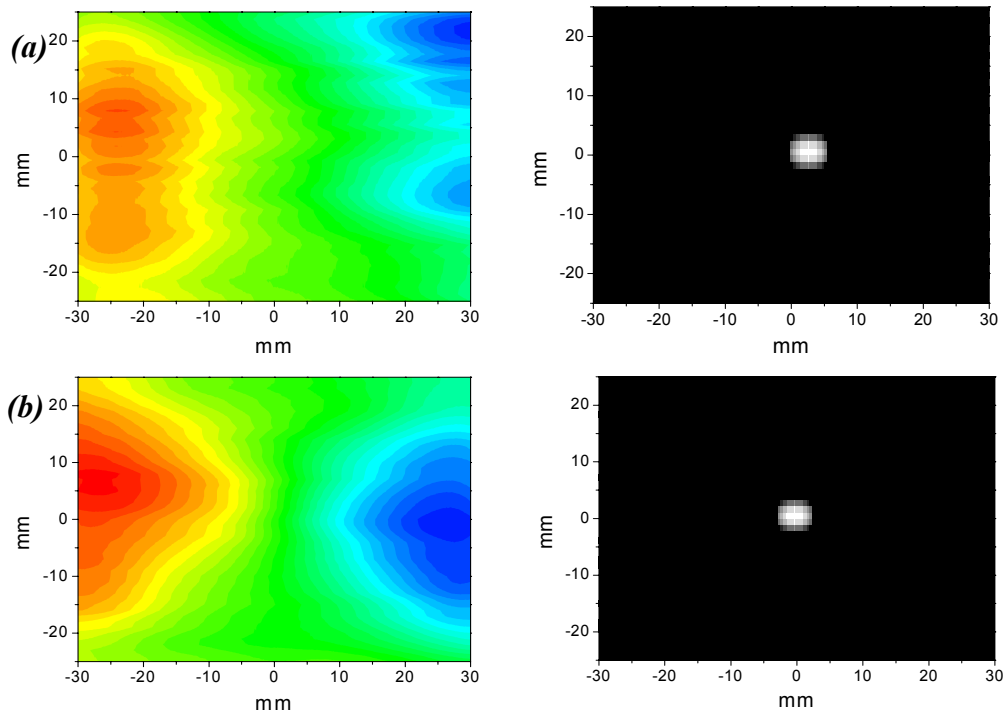


**Figure 33:** Comparison between the SQUID imaging and the ANN maps for the 2mm thick samples damaged at 2J (a), 7.7J (b), respectively.

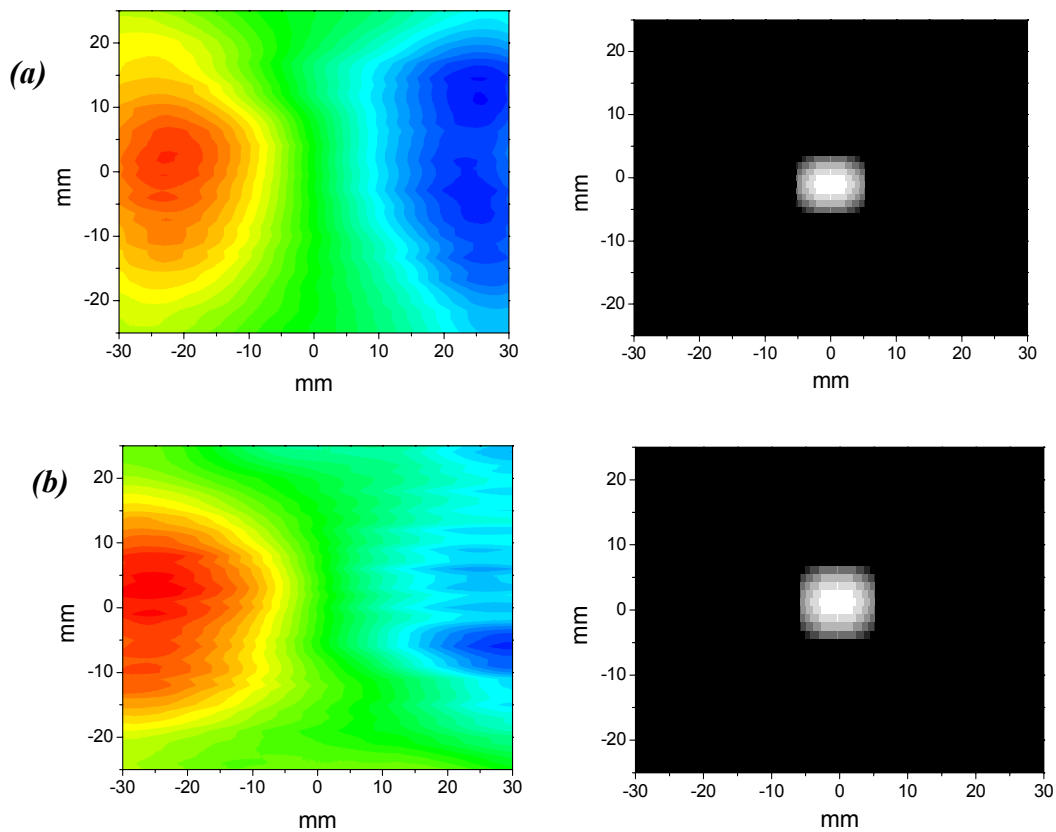


**Figure 34:** Comparison between the SQUID imaging and the ANN maps for the 3mm thick samples damaged at 9J (a) and 16J (b).

The results obtained from the second test demonstrate that the ANN system is not capable to recognize correctly the right damage at different energy for each thickness. In figure 35 the comparison of the lines scan related to the 2J and 7.7J (left), the 9J and the 16 J (right), is shown. In both cases the slopes of the magnetic phase are different and distinguishable, so that each energy level is characterized by a different slope value. This difference is lost after the normalization from 0 to 1 range, as shown in figure 36. It could be noted that the normalization of the curve in the range from 0 to 1 change the slope of the signals.

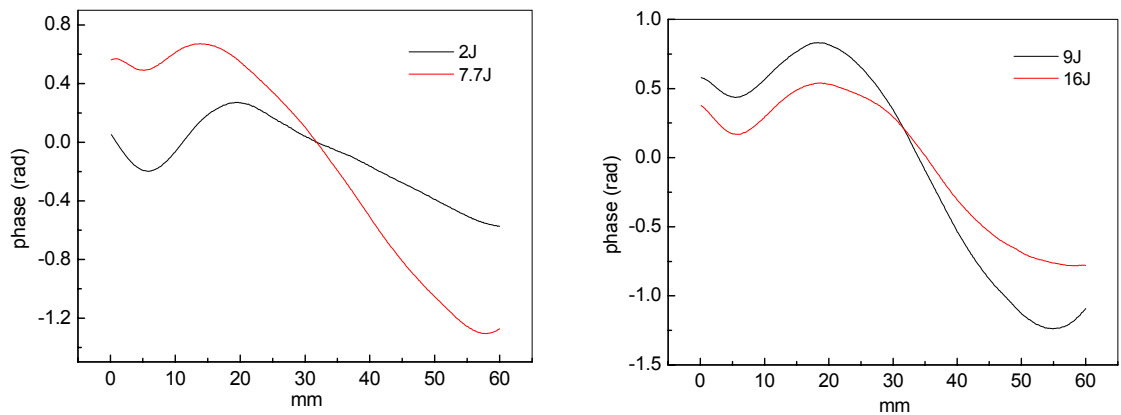


**Figure 35:** Line scans related to the magnetic phase extracted from the magnetic maps of the figure 1 and 2; scans related to the 2mm and 3 mm thick samples on the right and left hand, respectively .

In figure 36 (left) the 2mm thick sample damaged at 7J and 12J appear with the same slope as if they are damage both at comparable energy. This effect is present also for the 3mm thick samples impacted at 9J and 16J, as reported in figure 36 (right). In the latter the two curves related to the two different energies are overlapped and they look like as two curves extracted from a unique test sample. In other words, the normalization modifies the information included in the magnetic filed signals slope, which distinguish the different energy impact.

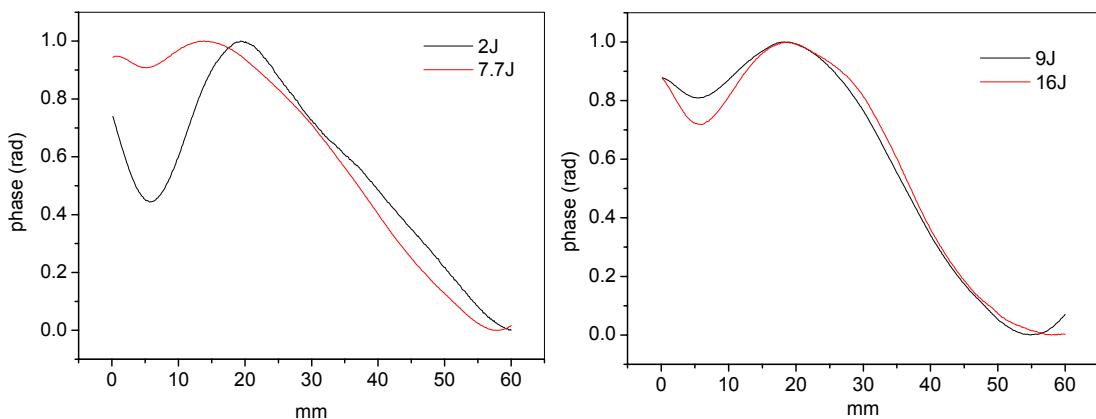


**Figure 36:** Comparison between the lines scans obtained from the latter experimental data for the 2 and 3 mm thick samples, normalized in the range 0-1.

Therefore, the ANN system during the training does not learn correctly the correspondence between the energy and the signal slope. The ANN results demonstrate that the present version of the algorithm does not recognize correctly the impact energy of the processed test sample and can not be used to classify the impacted sample with the appropriated impact energy because it needs an optimization of the training stage.

The application of the ANN system to the pattern recognition have some disadvantage, represented by the long time necessary to train the system and the high performance personal computer required to process the high quantity of data.

Moreover, the ANN system realized in this work needs to know previously the dimensions of the defect to be able to produce an imaging of the damaged sample. It is a limitation because the SQUID prototype system will be used to detect in CFRPs the damage even if they are not visible and their dimensions are unknown.

For these reasons at the present the ANN approach doesn't appear as the more advantageous technique to process the magnetic field signals to obtain a more simple data interpretation.

## 6.2 Magnetic flux imaging

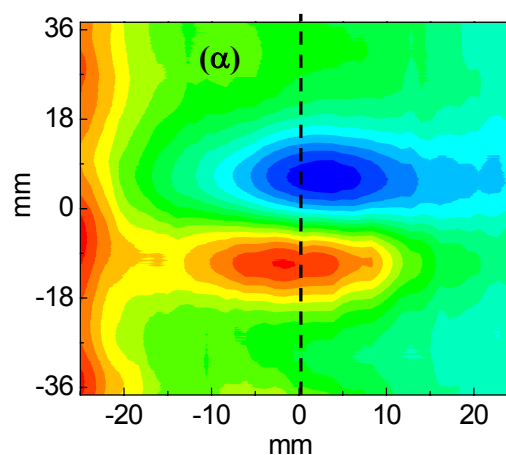


**Figure 37:** Imaging of magnetic field variation for sample impacted at 5J;

In figure 37 the magnetic field imaging related to the damaged sample, impacted at 5J, is shown. The distribution of the magnetic field induced in the sample is characterized by a dipole like image, which represents the damaged area after the impact.

As mentioned before (chapter I), the SQUID magnetometer measures the magnetic field variation produced by the test sample thanks the variation of the magnetic flux inside the pick up coil. Therefore, there is proportionality between the magnetic field and the variation of the magnetic flux in the SQUID pick up coil, as show in equation (1):

$$\frac{\partial\Phi(x,t)}{\partial t} \propto \frac{\partial B(x,t)}{\partial t} \quad (1)$$

thanks the constant speed  $v$  of the line scan, it is possible to write the  $\partial t$  as:

$$\partial t = \frac{\partial x}{v}$$

substituting in equation (1) the relation between the variation of the magnetic flux and the magnetic field can be obtained:

$$\frac{1}{A} \cdot \frac{\partial\Phi(x,t)}{\partial t} = \frac{\partial B(x,t)}{\partial x} \cdot v$$

with A is the pick up coil area.

The latter equation demonstrates that the magnetic flux variation along a line scan (during the time  $\partial t$ ) is proportional to the magnetic field derivative time the scan speed  $v$ .

In figure 38 the comparison of the magnetic filed signal respect to the corresponding derivative, which represents the magnetic flux variation  $\partial\Phi/\partial t$ , are reported.

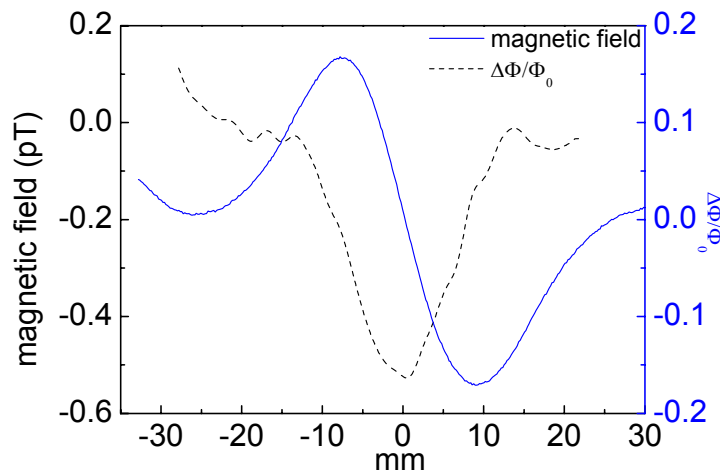


**Figure 38:** Comparison between the lines scan of the magnetic field and the magnetic flux variation normalized to the flux quantum  $\Phi_0$  across the center of the defect.

The center of the magnetic field inflexion that represents the center of the defect, using the magnetic field derivative it becomes the minimum of the magnetic flux signal. It could be noted that in the magnetic field imaging the inflection can give information about the presence of the defect, but it is not easy to localize it. Instead, the amplitude of

the magnetic field flux variation is directly linked with the impact energy, because it represents the slope value of the magnetic field inflexion, while the spatial coordinate (*x axis*) give information about the localization and dimension of the damage. The advantage of this representation is evident into the 2-D imaging as show in figure 39.

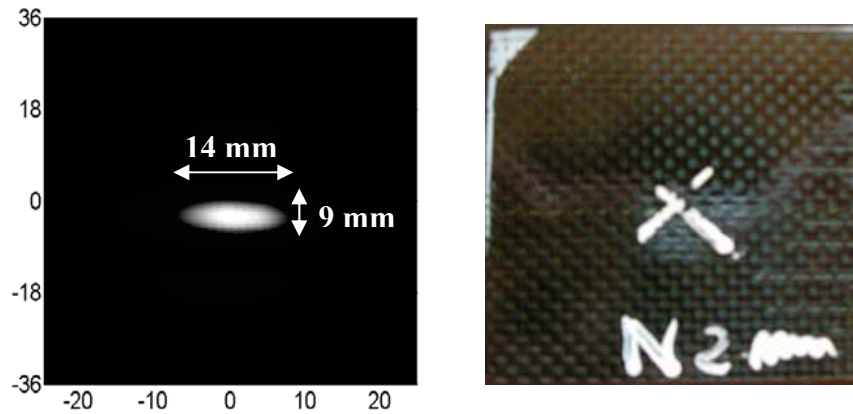


**Figure 39:** Imaging of magnetic flux variation of sample impacted at 5J.

The dipole-like image of figure 37 is replaced by a single spot (shown in fig.39) that represents the position and the correct dimension of the defect.

This result shows that to localize defect in CFRPs the magnetic field imaging due to the NDE SQUID based prototype could be replaced by the magnetic flux imaging, which represents the variation of the magnetic flux measured by the SQUID magnetometer. In this representation the defect appears as a white spot and the shape and the dimension of the latter are comparable with the damage detectable on the back side of the sample. It is important to note that the picture of the test sample defect can be obtained without any post processing technique, but only by measuring the magnetic flux variation using a dc SQUID sensor. It means that the NDE prototype based on SQUID sensor allows to obtain a magnetic flux imaging of the damage specimens in order to localize the damage and detect the correct dimension of the defect even if they are unknown and not visible. The flux magnetic field imaging offers the possibility to compare the results obtained by SQUID prototype with the conventional NDE techniques as Eddy Current using induction coils and ultrasound. In figure 40 the maps, obtained with Eddy Current based on induction coil, related to CFRP samples of 4mm thickness and impacted with three different energies (0.14J, 2.5J and 5J) are shown.

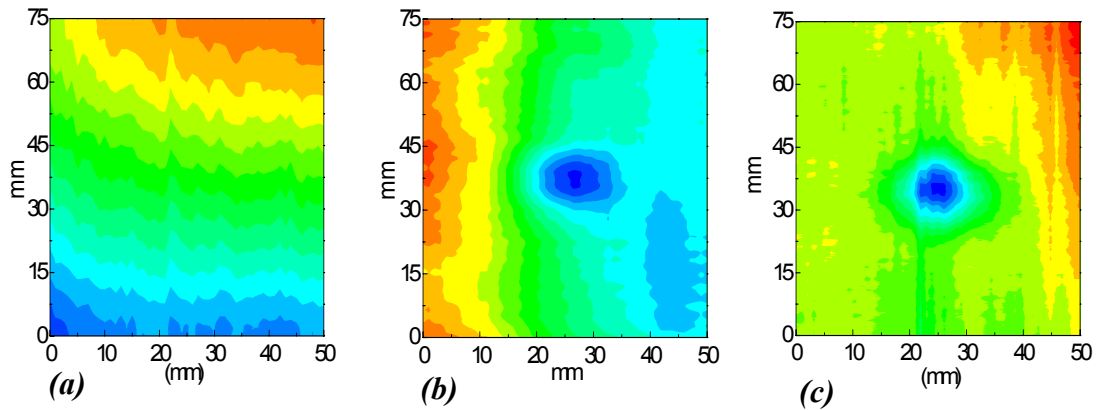


**Figure 40:** Eddy current imaging of specimens impacted at 0.14J (a), 2.5J(b) and 5J(c).

The results of Eddy Current based on induction coil have been performed using an Elotest B300 instrument supplied by Rohmann GmbH with an absolute ferrite core probe working at frequency of 2.5 MHz. The induction coil measurements reveal that for the lowest energy (figure 40(a)) there is not detectable any damage, while increasing the impact energy the images show a spots in the centre of the sample, across the impacted area (figure 40(b) and 40(c)).

In all three images the effect due to the no planarity of surface, especially for the lowest energy impact sample, are observable on the borders of the maps. One of the limitations of Eddy Current induction coil applied on CFRPs is represented by the surface planarity and roughness, due to the layers wool and the interface between the fibre and the matrix. In other words, the roughness of the surface can introduce a variation of lift off between the sample surface and the probe, modifying the results of the induction coils diagnosis. Since the EC technique is very sensitive to the lift off variation their imaging could present edge effect as shown in figure 40.

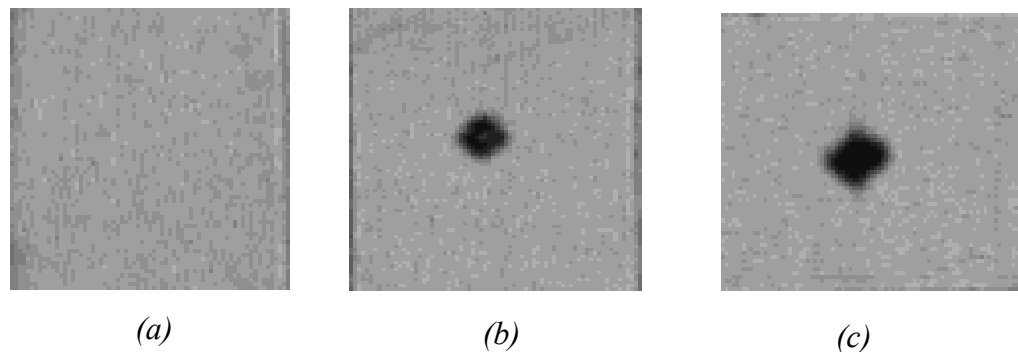


**Figure 41:** Ultrasound inspection of specimens impacted at 0.14J (a), 2.5J(b) and 5J(c), realized at the Department of Materials and Production Engineering, University of Naples “Federico II”, supported by a MURST project.

The same results can be achieved using the Ultrasound technique as shown in figure 41. The maps have been realized with a post processing method using Ecus Inspection Software, Krautkramer Branson USD 15 S with NAMICON SONIC 136 ULTRA, transducer 5MHz 0.25" A311S parametric with water coupling. The Ultrasound and the Eddy Current (EC) methods obtain the same results that could be compared with the magnetic flux imaging of the SQUID magnetometer. In figure 42 the magnetic flux distribution related to the tested samples analysed with the EC and Ultrasound, are reported.

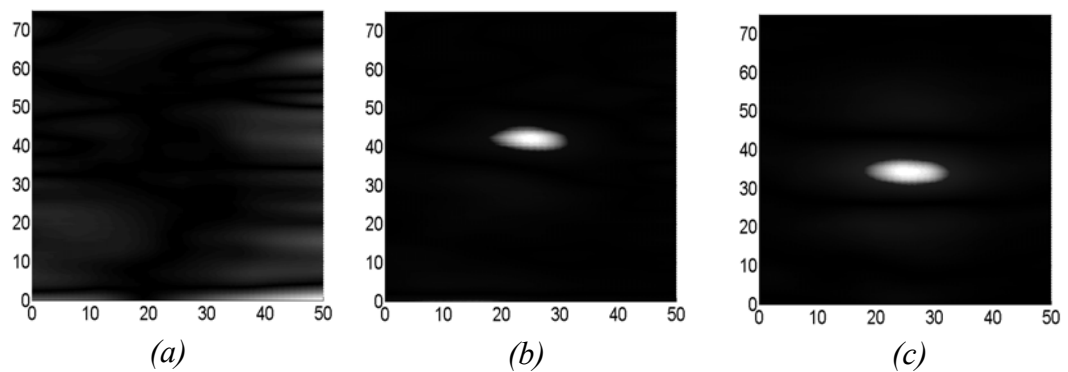


**Figure 42:** SQUID magnetic flux distribution of specimens impacted at 0.14J (a), 2.5J(b) and 5J(c). The scales are in mm, the defects dimensions are 10 x 7 mm and 14 x 9 mm for the 2.5J and 5J, respectively.

It is interesting to note that the prototype response gives results comparable to the conventional technique: Ultrasounds and Eddy Current with induction coils. The white spots in the pictures of figure 42 represent the defects on the samples.

The flux magnetic images reported in figure 42 give information about the dimension and the shape of the defects. The latter can be characterized by longitudinal and orthogonal axis lengths because of damage oval shape. The SQUID measurements show that increasing the impact energy the axis dimensions increase, in particular, for a 2.5J and 5J damage the dimensions are 10 x 7mm and 14 x 9mm, respectively. These results have been confirmed by measurements, performed using Ultrasound technique shown in figure 41.

It could be noted that the magnetic flux imaging is able to detect and localize defects even if they are not visible to the naked eyes, this is the case of the specimen impacted at 2.5J (figure 42(b)). To demonstrate the sensitivity of the SQUID measurements respect to the not visible defect, an imaging of a 4mm thick sample impacted at very low energy (0.18J) has been carried out. In figure 43 the magnetic field and the magnetic flux variation are shown. It is very interesting to analyse this test sample

because its impact represents an example of delamination damage, so that the defect is not visible to the naked eyes and there is not fiber rapture in the layers. Therefore, the variation of the detected magnetic field signals has been due only to the resistivity variation produced by the tensile and compressive stress applied by the impact. It should be noted that the delamination does not produce in the magnetic flux imaging a well delimited white spot, because delamination produces only an intralayer and interlayer delamination. Therefore, the fiber rapture allows to localize the damage even if it is not visible (sample impacted at 2.5J in figure 42(b)) thanks the localization of the fiber breaking, while the delamination does not have a well delimited shape.

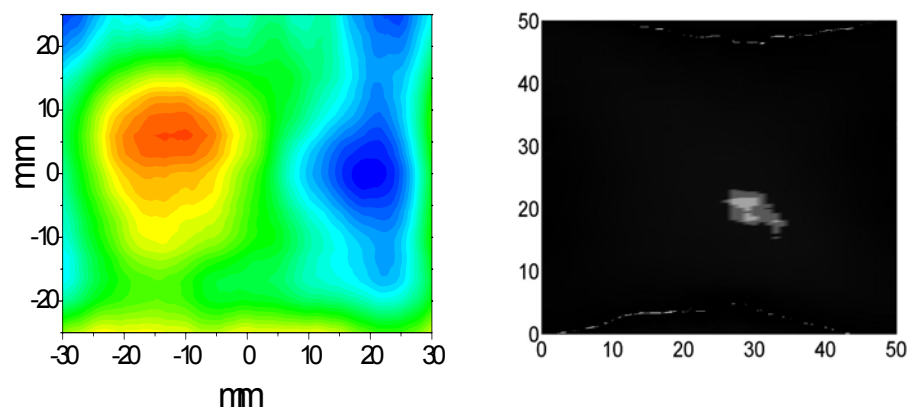


**Figure 43.** (left) and (right) SQUID magnetic and flux distribution of specimens impacted at 0.18J, respectively.

In figure 44 the maximum variation of the magnetic flux normalized to the quantum flux  $\Phi_0$  versus the impact energy is shown. The experimental results qualitatively confirm that in the energy range, which produces delaminations and matrix failures, the magnetic flux linearly increases against the impact energy as it has already demonstrated estimating the slope of the magnetic field signal [18].

In figure 44 the normalized flux behaviour reflects the severity of the damage inside the sample due to the impact energy. Increasing the impact energy the integrity of the specimen near the impacted area decrease, as a result a high magnetic flux variation could be detected. It means that the amplitude of the magnetic flux signal depends on the severity of the damage as reflected by the magnetic field slope.

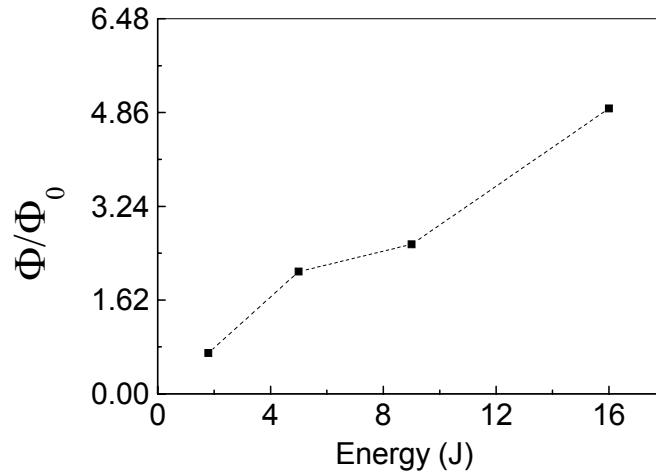


**Figure 44:** Magnetic flux variation versus impact energy related to the tested samples impacted at 0.18J, 5J, 9J and 16J.

Finally, the magnetic flux imaging can be considered as a useful tool for better representation of the magnetic field data. This representation gives results comparable with the conventional method EC and Ultrasound. Moreover it is interesting to note that the advantage of the non-destructive testing SQUID based technique respect to the induction coil and ultrasound is represented by the possibility to perform a contact less measurement, because of the low sensitivity of the SQUID sensor to the lift-off variation respect to the induction coil [25].

## 7. Conclusions

Measurements of the electrical resistance have been carried out using a four probe technique. longitudinal and transverse electrical resistance of unidirectional composites reveal the anisotropy of CFRPs material from an electrical point of view. The four probe technique obtains values of about 22000 S/m, 20 S/m and 7000 S/m for the longitudinal, transverse and cross-ply electrical resistance. It is interesting to note that the results obtained using the four probe technique show that even if the CFRPs is an inhomogeneous material thanks to the present of the conductive carbon fibers it is possible to calculate the electrical resistance. Moreover, the measurements show that orientations and thickness of the fibers, that represent the only conductive component respect to the insulated matrix, playing an important role in the evaluation of the electrical resistance. It has been demonstrated that increasing the thickness the conductivity decreases respect to a constant fiber volume fraction.

the penetration depth of magnetic field through the composite test samples and the CFRPs capability to shield electromagnetic field has been demonstrated applying the SQUID prototype. The measurements of the magnetic field signals show that the capability of CFRPs to shield e.m. waves depends on the samples thickness and the fiber orientations. Moreover, it has been demonstrated that the reflection in the cross-ply samples decreases with the thickness. It depends on the directly proportionality between the eddy current induced in the sample and its electrical conductivity, therefore samples with higher conductivity can reflect much more. Moreover, thanks to the sensitivity of the SQUID magnetometer, that allows to distinguish the longitudinal and the transverse electrical conductivity in unidirectional CFRPs, it has been demonstrated that the anisotropy of the carbon fiber could polarize the electromagnetic field.

The electromagnetic response of the CFRPs under the bending stress demonstrates that an electromechanical effect is present. The fibers displacement, due to the increasing or decreasing of fibers distance, produce a variation of the electrical resistance that has been detected by the SQUID measurements and confirmed by the four probe technique. It means that the SQUID prototype is capable to measure the effect on the electrical conductivity due to the fiber displacement. It is very important because until now the technique used for the stress sensing are invasive and need to be in contact with the fibers, instead the SQUID measurement, in a non invasive and contact less way, gives information about the electrical properties of this material.

Moreover, the detection of the electromechanical effect by means of the SQUID magnetometer is confirmed by the detection of early stage damage. The results related to the loading impact show that the magnetic field slope is a suitable parameter to distinguish the severity of the damage due to different impact energy. Since the localization of the impact defect in the composite materials is more difficult respect to the metallic material different techniques have been used. The ANN described it is not able to recognize the proper impact energy and does not represent correctly the shape and dimension of the damage. On the other hand, the magnetic flux variation imaging, measured by using the SQUID magnetometer, represents an appropriate method to obtain a damaged sample map, in which the position and the dimensions of the defect are detected. The results obtained using the SQUID magnetic flux representation has been compared with other techniques, such as Eddy Current with induction coil and Ultrasound. Even if the latter diagnostics methods obtain the same results of the SQUID magnetic flux variation, it must be considered some limitations that these conventional

technique present. The main drawback of the Eddy Current with induction coil technique is its sensitivity to the lift off variations that can alter the measurements, while the Ultrasound method needs of a coupling medium, like the water, to be in contact with the sample. For this reason the SQUID magnetometer measurements represent, respect to the eddy current with induction coil and Ultrasounds, an advanced method to detect damage and stress in the CFRPs in non invasive and contact less mode.

The fiber displacement due to impact and mechanical stress has been confirmed using an AFM analysis. The fiber-matrix interphase integrity has been investigated using the microscopic analysis. The results of this diagnosis show that damage, such as delaminations, produce in the CFRPs a fiber displacement because of the matrix weakening. Moreover, the detection of the fiber displacement, by using the AFM analysis, can explain the sensitivity of the Eddy Current method to detect little structural alteration, such as delaminations, in the composites. In fact, the changing of the fiber position changes the carbon fiber electrical resistance, producing a variation of the magnetic field signal detected by the SQUID magnetometer. Both the magnetic field and AFM measurements demonstrate that the damage inside the CFRPs doesn't extend uniformly in all directions, but the damage propagation depends on the fiber orientation. Finally, the results described in this chapter demonstrate the capability of the prototype based on the SQUID magnetometer to analyse the electromagnetic properties of very low conductive materials such as CFRPs in more advantageous mode respect to the other traditional non destructive methods.

## References

- [1] J.M. Ting and K.W. Chen “Electrical conductivity of discontinuous filament-reinforced unidirectional composites”, *J.Mater.Res.*, Vol.15, No. 4, Apr 2000.
- [2] D.D.L. Chung “Comparison of submicron-diameter carbon filaments and conventional carbon fibers as filler in composite materials” , *Carbon* 3, 1119-1125, 2001.
- [3] X. Liang, L. Ling, C. Lu, L. Liu “Resistivity of carbon fibers/ABS resin composites“ *Material Letters* 43, 144-147, 2000.
- [4] J.C. Abrya,b, S. Bochara, A. Chateaminois, M. Salvia, G. Giraudb, “In situ detection of damage in CFRP laminates by electrical resistance measurements”, *Composites Science and Technology* 59, 925-935, 1999.

[5] A. C. Lind, C. G. Fry, C.H. Sotak “Measured electrical conductivities of carbon-fiber composite materials: Effects on nuclear magnetic resonance imaging” J. Appl. Phys. 68 (7), October 1990.

[6] Jack Blitz “Electrical and Magnetic Methods of Non-destructive Testing” published by Chpman & Hall, 1991.

[7] X. Luo, D.D.L. Chung “Electromagnetic interference shielding using continuous carbon-fiber carbon-matrix and polymer-matrix composites” composites: Part B 30, 227-231, 1999.

[8] G. Binning, C. F. Quate and Ch. Gerber “Atomic Force Microscope” Phys. Rev. Lett. 56, 9, 1986.

[9] Rugar and Hansma et al. 1990

[10] Zhong et al. 1993.

[11] M Valentino, C Bonavolontà, G Peluso, G P Pepe “Real-time monitoring of fatigue damage in Carbon Fiber Reinforced Polymers for aeronautical applications using HTS SQUID magnetometer” submitted to proceeding of EUCAS, European Conference of Applied Superconductivity, Vien 2005

[12] K. Shulte, Ch. Baron “Load and failure analysis of CFRP laminates by means of electrical resistivity measurements”, Composite Science and Technology, 36, 63-76,1989.

[13] K. Shulte, H. Whittich “The electrical response of strained and/or damaged polymer matrix-composites”, Proceeding of ICCM-10, 6,349-56,1995.

[14] Wang X and Chung DDL 1995 smart mater. Struct. 4 363-7

[15] L. Lucente, undergraduate thesis “Analisi sperimentale dell’impatto a bassa velocita’ di laminati CFRP”,Department of Material and Production Engineering, University of Naples “Federico II”.

[16] Bar-Cohen Y, "Progress and challenges in NDE of composites using obliquely insonified ultrasonic waves", E-Journal of Non-destructive Testing & Ultrasonics 4, 9,1999.

[17] C. Bonavolontà, G. Peluso, G.P. Pepe, A. Ruosi, M. Valentino “Detection of early stage damage in Carbon Fiber Reinforced Polymers for aeronautical applications using an HTS SQUID magnetometer” Eur. Phys. J. B. 42, 491-496, 2004.

[18] A.Ruosi, M.Valentino, V.Lopresto, and G.Caprino ”Magnetic response of damaged carbon fibre reinforced plastics measured by an HTS-SQUID magnetometer” *Composite Structures* 56, 141 (2002).

- [19] D.Placko, I.Dufour, “Eddy current sensors for non-destructive inspection of graphite composite materials” *IEEE Industrial Application Society Annual Meeting* 1992, part II, p.1676.
- [20] Bhat C, Bhat MR and Murthy CRL “Acoustic emission characterisation of failure modes in composites with ANN” 2003 *Composites Science and Technology* 61 213-220.
- [21] Darabi A and Maldague X “Neural Network based defect detection and depth estimation in TNDE” 2002 *NDT&E International* 35 165-175.
- [22] Tsai C –D, Wu T –T and Liu Y –H “Application of neural networks to laser ultrasonic NDE of bonded structures” 2001 *NDT&E International* 34 537-546.
- [23] Zaremba T. Technology in search of a buck. In: Eberhart RC, Dobbins RW, editors. *Neural network tools*. London:Academic Press,1990
- [24] D.Graham, P.Maas, G.B. Donaldson, C. Carr “Impact damage detection in carbon fibre composites using HTS SQUIDS and neural network” *NDT&E international* 37(2004) 565-570.
- [25] C. Bonavolontà, , G.P. Pepe, G. Peluso, M. Valentino, G.Capriano and V.Lopresto, “Electromagnetic non-destructive evaluation of fiberglass/aluminum laminates using HTS SQUID magnetometer” *IEEE transactions on applied superconductivity*, vol. 15, No.2, June 2005.

# Chapter 5

## Fiber-glass aluminium (FGA) laminates electromagnetic characterization

### Introduction

FGA material is a new advantageous composite used in the aeronautical and aerospace industry. To increase the use of this material its properties respect to the loading damage and the corrosion ageing must be study. The aim of this chapter is to demonstrate the capability of the electromagnetic technique using SQUID magnetometer to study the damage process in the FGA due to loading impact and corrosion activity. At first the eddy current technique based on the HTS dc-SQUID magnetometer has been used to distinguish the different damage. The two in plane component of the magnetic field  $B_x$  and  $B_y$  have been measured and the magnetic field responses produced by the samples impacted with energies ranging from 5J to 36J have been monitored.

The corrosion damage can occurs into the aluminium layers subjected to an impact that had degraded their mechanical properties. To study the corrosion activity it has been fabricated an experimental copper made mock up to assess the corrosion effect and to verify the magnetic field sensitivity to the ongoing corrosion process. The mock up enable us to study two simple geometric configurations that can be modelled to calculate the current distribution during the corrosion process. The current distribution was obtained via electromagnetic inversion of the measured magnetic field. It is important to note that the copper made mock up is useful to optimise the measurement set up and the magnetic field inversion algorithm.

Static and dynamic measurements of the magnetic field response have been carried out obtaining information about the corrosion rate and the dissolved copper on the anodic surface. Moreover, an electromagnetic inversion of the magnetic field distribution, by using the Fast Fourier Transform (FFT) has been implemented to obtain the corresponding current distribution involved into the analysed processes. To test the FFT

algorithm two simple cell geometries with rectangular and shaped electrodes, have been used. The cell with a shaped anode has been realized to approximate the geometry of the deformation presents on impacted point that characterizes the surface of the fiber glass laminates after a loading impact.

## 1. Impact loading detection

One of the main characteristic of the fiber glass aluminium (FGA) composite after a loading impact is its surface deformation. As a consequence of an impact this material, thanks to the plasticity of the aluminium layers, before an irreversible structure degradation (cracking) is characterized by a permanent deformation. To resort to a quantitative evaluation of the permanent deformation, the residual displacement  $d_r$  of the specimens was measured. It is preferable to use the label ‘residual displacement’, instead of the more common term ‘indentation depth’, because the permanent deformation was not limited to a little zone surrounding the impact location. At the end of the impact event only the portion of the specimen boundaries clamped within the test frame was unaltered, whereas the rest of the plate exhibited a pronounced concavity (Figure 1). Of course, this impaired the possibility to easily separate the indentation depth (usually correlated with the local damage) from the overall residual displacement.



**Figure 1:** Permanent deformation of an FGA specimen after impact.

Figure 2 clarifies the meaning of the residual displacement, as conventionally defined in this work, i.e. the maximum depth of the profile with respect to the undeformed surface plate.



**Figure 2:** Conventional definition of the residual displacement,  $d_r$ :

The measurement of  $d_r$  was carried out after the impact test, using a profilometer with 1% sensitivity, putting its hemispherical tip, 2 mm in diameter, in contact with the indented panel (see Figure 3) and its vertical displacement across the indentation, with a length of 100mm, was measured.



**Figure 3:** Measurement of the residual displacement using a profilometer

The results of the surface profiles for the specimens damaged at 12 J, 20 J and 36 J, as measured are shown in Figure 4. As expected, the specimen indentation increases with increasing impact energy. Notably, the maximum indentation is larger than 6 mm, resulting in a corresponding variation of the lift-off between the probe and the sample during the SQUID inspection.

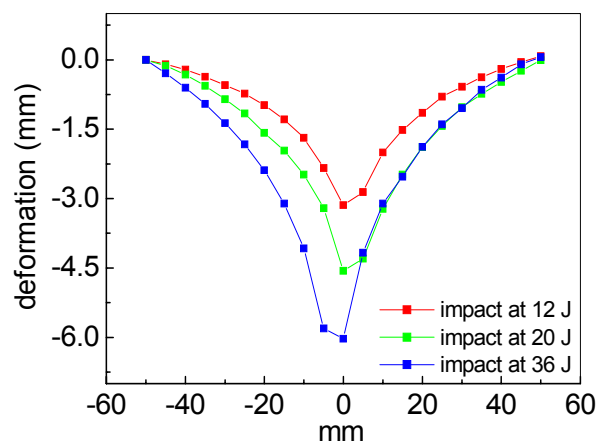


**Figure 4:** specimens surface profile obtained with a profilometer for samples damaged at 12 J, 20 J and 36 J.

In Figure 5, the magnitude of the magnetic field, measured by using the SQUID magnetometer on the same specimens, is shown. Even though, these signals were

obtained with a non-contact technique, the distance between the sample and the sensor is at least 8 mm, it is possible to distinguish three different defects due to the various impact energies. Considering Figure 5, it should be noted that the eddy-current technique utilizing an HTS dc-SQUID magnetometer is able to reproduce the surface profile of the specimens even for large stand-off between the probe and the sample. This result emphasizes the high sensitivity of the SQUID magnetometer in measurements where there is a large variation in lift-off.

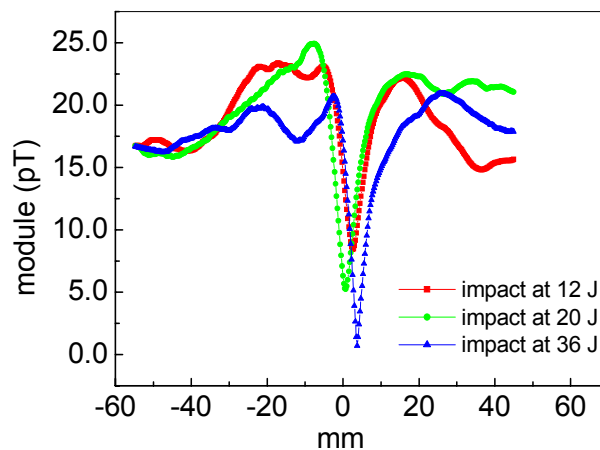


**Figure 5:** The magnitude of the magnetic field measured using an HTS SQUID for samples damaged at 12 J, 20 J and 36 J.

The failure analyses carried out on the specimens impacted at  $U = 12$  J revealed that, apart from the plastic deformation of metal sheets, damage consists essentially of delamination between the fibreglass layers, matrix microcracking in the fibreglass, and debonding at the fibreglass-aluminium interfaces. In figure 6 a fiber glass aluminium layer of a damage sample, after the removal of the aluminium layer is reported. The black arrow shows the fiber glass failure.

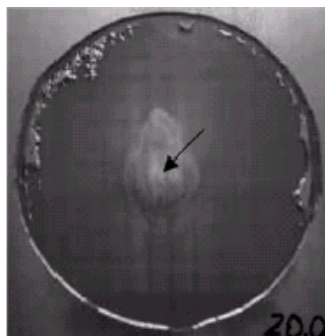


**Figure 6:** Fibre failures in the composite layers far from the impact point.

At  $U = 20 \text{ J}$ , the bottom aluminium sheet is cracked (Figure 7(a)), and damage was generated in the reinforcing fibres. Increasing the impact energy up to  $36 \text{ J}$ , crack is produced in the aluminium sheet located in the middle of the laminate (Figure 7(b)).

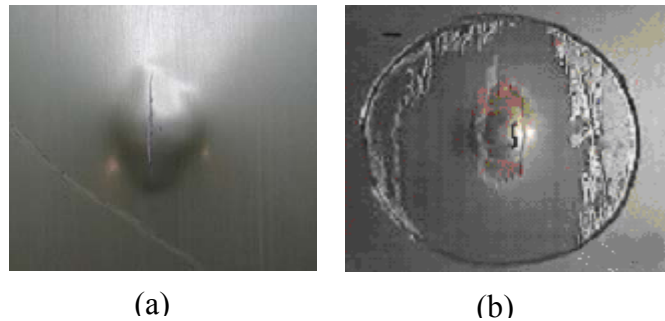


**Figure 7:** Cracks (a) in the bottom aluminium sheet at 20J, and, (b) in the central aluminium sheet at 36 J.

Of course, the detection of cracks in the metal sheet located in the middle of the laminate requires a suitable inspection method. The same holds for the crack in the bottom sheet, when it is inaccessible from the surface structure. For this reason a visual inspection is insufficient to distinguish simple deformation from the cracking of the hidden metallic sheets.

As it can see in figure 7(a) the indentation due to the impact appears in plane with an elliptical shape. Thus, for each damage impact the indented area could be characterized by a major and minor axis, which identifies the damage dimension. Moreover the crack in the aluminium surface usually has longitudinal to the major axis of the indented area, as shown in figure 7(a). Therefore, it is interesting to analyse the specimens following two different directions, longitudinal and transverse to the major axis, measuring the  $B_y$  and  $B_x$  magnetic field component, respectively. In figure 8 a schematization of the defect and the direction in which they has been scanned is reported.

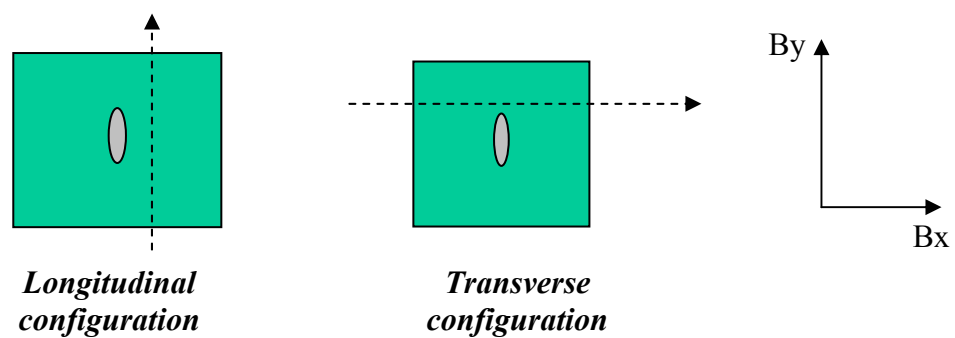


**Figure 8:** the two configurations used in the electromagnetic SQUID based technique.

At first the longitudinal configuration has been considered, to scan the damaged samples in the electromagnetic investigation based on HTS dc-SQUID magnetometer.

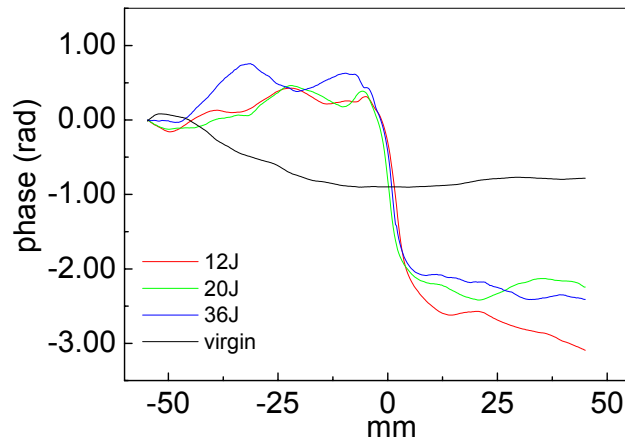


**Figure 9:** Phase of the magnetic field related to the virgin and damaged samples.

In Figure 9 the magnetic field phase (by means  $\theta = \text{tg}^{-1}$  that can be written as  $\frac{\text{Im}(B)}{\text{Re}(B)}$ ), ranging between 0 and  $2\pi$ , and measured by the SQUID system is shown. The phase shape presented in Figure 9 demonstrates that the phase signal is directly linked to the structural integrity of the specimens. It should be noted that the samples impacted at 12 J, 20 J and 36 J have a significant phase variation respect to the phase of the virgin sample.

To correlate the impact energies with the magnetic signals the phase derivative is calculated. The phase derivatives of the virgin and damaged samples are shown in figure 10(a). An enlargement related to its peak is shown in figure 10(b). The latter shows that the minimum value of the phase derivative increases with the impact energy.

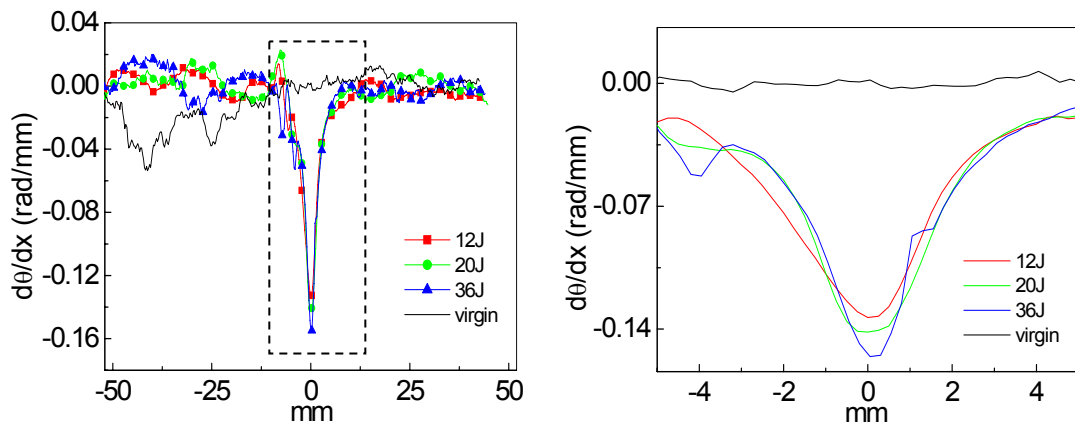


**Figure 10:** (left) The magnetic field phase derivative where the rectangular dot area represents the peak enlargement shown at right.

The relation between the magnetic phase and the damage features can be estimated considering the minimum of the magnetic phase derivative calculated in the range  $(0, 2\pi)$ . The minimum value as a function of the impacted energies is reported in Table 1.

Table 1: Correlation between the energy impact and the minimum of the  $d\theta/dx$ .

Impact Energies (J)	Minimum of the $d\theta/dx$
12	-0.13342
20	-0.1417
36	-0.15565

The characterization of the damage produced into the FGA specimens has been carried out considering measurements on a large range of the energy impact, from 5J to 36J. The relation between the increasing energy impact value and the magnetic field signal has been obtained. It has already seen in table 1 that the magnetic field derivative can be considered as a suitable parameter to distinguish three degree of damage due to the energy of 12J, 20J and 36J.

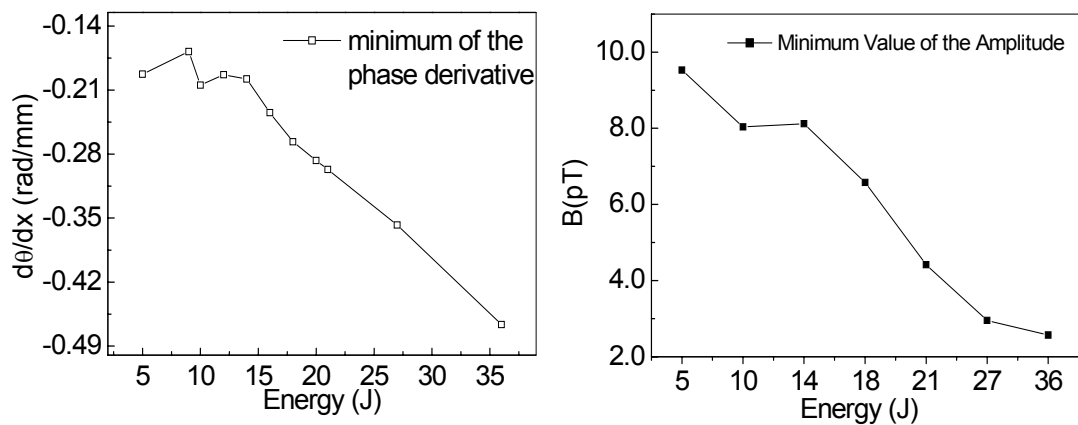


**Figure 11:** (left) and (right) Behaviour of the  $d\theta/dt$  and the minimum of the amplitude of the magnetic field versus the energy impact value, respectively.

In figure 11 the trend of the magnetic field phase derivative (Figure 11 (a)) and the minimum of the magnetic field amplitude (Figure 11(b)) versus the value of the impact energy, are reported. It is interesting to note that both the parameter follow the same behaviour. The magnetic field components, phase and amplitude, decrease when the energy impact increases. Since increasing the energy impact the residual deformation increases, a variation of the lift off that means a higher deformation of the specimen is produced. As a consequence the distance between the current source and the SQUID magnetometer increases, so that the minimum of the magnetic field amplitude goes

down. This effect is reflected in to a minor variation of the phase signal as shown by the  $d\theta/dx$ . Moreover, another effect a part from the lift off variation contributes to decreasing the magnetic field, it is the crack of the aluminium layers. When a crack appears in the sample, the conductivity of the material decrease in that area and it means a decreasing of the magnetic field signal. Obviously, in the SQUID detection this two effects are overlapped but at the same time they contribute to a variation of the signal.

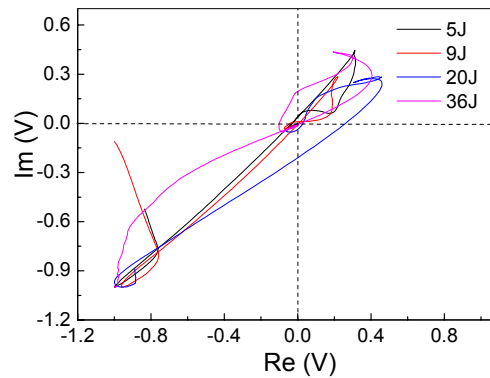


**Figure 12:** The impedance plane of the SQUID magnetometer response changing the impact energy.

The impedance plane representation of line scans related to the samples damaged at 5J,9J, 20J and 36J are presented in figure 12. It could be noted that the signals of the 5J and 9J samples are parallel, it is due probably to the fact that both are only deformed, without any cracked layer. Instead the line scan of the 20J and 36 J are different one another and differ also from the previous two line scans. These two last samples, in fact, present a cracking layer, the 20J damage sample has the inner aluminium layer damage, whereas the 36J specimen has the inner and the rear aluminium layer cracked. A suitable parameter that allows to distinguish the effect of the structural deformation from the irreversible damage could be the slope of the signal of the impedance plane. Therefore an estimation of the ratio  $Im(B)/Re(B)$  of the line scan represented in the impedance plane has been evaluated. The results versus the energy impact are shown in figure 13.

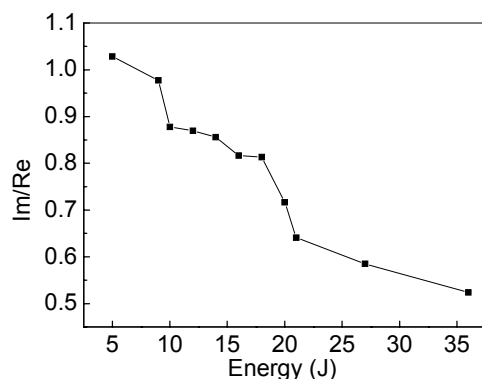


**Figure 13:** Behaviour of the  $Im/Re$  ratio versus the energy impact.

Also the slope of the curves reported in the impedance plane shows a decreasing of the response when the energy impact increases. Therefore, it is possible to assert that the response of the SQUID based prototype goes down while the energy impact increasing, so that a more damaged samples produce a lower magnetic field signal than the only deformed samples.

These results are confirmed also by the transverse configuration as reported in figure 14. In the latter, the trend of the minimum of the magnetic field amplitude decreases respect to the energy impact. Moreover, this configuration gives further information represented by the three different slopes that characterize the curve.

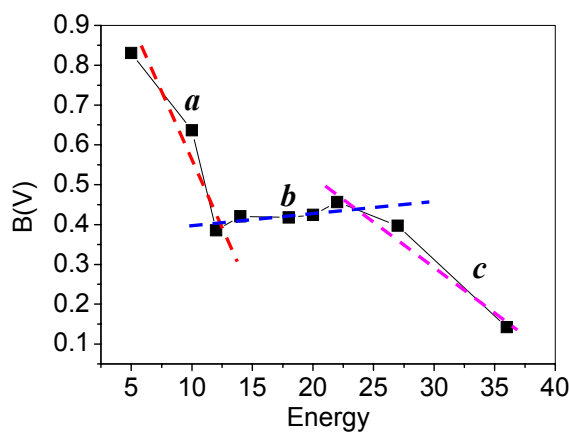


**Figure 14:** Minimum of the magnetic field amplitude versus the energy impact.

The slope *a* represents the range of the energy that produce only deformation, the range *b* includes the samples that undergoes a fracture of the inner layer and finally the *c* slope coincides with the energy impact that damage also the rear surface of the specimens. The energy range highlighted by the SQUID inspection is in agreement with the estimation of the mechanical analysis, based on the relation load-displacement [1].

The magnetic imaging of the damaged samples has been carried out. Figure 15 shows the magnetic imaging of an 80 mm x 100 mm scan over samples damaged at 5J and 36 J. The map represents the derivative  $dB_x/dx$  of the magnetic field measured by the HTS SQUID magnetometer. The dark area corresponds to the plastic deformation of the sample surface. In particular, the shape of the dark area can be correlated with the crack at the back surface.

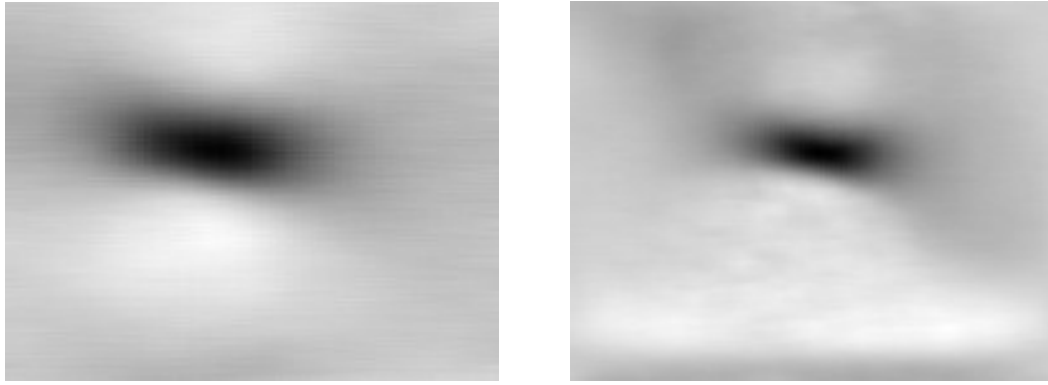


**Figure 15:** (left) and (right)  $dB_x/dx$  of the magnetic field imaging of specimens damaged at 5J and 36J, respectively.

It could be noted that the dark area in the map related to the 5J impacted sample has amplitude lower than the corresponding dark area of the 36J damaged sample. It means that at 36J the indentation is deeper than the 5J, and observing the white area down the dark spot, a permanent deformation that involves also the borders of the sample can be detected. Finally, from the imaging representation is not possible to distinguish the only deformed sample (5J) from the cracked one (36J), but an interpretation of the magnetic field maps can give qualitative information about the degree of the damage.

## 2. Modelization of corrosion activity in fiber-glass laminates

The fiber-glass laminates during the in service life could be affected by corrosion, localized in the impact area of the sample that can increase the material degradation process. The corrosion process converts the metal into its oxide or hydroxide forms, resulting in deterioration of its mechanical properties. Corrosion in aluminium alloys surfaces can often be recognized by dulling or pitting of the area, and sometimes by white or red powdery deposits. As a consequence of corrosion activity the corroded surface can be deteriorated or a concentration of corrosion products could appear on it.

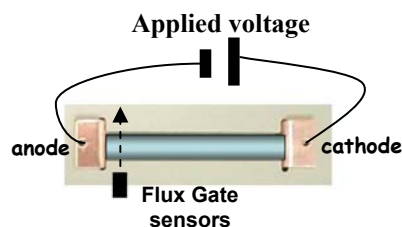


**Figure 16:** Schematisation of the rectangular cell used to study the effect of the electropolishing activity on the copper surface.

Therefore, to study the corrosion process on the FGA, from an electromagnetic point of view, a rectangular cell, with rectangular copper electrodes and a solution of 55% Phosphoric acid and 45% n-butanol has been used.

The copper electrodes allow to activate a corrosion process in a short time and applying a low voltage values. Using the flux gate sensor the in-plane component of the magnetic field produced by the ions current between the two electrodes has been detected. Moreover, to distinguish the three different stages present in the process: pitting, polishing and gas evaporation, which corresponded to three different corrosion rates, the voltage of 1.5V, 4.5V and 6.5V have been considered [2]. In particular, the pitting and evaporation gas stages (1.5V and 6.5V respectively) correspond to a non-uniform corrosion process, while at 4.5V the polishing regime guarantees a uniform corrosion.

A static measurement of the magnetic field in correspondence of the anode can give information about the rate of the corrosion activity. By using the value of the detected magnetic field an estimation of the corrosion rate and the copper dissolved at the anode, has been carried out.

The dissolved copper at the anode has been obtained using Faraday law:

$$w = \frac{jStM}{nF}$$

where  $w$  is the dissolved copper at the anode,  $S$  is the cross section of the cell,  $t$  is the time during the measurement,  $M$  (63.456 g/mole) is the copper atomic mass and  $F$  (96500 As/mole) is the Faraday constant.

Taking into account that the current density is  $\mathbf{j} = Nq\mathbf{v}$ , where  $N$  is the number of carriers per volume,  $q$  and  $\mathbf{v}$  are the carrier charge and its speed, the corresponding magnetic field is:

$$B = \frac{\mu_0}{4\pi} q \frac{v}{r^2} = \frac{\mu_0}{4\pi} q \frac{jV}{nqr^2} = \frac{\mu_0}{4\pi} \frac{jSl}{nr^2}$$

By using the above equation it is possible to write the number of carriers as a function of the magnetic field  $B$ :

$$n = \frac{\mu_0}{4\pi} \frac{jSl}{Br^2}$$

Considering the above relation the Faraday law became:

$$w = \frac{4\pi B_x M r^2 t}{\mu_0 l F}$$

Then, dividing the **w** to the time **t** the corrosion rate is calculated.

In the table 1 and 2 are summarized the results obtained changing the width of the electrodes in correspondence of two potential values 4.5V and 6.5V. The value obtained using the magnetic field has been compared with the weight of the anode measured by means of a balance before and after the magnetic detection.

Table 1: Corrosion rate and dissolved copper at 4.5V

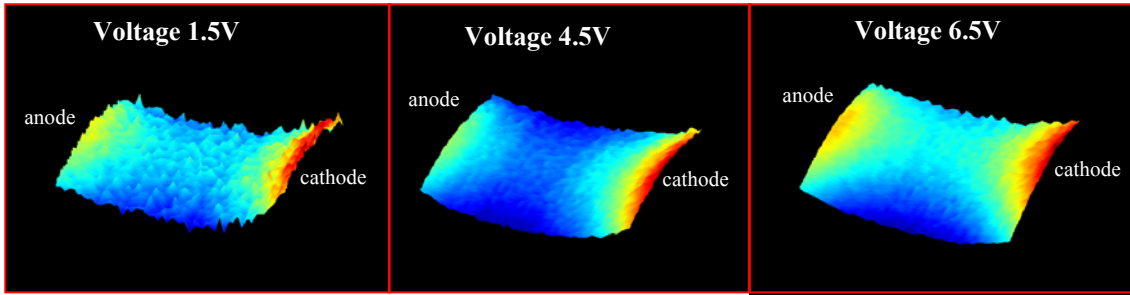
Cell width(mm)	w[g] at 4V by balance	w[g] at 4V by B <sub>x</sub>	w/t [g/s] at 4 V
8	0,012	0,011	4,00E-05
16	0,023	0,020	7,60E-05

Table 2: Corrosion rate and dissolved copper at 6.5V

Cell width (mm)	w[g] at 7V by balance	w[g] at 7V by B <sub>x</sub>	w/t [g/s] at 7 V
8	0,025	0,048	8,20E-05
16	0,035	0,020	1,17E-04

The data of the tables 1 and 2 show at 4.5V a good agreement between the balance and the magnetic field estimation of the corroded copper (the difference is less than 2%), while at 6.5V there is a relevant discrepancy between the data. It could be considered as a demonstration of the different regime of corrosion process that happens at 4.5V (uniform corrosion of the surface), and at 6.5 (prevalently pitting of the surface). It could be noted that a larger surface has a higher corrosion rate in both potential regimes. Moreover, it has been demonstrated that the magnetic field measurements can give information about the rate of corrosion and is able to monitor the effect of the corrosion activity that degrade the metallic surface, with the main advantage of contact-less and non invasive method. Moreover the proportionality between the magnetic field and the corrosion activity in terms of current between the electrodes has already been demonstrated [2,3]

Dynamic measurement of the magnetic field has been carried out to obtain an imaging of the corrosion process between the electrodes. The magnetic field imaging has been measured for each voltage moving the sensor along the length of the cell (50mm).



**Figure 17:** Magnetic field distribution of the rectangular cell in the three potential regime 1.5V, 4.5V and 6.5V.

In figure 17 the magnetic imaging of the rectangular cell, at the three different potential drops are reported. The magnetic field imaging changes respect to the voltage, and reflecting a more chaotic process at 1.5V, represented by the discontinuities of the magnetic field, instead a more uniform activity at 4.5V. At 6.5V the magnetic field on the cathode is higher than the other two voltages that mean a more accumulation of the corroded products. These three regimes are confirmed in the literature by the study of the current to voltage characteristic related to the electropolishing process [2].

It is not very simple to extrapolate information about the corrosion process from the magnetic field distribution. For this reason it is necessary to invert the magnetic field distribution to represent the corresponding current distribution, which reflects the electrochemical activity in the cell.

In general, the inverse magnetic problem does not have a unique solution but in the case of two dimensions geometry it can be solved uniquely. To obtain the current density distribution during the copper electropolishing of the rectangular cells, the mathematical technique based on the Fast Fourier Transform (FFT) has been applied. The magnetic inverse technique applied in this work to the electropolishing process of rectangular cells has been used successfully in other applications and it is described in detail by B. J. Roth et al [4].

To calculate the current density from the magnetic field data the rectangular cell has been approximated to a finite short dipole, which generates a magnetic field expressed by Biot-Savart law:

$$B(r) = \frac{\mu_0}{4\pi} \int \frac{J(r') \times (r - r')}{|r - r'|^3} d^3 r'$$

where  $J$  is the current density that produces the field and  $r$  the distance where the magnetic field is measured. The configuration of the Flux-Gate sensors allow to measure only the in plane components of the magnetic field, in this case the  $B_y$ , so the previous expression becomes:

$$B_y(x, y, z) = \frac{\mu_0}{4\pi} l \cdot z \cdot \iint \frac{J_x(x', y')}{[(x-x')^2 + z^2]^{3/2}} dx' dy' \quad (8)$$

In the formula above  $l$  and  $z$  are the length of the cell and the distance between the probe and current source, respectively. It could be noted that measuring the  $y$  component of the magnetic field,  $B_y$ , it is possible to obtain only the corresponding  $x$  component of the current density,  $J_x$ . Moreover, the  $B_y(x, y, z)$  equation represents the convolution between the current density  $J$  and Green function  $G$ , the latter expressed by:

$$G(x-x', y-y', z) = \frac{\mu_0}{4\pi} l \cdot z \cdot \frac{1}{[(x-x')^2 + z^2]^{3/2}}$$

By using the convolution theorem it is possible to rewrite the equation (8) in the Fourier space as:

$$b_y(k_x, k_y, z) = g(k_x, k_y, z) \cdot j_x(k_x, k_y)$$

where the  $b_x(k_x, k_y, z)$ ,  $j_x(k_x, k_y)$  and  $g(k_x, k_y, z)$  are the two-dimensional Fourier transforms of the magnetic field, the current density and the Green's function, respectively. The variables  $k_x$  and  $k_y$  are the components of the spatial frequency  $K$ . Then the current density in the Fourier space is given dividing the magnetic field by the Green's function:

$$j_x(k_x, k_y) = \frac{b_y(k_x, k_y, z)}{g(k_x, k_y, z)}$$

Finally, the current density distribution  $J_x$  can be obtained by the inverse Fourier transformer of the  $j_x$ .

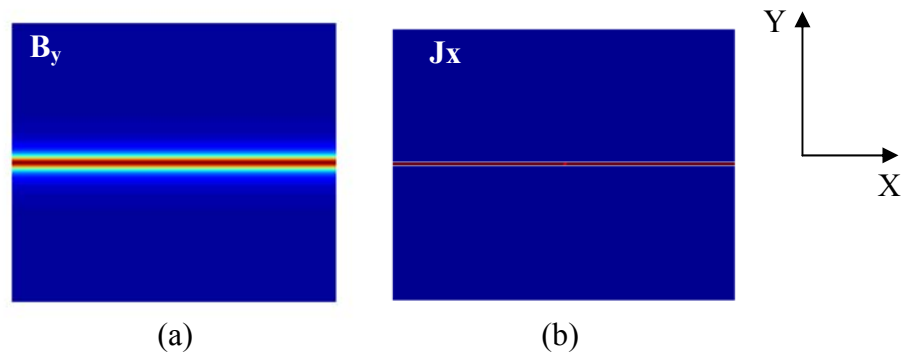


**Figure 18:** (a) and (b) Magnetic field component  $B_y$ , and its corresponding current distribution  $J_x$  generated from a wire with length  $l$  and parallel to the  $X$ -axis are reported, respectively.

This model has been tested at first for a magnetic field produced by a finite wire. In figure 18 (a) and (b) the magnetic field and its corresponding current distribution are shown, respectively.

The distribution and value of the current obtained applying the FFT algorithm is in agreement with the expected data.

The current distribution due to the corrosion process of the rectangular cell in correspondence of the three voltage values is reported in figure 19. These maps represent the current distribution of the magnetic field shown in figure 16.

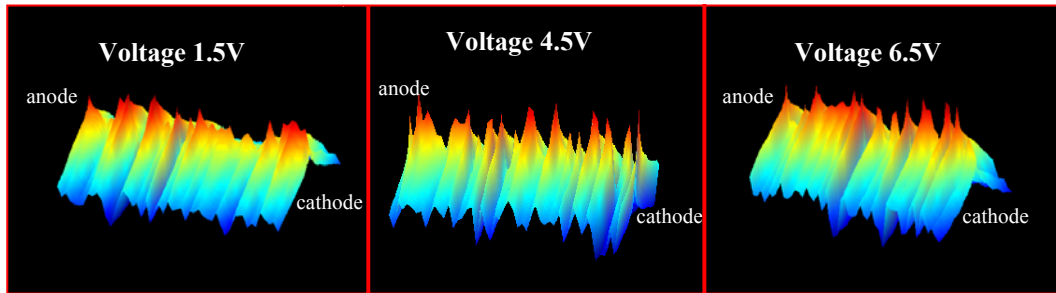


**Figure 19:** Current distribution obtained applying the FFT algorithm to the magnetic field measurements reported in figure 2.

It could be noted that the current distribution at 4.5V (Fig.4 (b)) is uniform along the total length of the cell, because of the uniform corrosion activity that characterize this potential value. Moreover, the other two current distributions reflect the non-uniformity of the activity at 1.5V and the higher density of corroded products at 6.5V.

Starting from these results about very simple cell geometry another electrode configuration has been used to approximate the shape of the FGA impacted surface, where the corrosion process could take place.

A picture of the cell is reported in figure 20. it is characterized by shaped and flat electrode, the anode and the cathode, respectively. This geometry is used to approximate the elliptical shape of the deformation produced by the impact loading on the aluminium layers.

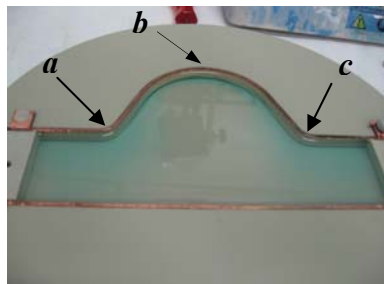


**Figure 20:** Picture of the cell geometry that approximate the deformation due to the impact loading on the aluminium surface. *a*, *b* and *c* arrows indicate the concavity of the electrode surface.

Applying a potential drop of 5V, between the electrodes, the electropolishing process has been monitored moving the flux gate sensors across the cell. The magnetic field

imaging is shown in figure 6. the geometry of the shaped electrode is very clear, in particular the two different magnetic field values (red and blue) are due to the current direction on the copper surface.

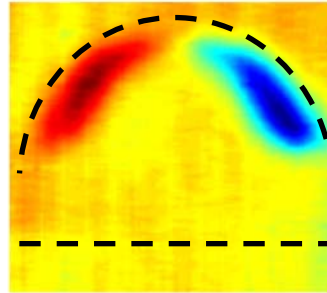


**Figure 21:** Magnetic field imaging of the cell with shaped and flat electrodes. The dashes lines represent the position of the electrodes.

Applying the FFT technique, considering a suitable Green's function related to the cell geometry, the current distribution across the anodes has been calculated. In figure 22 the current distributions related to the map in Fig.21 is reported.

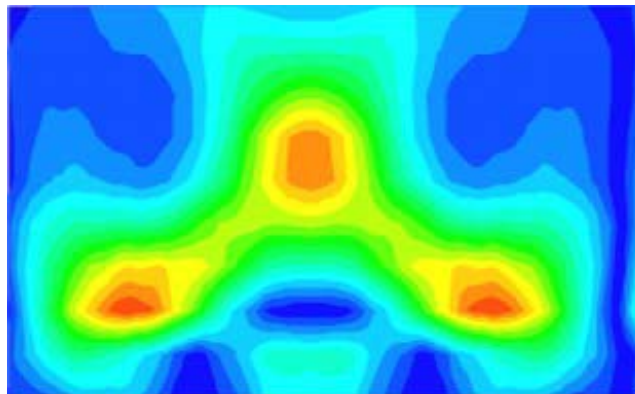


**Figure 22:** Current distribution obtained using the FFT method.

The three red spots represent the point in which there is a major current accumulation that is the concavity of the electrode surface. It is interesting to note that the electromagnetic inversion algorithm can give the current distribution even when the geometry is quite complex. Although, these measurements have been carried out on a mock up, the results can be useful for the study of corrosion process on FGA composites.

Finally, it can be noted that static and dynamic electromagnetic measurements are suitable methods to detect the two main effect of the corrosion activity: the removal of the material and the accumulation of the corrosion products. At present the experimental

set up to study the ongoing corrosion on the impact area of FGA sample is realized and the magnetic measurements are in progress.

### **3. Conclusions**

The electromagnetic characterization of the fiber-glass laminates has been focused on the impact damage detection and the study of the corrosion activity that can take place into deformed area due to impact process of this material. Concerning with the study of the damage due to impact loading the magnetic field detection is a suitable method to estimate the different degree of damage, even when the surface sample presents a high deformation that interest not only the impacted point but it is extended until the borders of the sample. Even if the deformation produces a variation of lift-off up to 10 mm, between the test sample and the HTS d.c. SQUID magnetometer, the SQUID high dynamic range produces high amplitude of magnetic field signal, and allows to distinguish the different deformation without loss its sensitivity. This represents a demonstration of the SQUID sensor superiority respect to the conventional induction coil in the eddy current applications, where high variation of lift off occur and low frequencies are request to detect deep defects.

The magnetic field phase derivative and the minimum of the magnetic field amplitude can be considered suitable parameters to detect defects due to different energy impacts. The value of these two parameters decreases when the energy impact increases, it means that when the deformation degenerates into a laminar cracking the magnetic field signals decreases. This effect is due to the overlapping of two effects: the variation of lift off and the presence of the defect. The latter produces a decreasing of electrical conductivity in correspondence of the cracking, as a consequence the magnetic field signal become lower.

The behaviour of the magnetic field signal as function of the phase and amplitude is confirmed by the magnetic field impedance plane representation. Reporting the ratio  $\text{Im}(B)/\text{Re}(B)$  versus the energy impact it has been shown as this parameter decreasing respect to the energy. Therefore, the variation of the imaginary component of the magnetic field respect to the real component can give information about the severity of the damage.

Moreover, detecting the magnetic field component orthogonal to the cracking of the aluminium layers it is possible to distinguish three different damage stages. The

component of the minimum of magnetic field amplitude is particularly sensitive to the different signal responses produced by the deformation and the cracking of the aluminium layers.

It has been demonstrated that the electromagnetic inspection on samples, impacted with increasing energies, can distinguish the energy ranges that produce fracture of the furthest metallic sheet and the cracking of an intermediate one. This feature allows us to investigate the mechanical tolerance of fibreglass/aluminium laminates thanks to a non-contact and non-destructive technique.

The fiber-glass laminates are degraded not only by the impact loading, but corrosion damage can alter their mechanical properties too, mainly in the area damaged by the impact. Therefore, to test the capability of the electromagnetic methods to give information on the corrosion activity, a copper made mock up has been realized and measured. It has been demonstrated that the magnetic field response can give information about the dissolution rate of the copper surface. Moreover, it is possible an estimation of as much copper as is dissolved using the Faraday law and the static measurements of the magnetic field signal. In this way an estimation of the removed material on the metallic surface can be obtained measuring the magnetic field amplitude. An electromagnetic inversion using the FFT method has been carried out at first to obtain the current distribution between the electrodes into a rectangular cell. After this test the current distribution corresponding to a magnetic field measured into a cell with a shaped geometry has been obtained. The shaped geometry allows to approximate the shape of the impacted surface of the FGA, where the corrosion activity can take place more easily. The calculated current distribution reproduces successfully the current activity on the shaped electrode. These results demonstrate the sensitivity of the electromagnetic monitoring of the ongoing corrosion using magnetic sensors. Moreover, further experimental measurements of the ongoing corrosion of FGA samples using the described methods are in progress.

## References

- [1] G. Caprino, G. Spatarob, S. Del Luongo, "Low-velocity impact behaviour of fibreglass–aluminium laminates" *Composite Part A*, 35, 605-616 (2004).
- [2] C.Bonavolontà, F.Laviano, V.Palmieri, M.Valentino, "Application of flux-gate magnetometry to electropolishing", in "Proceeding of the Workshop on RF Superconductivity 2003", held in Lubecca (Germany).

[3] V. Palmieri, F. Stivanello and M. Valentino, "Flux-gate Magnetometry: the possibility to apply a novel tool to monitor Niobium Chemistry", in "Proceedings of the "Ninth workshop on RF Superconductivity", B. Rusnak ed., held on Nov 1-5, 1999, Santa Fe' NM, USA.

[4] B. J. Roth, Sepulveda, Wikswo Jr,"Using a megnetometer to image a two-dimensional current distribution" in J.Appl.Phys, January 1989).

## CONCLUSIONS

The electromagnetic characterization of the CFRPs composites and fibreglass aluminium (FGA) has been carried out. Since the damage process in these composites principally interest the interface between matrix and fiber and the adhesion of aluminium and fiber-glass layers, a particular attention has been dedicated to the study of the impact loading effect on composites inter-phase. An electrical, electromagnetic and microscopic characterization of the CFRPs has been carried out.

Electromagnetic characterization demonstrates the electrical anisotropy of CFRPs material. By using the four probes technique the unidirectional CFRPs has been characterized respect to the longitudinal and transverse electrical resistance. The estimated values of the electrical resistance for longitudinal, transverse and cross-ply resistance are in agreement with the literature data. The measurements have demonstrated that the sample thickness and the orientations of the fibers, that represents the only conductive component respect to the insulated matrix, playing an important role in the estimation of the electrical resistance. Moreover, it has been shown that with a constant fiber volume fraction, increasing the specimen thickness the conductivity decreases. Thanks to the estimation of the electrical conductivity of the CFRPs others properties have been analysed, such as the CFRPs electromagnetic shielding capability, and the electromechanical effect which arises when a tensile or compressive stress is applied to the carbon fibers. Although, these properties partially have been already revealed in the CFRPs, the improvement of this work concerns the technique used to analyse them. Whereas to study the electromechanical effect or the shielding capability of the carbon reinforced composite, complex set up and invasive sensors, that need to be in contact with the fibers, are usually involved, the electromagnetic characterization, performed with the SQUID magnetometer prototype, represents a non-invasive and contact-less technique.

The measurements of the eddy current SQUID based prototype, related to the bending stress applied to CFRPs samples, demonstrate that an electromechanical effect is present thanks the capability of the carbon fiber to change its electrical resistance in the presence of tensile and compressive stress. The fibers displacement, due to the increasing or decreasing of fibers distance, produce a variation of the electrical resistance, that has been detected by the SQUID measurements and confirmed by the four probe technique.

This result shows that the SQUID prototype is capable to measure the very low variation of the magnetic field, produced by the changing of fiber electrical resistance. Moreover, the detection of the electromechanical effect by means of the SQUID's sensor demonstrates the capability of the SQUID magnetometer to detect also early stage damage in the CFRPs.

In this work, concerning the detection of damage in CFRP material, it has been demonstrated that impact damage at very low energy, less than 2J, can be detected by SQUID based system with high spatial and magnetic field resolution.

In the realized zero field detector configuration, the SQUID magnetometer is able to reveal delamination at very low energy, such as 1.8 J, even if it is not visible to naked eyes. This result confirms the superiority of the SQUID sensitivity respect to the conventional induction coil that is not capable to detect this low energy impact damage.

To check the validity of the SQUID magnetic flux representation a comparison with other techniques, such as Eddy Current with induction coil and Ultrasound, has been carried out. Even if the latter diagnostic methods obtain the same results of the SQUID based system, the induction coil shows some limitations. In fact, the main drawback of the Eddy Current with induction coil technique concerns its sensitivity to the lift-off variations that can alter the measurements, while the Ultrasound method needs of a coupling medium, generally the water, to be in contact with the sample. For this reason, the SQUID magnetometer measurements represent an advanced method to detect damage and mechanical stress in the CFRPs, in non-invasive and contact-less way and obtaining the same detection accuracy typical of ultrasound technique.

The results of the microscopic diagnosis (AFM) show that damage, such as delaminations, produce in the composite material a fiber displacement due to the matrix weakening. Therefore, the matrix breaking produces, at early stage of damage, the modification of the fiber position, and successively increasing the stress, the displacement degenerates into the fiber fractures.

This effect has been demonstrated by using the AFM analysis that confirms the presence of the electromechanical effect in CFRPs at microscopic level.

The changing of the fiber position produces a variation of the carbon fiber electrical resistance that “modulate” the eddy current into the sample. Due to this effect the magnetic field can be detected by the SQUID magnetometer. Complementary techniques demonstrate that the damage inside the CFRPs doesn't extend uniformly in all directions, but the damage propagation depends on the fiber orientation. The results

concerned with the CFRPs characterization demonstrate the capability of the prototype based on the SQUID magnetometer to analyse the electromagnetic properties of very low conductive materials, such as CFRPs, in more advantageous way respect to the other traditional non destructive methods.

The second class of composite material analysed in this thesis is represented by the fiber-glass aluminium (FGA) laminates. The electromagnetic characterization of the fiber-glass laminates has been focused on the impact damage detection, and the study of the corrosion activity, that can takes place into deformed layers of this material. The results concerned with the damage, due to impact loading, demonstrate that the magnetic field phase derivative and the minimum of the magnetic field amplitude can be considered suitable parameters to detect defects due to different energy impacts.

The amplitude of these magnetic field parameters decrease when the energy impact increases. It means that when the deformation degenerates into a laminar cracking the magnetic field signals decreases. This is due to the coexistence of two effects: the presence of the crack and the variation of lift-off. A cracking in the aluminium layer produces a decreasing of electrical conductivity, as a consequence the magnetic field signal becomes lower. Moreover, even if the impact produces a variation of lift-off up to 10 mm, between the test sample and the HTS DC SQUID magnetometer, it has been demonstrated by using the SQUID based prototype that the amplitude of the magnetic field is able to distinguish the different sample deformation without lose sensitivity. This result represents a further demonstration of the SQUID sensor superiority respect to the ultrasound and induction coil in the NDE applications.

The magnetic field measurements have been demonstrated that the damage process into FGA is characterized by three different stages: permanent deformation, fracture of internal aluminium layer and cracking of the prone surface. This information is revealed by the minimum of magnetic field amplitude, which is particularly sensitive to the signal responses associated with the deformation and the cracking of the aluminium layers. The results regarded the characterization of the impact damage demonstrate the possibility to study the mechanical damage process using a non-invasive and contact-less electromagnetic technique, such as the SQUID based prototype system.

It has already mentioned that the fiber-glass laminates are degraded not only by the impact loading, but corrosion damage can alter their mechanical properties too.

Therefore, to test the capability of the electromagnetic methods to give information on the corrosion activity, a copper made mock-up has been realized. It has been

demonstrated that the magnetic field response can give information about the dissolution rate of the copper surface and as much copper as is dissolved during a corrosion process. By using an electromagnetic technique an estimation of the removed material on a metallic surface can be obtained measuring the magnetic field amplitude. An electromagnetic inversion using the FFT method has been carried out to obtain the current distribution corresponding to the measured magnetic field. An electrode with a shaped geometry has been considered to approximate the shape of the deformed surface of the FGA, where the corrosion activity can take place more easily.

The calculated current distribution reproduces successfully the current activity on the shaped electrode. These results demonstrate the sensitivity of the electromagnetic monitoring of the ongoing corrosion using magnetic sensors. Moreover, further experimental measurements of the ongoing corrosion of FGA samples using the described methods are in progress.

Finally, in this research activity has been demonstrated that the eddy current SQUID based prototype can be employed successfully into the aeronautical and aerospace industry, to better understand the mechanical properties of these materials and to improve their performance. The results summarized in this work represent a demonstration of the potentiality of a new SQUID based eddy current prototype in the NDE applications. The prototype can become a complementary instrument for non destructive evaluation useful at research level and in the quality control of advanced material used in aerospace industry.